In Situ Transmission Electron Microscopy Investigation of All Solid-state Sodium Batteries

TECHNISCHE
UNIVERSITÄT
DARMSTADT

At the Department of

Materials and Earth Sciences of the Technical University of Darmstadt

submitted in fulfillment of the requirements for the degree of

Doctor of Engineering

(Dr. -Ing.)

Doctoral thesis by

Ziming Ding

Referee: Prof. Dr. Christian Kübel

Co-referee: Prof. Dr. Jürgen Janek

Darmstadt 2024

Ding, Ziming: *In Situ* Transmission Electron Microscopy Investigation of All Solid-state Sodium Batteries

Darmstadt, Technische Universität Darmstadt,

Year thesis published in TUprints 2024

URN: urn:nbn:de:tuda-tuprints-270091

Date of the viva voce 2024.01.30

Erklärung zur Dissertation

Hiermit versichere ich, dass ich meine Dissertation selbständig und nur mit den angegebenen Quellen und Hilfsmitteln angefertigt habe. Die Arbeit wurde bisher keiner anderen Prüfungsbehörde vorgelegt und noch nicht veröffentlicht.

Karlsruhe, 29.11.2023

Ziming Ding

Acknowledgments

The completion of my doctoral thesis has been a transformative journey, and I am deeply grateful for the guidance, support, and inspiration I have received along the way.

First and foremost, I owe a profound debt of gratitude to my esteemed supervisor, Prof. Dr. Christian Kübel, whose unwavering dedication, profound insights, and mentorship have been instrumental in shaping the course of my research. His wisdom and belief in my capabilities have pushed me to reach new heights. I extend my heartfelt appreciation to my second supervisor, Prof. Dr. Jürgen Janke, whose expertise and guidance have been invaluable. His willingness to engage in meaningful discussions and provide critical feedback have enriched the quality of my research.

I wish to express my sincere thanks to Dr. George Melinte and Dr. Yushu Tang, who kindly shared their skills and experience on my experiments and research. With their help I succeeded in the tough doctoral life. I am indebted to the other colleagues and fellow researchers in our group i.e. Ms. Vanessa Wollersen, Dr. Vinga Szabo, Dr. Sabine Schlabach, Dr. Di Wang, Dr. Andrey Mazilkin, Dr. Torsten Scherer, Dr. Svetlana Korneychuk, and Dr. Ali Ahmadian. It's an enjoyable time working and discussing with them. It's my pleasure to have Dr. Kai Wang, Dr. Xiaohui Huang, Dr. Sangjun Kang, Yuting Dai, Maxmilian Töllner, and Lucas Brauch as my colleagues and to enjoy our common doctoral life together at KIT and TU Darmstadt.

I would also like to recognize the study participants, such as Dr. Marcus Rohnke, and Mr. Till Ortmann, who generously shared their time and knowledge. Their contributions have added depth and significance to this thesis.

To my friends and parents, I am deeply grateful for their unwavering belief in me and for standing by me during the most challenging phases of this pursuit. Their encouragement and understanding have been my pillars of strength.

Ziming Ding,

Karlsruhe, 2023

Abstract

All solid-state batteries (ASSBs) utilizing metal anodes such as lithium and sodium hold great promise for achieving high energy and power density, surpassing the safety limitations associated with liquid-electrolyte counterparts. However, the development of commercially viable ASSBs operating at room temperature remains limited. This is primarily due to the sluggish kinetics and solid-solid interfacial issues that impede the performance of batteries. Among the various interfacial challenges, the growth of dendritic structures leading to cell failure is a persistent problem that cannot be mitigated solely by the initially anticipated high elastic modulus of solid electrolytes (SEs) for ASSBs. Despite significant progress in understanding the filamentary growth mechanism in lithium metal based ASSBs using inorganic SEs, the understanding of sodium ASSBs remains far from complete.

To gain insights into the microstructural influences on sodium filament growth and Na^+ ion transport, polycrystalline Na-β''-alumina SE was employed as a model material due to its outstanding stability with Na metal. In this work, *in situ* biasing transmission electron microscopy (TEM) measurements were conducted to realize the cathodic sodium deposition at the interface between the Na-β''-alumina and the electrode, as well as grain boundaries (GBs) within Na-β''-alumina TEM lamellas. Based on orientation analysis and composition distribution, the layered crystal structure induces anisotropic Na^+ ion transport under the electric field, significantly facilitating the blockade of Na^+ ion transport at some GBs and consequently influencing the position of Na filament growth. Furthermore, the microstructural evolution of the Au interlayer, which is believed to protect against dendrite growth, was explored during the inhomogeneous sodium deposition using the same *in situ biasing* TEM setup. Notably, while Na-Au alloy particle forms by cathodic sodium deposition, Na-Au interdiffusion occurs at the interface, rather than solely sodium diffusion along the Au interlayer. Sodium diffusion along the Au interlayer leads to alloy formation, while the diffusion of Au towards the sodium deposition site may result in the redistribution of the Au interlayer. Additionally, the Au interlayer exhibits distinct behavior under different conditions, e.g. different bias voltages and layer morphology including the Au interlayer thickness and gap between Au particles.

In addition to investigating interfacial issues in sodium metal based ASSBs, the study on the influence of scanning electron microscopy (SEM) imaging and focused ion beam (FIB) processing on the SEs was conducted to ensure the reliable preparation of TEM samples for *in situ* TEM measurements. The irradiation damage mechanism and the corresponding solution were understood during this investigation.

Table of Contents

List of Figures

List of Tables

List of Abbreviations

ADF	Annular dark field
ACOM	Automated crystal orientation analysis
ASSB	All solid-state battery
ASSNB	All solid-state Na battery
ASSLB	All solid-state Li battery
BASE	Beta-alumina solid electrolyte
BF	Bright field
CBED	Convergent beam electron diffraction
CCD	Critical current density
CEI	Cathode-electrolyte interphase
CSL	Coincidence site lattices
DF	Dark field
EDX	Energy-dispersive X-ray spectroscopy
EELS	Electron energy-loss spectroscopy
ESS	Energy storage system
FEG	Field emission gun
FFT	Fast Fourier transform
FIB	Focus ion beam
FWHM	Full width of half maximum
GBs	Grain boundaries
GIF	Gatan image filter
HAADF	High-angle annular dark-field
HR(S)TEM	High-resolution (scanning) transmission electron microscopy
LCO	$LiCoO_2$
LIB	Li^+ ion battery
LLZO	$Li_7La_3Zr_2O_{12}$
MEMS	Microelectromechanical system
MIEC	Mixed ionic and electronic conductor
NaSICON	Na superionic conductor
NBED	Nanobeam electron diffraction
NMC	$LiNi_xMn_yCo_{1-x-y}O_2$

NVP	$Na_3V_2(PO_4)_3$
NZSP	$Na_{1+x}Zr_2Si_xP_{3-x}O_{12}$
RT	Room temperature
SAED	Selected area electron diffraction
SCLs	Space charge layers
SDD	Silicon drift detector
SEI	Solid-electrolyte interphase
SEM	Scanning electron microscopy
STEM	Scanning transmission electron microscopy
STM	Scanning tunneling microscope
TEM	Transmission electron microscopy
ToF-SIMS	Time of flight-secondary ion mass spectrometry
XRD	X-ray diffraction
ZL	Zero-loss
2D	Two-dimensional
3D	Three-dimensional
4D	Four-dimensional

Chapter 1

1. Introduction

Unsustainable deforestation and consumption of fossil fuels result in excessive CO_2 emissions, widely recognized for their role in inducing the greenhouse effect on Earth. [1-3] According to McKinsey's predictions, electricity, along with hydrogen, would become the largest energy source, accounting for 50% of global energy consumption by 2050. [3] As a result, the development of renewable and clean energy resources such as solar, wind, and tidal energy has gained popularity worldwide. However, these energy resources are time-, weather-, season-, and location-dependent. This has fostered the advancement of energy storage systems (ESSs), particularly rechargeable batteries. Among the various options, Li^+ ion batteries (LIBs) stand out due to their desirable characteristics, including long cycle life and controllable power and energy. [2, 4-6] However, the increasing demand for distributed ESSs, especially at the multi-megawatt (MW) level, presents a challenge for the application of current energy storage devices. Forecasts indicate that global battery demand will exceed 2600 GWh by 2030, with the electric vehicle market driving over 80% of the consumption. [7] Given that high-energy-density LIBs currently dominate the commercial market, the worldwide demand for Li is expected to surge from 292 thousand metric tons in 2020

to approximately 2.5 million metric tons by 2030. [8] This poses a considerable challenge for Li reserves and the cost of LIBs. [9] Consequently, alternative battery candidates and technologies are needed to ensure long-term development goals, reducing reliance on LIBs. It is expected that post Li^+ ion and advanced batteries, under favorable conditions, will make up a large portion of the future battery market. [10]

Na-based batteries, with their lower materials cost (approximately $2,243 pro metric ton for Na metal vs. $ 255,633 pro metric ton for Li metal in 2023 based on Shang Metal Market [11, 12]), abundant mineral resources (around 2.74%), and (almost) comparable electrochemical performance, have emerged as promising candidates, particularly for stationary large-scale ESS applications that prioritize energy density less strongly. [9] Furthermore, all solid-state batteries (ASSBs) have received attention from original equipment manufacturers like Toyota [13] and Samsung [14], owing to their non-flammable components and potential for high energy and power density through the use of Na as a substitute for Li. Similar to their Li counterparts, all solid-state Na batteries (ASSNBs) also offer advantages such as no leakage, no volatile compounds, separator-free design, a wide cathode material selection window, and comparable theoretical energy and power densities (**Figure 1.1**). [15, 16] Furthermore, analogous to Li metal-based ASSBs, Na metal exhibits a high theoretical specific capacity (Na: 1166 mA h g^{-1}) and low reduction potential (Na: -2.71 V vs. SHE). Therefore, Na metal-based ASSBs have the potential to meet industrial requirements for high energy density and are expected to serve as stationary large-scale ESSs.
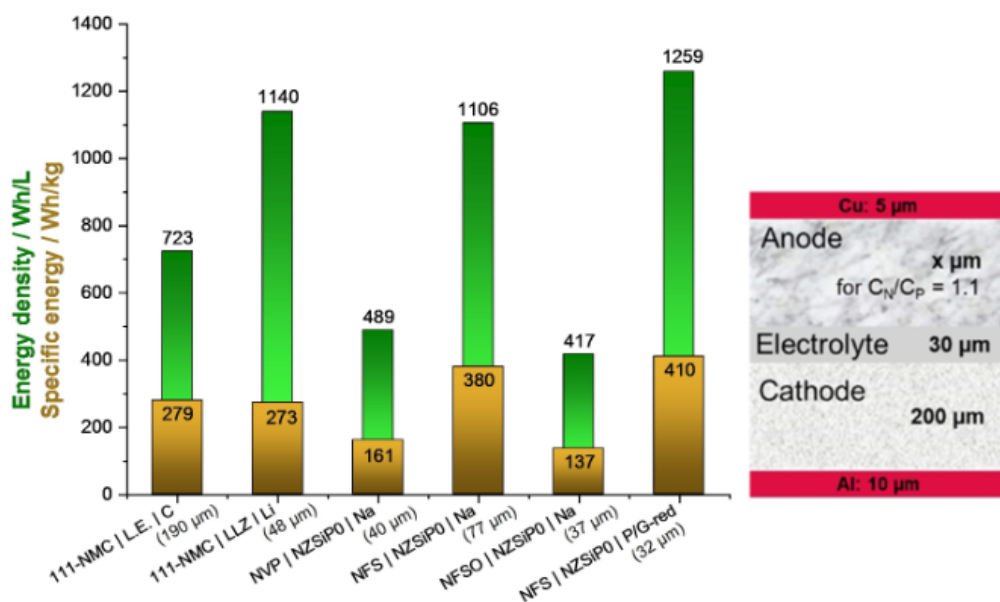
Figure 1.1. Comparison of the energy density (Wh L^{-1}) and specific energy of some Li$^+$ and Na$^+$ ion liquid and solid cells based on the cell architecture on the right side; adopted from [16].

Solid electrolytes (SEs), the key component of ASSBs, have a history dating back to the 1930s when fast 2D Na$^+$ ion-transport was discovered in β-alumina (Na$_2$O-11Al$_2$O$_3$). [17, 18] It was commercially applied in high-temperature Na-S batteries in the 1960s [19] and Na-NiCl$_2$ batteries in the 1980s [20]. Subsequently, the investigation of SEs expanded to other material groups, including oxides, sulfides, halides, and polymers, starting in the 1980s. At present, high ionic conductivity for Li$^+$ and Na$^+$ is achievable in many cases (> 10^{-4} S cm^{-1}) at room temperature (RT), while some outstanding SEs even exhibit an ionic conductivity higher than 10^{-3} S cm^{-1} like Na$_{3.4}$Sc$_{0.4}$Zr$_{1.6}$Si$_2$PO$_{12}$, as high as 4^10^{-3} S cm^{-1}. [16]

Despite the significant advances in increasing the ionic conductivity of SEs, the commercialization of room-temperature ASSBs is still under development. Toyota, for instance, has announced that their ASSB-based electric vehicles may enter the market in 2025. [13] One of the key challenges faced by battery engineers is the presence of severe interfacial problems within all solid-state cells. So far, with the commercial progress of all solid-state Li batteries (ASSLBs), extensive research has been conducted on their interfacial problems and corresponding strategies, e.g. poor physical contact between particles, cathode-electrolyte interphase (CEI) and solid-electrolyte interphase (SEI) formation, and dendrite growth. [21-23] However, the physical, chemical, and mechanical differences between Na and Li necessitate a deeper understanding of the behavior at these interface as the Na metal anode has been demonstrated to behave distinctive from lithium in corresponding

liquid systems. [24] This strongly motivates studying Na metal induced interfacial problems specific to ASSNBs.

In addition, significant interfacial problems are always linked to specific features at different length scales, ranging from atomic to micrometer level, e.g. point defects, grain boundaries, crystal lattice, voids, impurities, and cracks. Averaged structural and chemical information alone is insufficient to fully understand these mechanisms. Moreover, in comparison to liquid batteries, inorganic SE always introduce stronger microstructural features, potentially worsening the interface and subsequently the performance of ASSNBs. [21] Thus, to gain a deep understanding of these interfacial problems in ASSNBs, exploring their microstructure and their evolution down to the atomic level, especially in inorganic SEs during operating, is crucial, as the literature in this direction is scarce. Hence, in this work, *in situ* transmission electron microscopy (TEM) accompanied by analytical techniques is utilized for high spatial and temporal resolution analysis to develop an understanding of interfacial effects and interfacial evolution.

1.1. Inorganic Solid Electrolytes of ASSNBs

The key distinction between liquid batteries and ASSBs lies in the utilization of SEs with solid-solid interfaces to the electrodes instead of liquid electrolytes with isolated porous separators, as illustrated in **Figure 1.2**. The concept of utilizing SEs for ion transport in batteries, with historical applications dating back to the 1960s, has evolved over time. [16] Na-β-alumina, the first generation of commercialized SEs, found applications in Na-S and Na-NiCl$_2$ high-temperature batteries. However, current SE development primarily focuses on achieving functional batteries for application at RT, avoiding additional costs and efficiency reduction associated with maintaining elevated operation temperatures.
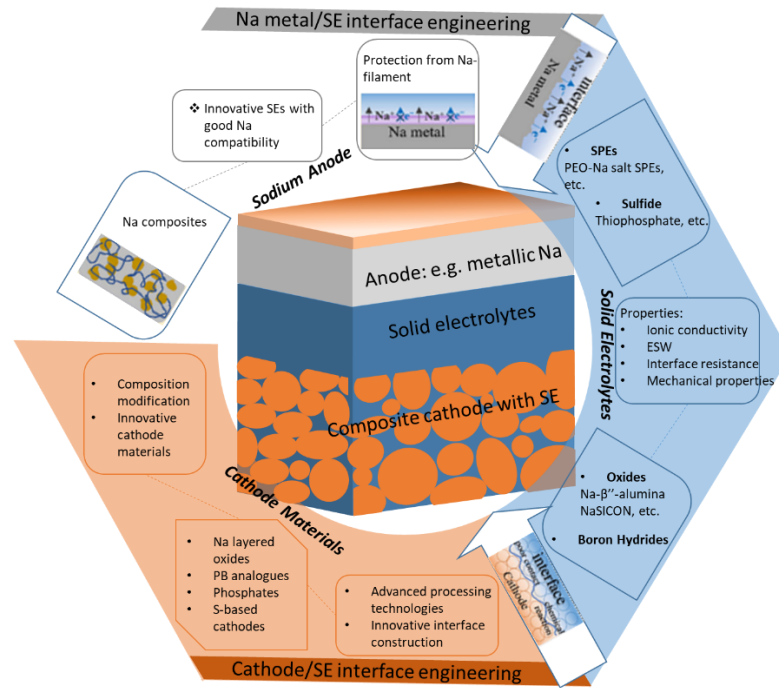
Figure 1.2. Configuration of ASSNBs and study trends, modified from [25].

As a general consensus, SEs should possess a high ionic conductivity exceeding 10^{-4} S cm^{-1} at RT and higher than 10^{-3} S cm^{-1} for a better battery performance [16, 26, 27] and negligible electronic conductivity (ideally below 10^{-12} S cm^{-1}), at least lower than 10^{-8} S cm^{-1}, to prevent self-discharge. [26, 28] In pursuit of improving the ionic conductivity of SEs, a multitude of Na-based SEs, both inorganic and organic materials have been developed. The temperature-dependent ionic conductivities of these SEs are depicted in **Figure 1.3**. Among the extensive range of SEs, inorganic SEs demonstrate relatively high ionic conductivity at RT and a high Na$^+$ transference number (close to 1) in comparison with organic SEs. They are anticipated to exhibit comparable ionic conductivity with liquid electrolytes.
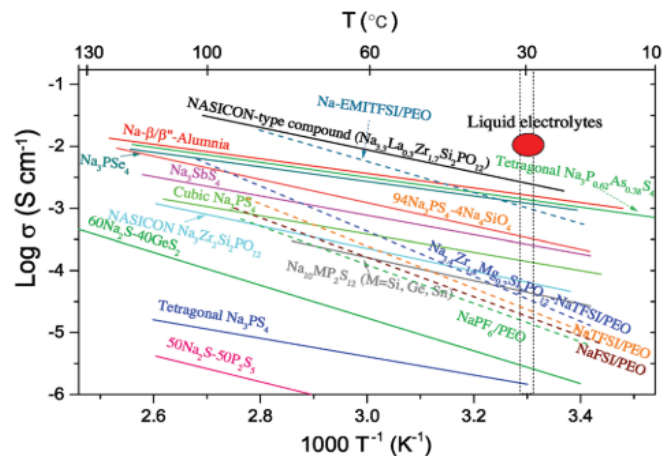
Figure 1.3 Schematic of temperature-dependent ionic conductivity for representative Na-based SE classes. Adopted from [29].

1.1.1 Ion Transport Mechanisms

In inorganic Na-based SEs, ionic conduction relies on the structural characteristics at both the long- and short-range scales. For ionic conduction to occur, mobile species such as Na$^+$ ions or vacancies need to undergo long-range migration, necessitating their movement or hopping from one local site to an adjacent site overcoming the associated energy barrier. The diffusion mechanism of ions in single crystalline regions follows the model for Schottky and Frenkel point defects (**Figure 1.4a & b**), which is termed "direct hopping" or "single-ion hopping". [26] The number of mobile species and their mobility, defect structure, lattice dynamics, and crystal structure fundamentally determine the ionic conductivity, and these factors also affect each other. [30] The Na$^+$ ion conductivity (σ) can be described by:

$$\sigma = q\, n\, \mu \quad \text{with} \quad \mu \propto \frac{1}{T} e^{-E_a/(k_B T)} \qquad \textbf{Equation 1-1}$$

Where n and μ are the concentration and mobility of Na$^+$ ions, q is the elementary charge, E_a the activation energy, k_B Boltzmann constant, and T the absolute temperature. To achieve the goal of SEs with high ionic conductivity, besides increasing the concentration of mobile Na$^+$ ions, the ion mobility should be enhanced by decreasing the activation energy. The activation energy is determined by the energy landscape (**Figure 1.4b**), which mobile ions experience during diffusion in the (crystalline) ion conductor framework. [31-33] By altering lattice parameters, bonding length and strength, the mobility and activation energy can be modulated. For instance, dopant ions with larger radius replacing sites can enlarge the transport path enabling easier ion migration. [34-36]
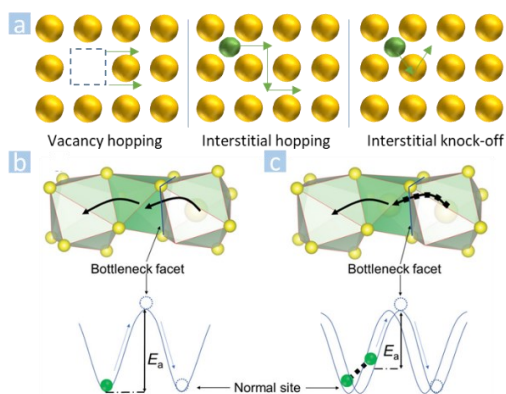
Figure 1.4. Illustration of Na^+ ion migration in inorganic SEs. **a**. Ion migration mechanism; Migration pathways of low (**b**) and high (**c**) concentration of Na^+ ions and the corresponding energy states of Na^+ ions. **b** & **c** are adopted from [30].

Besides the mechanism based on classical "direct hopping", a correlated migration mechanism, called "concerted migration" has also been proposed for the fast ionic conductors. [37] In this case, the SEs possess a high mobile ion concentration and a specific mobile ion sublattice configuration (**Figure 1.4c**), which can be obtained by doping. [32] The Na^+ ion can be activated by the motion of the neighboring Na^+ ion as their strong ion-ion Coulomb interactions in the mobile Na^+ ion sublattice configuration leads to the reduction of its energy barrier as illustrated in **Figure 1.4c** . This is the reason for the high ionic conductivity of the well-known Na superionic conductor (NaSICON, $Na_{1+x}Zr_2Si_xP_{3-x}O_{12}$) at certain compositions with increasing Na^+ ion concentration. [26, 32] Si^{4+} ions partially substitute P^{5+} ions in $NaZr_2(PO_4)_3$ giving rise to the general formula $Na_{1+x}Zr_2Si_xP_{3-x}O_{12}$ (NZSP) with $0 \leqslant x \leqslant 3$. [38] This aliovalent ion-doping introduces interstitial Na^+ ions, resulting in increased concentration of mobile Na^+ ions (**Figure 1.4b & c**). The concerted migration with lower activation energy is achieved via the skeleton of linked ZrO_6 octahedra and $(Si, P)O_4$ tetrahedra (**Figure 1.5a**), which form a 3D transport frame work. However, with increasing Si content, the crystal structure changes from the rhombohedral structure with space group R-3c for $0 < x < 1.8$ at RT in NZSP to a monoclinic with space group C2/c for $1.8 < x < 2.3$, and transforms back to rhombohedral for $2.3 < x < 3$. [39] The distinctive spatial arrangement and structure of the immobile framework of ZrO_6 octahedra and $(Si, P)O_4$ tetrahedra change between the different crystal structures, thus changing their ability to contribute to the Na^+ ion migration path.

In addition to being sensitive to the excess of mobile interstitial Na^+ ions, in some sulfide SEs, e.g. $Na_{11}Sn_2PS_{12}$, the number of available vacant sites also contributes to the conductivity, which may

increase due to doping. [40] It is also worth noting that charged defects may trap Na^+ ions or vacancies because of the electrostatic attraction, impeding Na^+ ion transport. [41] Therefore, the crystal structure together with the variable Na^+ ion distribution and defect structures introducing interstitial Na^+ ions or vacancies significantly impacts the concentration of effective charge carriers.

Furthermore, most inorganic SEs exhibit a polycrystalline nature, which consists of bulk grains and grain boundaries (GBs) in between. Due to the lattice mismatch and disordered structure between adjacent grains, the resistance of ion migration across GBs is typically higher than within the grain itself. [42] Therefore, it is well accepted that the overall ionic conductivity and activation energy of polycrystalline SEs are limited by the small grain size. [42, 43] Moreover, the presence of a space charge layer at GBs has also been proposed as a factor contributing to sluggish ionic conductivity, resulting in a blocking behavior of GBs. [44, 45] Contrary to high migration resistance across GBs, fast ion transport at GBs was reported in some solid sulfide and oxide electrolytes as a low activation energy for diffusion along GBs was shown. [46, 47] These interfacial behaviors of GBs will be discussed in detail in **section 1.2.2**.

1.1.2 Classification of Inorganic SEs

The crystal structure comprises immobile ion frameworks and mobile Na^+ ion sublattices. The distinctive arrangement of the immobile frameworks and the Na^+ ion sublattice leads to variations in conduction pathways for different crystal structures. For example, in oxide-based SEs, 2D conduction planes exist in layered Na-β-alumina and 3D tunnel appear in Na superionic conductors as depicted in **Figure 1.5a & b**, which are introduced more in the following part. Apart from oxide-based SEs, the other category of inorganic SEs is sulfide-based SEs based on the different composition and crystal structure. Furthermore, some complex hybrids (e.g. *closo*-borates and *closo*-carbaborates) have also been reported recently to exhibit high Na^+ ionic conductivity, such as $Na_2B_{12}H_{12}$ and $Na_4B_{10}H_{10}(B_{12}H_{12})$. [48] Apart from crystalline solid oxide and sulfide electrolytes, some glasses also exist, e.g. $Na_2O-Y_2O_3-SiO_2$ [49] and $75Na_2S-25P_2S_5$ [50]. However, since the long-range ordered arrangement of atoms in crystalline ceramics provides well-defined conduction path for Na^+ ions, the crystalline SEs typically exhibit higher conductivity compared to pure glassy inorganic SEs, where the activation energy for Na^+ ion diffusion is higher as they are dominated by single ionic jump mechanisms. [16, 51] To characterize the crystal structure of inorganic SEs, X-ray or neutron diffraction is more commonly used compared to electron

diffraction or high-resolution imaging in TEM, where damage induced by electron irradiation is a challenge. [52-54]
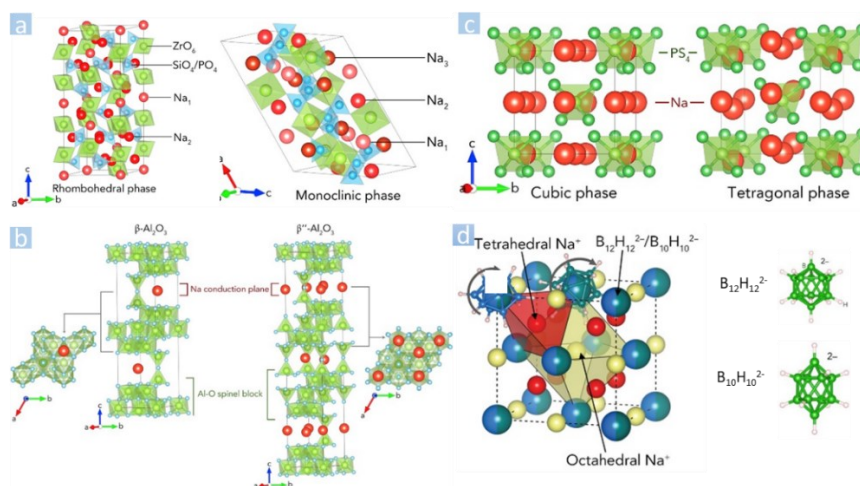
Figure 1.5. Representative crystal structures of some typical inorganic SEs. **a.** NaSICON ($Na_3Zr_2Si_2PO_{12}$) with rhombohedral (left) and monoclinic (right) phase; **b**. β-Al_2O_3 (left) and β''-Al_2O_3 (right); **c.** Na_3PS_4 with cubic (left) and tetragonal (right) phase; **d.** $Na_2(B_{12}H_{12})_{0.5}(B_{10}H_{10})_{0.5}$; Reorganized from [55].

1.1.2.1. Oxide-based SEs

- *Beta-Alumina Solid Electrolyte (BASE)*

Extensive research has been performed on BASE due to its favorable properties, including high ionic conductivity, low electronic conductivity, excellent chemical and thermal stability, and suitable mechanical properties. The structure of BASE consists of alternatively stacked Na^+ ion conduction planes and spinel blocks containing oxygen and aluminum ions. This typical layered structure leads to a 2D Na^+ transport path. Based on differences in chemical composition and stacking sequence, layered BASEs can be categorized into two groups as shown in **Figure 1.5b**: β-Al_2O_3 ($Na_2O \cdot xAl_2O_3$ (x = 8-11), hexagonal; $P6_3/mmc$; a=b=5.58 Å; and c=22.45 Å) and β''-Al_2O_3 ($Na_2O \cdot xAl_2O_3$ (x = 5-7) rhombohedral; $R\bar{3}m$; a=b=5.61 Å; and c=33.85 Å). [56] Compared to β-Al_2O_3, β''-Al_2O_3 consists of three spinel blocks and two Na^+ conduction planes resulting in higher Na^+ content and higher ion conductivity. However, thermodynamically, it is a metastable phase, and impurities such as β-Al_2O_3 and $NaAlO_2$ are typically present from solid-state synthesis (above 1000℃). To prepare state-of-art BASE with high purity β''-Al_2O_3 (>95%), various dopants have been introduced as stabilizers such as Li^+, Mg^{2+}, Ni^{2+}, and Ti^{4+}. [19]

The Na$^+$ ion conductivity of β''-Al$_2$O$_3$ ceramics lies in the range of 0.2–0.4 S cm^{-1}, although the conductivity of β''-Al$_2$O$_3$ single crystals can be as high as $\approx$ 1 S cm^{-1} at 300℃ (**Figure 1.3**). [57, 58] The discrepancy in conductivity between polycrystalline and single crystal samples can be attributed to the high resistance of GBs and the random orientation of the grains, which limit the overall ionic conductivity along the 2D transport path. [59, 60]

- *Na Superionic Conductor (NaSICON)*

Unlike the 2D ion conduction planes in BASE, NaSICON offers open 3D Na$^+$ conduction channels, which are formed by the corner-sharing (Si, P)O$_4$ tetrahedra and ZrO$_6$ octahedra (**Figure 1.5a**). The representative Na$_3$Zr$_2$Si$_2$PO$_{12}$, initially proposed by Goodenough et al. in 1976, exhibits a conductivity in the range of ~10^{-4} S cm^{-1} at room temperature and ~10^{-1} S cm^{-1} at 300℃. [61] To date, the conductivity of NZSP can be enhanced by adjusting the amount of Si$^+$ doping. [39]

Aside from the Si^{4+} substitution of P^{5+} mentioned earlier, an enlargement of the bottleneck size can be achieved by the substitution of Zr with alkaline earth ions such as Mg, Ca, Sr, and Ba. [38] This aliovalent-substitution approach primarily focuses on enhancing the ionic transport within the grain bulk of NaSICON. Furthermore, extensive research has been conducted on adjusting GB contributions by tuning the grain size [62] and chemical composition [63, 64] to improve the overall ionic conductivity. A detailed discussion of these aspects will be presented in **section 1.2.2**.

1.1.2.2. Sulfide-based SEs

Sulfide-based SEs exhibit significantly higher ionic conductivity at ambient temperature compared to their oxide-based counterparts due to the combined effects of the larger ionic radius and higher polarize ability of sulfur compared to oxygen, which weaken the electrostatic interaction between Na$^+$ and the crystal framework. [56] In addition, processability is another desirable factor for the industry. Thiophosphate-based (Na$_3$PS$_4$) electrolytes are commonly studied in sulfide electrolytes. This electrolyte exists in two phases, namely cubic and tetragonal (**Figure 1.5c**). It can transform from the tetragonal phase to the cubic phase at high temperatures. [29] Additionally, sulfides with a NaSICON structure, such as Na$_{11}$Sn$_2$PS$_{12}$ [40] and Na$_{11}$Sn$_2$AsS$_{12}$ [65], have also demonstrated high ionic conductivity.

As the ionic conductivity depends on the defect concentration (Na$^+$ vacancies or interstitials), rather than the phase transformation between cubic and tetragonal structure, doping/substitution of S^{2-} sites or P^{5+} sites can promote the ionic conductivity of sulfide-based SEs. Notably, anion

substitution exerts a more substantial influence on ionic diffusivity compared to cation substitution, as they contribute to enlarging the lattice and weakening the binding energy. For example, the ionic conductivity of $Na_3PSe_{4-x}S_x$ is monotonically increasing with increasing concentration of Se. [66]

1.1.3 Electrochemical Stability Window (ESW)

Despite the significant advancements in the ionic conductivity of state-of-the-art SEs, their practical application remains limited. To operate within a safe voltage range, where the electrolyte is neither oxidized nor reduced, understanding the electrochemical stability window (ESW) provides valuable insights (**Figure 1.6**). A wide ESW is a crucial factor in the pursuit of ASSBs with higher energy and power densities. [67, 68]
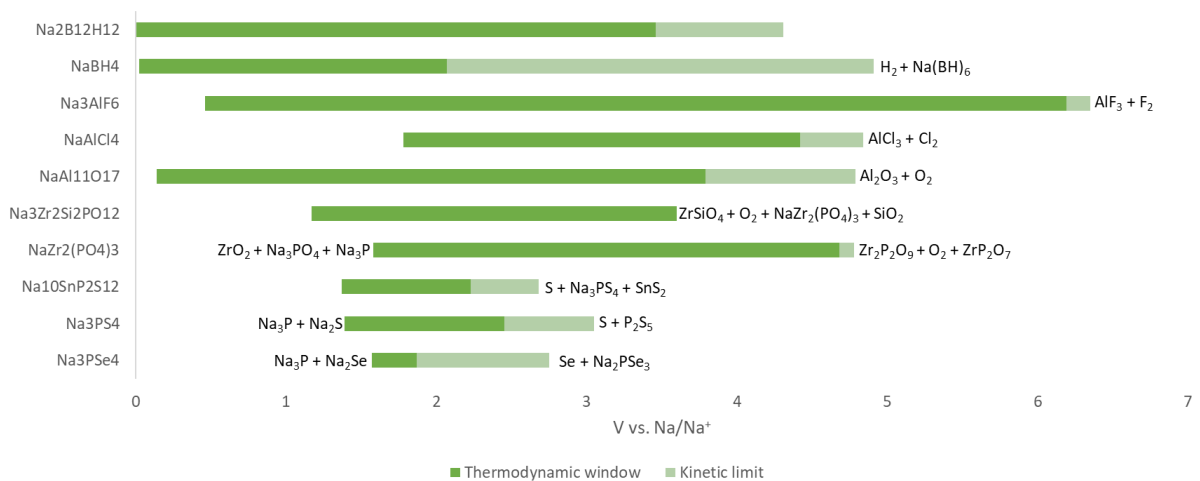
Figure 1.6 ESWs of some representative Na-based inorganic SEs based on thermodynamic calculations. Data reference [69, 70]. Some oxidation and reduction reactions against Na metal are shown.

1.2. Interfacial Problems in ASSBs

Considering the architecture of ASSBs depicted in **Figure 1.2**, the interfaces can be broadly categorized into two types: electrode (cathode/anode)-electrolyte interfaces and electrolyte-electrolyte interfaces. Furthermore, the functional components of an ASSB cell also encompass the current collector and carbon additives to the electrodes, which enhance the electronic

conductivity. However, they introduce numerous interfaces to the electrolyte and the active electrode material, particularly on the cathode side. These components are considered part of the electrode-electrolyte interface. In addition, intrinsic defects in polycrystalline SEs such as voids and grain boundaries (GBs) are considered as electrolyte-electrolyte interfaces. Given that these interfaces possess distinct chemical and physical properties compared to the two bulk components, a range of challenges arises during the operation of ASSBs, including structural, chemical, and mechanical degradation of materials and high charge transfer resistance at interfaces. These challenges have been widely discussed for ASSLBs [22, 23, 71-74] and similar challenges are also observed and expected for ASSNBs. [15, 29, 30, 75]

1.2.1. Electrode (Cathode/Anode)–Electrolyte Interfaces

The properties of electrode-electrolyte interfaces primarily depend on the chemical and electrochemical stability of SEs and, consequently, their compatibility with cathodes and anodes as well as the operating voltage window. A spontaneous chemical reaction may occur when the valence band of an SE lies above the chemical potential of the cathode (μ_c) or if its conduction band lies below the chemical potential of the anode (μ_a). [21, 76] As a consequence, cathode-electrolyte interphases (CEI) form on the cathode side, and solid-electrolyte interphases (SEI) develop on the anode side, analogous to their counterparts in liquid batteries. The battery performance can benefit from conductive SEI/CEI that allows for ion transport while impeding the passage of electrons. However, if the SEI/CEI acts as a mixed ionic and electronic conductor (MIEC), it will continue to grow, leading to the degradation of ASSB cells.

Furthermore, if the operating voltage of ASSBs exceeds the ESW, SEs may undergo oxidation or reduction upon sufficient electronic contact with the cathode/anode, current collector, or conductive additives. This can also contribute to the formation of SEI/CEI and an increase in charge transfer resistance at the interface. As different classes of SE materials exhibit distinctive ESW ranges and decomposed products (**Figure 1.6**) [21], the electrode-electrolyte interface necessitates separate discussions regarding the cathode and anode side as well as the compatibility of electrode and electrolyte materials.

● *Cathode-Electrolyte Interface*

To date, the majority of cathode materials utilized in ASSNBs share similarities with those employed in Na$^+$ ion liquid batteries. Examples for cathode materials include typical layered

oxides (such as $NaCoO_2$ [77], $Na_{0.67}Fe_{0.5}Mn_{0.5}O_2$ [78]), NaSICON-related phosphate (such as $Na_3V_2(PO_4)_3$ (NVP) [79-84], $NaTi_2(PO_4)_3$ [85]), and sulfide (such as MoS_2 [86], Mo_6S_8 [87], and TiS_x [41, 88, 89]). They have been investigated in various ASSB configurations with different SEs. Although oxide-based SEs (NZSP and Na-β″-alumina) and thiophosphate have demonstrated promising performance, the limited deformability of oxide-based SEs and the low chemical stability of sulfide-based SEs affect the charge transfer at the cathode/electrolyte interface (see **Figure 1.7**) and limit their practical application.
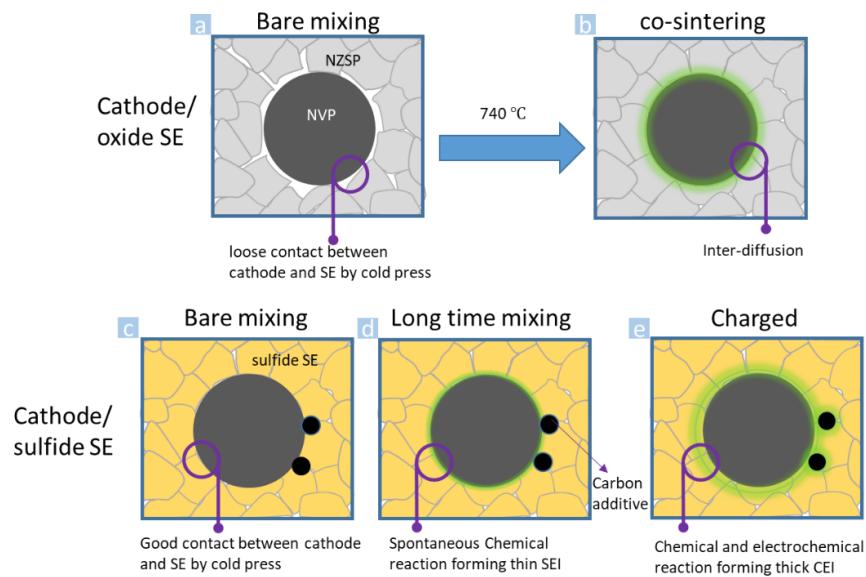
Figure 1.7. interfacial contact between cathode and oxide SE through cold-pressing (**a**) and co-sintering (**b**); interfacial contact between cathode and sulfide SE through cold-pressing for short time (**c**) and long time (**d**); e. the interfacial contact between cathode and sulfide SE as well as carbon additive and sulfide SE. Modified based on [21].

One of the primary issues that leads to poor physical contact and high interfacial resistance at the cathode/electrolyte interface is the presence of voids at the interfaces (**Figure 1.7a**). These voids can originate from the initial fabrication process and cycling-induced effects such as electrode volume expansion and contraction. [90-92] Dzmitry Hlushkou et al. demonstrated that these residual voids not only reduce the available phase volume for ion transport but also increase the tortuosity of the ion transport path, hindering efficient ion diffusion. [93] To enhance the physical contact, a common approach for the cathode is to create a compressed composite consisting of the active material, SEs, and carbon additive or to apply high-temperature co-sintering.

Nevertheless, achieving a void-free dense composite remains a challenge. Even when applying a high pressure ($\geq$ 370 MPa) during cell preparation, it still contains a residual porosity of 10% to 40%, depending on the fabrication pressure and mechanical properties of the electrolyte and electrode materials. [21, 94] In general, among inorganic SEs, sulfides [88] and borohydrides exhibit a more densely packed cell structure compared to oxides due to their lower mechanical strength and hardness (**Figure 1.7a & c**). [30, 95] A hybrid SE approach applied to oxide-based ASSBs has shown promise in improving the physical contact between the cathode and SEs. For instance, in an ASSNB stack $NaCrO_2$ infiltrated with $Na_4(B_{12}H_{12})(B_{10}H_{10})$ │ Na-β''-alumina │ Na, the cathode-electrolyte interfacial resistance was as low as 25 Ω cm^2 after cold pressing at 70 MPa. [96] Apart from high-pressure fabrication, stack pressure has been suggest in numerical studies to prevent contact losses between electrodes, electrolytes, and current collectors during cycling. [94] However, Ying Shirley Meng's group demonstrated that a low operating stack pressure during cycling does not adversely affect the cyclability of sulfide-based ASSBs. [94]

Additionally, high-temperature co-sintering of cathode materials and oxide SEs has emerged as a potential strategy to enhance the contact in Na-β''-alumina- and NZSP-based ASSBs. [78, 83, 97] However, the formation of an interlayer after sintering, resulting from chemical reactions and interdiffusion between cathode and SE at high temperatures, needs to be considered for electrode-electrolyte compatibility. In the case of NVP │ NaSICON │ Na cells, an intimate interfacial contact was achieved by co-sintering of a NVP precursor solution and a porous NaSICON layer. A nanometer-scale interdiffusion layer with V incorporated in NaSICON and Si and Zr in NVP was observed through the scanning transmission electron microscopy-energy dispersive X-ray spectroscopy (STEM-EDX) (**Figure 1.7b and Figure 1.8**). [83]
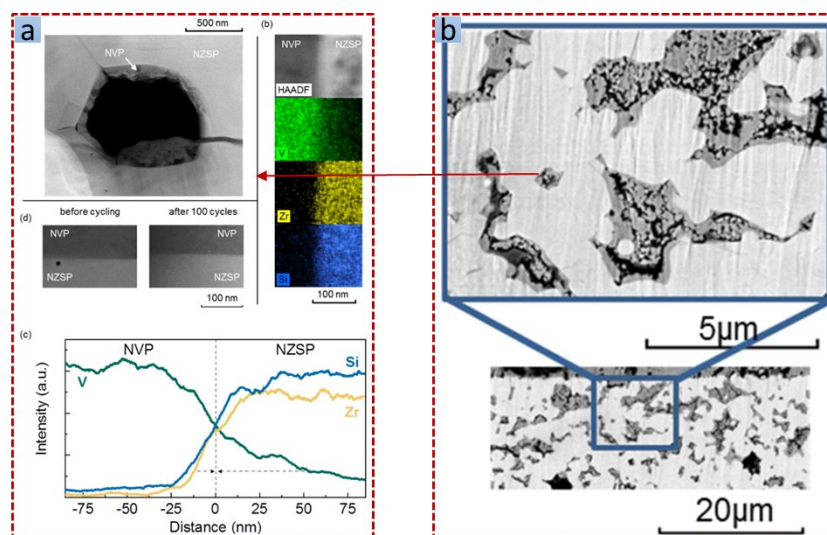
Figure 1.8. a. High angle annular dark field - scanning transmission electron microscopy (HAADF-STEM) imaging and EDX Elemental Mapping for the characterization of the interdiffusion between NVP and NZSP after co-sintering [83]; **b.** SEM imaging for the morphology of the co-sintering cathode composite [83].

Moreover, the formation of a passive layer at the cathode/SE interface due to chemical and electrochemical reactions contributes to the degradation of SEs and an increase in interfacial transfer resistance (**Figure 1.7d & e**). In contrast to the high stability of oxides (**Figure 1.6**), sulfides exhibit limited working potentials due to the decomposition of sulfur-bridging (-S-) diphosphorus compounds and sulfur at the CEI. [21] When sulfide-based ASSBs employ some oxide electrode materials such as $LiCoO_2$ (LCO) and $LiNi_xMn_yCo_{1-x-y}O_2$, (NMC) oxidation products accumulate at the interface even at low working voltages of 2-2.5V vs. Li/Li^+. Therefore, cathodes operating voltages $\leqslant$ 3V Na/Na^+ for ASSNBs, such as Mo_6S_8 and TiS_x, are frequently employed to prevent these detrimental side reactions. Moreover, these sulfide cathodes show a favorable affinity to sulfide-based SEs, facilitating smoother ion transportation across the interface. For instance, TiS_2 │ Ca-doped Na_3PS_4 │ Na-Sn exhibits a high charge capacity of 200 mAh g^{-1} at 0.06 C, with a retention of 91% after 100 cycles. [41] Severe electrolyte oxidation remains the most critical challenge for most sulfide-based SEs as it is inherently unavoidable. However, the thermodynamic stability of some CEI is significantly higher than that of the pristine sulfide-based SE and the decomposition kinetics are reduced. [98] Therefore, the operating voltage window can be extended for a higher energy density. [99]

In addition, electronically conductive surfaces (such as the cathode and carbon additive [100]) can also lead to the decomposition of SEs. [22] Zhang et al. revealed that carbon boosts the electrochemical decomposition of the sulfide-based SE at the cathode/electrolyte interface by transferring the low chemical potential of Li in the charged state deeper into the SE, thereby extending the decomposition region. [100] Coating with protective layers is widely used to modify the surface of the cathode and improve the stability of the interface. [21]

Aside from the CEI formation due to side reactions, space charge layers can also form as a result of Li^+ ion exchange between electrolytes and electrodes, driven by their potential differences. This increases ion transfer resistance and degradation rate. [21, 74] Besides first-principle calculations [101] and impedance spectroscopy analysis [102], advanced techniques in TEM provides direct observations of the formation of such nanometer-scale space charge layers (SCLs) in sulfide- and oxide-based ASSLBs. [103, 104] For instance, the increasing intensity at the interface between LCO and LPSCl with potential (see **Figure 1.9a**) indicates that space charges i.e. Li^+ ions accumulated at the interface between LCO and LPSCl during discharging. Moreover, as depicted in **Figure 1.9b**, an electric potential shift appeared at the interface between Cu and $Li_{1+x+y}Al_x(Ti,Ge)_{2x}Si_yP_{3y}O_{12}$ (LASGTP), while the Li content increased based on the line-profile of the electron energy loss spectroscopy (EELS). This suggests that the SCL forms at the interface between electrodes and SEs due to the blockade of Li^+ ion.
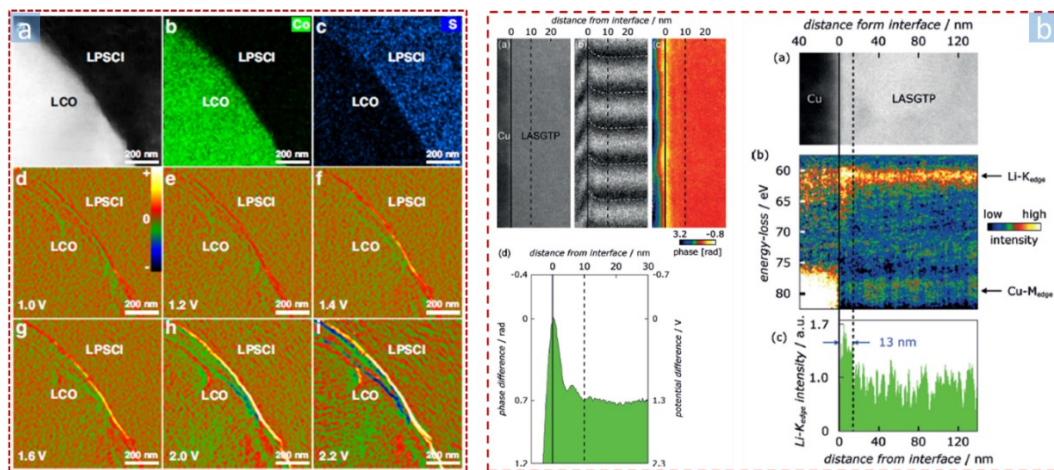
Figure 1.9. **a.** *In situ* charge-density-distribution acquired at the interface between LCO/LPSCl, adopted from [104]; **b.** Electric potential distribution (left) and Li^+ ion distribution (right) acquired at the $Cu/Li_{1+x+y}Al_x(Ti,Ge)_{2x}Si_yP_{3y}O_{12}$ (LASGTP) interface obtained from phase-shifting electron holography and adopted from [103].

- *Anode (Na Metal)-Electrolyte Interface*

Unlike the broad range of materials investigated for the cathode, Na metal is the most desirable choice for the anode to achieve high energy density. However, the reactivity of metallic Na necessitates careful consideration of the SEI formed at the Na/electrolyte interface, which relies on the chemical and electrochemical stability of the SEs. Among various ASSNBs, the interfaces of Na to oxide-based SEs exhibit notably higher stability. For instance, the high thermodynamic stability of Na-β''-alumina results in the absence of side reactions and SEI formation at the interface with the Na metal. [105] Similarly, although a thin layer (NaO$^-$) may form at the interface of the Na|NZSP, its kinetic stability is desirable as it prevents further degradation of NZSP and retains a high ion conductivity while being electronically non-conductive. [106] The interface of Na and borohydrides (e.g. $Na_2B_{12}H_{12}$ and $Na_4B_{10}H_{10}(B_{12}H_{12})$) exhibits analogous behavior. [69, 107]

In contrast, the Na/sulfide-based SE interface gives rise to side reactions, such as the formation of MIEC products (e.g. Na_2S [108]). These side reactions result in an increased charge transfer resistance during cycling, thereby limiting the performance of sulfide-based ASSBs. [86, 105] Yaosen Tian et al. reported that surface hydration of Na_3SbS_4 can stabilize the SEI by promoting the formation of NaH and Na_2O, rather than the MIEC product. [109] Besides, instead of using Na metal as anode, the Na_xSn alloy has gained popularity due to its higher electrochemical stability against sulfide-base SEs and comparable specific capacity (847 mAh g^{-1}). [86]

Apart from SEI formation, another source of interfacial instability arises from the poor contact between Na and SEs, leading to large transfer resistance and inhomogeneous Na plating. Utilizing the low mechanical strength of Na, cold pressing is commonly employed to achieve intimate contact. [110] However, even in cold-pressed cells utilizing oxide SEs, such as Na-β''-alumina [111] and NZSP [112], a significant area-specific resistance still persists. This can be attributed to the presence of low or non-ionic conductive functional groups (e.g., carbonates and hydroxyl) accumulating at the surface of oxide-based SEs due to exposure to ambient air. Consequently, the contact area with Na metal decreases, leading to increased interfacial resistance. Nevertheless, simple heat treatment can eliminate these groups and promote better wetting of metallic Na on the surface of oxide-based SEs. [85, 111] Furthermore, surface coating (e.g. SnO_2 [84]) on bare planar oxide-based SEs has been shown to effectively reduce the interfacial resistance. Moreover, voids were observed at the interface between Na │ oxide-based SE after Na stripping (**Figure 1.10a**), and the volume of the voids increases with each stripping cycle. [106, 113] These voids can contribute

to increased interfacial resistance and a reduction of the critical current density (CCD) during cycling. It has been demonstrated that an increased stacking pressure can be helpful in restraining the formation of voids. [94]
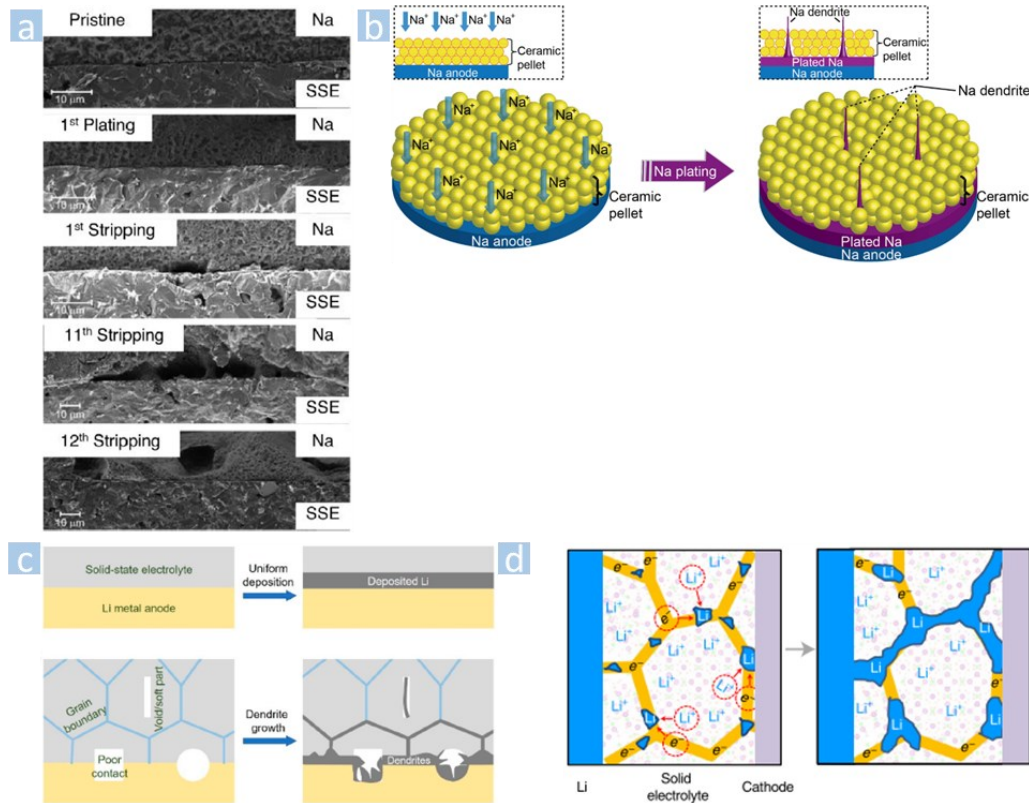
Figure 1.10. **a.** Void formation at a Na/Na-β''-alumina interface during Na stripping; adopted from [113]; **b.** Schematic diagram of Na dendrite in the Na ASSB; adopted from [85] **c.** & **d.** Models for Li filament growth in the ASSBs based on references [114] and [115].

The occurrence of inhomogeneous Na plating can lead to dendrite growth, increasing the risk of cell failure. [75] This risk is particularly concerning in Li/Na metal-anode liquid-based battery systems, and the mechanisms of dendrite growth have been systematically established. [116] While inorganic SEs possess high mechanical strength, which helps suppress dendrite formation, research has shown that Li filamentary dendrites can still nucleate at the interface between Li and SEs in areas with poor contact, as well as at internal interfaces in SEs (e.g. voids and grain boundaries). These filaments can propagate along the SE GBs towards the cathode (Error! R eference source not found.**Figure 1.10c & d**). [114, 115, 117] Fudong Han et al. attribute the filamentary dendrite formation to the high electric conductivity of SEs, e.g. $Li_7La_3Zr_2O_{12}$. [118]

Nevertheless, filamentary dendrite growth and propagation are SE-dependent as the surface band gaps differ from each other. [118, 119] The morphology of Na dendrites in liquid batteries differs from that of Li dendrites. [24] Moreover, metallic Na reacts with carbonate-containing liquid electrolytes in fundamentally different ways. [120] However, the mechanism of Na filamentary dendrite growth in ASSNBs is not well-established. Caution needs to be exercised when drawing analogies between Li and Na filamentary dendrite formation mechanisms in ASSBs as the properties of SEs used in ASSNBs may differ. Sen Xin and John B. Goodenough et al. reported that ASSNBs also suffer from Na dendrite formation at the interface between Na and NZSP, but they were successfully suppressed by the formation of a SEI through thermal treatment and Na wetting. [85]

The concept of "anode-free" cells in ASSBs, as introduced by Yong-Gun Lee et al., has garnered significant attention due to its potential for high energy density, stable coulombic efficiency, and long cycle life. [14] In this setup, an interlayer, such as a lithiophilic alloy (**Figure 1.11a**) and carbon (**Figure 1.11c & d**), between the SE and current collector, was utilized to suppress filamentary dendrite growth starting from the interface. Recently, researchers investigated the morphological and microstructural evolution during Li deposition on a bare Cu current collector with different thickness, as schematically illustrated in **Figure 1.11b**. [121] However, the behavior of the interlayer formation during both Li and Na deposition have not been extensively described in the existing literature.
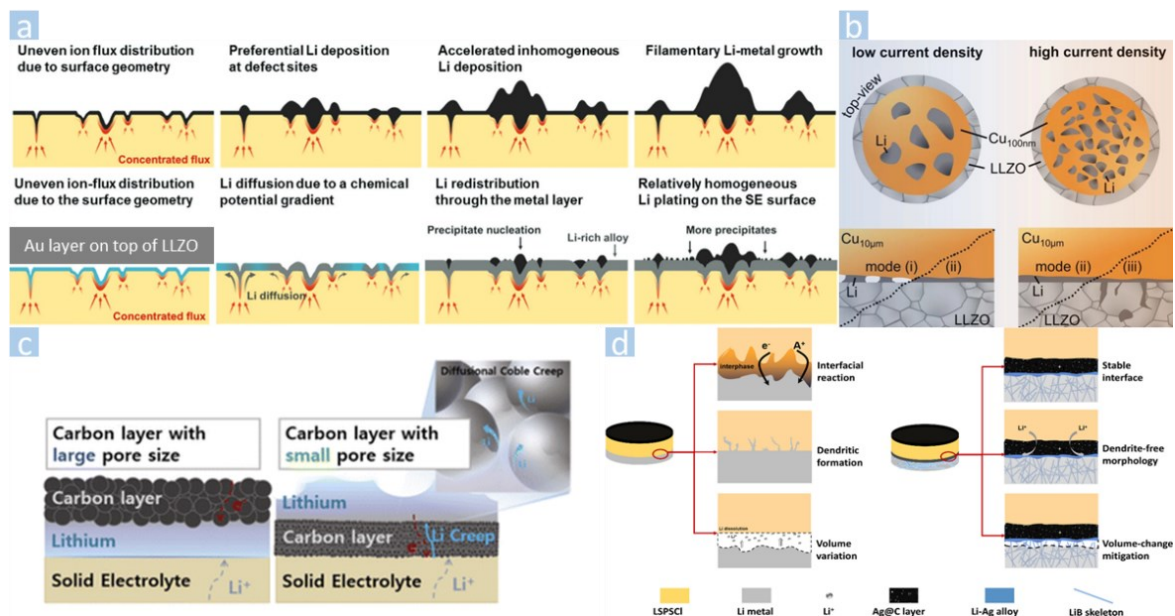
Figure 1.11. Schematic illustration of the Li deposition at an "anode-free" cell with various types of interlayers. **a.** Mechanism of Li deposition on pristine $Li_7La_3Zr_2O_{12}$ (LLZO) (upper) and a lithiophilic Au coated LLZO (lower), adopted from [122]; **b.** Li deposition at Cu with different thickness and using different current density, adopted from [121]; Carbon (**c**) and carbon@Ag (**d**) behavior during Li deposition based on references [123] and [124].

1.2.2. Electrolyte–electrolyte Interfaces

Inorganic SEs are typically composed of polycrystalline materials. Within these materials, GBs play a crucial role as the dominant solid-solid interfaces. Additionally, voids are inevitable interfaces that can form during synthesis of SEs, such as in sintered and cold-pressed SE pellets.

Numerous studies have demonstrated that these interfaces exhibit distinct properties compared to the grain bulk, and their presence can limit the performance of SEs as well as ASSBs.
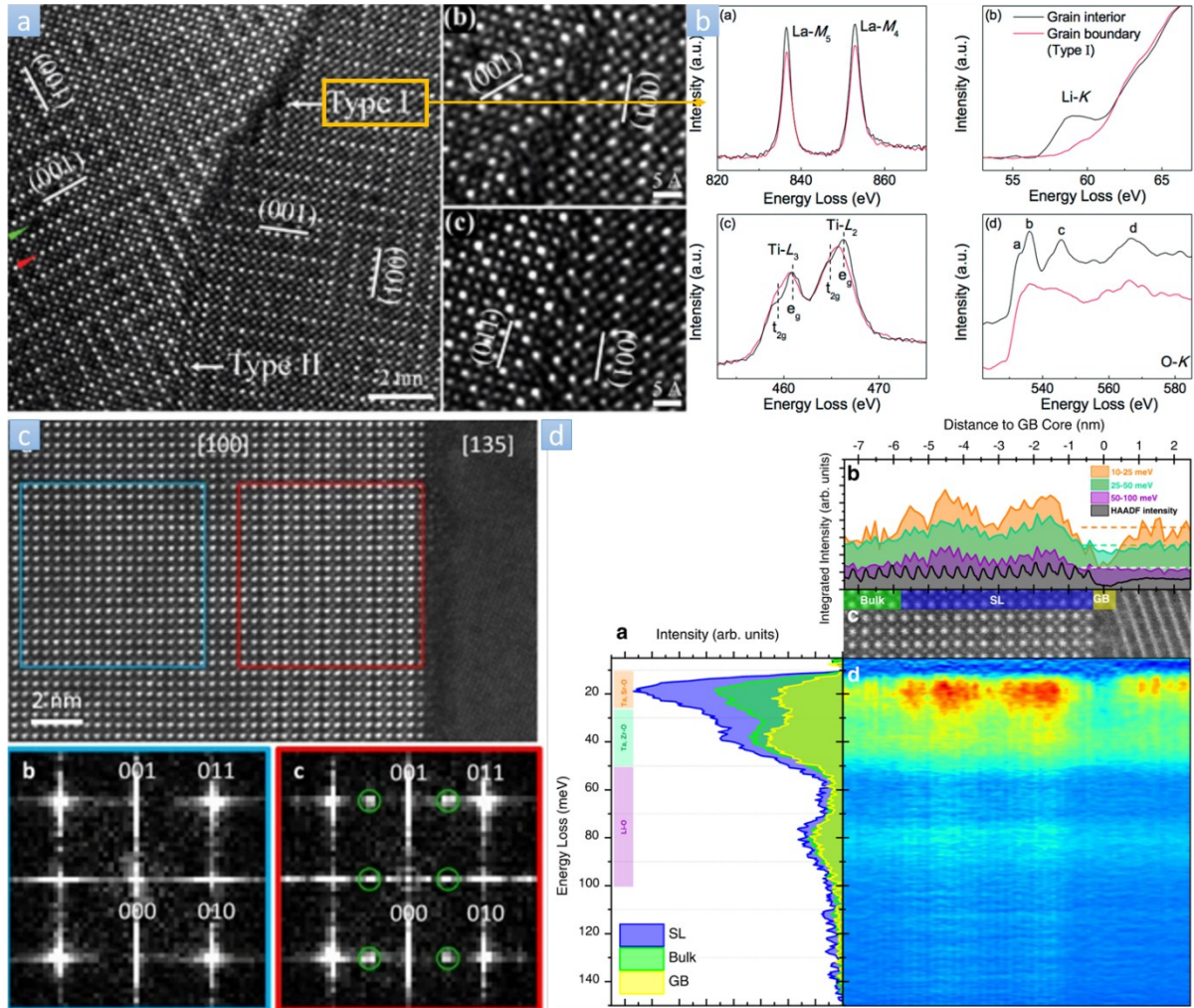
Figure 1.12. Atomic-resolution HAADF-STEM images (**a**) and electron energy loss spectroscopy (EELS) (**b**) of a perovskite-type $Li_{3x}La_{2/3-x}TiO_3$, x=0.11, adopted from [125]; Atomic-resolution HAADF-STEM image and the corresponding fast fourier transform (FFT) images (**c**) and vibrational EELS (**d**) at a (010) faceted GB in a perovskite-type $Li_{0.375}Sr_{0.4375}Ta_{0.75}Zr_{0.25}O_3$, adopted from [126].

● *Limit of Ionic Conductivity*

The influence of interfaces on the ionic conductivity of inorganic SEs is a critical consideration in material design. Spectroscopic and computational studies have revealed that GBs exhibit higher migration activation energy and significantly lower ionic conductivity compared to the grain bulk

in many inorganic SEs due to the disordered and/or structure mismatch between adjacent grains. The atomic-scale origin was revealed based on the high-resolution STEM/EELS as illustrated in **Figure 1.12** for perovskite-type polycrystalline $Li_{3x}La_{2/3-x}TiO_3$. [30, 43, 127, 128] Severe structural deviations are present at GBs, for instance, deformation of the Ti-O polyhedra. Besides, according to the EELS, a decrease in La content, partial reduction of Ti^{4+} to Ti^{3+}, and a depletion of Li^+ also contribute to the low conductivity at Type I GB. These structural and chemical factors inhibit Li^+ ion accommodation and transport. However, some SEs have been shown to contain GBs with low resistance, for instance, in another perovskite $Li_{0.375}Sr_{0.4375}Ta_{0.75}Zr_{0.25}O_3$. [126] This has been attributed to the maintained structural framework and Li^+ content at GBs, which was proved by atomic-resolution HAADF-STEM imaging and vibrational EELS. By proper doping, additional A-site vacancies are introduced at GBs, which result in an increased number of percolation pathways and an enhanced ion transport pathway. In general, the resistive behavior of GBs is less pronounced in sulfide SEs than in oxide SEs. This can be attributed to the distinct local structure, including over-coordination of Na^+ ions at GBs in oxide materials. [127] Furthermore, the presence of impurities with different chemical compositions can also limit the ionic conductivity. For example, $NaAlO_2$ may appear between neighboring grains in BASE. [19] However, this is not universally observed in all inorganic SEs. In some cases, the appearance of Na_3PO_4 as a second phase at GBs in NZSP was found to enhance the ionic conductivity. [63] Besides, the introduction of new phases such as $Na_3La(PO_4)_2$, La_2O_3, and $LaPO_4$ in La^{3+}-doped NZSP was also shown to facilitate Na^+ ion migration. [46] Notably, the concept of GB free volume, which is highly studied in metallic system and significantly influence the diffusion property of materials, and its influence on ion transport are less pronounced in the inorganic SEs. [129, 130]

Furthermore, the presence of a space charge layers (SCLs) at GBs in SEs was proposed as a contributing factor to the GB blocking effect in oxygen ion conductors by Xin Guo and Joachim Maier. [44] Subsequently, this phenomenon was further transferred to Li^+ ion conductors, such as $Li_{3x}La_{0.67-x}TiO_3$, through spectroscopic and theoretical analysis. [45] The GB core is rich in positively charged point defects, which can lead to repulsion of the Li^+ ions in the adjacent grains. As a result, the Li^+ ion concentration is significantly reduced (by over 5 orders of magnitude) within the SCLs, impeding efficient ion transport across GBs. To address this challenge, strategies such as rare earth element doping [45] and GB modification with additives [131] have been successfully employed to enhance the ionic conductivity of GBs.

However, the impact of GBs on the overall kinetics of Na^+ ion transport extends beyond the consideration of differences in ionic conductivities between GBs and the grain bulk. Yixuan Wang et al. showed anisotropic effects of Na^+ ion diffusion at GBs through first-principles calculation

and phase-field simulation. [46] They found that the energetically preferred diffusion path occurs along the GBs, where the energy barrier is approximately five times lower compared to diffusion across the GB. Furthermore, experimental observations and spectroscopic analyses in other ion conductors, such as Al-substituted LLZO [132] and $La_{0.8}Sr_{0.2}MnO_{3+\delta}$ [133], have also indicated superior diffusivity along GBs.
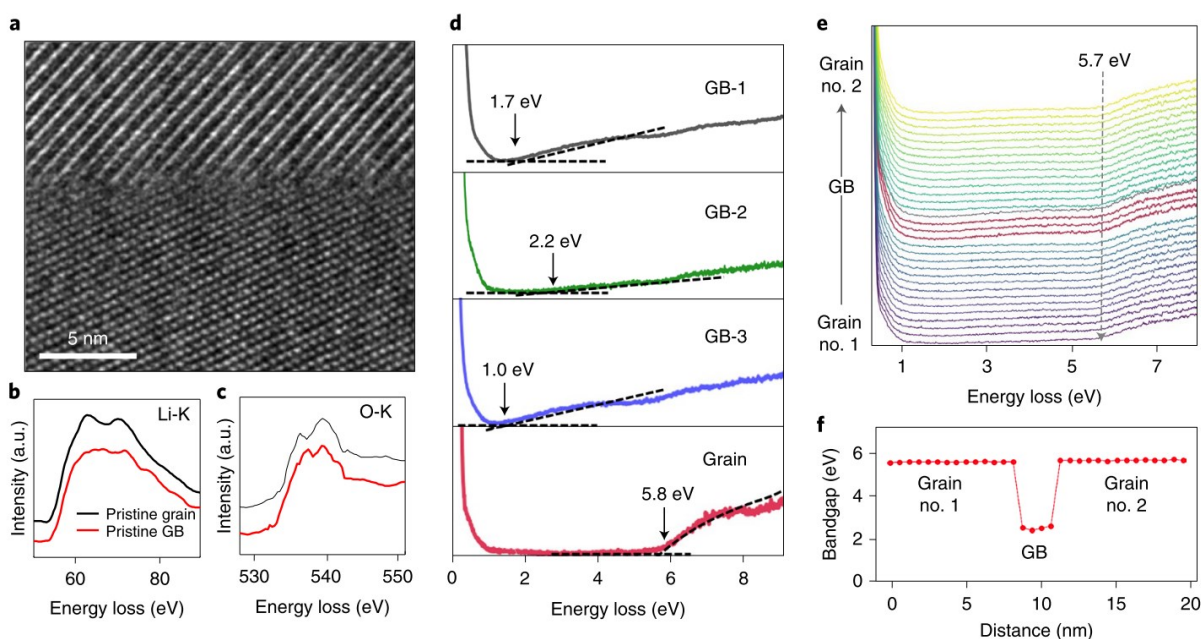
Figure 1.13. High-resolution TEM image and low-loss EELS at some GBs of a cubic LLZO, adopted from [115].

● *Origin of Na Filament Growth and Propagation inside SEs*

As discussed previously, the nucleation and growth of Li filaments occur not only at poor contact regions between the anode and SE but also inside SEs along GBs and/or voids. F. Han et al. have attributed the mechanism of this internal growth to electronic conductivity-induced processes. [118] Density functional theory (DFT) calculations predict a lower band gap at internal surfaces (e.g. pores and cracks) for various SE materials (E_g: Li_2PO_2N > β-Li_3PS_4 > $Li_{1.17}Al_{0.17}Ti_{1.83}(PO_4)_3$ > cubic LLZO) compared to the bulk. [134] Cubic LLZO is expected to have the lowest surface band gap with 2.19 eV at the surface (reduced from 5.79 eV in the bulk), approaching the level of a semiconductor and pushing the conduction bands below the Li plating potential. A similarly reduced band gap at GBs was also observed experimentally through Low-loss EELS (**Error! R eference source not found.**). [115] This facilitates electron transfer from Li metal to LLZO,

leading to Li filament nucleation and growth at GBs and voids. In addition to the low local band gap at GBs and voids, their mechanical properties also play a non-negligible role for the growth and propagation of filaments as the Li growth has to overcome the mechanical barrier by the neighboring grain network. [135] A 50% reduction in the elastic constant of GBs compared to the bulk and a lack of back stress in voids facilitates the potential of propagation. [135, 136] However, the microstructure related mechanism of Na filament growth within SEs is not as well understood as its Li counterpart.

1.3. Interface Characterization Through *In Situ* TEM

In the preceding section, the limited performance of ASSBs at room temperature has been attributed to the sluggish kinetics and significant interfacial charge transfer resistance, which is influenced by various factors such as physical contact, elemental composition and distribution, and electronic and ionic properties of battery materials. Moreover, their structural and chemical evolution at interfaces during cycling are often critical, resulting in electrochemical and mechanical degradation processes, which are not well understood to date. To study these mechanisms, a great number of structural, compositional and electrochemical characterization techniques are utilized, e.g. X-ray and neutron diffraction, X-ray absorption spectroscopy, Raman and infrared spectroscopy, nuclear magnetic resonance, cyclic voltammetry, and electrochemical impedance spectroscopy, etc. [92] Most of them provide spatially averaged structural and chemical information. However, both the bulk transport properties and the significant changes during electrochemical cycling are the result of the cumulative behavior of specific features ranging from the atomic to the micrometer scale (**Figure 1.14a**), including point defects, GBs, interfaces, lattice structure, voids, and cracks. For instance, Na dendrite formation was imaged at the mm-level by ^{23}Na magnetic resonance and at the µm-level by secondary electron microscopy (SEM) (**Figure 1.14d**) [137], whereas the origin of the spalling dendrites and their relationship with the fine microstructure are still unclear. To gain a deeper understanding, a characterization method with high spatial and temporal resolution is necessary. Satisfying this requirement, analytical TEM techniques allow to precisely probe morphological, structural, and chemical information and their changes due to electrochemical cycling and thus provide direct insights into the aforementioned microstructural properties of interfaces, both in static (*ex situ*) and dynamic (*in situ*) mode.
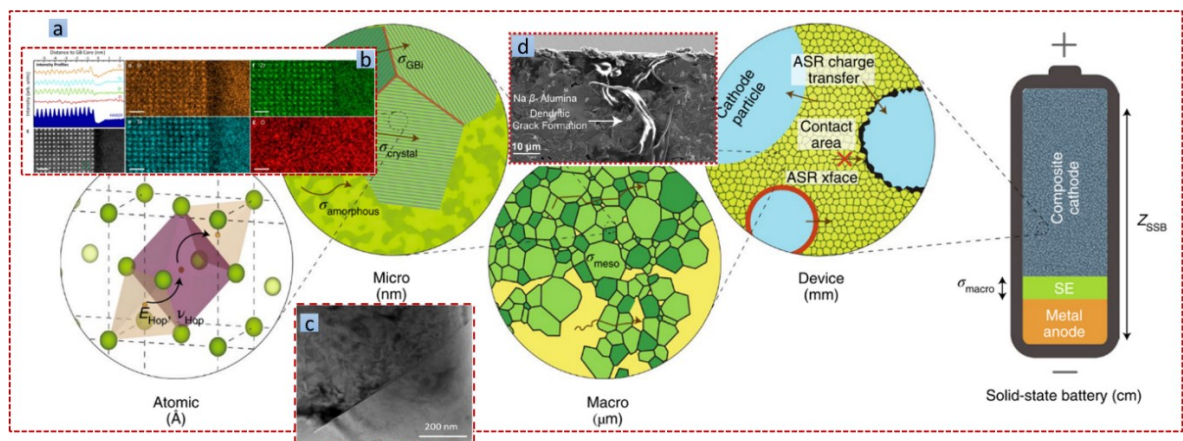
Figure 1.14. **a**. Multiscale structure-dependent ion transport, adopted from [92]; **b**. High resolution HAADF-STEM image associated with EELS of a GB of $Li_{0.375}Sr_{0.4375}Ta_{0.75}Zr_{0.25}O_3$, referring to [126]; **c**. TEM imaging of $Li_{3x}La_{2/3-x}TiO_3$, referring to [45]; **d.** SEM imaging of Na dendrite at Na-β″-alumina [137].

1.3.1. Interface Characterization by Analytical TEM

Advanced analytical TEM techniques, including high-resolution (S)TEM imaging, energy dispersive X-ray spectroscopy (EDX), EELS, 4D STEM, and *in situ* methods, are extensively employed to address questions related to battery interface engineering. These techniques enable the visualization of atomic to nano scale microstructures and chemical environments. As a result, they facilitate the investigation of the origin of high charge transfer resistance along/across GBs in SEs and at electrode/electrolyte interfaces has been probed. For instance, given that GBs are typically as thin as several unit cells, high resolution STEM imaging (**Figure 1.12a**) has been utilized to reveal local structural fluctuations that hinder ion migration across them. Moreover, their chemical variations such as decrease of Li content and chemical state change of Ti^{4+} to Ti^{3+}, are the other contributions indicated through EELS. Nevertheless, it has also been demonstrated that the resistive behavior can be modified in the SEs with the same crystal structure through the enhanced structural frameworks and mobile ion content of GBs through HRSTEM and vibration EELS (see **Figure 1.12b**). At the electrode/electrolyte interface, the high charge transfer resistance is attributed to structural and chemical changes due to the chemical reactions between electrode and electrolytes (nanoscale SEI and CEI formation), dendrite formation, and poor physical contact after electrochemical cycling. For example, mutual diffusion between the cathode and SE leading to CEI formation has been demonstrated by combining imaging and energy dispersive X-ray

spectroscopy (EDX) and/or EELS analysis as well as diffraction characterization. [98, 138] Moreover, the origin of the critical dendritic formation within the SEs, i.e. at GBs, was revealed by low-loss EELS (**Figure 1.13**), demonstrating a small band gap of some GBs in the range of typical semiconductors compared to the insulative bulk. [115]

1.3.2. *In Situ* TEM Characterization at the Interface

Although *ex situ* characterization and *post mortem* analysis provide valuable insights into the intrinsic structure, chemical and physical properties, and cycling performance of battery materials, it is imperative to observe their real-time evolution under relevant operating conditions with high spatial and temporal resolution. This observation is essential for understanding the dynamic electrochemical processes to complement the static information. In addition, it is also crucial to consider the potential interference or alteration of sample properties due to prolonged relaxation, air exposure, and other factors during interpretation. Towards this goal, *in situ* TEM approaches are employed, using the aforementioned advanced techniques for imaging the morphological, structural, and chemical evolution down to the atomic level in a model battery.

In situ TEM setups for battery studies usually employ sealed liquid cell or open cell configurations. Liquid cells are used to study liquid electrolyte based batteries, which are not included in this work. Open cell setups play a vital role in studying solid batteries, including the charge and discharge behavior of electrode materials and structural and chemical changes of interfaces. In 2010, JianY. Huang et al. achieved an important milestone by observing lithiation and delithiation processes of SnO_2 and Si nanowires inside a TEM (**Figure 1.15a**). [139, 140] Since then, numerous *in situ* TEM studies have been conducted using the same configuration based on a scanning tunneling microscope (STM) tip to stimulate the reaction processes of electrode nanomaterials such as nanowires. It is important to note that this specific investigation, utilizing an STM tip, provides a direct understanding of the evolution of volume, structure, elemental distribution, and chemical state of electrode materials during electrochemical processes, ranging from the micro- to atomic scale. This setup can be easily implemented for pristine nanomaterials, e.g. individual nanowires in a half-cell, whereas real ASSBs require a more complex setup and do not use Li_2O (Li_2CO_3) or Na_2O as the electrolyte, which limits the information obtained regarding actual interfaces in ASSBs.
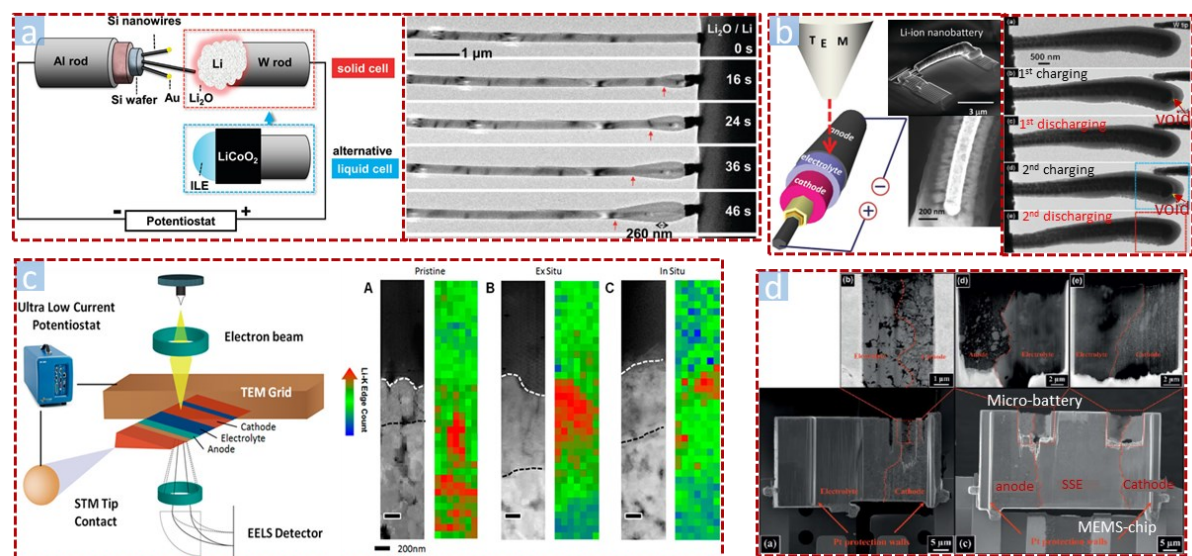
Figure 1.15. Different generations of open cell setups for *in situ* TEM characterization of ASSBs. **a.** Schematic diagram of open-cell configuration for *in situ* lithation and delithiaion of Si nanowires. Li metal serves as electrode and Li_2O as electrolyte; [140]. **b.** Specific nano-battery fabricated through deposition for *in situ* TEM characterization revealing the thickness effect of the SE on the self-discharge and the poor interfacial contact evolution during cycling [141]; **c.** Focused ion beam (FIB) fabricated micro-battery for scanning tunneling microscopy (STM) TEM holder based setup for revealing the CEI evolution by EELS [142]; **d.** FIB fabricated micro-battery in a microelectromechanical system (MEMS) based *in situ* TEM characterization setup [143].

Dmitry Ruzmetov and Jian Y. Huang et al. developed a nanowire based solid-state battery using sputter coating and followed the electrochemical process in the TEM (**Figure 1.15b**). This pioneering work provided insights into the morphological changes such as the formation and healing of nano-voids occurring at the cathode/SE interface during cycling. This shows that during operation, poor physical contact at the nanoscale can develop resulting in a high charge transfer resistance. However, due to the buried interfaces within this 3D architecture, it was still challenging to gather information regarding both structural changes and chemical evolution at the interfaces.

Micro-batteries fabricated by FIB techniques have been developed to enable access to the buried interfaces in ASSBs and providing experimental conditions that closely resemble real battery setups. [142, 143] The electric biasing was achieved using an STM setup (**Figure 1.15c**) or a microelectromechanical system (MEMS) (**Figure 1.15d**). By conducting electrochemical cycles within the TEM, the interface evolution was observed.

So far, a number of studies have been conducted based on these setups to investigate the aforementioned interfacial effects and they are introduced in previous sections.

1.3.3. Challenges

Although i*n situ* TEM characterization of micro-batteries has provided valuable insights into interfacial processes, challenges remain in terms of electron beam damage and micro-battery sample preparation. Compared to the cathode materials, SE materials suffer much more severe electron beam irradiation effects due to the extreme low electric conductivity, e.g. Nan Jiang reported that the SE Li_4SiO_4 is decomposed by the radiation of the electron beam. [144-146] Recently, using low-dose and cryogenic techniques has been demonstrated to be effective to enhance the stability of the battery materials during advanced analysis. [115] FIB fabrication is widely used for sample preparation, whereas Jungwoo Z. Lee et al. also reported that the cryogenic conditions are necessary to preserve the pristine Li/SE interface, as ion beam polishing can alter their morphology and chemistry. [147] In addition, the compressed composite architecture of ASSBs can result in poor physical contact (**Figure 1.15d**), rendering the micro-battery ineffective. Consequently, soft sulfide-based and/or thin-film-based Li ASSBs have been favored for these characterizations. [104, 142, 148] Furthermore, the welding process of the micro-battery to the MEMS chip or TEM grid may introduce high leakage-currents due to Pt deposition, rendering the battery unsuitable for electrochemical cycling. [142, 143]

1.4. Motivation and Outline of the Present Work

As mentioned above, although much research has been conducted to understand interfacial effects in ASSLBs, the physical, chemical, and mechanical differences between Na and Li necessitate a deeper analysis of the interface behavior in ASSNBs. Na-β''-alumina [105] and NaSICON type $Na_{3.4}Zr_2Si_{2.4}P_{0.6}O_{12}$ [149] exhibit a good chemical and electrochemical stability against Na metal, but when used in ASSBs, filamentary dendrite growth during Na deposition is reported, which ultimately results in battery failure. [85, 137] This strongly motivates further exploration of these interfacial problems within SEs. The microstructural features of inorganic SEs including crystal structure, GBs, impurities, and voids are expected to affect the battery performance. However, the influence of the microstructures on battery performances, i.e. Na^+ ion transport and Na deposition behavior within ASSNBs and the corresponding microstructural evolution has not been studied in much detail. The aim of this work has been to advance the understanding of the fundamental

processes governing Na deposition and, with this, to provide practical guidance for enhancing the efficiency and reliability of next-generation solid-state battery technologies.

Since *in situ* TEM measurements are capable of observing the morphological, structural, and chemical evolution down to atomic level during dynamic processes, the correlation between the microstructure and battery performance can be addressed. Therefore, in this work, *in situ* biasing was utilized to realize Na deposition for SEs in a TEM, using imaging and spectroscopy techniques to correlate the microstructure and its evolution with the Na deposition behavior. The required techniques are explained in **chapter 2.**

Although FIB is widely used for getting access to buried interfaces in TEM sample preparation, the influence of the high energy electrons and ions on SE related samples has been unclear. Hence, FIB induced damage to SEs has been initially investigated in **chapter 3** and the strategies are introduced for a reliable TEM sample preparation and analysis. The damage induced by SEM imaging and FIB processing and the mechanisms leading to this damage were investigated for three common SEs: LiPON, Na-β''-alumina, and $Na_{3.4}Si_{2.4}Zr_2P_{0.6}O_{12}$ (NZSP). Based on this understanding, an efficient cryo-FIB approach is introduced to prevent significant changes during TEM sample preparation enabling reliable preparation for *in situ* and *ex situ* analysis of these materials in the TEM.

Anisotropic ion transport due to the crystal structure has been reported within oxide SEs, however, its influence on the ion transport and filament growth, especially at GBs, is not well-understood. Na-β''-alumina is used as model SE material in **chapter 4** to investigate microstructural features and the associated anisotropic ion transport and filament formation. *In situ* biasing was conducted in a TEM to observe the dynamic processes during Na deposition in the vicinity of the interface between Na-β''-alumina and Au/e(i)-Pt(C) electrode. Crystal orientation analysis was applied to investigate the relationship between Na^+ ion migration/Na filament growth at GBs and anisotropic ion transport. Current density modeling was further used to assess the influence of anisotropic ion transport. Finally, *post mortem* SIMS analysis was conducted on the cycled Na-β''-alumina to examine the macroscopic behavior after the cycling process, also acting as bulk reference for the *in-situ* TEM work.

Besides the Na deposition within the SEs, the interface between the SE and anode is a critical site for the initiation of Na filament growth. To address this issue, the incorporation of an Au interlayer has been proposed as a strategy for "anode-free" ASSBs to mitigate and control filament growth at the SE-anode interface. However, the behavior of the Au interlayer and its influence on Na filament growth remains insufficiently understood. **Chapter 5** explores the microstructural

evolution of Au interlayers, observing morphological, structural, and compositional changes during inhomogeneous Na deposition at the interface between it and SE using the same TEM setup as in **chapter 4**. The focus was on examining the influence of bias voltages and Au thin film morphology, shedding light on conditions that impact "anode-free" battery performance. This exploration provided valuable insights into the interplay between the Au interlayer and Na deposition, offering a first foundation for optimizing the design and performance of "anode-free" ASSBs.

Chapter 2

2. Methods and Characterization Techniques

This chapter provides an overview of the basics of this work. It starts with the interaction processes between the accelerated electron beam and matter and the signals that are produced by the interaction. The second part of this chapter focuses on the different microscopy techniques that were used to obtain the results described in the result chapters (**chapter 3 – chapter 5**). The instruments used in this work are introduced in the last section.

2.1   Electron-matter Interaction

When an accelerated electron beam interacts with matter, the electrons change their trajectory. This change is determined by the interaction between the incident electrons and the electrons as well as the nucleus of the atoms in the sample. The scattered electrons and stimulated secondary signals (Error! Reference source not found.) will emerge from the surface of the specimen or t ransmit through a thin sample. The interaction volume (sampling depth) ranges from submicron to several micron range in a thick (bulk) sample, depending on the energy of the incident electron beam and the density of the sample, whereas the sampling depth of thin samples (< 100 nm)

corresponds to the sample thickness. Using different electron microscope types and spectrometers to collect, organize and analyze these signals, one can obtain various information about the sample under investigation, for instance, its crystal structure, morphology, chemical composition, and chemical state.

Concerning energy transfer during scattering, these events can be classified into two main categories: elastic and inelastic interactions. The incident electrons undergo different scattering processes that can be understood by thinking about electrons in terms of particles and waves.
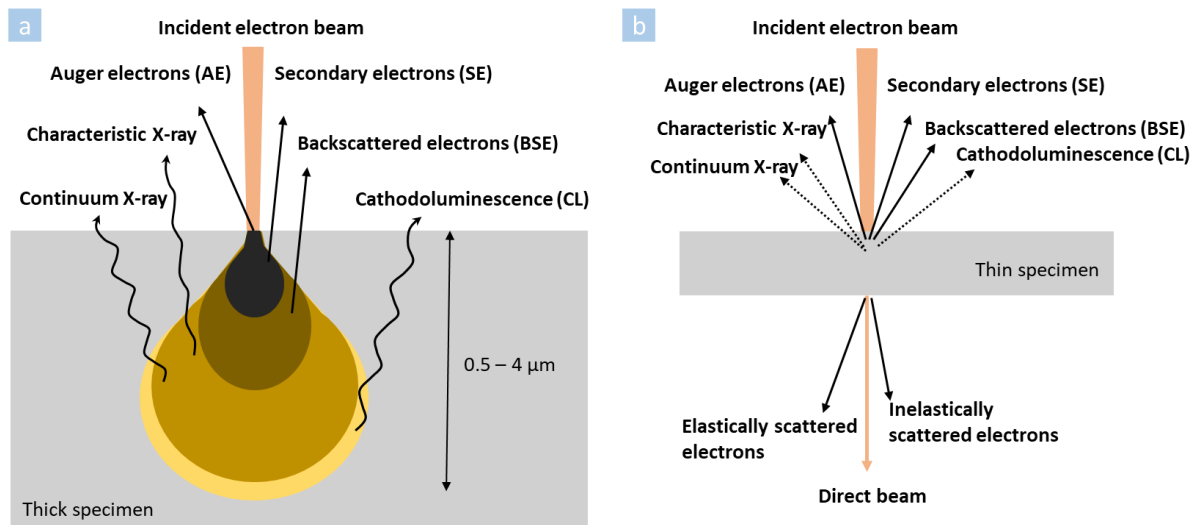
Figure 2.1. Schematic illustration of the electron-matter interaction in bulk (**a**) and thin specimens (**b**).

2.1.1 Elastic Interaction

No energy is transferred when incident electrons are elastically scattered. Elastic scattering occurs when the electrons are scattered either by the atomic nucleus leading to a large scattering angle Θ_1 or by the interaction with the electron cloud resulting in a small angle Θ_2 deflection. This is schematically illustrated in **Figure 2.2**. The Coulomb attraction by the nucleus can be very strong, in some cases leading to scattering angles above 90°, resulting in the formation of backscattered electrons (BSE). The Rutherford elastic cross section depends on the energy E of incident electrons and the atomic number Z. Therefore, specimens with large atomic number Z result in a large number of BSEs. The differential cross-section $\frac{d\sigma}{d\Omega}$ can be described by

$$\frac{d\sigma}{d\Omega} = \frac{e^4 Z^2}{16E^2 \sin^4 \frac{\theta_1}{2}}$$

where E is electron kinetic energy.

However, the higher the angle of scattering of an electron emerging from the specimen, the greater the chance that it will have undergone an inelastic event when it travels through the specimen. In addition to the high-angle Rutherford scattering, the electrons coherently scattered to small angles $\Theta < 3°$ by the ordered arrangement of atoms in a crystal lead to constructive and destructive interference, which gives rise to a diffraction pattern. This will be discussed in detail in section 2.5.
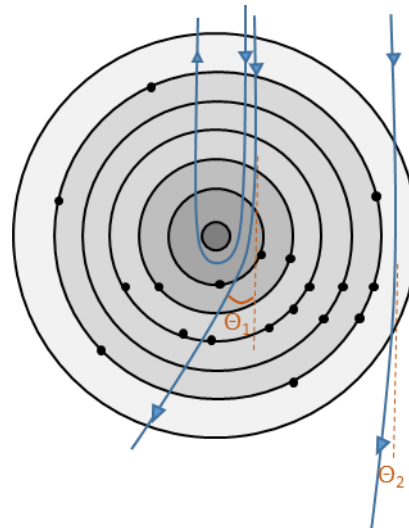
Figure 2.2 Scattering of incident electrons by an atom. scattering angle: Θ.

2.1.2   Inelastic Interaction

Inelastically scattered electrons transfer some of their kinetic energy to an atom. This can occur as result of the momentum of an incident electron being altered by the Coulomb attraction of the nucleus, which lead to the emission of X-ray Bremsstrahlung. When a high-energy incident electron collides with an inner-shell electron in an atom, the inner-shell electron can be exited into an unoccupied state or leave the sample as secondary electron (SE), leaving a hole in the inner shell. During this process the incident electron loses the corresponding amount of energy. **Figure 2.3a** illustrates this process. To return to the ground state, the atom fills the hole in the inner shell by relaxation of an electron from an outer shell, accompanied by the emission of an X-ray. [150]

The energy of this X-ray is characteristic and dependents on the energy difference between the two shells, as shown in **Figure 2.3b**. The application of these characteristic X-rays for elemental analysis is explained in more detail in section 512.6.2. Alternatively, the excited atom can also relax by release of an Auger electron as a process competing with X-ray emissions, especially for low atomic number elements. [151] Due to their low energy and strong interaction with the specimen, Auger electrons (AEs) can only be detected within a surface region of approximately 1-2 nm, making them useful for elemental analysis. SEs have a typical energy of 1-20 eV and the specified upper limit is 50 eV. Therefore, only those electrons which are excited within a few nanometers from the sample surface can escape to vacuum. [152] These electrons provide information about the morphology and surface topography in the SEM.
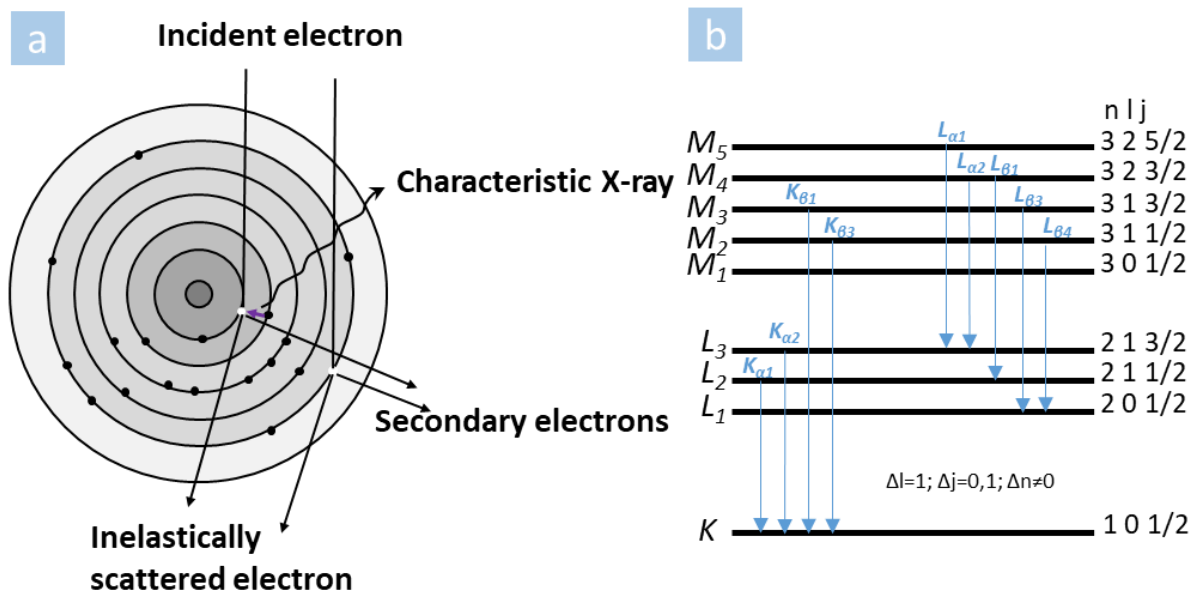
Figure 2.3. **a.** Schematic illustration of the origin of characteristic X-rays and secondary electrons; **b**. The most important allowed X-ray emission transitions; n, l, and j are the corresponding princple quantum number, orbital quantum number, and spin quantum number.

2.1.3 Electron Beam Damage

The interaction of the incident electrons with matter also leads to undesirable temporary or permanent changes of the sample. Egerton et al. have summarized the typical types of the electron beam effects that occur during TEM and SEM experiments: knock-on displacement, ionization

damage (radiolysis), electrostatic charging, electron-beam heating, sputtering and hydrocarbon contamination. [145, 153]

- *Knock-on Displacement (and Surface Sputtering)*

Knock-on damage may happen when an incident electron is scattered by the atomic nucleus. When the transferred kinetic energy E is higher than the atomic displacement energy E_d or the surface binding energy, the atomic nuclei will be kicked out to an interstitial position or sputtered from the surface. E_d determines the threshold energy E_0^{th} of the incident electrons, below which no knock-on damage occurs. The displacement and threshold energies depend on the position and bonding of the atoms. E_d and E_0^{th} of the atoms in a compact crystal are in the range of $30 - 80$ eV and $150 - 1500$ keV, while they vary from $1 - 10$ eV and $30 - 300$ keV for the atoms on the external surface of a compact crystal. [153] Knock-on effect increases with increasing operation voltage and are dominating in metals and conducting samples. [145, 153]

- *Radiolysis (and Hydrocarbon Contamination)*

Radiolysis arises from inelastic scattering events, which results in the excitation of an inner shell electron to an anti-bonding excited state. This corresponds to a chemical bond between atoms being broken. If the relaxation from the exited state is slow enough, the atoms involved can move leading to structural changes. This process is also the primary cause for hydrocarbon contamination build-up by cracking/reaction of mobile hydrocarbons on the sample surface during TEM or SEM imaging. In contrast to knock-on damage, radiolysis effect decreases with increasing operation voltage and dominate in organic materials, insulators and some semiconductors. [154, 155]

- *Electrostatic Charging*

Electrostatic charging of a sample is attributed to the net charge accumulation, which depends on the escape of SEs and BSEs relative to the absorption of primary electrons. Occurs in poorly conducting specimens where the charges cannot be compensated by the connection to a grounded sample holder. [53, 54, 155] This charging effect are influenced by the electron beam current, the acceleration voltage, the thickness and geometry of samples, and the properties of materials such as electronic property and orientation. [53, 145, 156, 157] In addition, the induced electric field was found to damage the insulating materials unlike the knock-on displacement and radiolysis. [53, 54, 158]

- *Electron-beam Heating*

Due to the electron-induced excitation of phonons by the inelastic interaction between incoming electrons and atomic electrons, the local temperature of the irradiation area may rise. Beam heating can be critical for high incident electron currents and when the beam diameter is small.

For studying battery materials, electron beam damage remains a critical obstacle for the application of electron microscopy techniques. [54] In terms of the quantifying radiation in electron microscopy, the dose is typically expressed as the number of incident electrons hitting an exposed area (C/nm^2 or e/nm^2). [153] The dose rate is the number of incident electrons hitting a unit area of the sample during a unit time. Generally speaking, the electron beam induced damage is influenced by the electron dose, electron dose rate, and acceleration voltage as well as the sample thickness, coatings, and the temperature. It is well accepted that the beam damage decreases in general with decreasing electron dose as well as under cryo-condition. Furthermore, to minimize beam damage, the acceleration voltage needs to be optimized based on the different radiation damage mechanisms of the specific materials.

2.2 Ion-solid Interaction

In addition to using electrons for a characterization of materials, interaction of ions with solids can be leveraged for characterization and structuring, e.g. in a focused ion beam system or secondary ion mass spectrometry (SIMS).
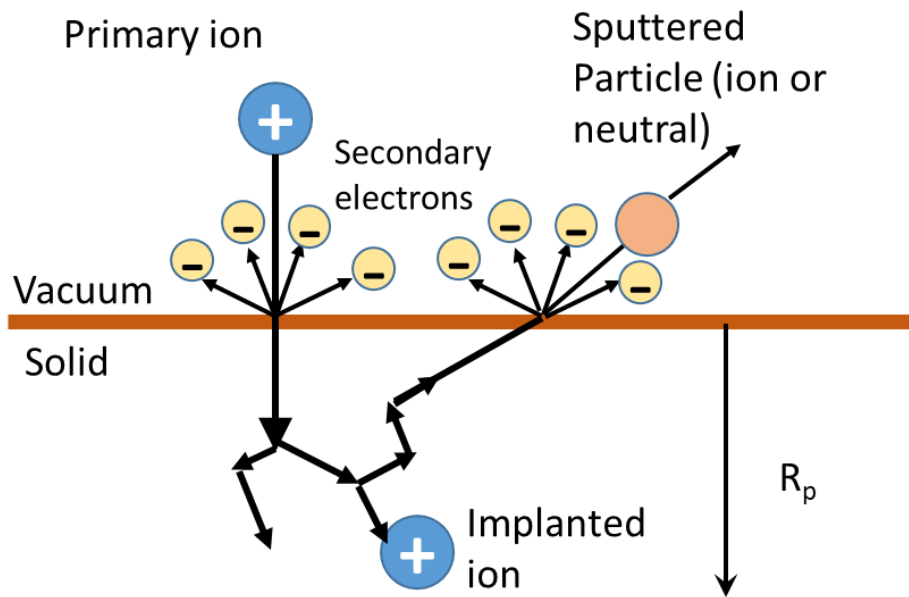
Figure 2.4. Schematic of ion-solid interactions, modified according to [159].

Figure 2.4 illustrates some of the possible effects that result from the ion bombardment of a solid. Sputtering occurs as the result of a series of elastic collisions where the momentum of a primary ion is transferred to the solid within a collision cascade. This collision cascade can also result in a momentum transfer towards the surface and lead to a surface atom being ejected as a sputtered particle, if the component of the kinetic energy transferred is sufficient to overcome the surface binding energy of the material. A portion of the ejected atoms may be ionized and collected to either form an image (FIB) or be analyzed in terms of mass to charge ratio (SIMS). In addition to the elastic collision, inelastic scattering during the ion bombardment results in the production of phonons (heating sample), plasmons, and the emission of SEs (collected for imaging by FIB). In general, the number of SEs generated per incident ion is ~1 and thus 10-1000x larger than the number of secondary ions generated per incident ion. [160] Hence, SEs imaging in a FIB is more efficient. Nevertheless, charging effects in non-conductive materials due to the net positive-charge accumulation from the impinging Ga^+ ions can cause dark features SE imaging. Secondary ion imaging can be an alternative to circumvent charging artifacts during FIB imaging.

The interaction between the primary ion and a solid material occurs by conversion of the initial kinetic energy of the ion. Consequently, if the ion is not backscattered from the target surface, it will gradually lose its kinetic energy and eventually come to rest, becoming implanted within the target material at a specific depth denoted as R_p (as illustrated in **Figure 2.4**) below the surface of the specimen. In contrast to high-energy electrons, which possess a large penetration depth (on the

order of micrometers), ions exhibit a shallower penetration depth in solids (in the range of nanometers for ions such as Ga^+, Ne^+, and Xe^+ in Au [161]). However, despite this low penetration depth, ions with high energy can induce a series of physical and chemical reactions. This is because the energy carried by the ions is sufficient to cause cascading collisions of atoms near the surfaces of solids. The actual penetration depth of ions is dependent on several factors, including the species and energy of the incident ions as well as the characteristics of the target material. [162, 163]

2.3   Scanning Electron Microscope (SEM) and Focus Ion Beam (FIB)

2.3.1. Scanning Electron Microscope (SEM)

SEM imaging is one of the most widely used electron microscopy techniques for morphological and topological characterization of a large number of materials. The basic setup is schematically shown in **Figure 2.5** and includes: electron source condenser electromagnetic lenses, aperture, scanning coils, and objective lens are part of the column, while the sample stage and various detectors are located in the high vacuum chamber. High vacuum is needed to reduce the scattering of electrons by the atmosphere.
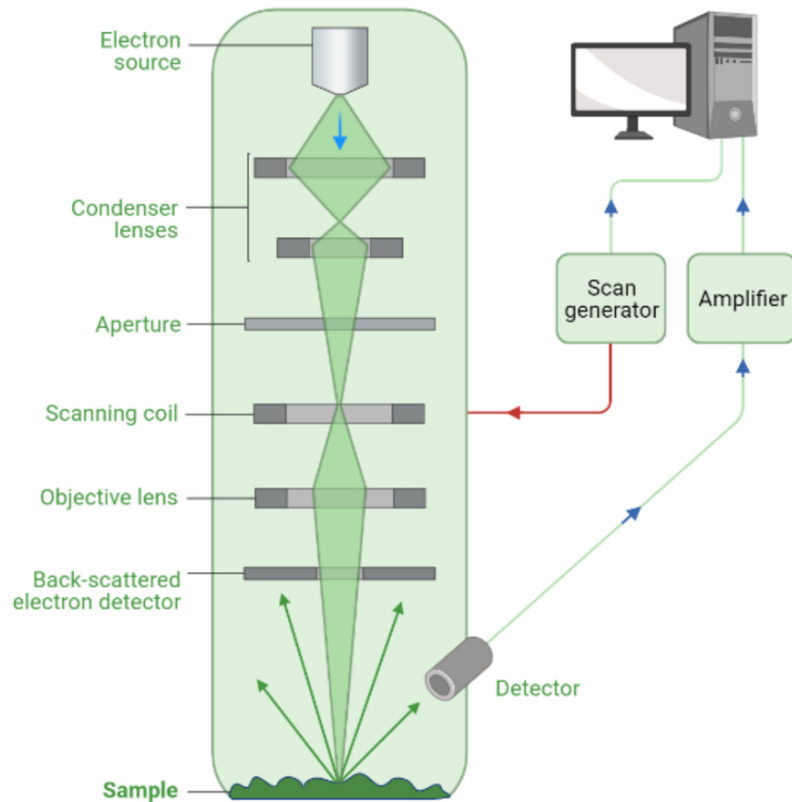
Figure 2.5. Schematic setup of a scanning electron microscope, adopted from [164].

At the top of the microscope column, the electron source emits electrons, which are extracted to form a fine beam through the positively charged anode plate and accelerated in the range from E_0 = 0.1 to 30 keV for the instruments used in this work. There are three main types of electron sources for electron microscopes (SEM as well as TEM): tungsten filament, Lanthanum hexaboride (LaB_6) or Cerium hexaboride (CeB_6) cathode, and field emission gun (FEG). A fine beam of electrons focused by the condenser lenses and finally by the objective lens is used to scan a sample's surface, where the different signals discussed in section 2.1 are generated by the interaction. The condenser and objective lenses and aperture control the beam diameter enabling high spatial resolution imaging. These signals provide information about morphology, topology, composition, crystal structure, and crystal orientation. By utilizing the appropriate detectors, a modern SEM can effectively achieve a wide range of research objectives. For example, the combination of an Everhardt-Thornley detector (collecting secondary electrons) and an in-lens detector (detecting backscattered electrons) enables the acquisition of topographical and compositional information through imaging. In addition to imaging, an analytical SEM is additionally equipped, for instance, with an energy dispersive spectroscopy detector for

composition analysis using X-rays and an electron backscatter diffraction (EBSD) detector for crystal structure and orientation analysis.

2.3.2. Focused Ion Beam Microscope (FIB)

The basic idea behind FIB is the use of a focused ion beam, in case of the instruments used in this thesis Ga^+ ions, which is scanned across the sample surface inducing a collision cascade. The emitted secondary electrons are collected for imaging (**Figure 2.6a**). Sputtering of neutral and ionized substrate atoms from the surface results in a milling process of the substrate (**Figure 2.6b**). Furthermore, the interaction with induced gases, which is breaking chemical bonds in a precursor, can be used for deposition (**Figure 2.6c**). However, as a side effect, displacement of atoms and ion deposition in the sample can introduce damage to the sample and heat it as well. [165]
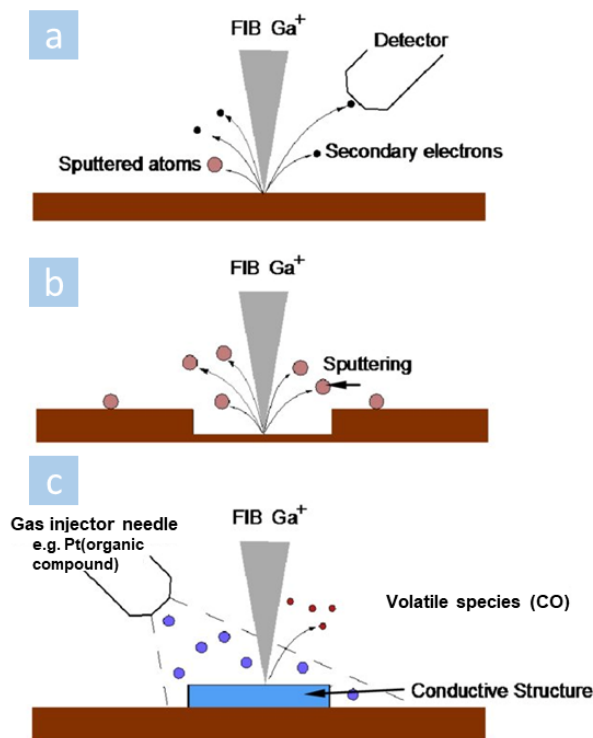
Figure 2.6. Working principle of FIB imaging (**a**), FIB milling (**b**), and FIB-induced deposition (**c**).

FIB is a fairly recent techniques, which became commercially available in the 1990s. [166] The basic FIB is similar to an SEM, as shown in **Figure 2.7a**. FIB is used widely for nano and micro manufacturing and structuring as well as TEM sample preparation.
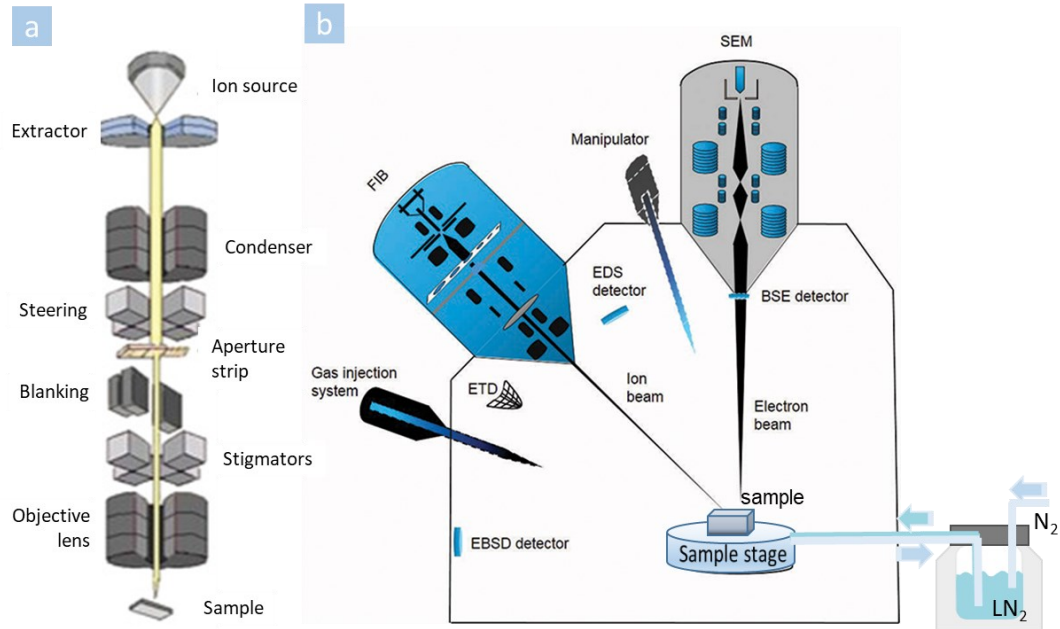
Figure 2.7. Schematic setup of a (**a**) focused ion beam column and (**b**) cross-section of a dual-beam FIB instrument. Modified based on [167].

To achieve the goal of a targeted preparation from a specific area and ion-dose limit application, a combination of SEM and FIB in one system (dual beam FIB system, as schematically illustrated in **Figure 2.7b**) is the standard solution. Electron imaging is used as reference for patterning by FIB. There is usually an angle between the ion beam and electron beam. For instance, the angle is 52 ° for FEI strata 400s, and 54 °s for Zeiss Auriga, which makes the cross-section producing and imaging as well as functional analysis realistic without sample transfer. In addition, a gas injection system (GIS) and micromanipulator are used to manage the *in situ* lift-out procedure for TEM sample preparation. [168, 169] In the further course of this work, the term FIB will be used for the dual-beam instruments, combining SEM and FIB.

To avoid or at least reduce the ion beam-induced damage to samples, FIB preparation can be performed at cryogenic condition, e.g. for alloys [170, 171] and batteries [147]. In the conventional dual beam FIB system, the cryogenic condition can be achieved by replacing the normal sample

stage with a liquid N_2 cooling stage as shown in **Figure 2.7b**. However, the GIS has to be heated up to 80 °C to provide the precursor organic molecular for Pt or C deposition, which does not work for a cooled sample. [172] In addition, a micromanipulator at room temperature may lead to problems in cryo FIB. [172] Therefore, even for the cryo FIB preparation, the deposition and lift-out processes had to be performed at room temperature.

2.4   Time-of-Flight Secondary Ion Mass Spectroscopy (ToF-SIMS)

ToF-SIMS has been established as a routine analytical method in the 1980s. [173] Although overcoming the difficulty of the ToF detector took a long time [174], the working principle of ToF-SIMS is conceptually simple. Through the bombardment of a surface by a pulsed high energy ion beam (typically Cs or Ga), the mass of the secondary ions generated is analyzed by measuring the time required for the ions to fly from the sample to the detector, as schematically illustrated in **Figure 2.8**. An electron flood gun is used for charge compensation. In this work, the primary ions used were Bi_3^{2+}. During the collision process, the primary ions penetrate slightly into the surface and, the secondary ions induced by the ion-solid collision cascade are emitted from the topmost atomic layer of the sample. [174] Hence, ToF-SIMS is one of the most surface-sensitive techniques available with an information depth of less than 1 nm. ToF-SIMS can provide average mass spectral information, XY surface imaging and also 3D depth profiling into a sample. However, no direct crystallographic information is obtained.
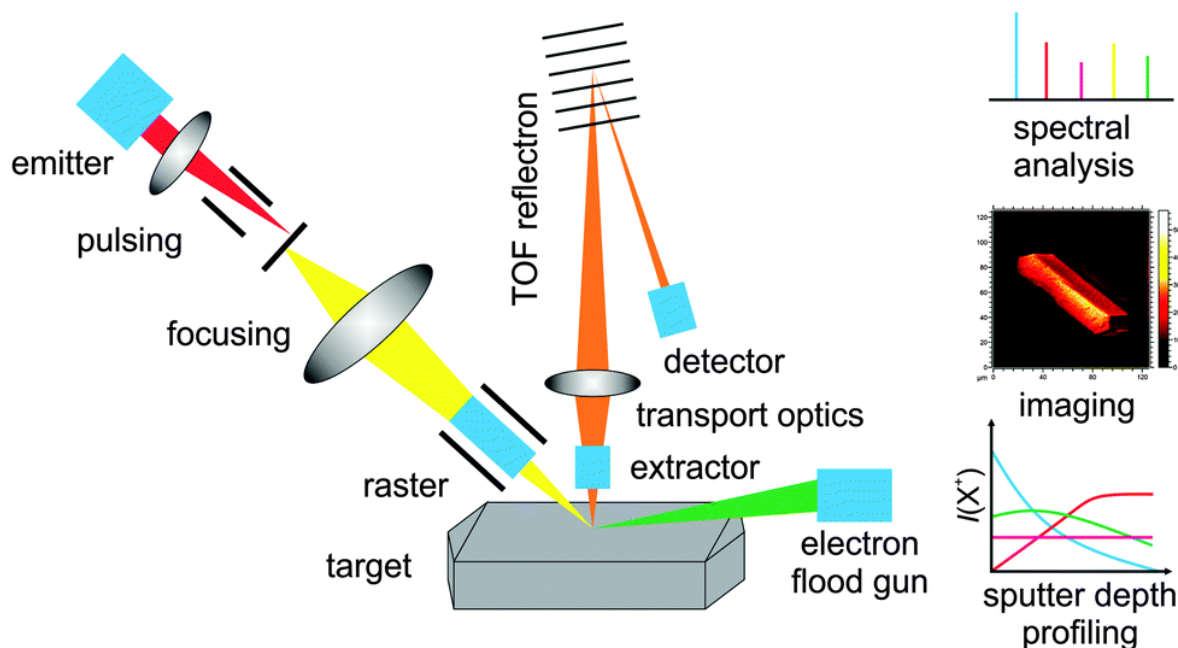
Figure 2.8 schematic illustration of the working principle of a ToF-SIMS instrument and options for surface and bulk analysis [174].

Due to the wide range of detectable elements, an excellent detection limit in the ppm range and multi-dimensional imaging, this technique is nowadays commonly applied in battery research to investigate e.g. the composition evolution e.g. $LiNi_{0.6}Co_{0.2}Mn_{0.2}O_2/\beta\text{-}Li_3PS_4$ [175] and $LiNi_{0.6}Co_{0.2}Mn_{0.2}O_2/Li_6PS_5Cl$ [176] catholyte solid-solid interface degradation after cycling and Li content distribution of electrode material [177-179].

2.5 Transmission Electron Microscopy (TEM)

Transmission electron microscopy allows to image thin specimens based on the interaction of the electrons with the sample. As in light microscopy, the resolution depends on the wavelength of the raddiation used. Using the particle-wave duality in quantum mechanics, the wavelength (λ) of electrons in the vacuum determines by:

$$\lambda = \frac{h}{p} = \frac{h}{\sqrt{2mE_0}}$$

Equation 2-2

Where h is Plank's constant, p is electron momentum, m is relativistic mass of the electron, and E_0 is kinetic energy ($E_0 = e\Phi$ with Φ standing for the acceleration voltage in volts). The wavelength of accelerated electrons (0.0487 and 0.0197 Å for acceleration voltages of 60 and 300 kV) indicates

the possibility for atomic-level imaging with TEM. [180] Both, imaging and spectroscopic analyses, can routinely be performed in a modern analytical TEM with high resolution (currently up to sub-Angstrom level by aberration-corrected TEM) and precision, providing information on morphology, structure, chemical state of elements, and composition of a sample.

The basic optical setup of a TEM can be described analogous to a (visible) light microscope. The basic components are schematically illustrated in **Figure 2.9**, including the detectors and spectrometers. The electrons are emitted from the electron gun, which is located at the top of the TEM column. They are accelerated in high vacuum by a potential typically in the range of 60 - 300 kV for Themis 300 and Themis Z. The high-energy electron beam then passes through the electromagnetic condenser lens system and apertures, which control the electron beam current, diameter, and convergence angle. After the interaction between the electron beam and the thin specimen, the different signals generated (as discussed in section 2.1) are collected by different detectors or spectrometers as shown in **Figure 2.9**. Ray paths of the forward scattered and transmitted electron beam from the condenser and objective lenses via the projection lenses to the detectors depend on the operation modes (diffraction, bright- and dark-field TEM imaging, and STEM modes). These will be discussed in detail in the following sections.
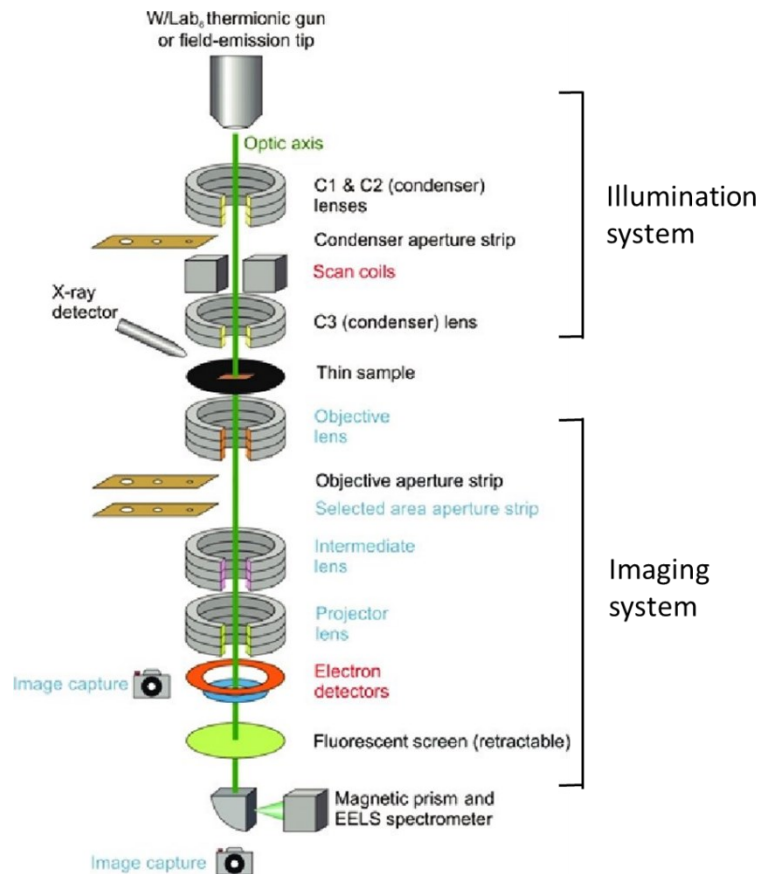
Figure 2.9. Schematic illustration of the main components of a common TEM that can be operated in S/TEM modes; The components used for both TEM and STEM modes are named in black, while components in red are only for STEM and in blue only for TEM. Adopted from [181].

2.5.1. Diffraction and Imaging Modes

In TEM, diffraction and imaging are two main operation modes (**Figure 2.10**). With a parallel electron beam illuminating a thin specimen, the projected structural/morphological information of the sample is encoded in the phase and electron density distribution at the exit surface of the specimen. Following the general lens properties, a diffraction pattern is formed in the back focal plane of the objective lens below the sample due to the interference of the forward scattered electron wave and the recombination of the diffracted and transmitted beams results in the formation of an image in the image plane of the objective lens. The diffraction, projection, and intermediate lenses below the objective lens are used to focus and magnify either the diffraction pattern (diffraction mode) or the image (imaging mode) onto a detector, which converts the electrons into visible light or an electronic signal.
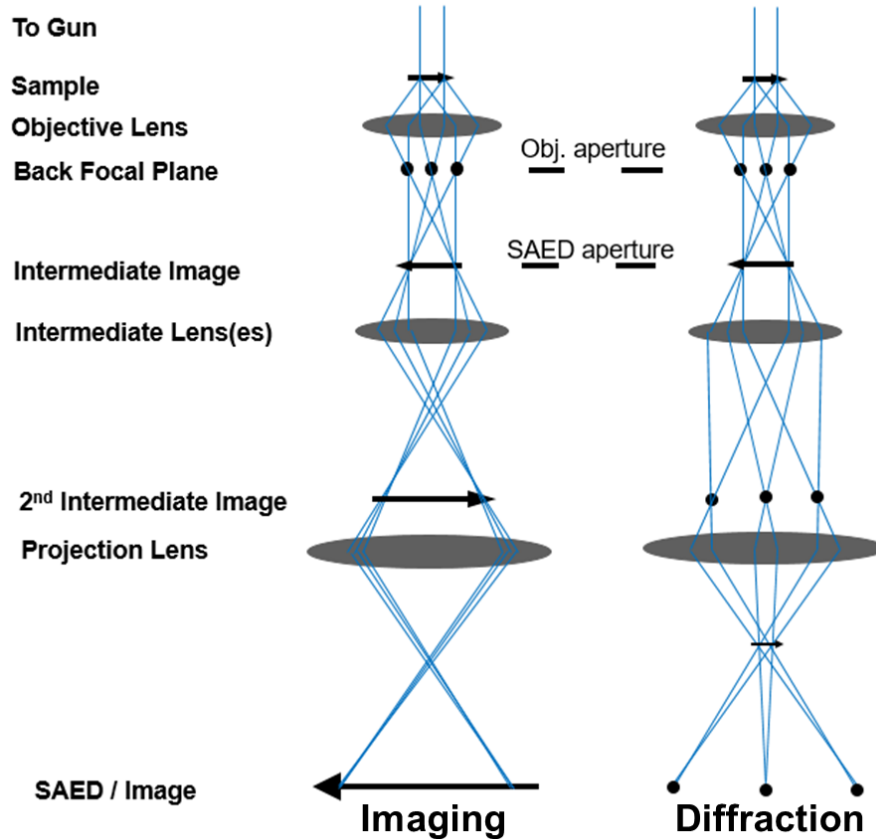
Figure 2.10. TEM imaging and diffraction operation modes.

● *Electron Diffraction*

Diffraction occurs as the electrons are elastically scattered by the atomic nuclei in a crystalline material. Due to the periodic arrangement of these atomic nuclei within the crystal lattice, the distribution of forward scattering possibility depends on its angle as these scattered electron waves can interference with each other at some angles. This process can be described by "Bragg's law" as a simple relationship between the electron wavelength and the ordered atomic distances in a crystal as illustrated schematically in **Figure 2.11**. When the path length difference AB + BC between the upper and lower planes is an integer multiple of the wavelength coherent interference occurs.

$$n\lambda = 2d \sin \theta_B \ (n \ is \ an \ integer) \hspace{2cm} \textbf{Equation 2-3}$$

With the known wavelength (λ) of the incident electron beam and the experimentally measured Bragg angle (θ_B), the interplanar spacings can be determined to obtain crystallographic information.
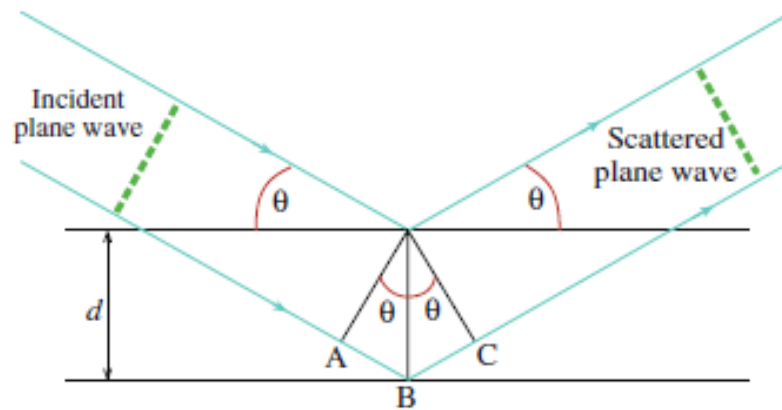
Figure 2.11. Schematic description of diffraction in terms of reflection of a plane wave (wavelength λ) incident at an angle θ to atomic planes of spacing d. The path difference between reflected waves is AB + BC. Adopted from reference [154].

The amplitude of the scattered electrons depends on the unit cell of a crystal structure can be described by the structure factor $F(\theta)$, which is defined as the sum of the atomic scattering factor $f(\theta)$ from all atoms in the unit cell multiplied by a phase factor. The scattering intensity is determined by $|F(\theta)|^2$. The term of $F(\theta)$ is approximated by:

$$F(\theta) = \sum_{i}^{n} f_i e^{2\pi i(hx_i+ky_i+lz_i)}$$ **Equation 2-4**

The amplitude of the scattering factor depends on the type of atom ($f(\theta)$), the position of the atoms in the cell (x, y, z), and the specific atomic planes (h k l) diffracting the electron beam. The scattering amplitude can be zero in some cases, which is known as a kinematically forbidden reflection. These reflections can sometimes still be observed due to dynamical scattering events (influenced by sample thickness). [154] Precession electron diffraction can reduce dynamical effects in electron diffraction resulting in high-quality data approximating the kinematic diffraction and therefore, be used for the crystal structure characterization.

In the case of quasi-parallel illumination, an electron diffraction pattern (selected area electron diffraction, SAED) can be acquired for a specimen area as small as ~500 nm by means of a selected area aperture located in the intermediate image plane. Nevertheless, in the case of convergent illumination, convergent beam electron diffraction (CBED) or nano beam electron diffraction

(NBED) allows spatially much better resolved determination of lattice parameters down to areas below 5 nm diameter.

To index diffraction patterns of specimens with a complicated crystal structure and chemical components, the reflection conditions can be simulated i.e. using software of JEMs [182]. In addition, automated crystal orientation map (ACOM) [183] analysis is also a powerful method to index the well-known crystal orientation.

- *TEM Imaging*

In addition to electron diffraction, the differential scattering and absorption of electrons creates intensity variations at the exit plane of the sample, which can be imaged. Such image contrast can be attributed to three mechanisms: mass-thickness contrast, diffraction contrast, and phase contrast. Consequently, the bright-field (BF), dark-field (DF), and high-resolution (HR) TEM imaging modes are used to acquire morphological and structural information.

Mass-thickness contrast arises from incoherent elastic and inelastic scattering of electrons by the specimen, which depends on the atomic number (Z) and the thickness of the specimen. Furthermore, diffraction contrast is the dominant mechanism in crystalline specimens producing differential intensity in BF- or DF-TEM mode. Here, only the primary or selected diffracted beams are used for imaging by a small aperture (objective aperture) in the back-focal plane of the objective lens.

In addition to the mass-thickness contrast and diffraction contrast, phase contrast imaging is the basis for HRTEM, which can be used to directly image the atomic structure of crystalline specimens. In crystalline samples the electron wave experiences phase shifts, which reflect the periodic arrangement of the atoms in the crystal lattice (phase contrast).

2.6   Scanning Transmission Electron Microscopy (STEM)

The dedicated STEM has been invented by Manfred von Ardenne in 1937 as an alternative to TEM imaging [184] and further developed to enable atomic resolution imaging by Albert Crewe in the 1970s [185]In STEM imaging a highly focused probe is scanned line by line to generate images by integrating the scattered electrons over a range of scattering angles. In addition, various other signals can be collected as a function of the position of the scanned probe to construct scanning images of the composition, chemical state of the sample, or structural information by energy dispersive X-ray spectroscopy, electron energy loss spectroscopy, or CBED/NBED. In most

modern TEMs it is possible to switch between TEM and STEM mode and use both techniques complementary.

The diffraction-limited resolution of in STEM can be described using the Rayleigh criterion for the minimum resolvable distance δ of two independent object points and is given by

$$\delta = \frac{0.61\lambda}{\mu \sin \beta}$$

<div align="right">**Equation 2-5**</div>

where λ is the wavelength of the incident electrons, μ is the refractive index of the viewing medium, and β is the convergence semi-angle of the magnifying lens. [154] The term "$\mu \sin \beta$" is called the numerical aperture (NA) of the lens. However, the resolution in STEM is constrained by various other factors. These include the spread of electron energy and microscope stability as well as the capability to correct residual lens aberrations. It is given by:

$$r(\beta) \propto \left[\left(\frac{\lambda}{\beta}\right)^2 + (C_s\beta^3)^2 + \left(C_c \frac{\Delta E}{E_0}\beta\right)^2 \right]^{\frac{1}{2}}$$

<div align="right">**Equation 2-6**</div>

where C_S is the spherical aberration coefficient and C_c is the chrommatic aberration coefficient. Consequently, for pursuing higher resolution, one can use higher acceleration voltages. Alternatively, an electron beam emitted by a field-emission gun is characterized by a smaller energy spread compared to the W or LaB_6 electron sources. This also improves resolution. Furthermore, transmission electron microscopes can be equipped with aberration correctors and monochromator to limit the spherical and chromatic aberration of stat-of-art STEM. The new generation of aberration-corrected STEM has pushed resolution limits beyond the 100 pm barrier. [186-188]

Furthermore, depending on the scattering angle of the transmitted electrons being detected, STEM images can be classified as bright-field (BF), annular dark-field (ADF), or high-angle annular dark-field (HAADF) as illustrated in **Figure 2.12a**. Analogous to conventional TEM the intensity distribution in BF-STEM images is governed by the mass-thickness and diffraction contrast mechanisms. Here, the electrons are collected, which have been scattered in a limited angle, typically less than 10 mrad. Alternatively, if only electrons scattered to large angles (more than 10 mrad) are detected, dark field images are obtained, whose contrast is dominated by differences in the mean of atomic number and the sample thickness, so-called ADF- and HAADF-STEM. While the intensity of ADF-STEM arises from the scattered electrons detected in the angle range of 10 –

50 mrad, at HAADF-STEM the electrons scattered above 50 mrad are collected (**Figure 2.12a**). Since this high-angle scattering is largely from electrons elastically scattered by the inner cores of atoms, their contribution is proportional to Z^2 as this scattered intensity approximately follows the Rutherford-scattering cross-section described in **Equation 2-1** when $\theta > 3°$ and the structure-factor approach is a complementary while $\theta < 3°$. [154] Besides, Howie pointed out that the scattering to more than 100 mrad for HAADF imaging is largely due to the thermal diffuse scattering, i.e. quasi-elastically phonon excitation. [189] This strongly reduce the strength of the coherent scattered Bragg beams. The strong atomic number sensitivity and the strong reduction of diffraction contrast at higher scattered angle allows imaging local variations in chemical composition at the nanometer and atomic scale.
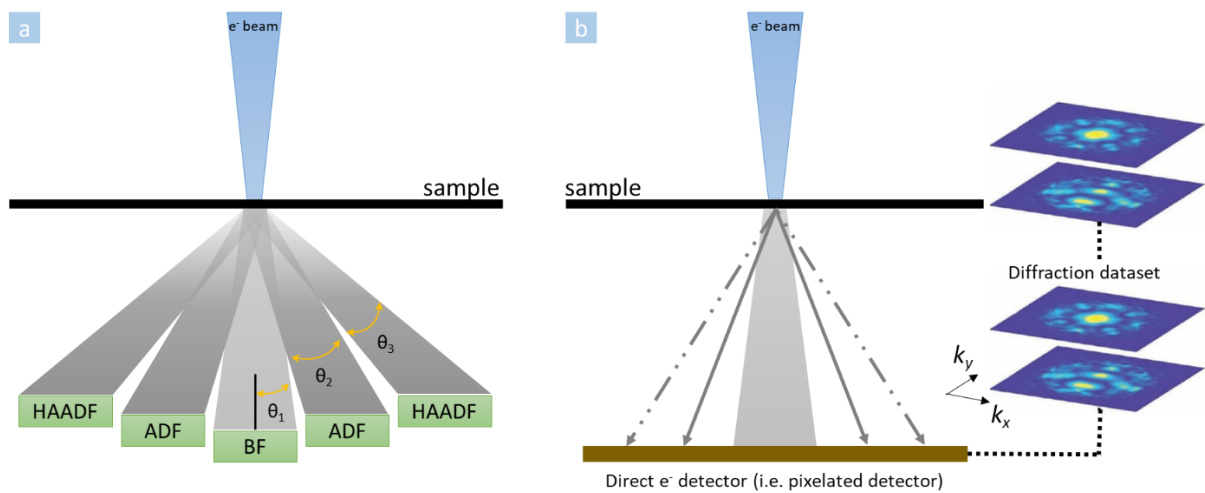
Figure 2.12. Schematic illustration of conventional STEM and 4D STEM. **a**. In conventional STEM, monolithic detectors are used to produce images by integrating a signal from different angular regions of the diffraction plane; collection angles in the ranges $\theta_1 < 10$ mrad, 10 mrad $< \theta_2 < 50$ mrad, $\theta_3 > 50$ mrad. **b**. In 4D STEM, an entire 2D CBED or NBED pattern is recorded at each probe position of a 2D STEM array, resulting in a 4D Diffraction dataset.

2.6.1. 4D-STEM

In contrast to the conventional detectors used for STEM imaging, in four-dimensional (4D) STEM the full 2D CBED or NBED pattern $I(k_x, k_y)$ is imaged on a direct detector at each probe position (x, y), thus generating a 4D data cube $I(k_x, k_y, x, y)$ that can be further analyzed, as schematically illustrated in **Figure 2.12b**. The size of diffraction discs in the CBED or NBED pattern may be

controlled by varying the convergence angle of the STEM probe. The choice of camera length and convergence angle will depend on the types of data that one wishes to extract from the 4D STEM dataset. 4D-STEM is mainly used for virtual imaging, [190, 191] orientation mapping, [192, 193] differential phase contrast (DPC), [194] and strain mapping, [195, 196] as explained below.

The 4D dataset captures the full diffraction signal necessary for 2D STEM imaging of a sample. By utilizing a selected range of pixels in diffraction space, virtual bright or dark field images can be generated. By averaging the diffraction patterns from multiple real space probe positions from the 4D data cube, a selected area diffraction pattern can be obtained.

Furthermore, the diffraction patterns (spot-type or Kikuchi lines) can be indexed with a template matching method to perform so-called automated crystal orientation mapping (ACOM). This allows to track the orientation at each pixel in the sample, which can be represented in an inverse pole figure.

2.6.2. Electron Dispersive X-ray Spectroscopy (EDX)

Energy dispersive X-ray spectroscopy (EDX) is a qualitative and quantitative X-ray microanalytical technique based on the emission of characteristic X-rays of elements due to the inelastic scattering events of the primary electrons with the atoms in the sample as discussed in section 2.1.2. When an incident X-ray hits the silicon drift detector (SDD) (**Figure 2.13a**), its energy is absorbed by a series of ionizations within the semiconductor to create several electron-hole pairs. The electrons are then raised to the conductive band of the SDD and they are free to move within the crystal lattice. The left "holes" behave like free positive charges in the crystal. A bias voltage applied across the SDD "drifts" the electrons down a field gradient between the drift rings. The electrons are then collected at the anode as depicted in **Figure 2.13b**. As a consequence, the individual X-rays are converted to an electric signal proportional to their energy. Based on this X-ray energy, the elements present in the sample can be identified. The detection rate (intensity) of these characteristic X-rays can further be used to measure the amount of each element present. In addition to single spectrum analysis, an area or line scan of electron beam in STEM can be used to acquire X-ray maps or lines to analyze the spatial distribution of elements in the sample.

For quantification of elemental composition in a specimen, the Cliff-Lorimer factors (k-factors) [197] are used to describe the relationship between measured X-ray peak intensities (I) and relative concentration of two elements α and β:

$$\frac{C_\alpha}{C_\beta} = k_{\alpha-\beta} \frac{I_\alpha}{I_\beta}$$

Equation 2-7

where $C_{\alpha, \beta}$ is the weight fraction of element α and β. Moreover, the characteristic X-ray intensity for the given elements α and β is determined by material and detection parameters and proportional to the mass thickness (ρt). It can be derived from:

$$I_\alpha = \frac{K C_\alpha \rho t N_0 Q_\alpha \omega_\alpha a_\alpha i}{A_\alpha}$$

Equation 2-8

where K is a geometry detection factor, C_α is the weight fraction of element α, ρ is the density of the sample, Q_α is the ionization cross-section, ω_α is the fluorescence yield, a_α is the relative intensity factor (fraction of the total measured K line intensity of element α), N_0 is Avogadro's number, i is the beam current, and A_α is the atomic weight of element α. [198] However, in the real sample with a thickness t, the measured X-ray intensity is furtherly influenced by the absorption and fluorescence of X-ray within the sample and the detector efficiency ε. Hence, the Cliff-Lorimer factor can be theoretically calculated with the assumption of an infinitely thin sample as $k_{\alpha-\beta} = \frac{(Q\omega a\varepsilon/A)_\alpha}{(Q\omega a\varepsilon/A)_\beta}$. As a consequence, the C_α and C_β can be determined through measuring X-ray intensities.

Figure 2.13a schematically shows the geometry of the Super-X™ EDX detector used in this work on both the Thermofisher Scientific Themis 300 and Themis Z. The specific geometry of each detector, in particular the shadowing from stage tilt and sample influences the X-ray detection and needs to be included in the quantification. Furthermore, the Bremsstrahlung background has to be subtracted from the spectrum. In practice, k-factor, absorption correction, and background fitting are embedded in the processing software (e.g. Velox used in this work) for EDX quantification.
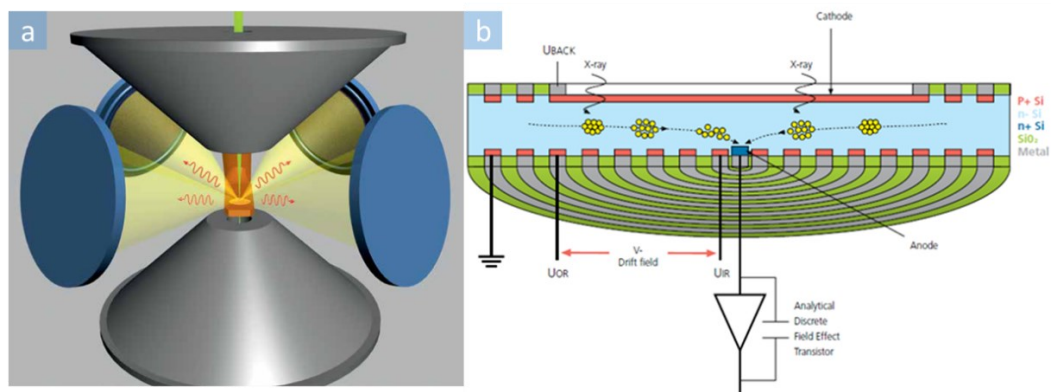
Figure 2.13. **a.** Schematic illustration of Super-X™ EDX detector geometry including 4 silicon drift detectors (SDDs) arranged symmetrically around the sample and the objective lens pole pieces; referring to [199] **b.** Construction and operation of an SDD referring to [200].

2.6.3. Electron Energy Loss Spectroscopy (EELS)

Electron energy loss spectroscopy (EELS) is a complementary analytical technique that takes advantage of the inelastically scattered electrons that transmit a thin sample. The inelastically scattered electrons are bent to 90° and consequently dispersed based on their kinetic energies through the energy dispersing magnetic prism in Gatan image filter (GIF) system (**Figure 2.14**). For instance, zero-loss electrons are bent least and appear at the bottom of the vertical distribution. After passing through the energy selecting slit, the dispersed electron beam is projected back into a spectrum at the plane of the GIF detector. As a consequence, the inelastically scattered electrons are analyzed as a function of electron kinetic energy loss.
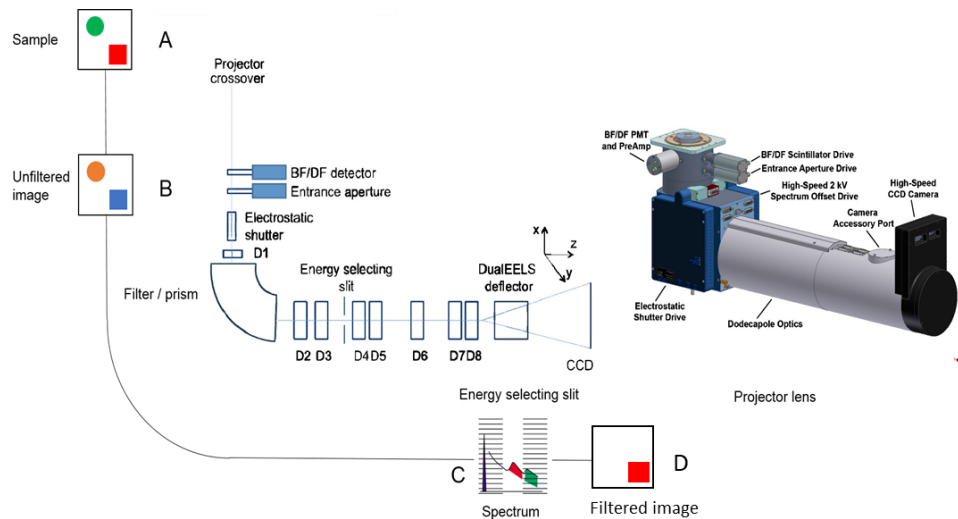
Figure 2.14. Schematic lay-out and CAD model of the GIF showing the location of the key components, Modified from the reference [201].

Based on the energy loss of the incident electrons during the interaction with the inner-shell and outer-shell electrons of sample atoms, an EELS spectrum is composed of three main parts: zero-loss (ZL), low-loss (LL), and core-loss (CL) regions as shown in **Figure 2.15**.
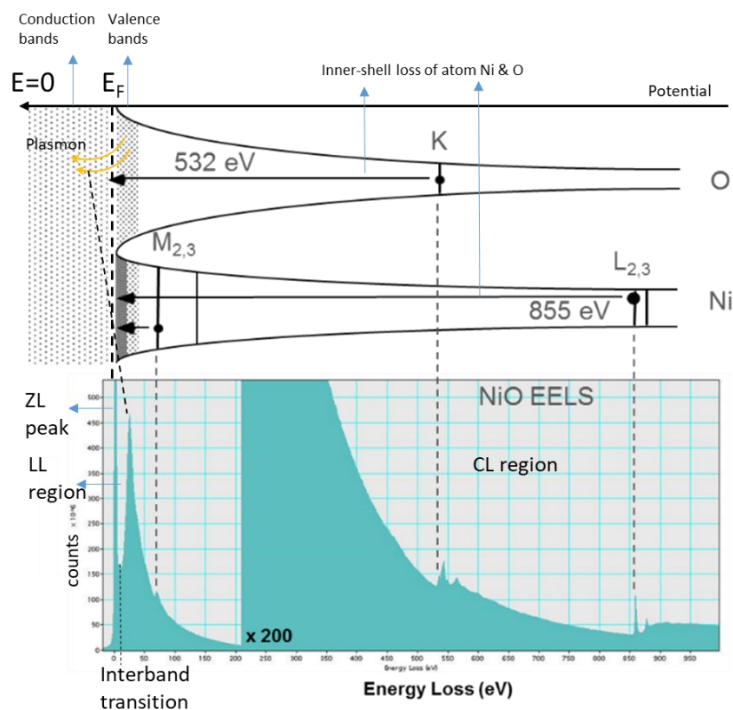
Figure 2.15. A typical electron energy loss spectrum of NiO, its plasmon excitation and core ionization diagram, modified from the reference [202].

The Zero-Loss (ZL) Peak stems from the transmitted electrons that have not been significantly inelastically scattered by the sample. As a consequence, it is located at 0 eV and its full width of

54

half maximum (FWHM) mainly reflects the energy distribution of the electron source and the detection system. It is typically 0.2 – 2.0 eV but may be as narrow as 10 meV or lower in a monochromated electron source. [202] The ZL peak is used as a reference to define the energy loss in the spectrum. Using the ratio of the integrated ZL intensity over the total intensity can be used to determine the inelastic scattering fraction, a measure for the thickness t of the sample in units of the inelastic electron mean free path λ for scattering in the sample. [203]

The Low-loss Region ranges from the ZL peak to about 50 eV energy loss. It is typically dominated by the plasmon peak, the response of the collective excitation of valence electrons or the combined response of the valence electrons and the electromagnetic field on the surface and in the bulk. This response depends on the optical properties of the sample and can be encoded in the complex dielectric function $\varepsilon(\omega)$ (or, in models including spatial dispersion, $\varepsilon(\boldsymbol{k},\omega)$). [204]

The Core-loss region extends from about 50 eV to several thousand electron volts and corresponds to the excitation of core electrons a single atomic site to unoccupied electron energy levels just above the Fermi level E_F of the material or even to free-electron states above the vacuum level. The core loss EELS signal is sensitive to both the atom type and its electronic state. The various ionization edges are classified using the standard spectroscopic notation similar to that employed for labeling X-ray emission peaks; e.g., K excitation for ionization of 1s electrons, L1 for 2s, L2 for 2p1/2, L3 for 2p3/2 and M1 for 3s, etc as shown in Error! Reference source not found.**Figure 2.3b**.

Moreover, accompanying a focused beam scanning a sample by STEM imaging with a resolution up to atomic level, spatially resolved EELS spectra can be acquired. It can provide information about the chemical, physical, and even optical properties of materials in parallel with structural information.

2.7   Instruments Used in This Work

1) Sputter Coater

A magnetron sputter coater (Quantum Technology GmbH) was used to deposit Au conductive layers on the surface of the specimens. It is comprised of three main parts: the cabinet assembly, the vacuum chamber, and the sputter head, which is operated at a fixed voltage of 800V or 1200V DC (variable with plasma current). The ionization gas is Argon.

2) Dual-beam Focused Ion Beam (FIB)

In this work, two conventional dual-beam focused ion beam microscopes were used for SEM imaging and fabrication of TEM lamellas.

FEI Strat 400 S is equipped with a (Schottky) field emission gun as an electron source, a Gallium liquid metal ion source, and a variety of detectors (through-the-lens (TLD) detector, Everhart-Thornley detector (ETD), a backscatter electron detector (BSD), a continuous dynode electron multiplier (CDEM) and a scanning transmission electron microscopy (STEM) detector. The micromanipulator (Omniprobe 200, Oxford Instruments) is also equipped for the in-situ lift-out process during TEM sample preparation. The GIS including Pt, C, and W has to be heated (e.g. for Pt 80℃) to release the gas for deposition. The acceleration voltages used for SEM imaging varied from 0.2 kV to 20 kV, and the range for FIB was between 2 kV - 30 kV. The angle between the ion beam column and the electron beam column is 52°. The detailed parameters used for TEM sample preparation including electron/ion currents will be provided in chapter 3.

Zeiss Auriga 60 is equipped for SEM imaging and FIB processing and an Omniprobe 400 (Oxford Instruments) micromanipulator. The angle between the ion and electron beam columns is 54°. The sample stage can be switched from the regular one to a liquid N_2 cooling stage. The cooling stage (Ametek-Gatan Inc.) can work at temperatures as low as 84K during SEM imaging and the ion beam milling process.

3) Time of Flight Secondary Ion Mass Spectrometer (ToF-SIMS)

In this work, ToF-SIMS analysis was performed by Till Ortmann from the group Prof. Jürgen Janek (Uni Giessen) on an M6 hybrid SIMS (IONTOF GmbH, Münster, Germany). The instrument was operated with 60 keV Bi_3^{2+} primary ions and equipped with electron flood gun to compensate for charging. An O_2^- sputter source was used to remove the materials for depth profiling. The sputter depth was calibrated by confocal microscopy (S Neox, Sensofar, Terrassa, Spain). The software package SurfaceLab 7.2 (IONTOF GmbH, Münster, Germany) was used for data analysis.

4) Transmission Electron Microscopes

A Themis 300 and a Themis Z (Thermofisher Scientific) were used in this thesis. The probe-corrected Themis 300 is equipped with a Super-X EDX detector, a Ceta camera, and a Detrics pixelated detector as well as a NanoMegas ASTAR system. The microscope can be operated at 80, 200 or 300 kV. The double-corrected Themis Z is equipped with a monochromator, a Super-X EDX detector, a Gatan OneView CMOS camera and a Gatan imaging filter (GIF) with a Continuum and K3 IS camera. The Themis Z can be operated at 60, 80 or 300 kV. The detailed

parameters for EDX and EELS acquisition are described in each chapter as different setups were used. The data analysis was performed using TEM Imaging & Analysis (TIA), DigitalMicrograph, and Velox software.

5) *In situ* Biasing System

In situ biasing experiments in **chapters 4 & 5** were carried out to extract Na from the electrolyte through the setup based on a double-tilt STM-TEM holder (ZEPTools, see **Figure 2.16**). The holder has a fixed slot for a sharp nanoscale tungsten tip opposite to a second slot for a FIB-lift-out-TEM-grid. The tip can move in x, y, and z directions with sub-nanometer precision through a piezo-based device and is grounded. The STM tip and the TEM sample are connected with an integrated circuit inside the ceramic head of the holder. To conduct an experiment, the FIB fabricated lamellas were soldered onto the FIB-lift-out-TEM-grids in advance in FIB with Pt for good electric contact. With STEM imaging, the W tip was brought in contact with the lamella. After fixing the contact position, an external voltage was applied typically in the range of -15 V to 23 V, in some extreme cases up to 70 V.
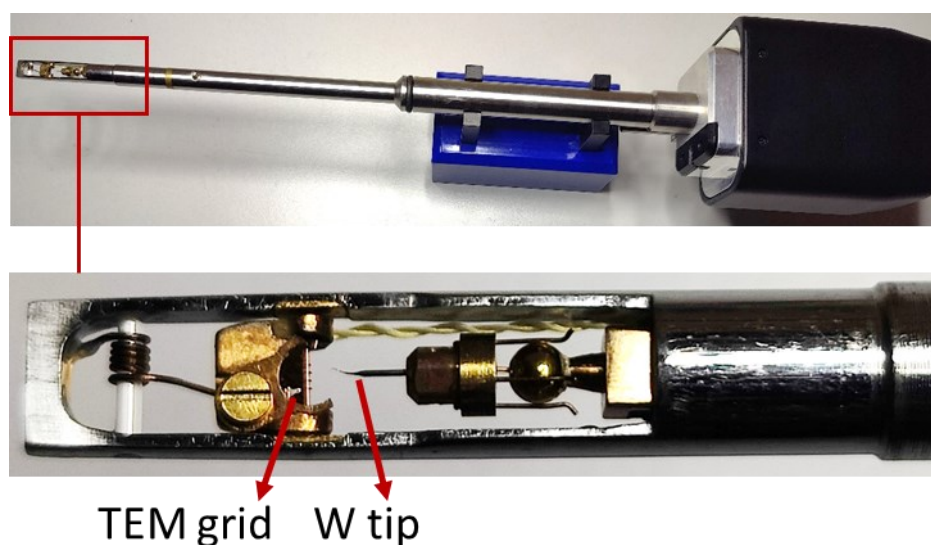
Figure 2.16. STM-TEM holder. A TEM grid and tungsten tip are pointed out by red arrows.

Chapter 3

3. Influence of FIB Processing and SEM Imaging on Solid Electrolytes

3.1 Introduction

Although ASSBs received a lot of attention in recent years, solid-solid interfaces, both in between electrode and solid electrolyte as well as within SEs, are still a major bottleneck for ASSBs to enter the market as discussed in **chapter 1**. [22] To gain insights into and visualize these interfaces, electron microscopy including SEM and TEM coupled with electron and X-ray spectroscopy have emerged as highly advanced characterization methods to reveal their morphology, structure, composition, and oxidation state, either through static imaging or *in-situ*/*operando* with a resolution reaching the atomic scale. [146] However, getting access to the interfaces and producing electron-transparent specimens of the region of interest for TEM analysis without altering or damaging their structure is one of the obstacles to discover the processes responsible for materials degradation during battery cycling. Previous studies have reported various TEM sample preparation methods for different electrode materials [205-207] and solid-solid interfaces [208, 209]. These methods primarily involve mechanical methods (e.g. using ultramicrotome [205] and

diamond-tipped pen [209]), broad ion beam polishing (e.g. ion slicer [207, 210] and FIB [175, 176, 211]) as well as the combination of FIB and ultramicrotomy [206]. While mechanical and broad ion beam polishing methods are suitable for large-scale samples, they can be challenging when dealing with brittle and air-sensitive materials like oxide solid electrolytes [208] or when precise preparation is required from specific areas. Currently, FIB fabrication is the most commonly employed approach and has been applied to a variety of SEs including LiPON- [142], oxide-based [212] and sulfide-based [104] Li and fluoride [143] fast ion conductors. Specifically, in the context of *in situ* TEM investigation for understanding the dynamic evolution of materials, FIB fabrication techniques have been the only reported approaches, both in mainstream *in situ* setups, i.e. MEMS based [143] and STM-TEM) based [142].

However, the influence of FIB processing including SEM imaging on solid electrolytes is reported in detaill in literature. In addition to the well-known air and moisture sensitivity of many battery materials [213] and charging problems of SEs due to their low electric conductivity [53, 54], a fundamental concern lies in the inherent damage caused by electron and ion beam on the structure, chemistry and oxidation state of battery materials. [214] Hence, exploring the effect of the FIB process on SEs is an essential step to reveal the real solid-solid interface with electron microscopy, especially for *in situ* investigations. Moreover, this work was published in *Microscopy* [215].

In this chapter, the morphological, structural, and chemical changes of three common SEs, i.e. LiPON, Na-β''-alumina, and $Na_{3.4}Si_{2.4}Zr_2P_{0.6}O_{12}$ (NZSP) induced by SEM imaging and FIB processing were investigated. Furthermore, an efficient cryo-FIB approach to prevent significant changes during TEM sample preparation was developed to enable reliable *in situ* and *ex situ* TEM analysis of these materials in the following work.

3.2   Experimental

3.2.1   Materials

Pellets of commercial Na-β''-alumina (Ionotec Ltd.) and $Na_{3.4}Si_{2.4}Zr_2P_{0.6}O_{12}$ (NZSP) (prepared by Frank Tietz's group at Forschungszentrum Jülich) [216] as examples for Na^+ ion conductors were used to investigate the impact of FIB processing. In addition, LiPON thin films (prepared by the group of Wolfgang Jägermann at Technical University Darmstadt) [217] as an example for a Li^+ ion conductors and Na-β''-alumina were used to explore the influence of SEM imaging.

3.2.2 Methods

3.2.2.1 Working Procedures and Conditions for SEM Imaging and Standard and Cryogenic FIB Fabrications

To explore electron beam effects in the SEM for SEs in more detail, a systematic series of dose experiments at various acceleration voltages (0.5-30 kV) using the SEM inside the Strata 400 dual beam FIB were conducted on LiPON thin films (provided by the group of Wolfram Jägermann at Technical University Darmstadt) as well as on the Na-β″-alumina pellet sample (Ionotec Ltd.). The experiments for LiPON thin film were conducted by Dr. Venkata Sai Kiran Chakravadhanula. For this analysis, the morphological changes in the sample were investigated at a fixed magnification with different electron doses and acceleration voltages.

Standard and cryogenic FIB fabrication and SEM imaging have been conducted using a Strata 400 S (FEI Company) dual-beam FIB and an Auriga 60 cross beam FIB (Zeiss). For cryogenic FIB preparation of TEM samples, a home-made stub with specimen and TEM grid positions was made for the liquid nitrogen cooling stage (Gatan Inc.) as shown in **Figure 3.1**. For the Na-β″-alumina and NZSP (prepared by the group of Dr. Frank Tietz) preparation, a ~100 nm thick Au layer was deposited on the SE pellets in a sputter coater (Quantum Design GmbH) and silver paste was used to connect the surface of specimens and the SEM stubs. This helps to enhance the electric conductivity for SEM/FIB imaging. Afterwards, both standard (here labeled s-FIB) and cryogenic FIB processing were performed as shown in **Figure 3.1**. The whole process of s-FIB was conducted at room temperature (RT). Electron-deposited of Pt on the specimen was first performed using the electron beam with an acceleration voltage of 5 kV and a current of 1.6 nA. The total electron dose for the deposition was around 8.1×10^8 e/nm^2. Pt deposition by FIB followed with a total ion dose of around 1.4×10^4 Ga$^+$/nm^2. Afterwards, trench milling and cutting-off were carried out with 30 kV Ga$^+$ ion beam with a current of 9.3 nA. In this process, a total ion dose of 1.7×10^5 Ga$^+$/nm^2 was used to prepare a lamella with a thickness of around 2.5 μm. The lamella was transferred to a TEM grid with a micromanipulator. The lift-out and transfer process required around 1200 e/nm^2 for SEM imaging and 400 Ga$^+$/nm^2 for attaching/removing the micromanipulator. For the final thinning and polishing, a dose of around 6.2×10^4 Ga$^+$/nm^2 at 30 kV was used. At the end, to remove redeposited material and Ga$^+$ ions from the surface of the TEM lamella, the specimen was briefly cleaned using a 5 kV ion beam. SEM imaging to support the milling and polishing procedures (including intermittent viewing and patterning) was conducted at 5 kV and with a current of 1.6 nA and a viewing frequency of 1 Hz. The final dose

was estimated to be 1200 e/nm^2 for the milling and polishing. The detailed parameters are listed in **Table 3-1.**
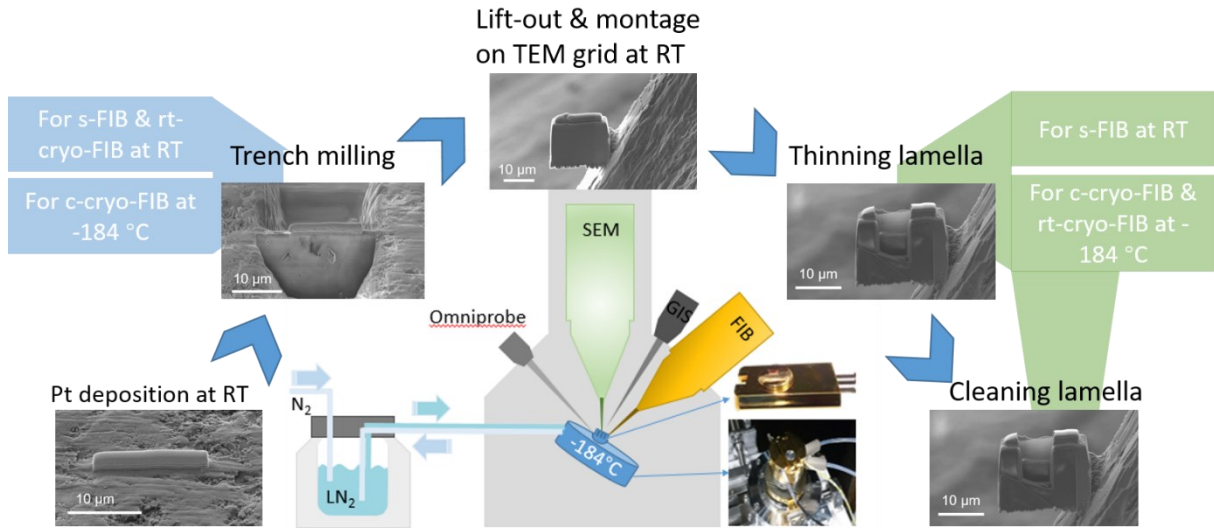
Figure 3.1 Working procedures of different FIB processes.

Table 3-1. Work parameters for the different FIB processing conditions

Step	FIB process	Working temperature/℃			Acceleration voltage & beam current	The angle between specimens surface and the ion or electron beam/degree
		s-FIB	c-cryo-FIB	rt-cryo-FIB		
1	Pt deposition		RT		Electron beam: 5kV/1.6nA	0
					Ion beam: 30kV/280pA	52 (strata) 54 (Auriga)
2	Trench milling	RT	-184	RT	Ion beam: 30kV/9.3nA for s-FIB/rt-cryo-FIB & 16nA for c-cryo-FIB	0
3			RT		Electron beam: 5kV/1.6nA	0

	Lift-out and glue to TEM grid				Ion beam: 30kV/280pA	52 (strata) 54 (Auriga)
4	Thinning lamella	RT	-184	-184	Ion beam: 30kV/93pA-430pA for s-FIB & 240 pA for c-cryo-FIB & rt-cryo-FIB	Upside: -1.5 Downside: 1
5	Cleaning surface	RT	-184	-184	Ion beam: 5kV/48pA	Upside: -7 Downside: 1.5

Analogously, the preparation labeled c-cryo-FIB was performed with similar parameters, but both the trench milling and the final polishing were conducted at cryogenic conditions (-184 °C) using a liquid nitrogen cooling stage. For the sample labeled rt-cryo-FIB only the final polishing was performed at -184 °C, but the trench milling was performed at room temperature. In all cases, the doses and dose rates were similar. The micromanipulator was kept at room temperature and the gas injection needles (GIS) were heated to 80 °C. This makes cryogenic preparation available for lift-out process, using a regular FIB only equipped with a cryogenic stage.

3.2.2.2 Working Conditions for TEM Characterization

A probe-corrected Themis 300 TEM operated at 300 kV was used for TEM analysis of the (cryo) FIB prepared samples. The electron beam diameter was nominally 170 pm with a convergence angle of 30 mrad and a screen current of 70 pA. HAADF-STEM imaging with EDX spectroscopy and electron diffraction were used to characterize the composition and microstructure of the TEM lamellas prepared by the different FIB processes. The dose for one EDX map was around 2000 e/nm^2. The Brown-Powell ionization cross-section model was used for the EDX quantification after second order multi-polynomial modelling and subtraction of the background; the sample thickness and density were estimated for adsorption correction. Prior to TEM characterization, the TEM lamellas were cleaned by an argon-oxygen plasma using a 1070 Plasma Cleaner (Fischione Inc.) to remove carbon compounds absorbed on the surface. The FIB-processed SE specimens were kept in a glove box for intermediate storage due to their sensitivity to humidity. Long-term exposure to air leads to a Na-loss from the SE. [218] However, the short transfer from the glove box to the TEM through air did not seem to be critical.

3.3 Results and Discussion

3.3.1 Influence of SEM Imaging on LiPON

It is widely accepted that charging effects occur in insulating materials resulting in a buildup of electric fields due to the accumulated surface electrons during SEM imaging. [219, 220] Moreover, STEM imaging in the TEM is known to facilitate Li^+ ion diffusion and phase separation, which is driven by the electric field gradient in the material. [144] However, there is little information on the influence of the electron beam on the SEs in the SEM. Herein, morphological changes of SEs in the SEM were explored depending on the dose and acceleration voltage of the electron beam.

During SEM imaging, distinct morphological changes were observed in the LiPON thin film with increasing dose. First morphological changes appeared as small bright spots randomly distributed on the previously uniform thin film surface with a dose as low as 22 e/nm^2 at 2 kV acceleration voltage (**Figure 3.2b**). These bright spots disappeared gradually and turned dark with increasing dose as shown in **Figure 3.2c**. The surface charging of the LiPON thin film due to the limited electrical conductivity could be a potential reason for this morphological evolution. As the surface charging results in Li^+ migration to the surface, where they are reduced to Li as schematically illustrated in **Figure 3.2f**. The thin Li deposits might react with residual air/water in the FIB chamber and/or will be damaged by the continuous electron beam illumination leading to the dark features observed during SEM imaging. In addition, the dose applied to the sample is at a level where previous studies indicated that first damage happens in the oxide structure. [221, 222] This might also be the origin for the observed changes.
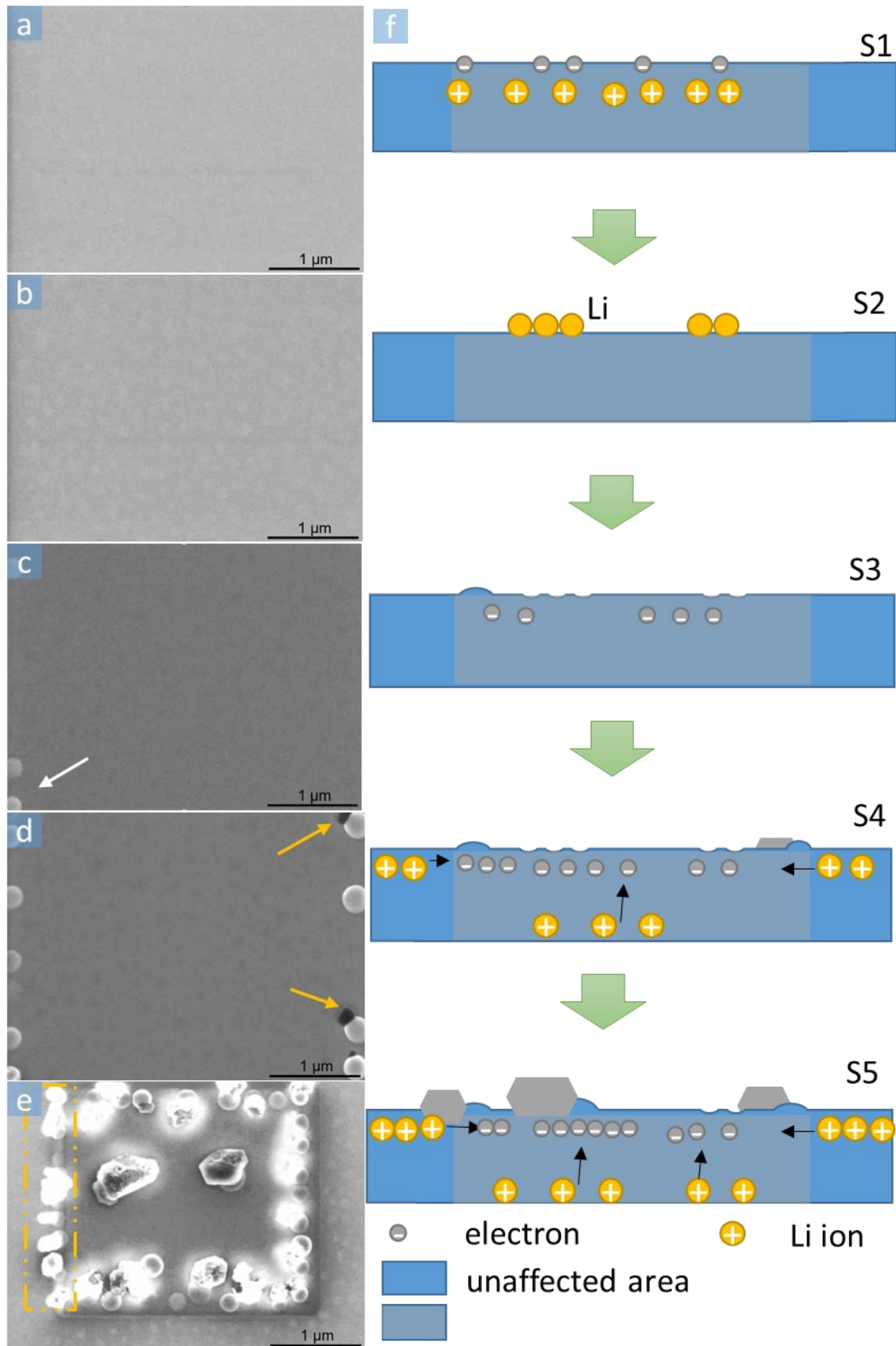
Figure 3.2. SEM imaging at 2 kV of a LiPON thin film with increasing dose and corresponding simplified model of the processes in the SEM: **a.** Initial status; **b**. After 22 e/nm^2; **c**. After 433 e/nm^2; **d.** After 995 e/nm^2; **e.** De-magnified SEM image after 3500 e/nm^2; **f.** Simplified model of the structural changes observed with increasing dose in the SEM.

With further increasing dose, larger spherical particles appear as pointed by a white arrow in **Figure 3.2c**. Afterwards, whiskers from the substrate start to grow at one edge of the spherical particles as pointed out by the orange arrows in **Figure 3.2d**. The whiskers are assumed to be metallic Li due to their well-defined polyhedral-like shape with characteristic faceting angles of around 120°. Interestingly, the spherical particles and the whiskers always start from the left boundary of the scanning area followed by the right, top/bottom edge of the scanning. Only when reaching much higher doses of around 2300 e/nm^2, they appear in the middle of the scanning area. Surface charging leads to the largest electric field gradient at the boundary between the scanned and the surrounding area leading to the preferential Li whisker growth there. The slightly higher dose applied there due to the fly-back time of the SEM beam during scanning is presumably the reason for the initial start of the growth on the left side of the scanned area (orange dashed rectangle region in **Figure 3.2e**). At lower magnification (**Figure 3.2e**), it becomes obvious that the whiskers grow pointing away from the edge of the scan frame. This can be attributed to the orientation of the electric field gradient. Only on the marked side in **Figure 3.2e** the whiskers grow to the left pointing away from the frame as the actual illuminated region starts there. Another contribution to the observed directed Li dendrite growth could be the number of surface charges present, which would lead to faster Li reduction and higher growth speed in locations with higher amount of surface charges.

In addition to the dose, the influence of the acceleration voltage was also explored as shown in **Figure 3.3**. The same final dose of 3500 e/nm^2 was employed during SEM imaging of LiPON at the different acceleration voltages. When the voltage was as low as 0.5 and 1 kV, no whisker growth was observed, but only some surface changes and slight carbon contamination build up. With increasing acceleration voltages (2 kV, 3 kV, 5 kV, and 10 kV), whisker growth was observed clearly. The whisker density decreased with increasing acceleration voltage in this range, whereas their size increased. This can be related to the distribution of surface electrons and the involved excitation volume. At low acceleration voltages (0.5 kV and 1 kV), surface charging leads to limited electric field buildup to induce Li$^+$ ion migration. However, intermediate acceleration voltages (2 kV, 3 kV, 5 kV, and 10 kV) lead to a larger electron penetration depth and interaction volume as surface charging increases. As a consequence, a larger amount of Li$^+$ ions contribute to Li whiskers growth. The increasing acceleration voltage may have an influence on the nucleation and diffusion rates, which limits the density changes. When the acceleration voltage was raised to 15 kV, 20 kV, and 30 kV, the morphological changes became less pronounced. A potential contribution could be increased surface sputtering of Li at high acceleration voltages, thus removing Li grown on the surface. The threshold voltage for surface sputtering of Li has been

estimated to be around 5-9 kV, [145] fitting to the significantly reduce observation of Li wires above 10 kV acceleration voltage. Moreover, the increasing penetration depth with higher acceleration voltages presumably results the reduction of surface charging, i.e. electric field, and consequently a less driving force for Li^+ migration towards sample surface. Based on the morphological evolution at different acceleration voltages, extremely low acceleration voltage of 0.5 kV and 1 kV are the best conditions for SEM imaging of LiPON during FIB preparation to reduce electron beam-induced damages.
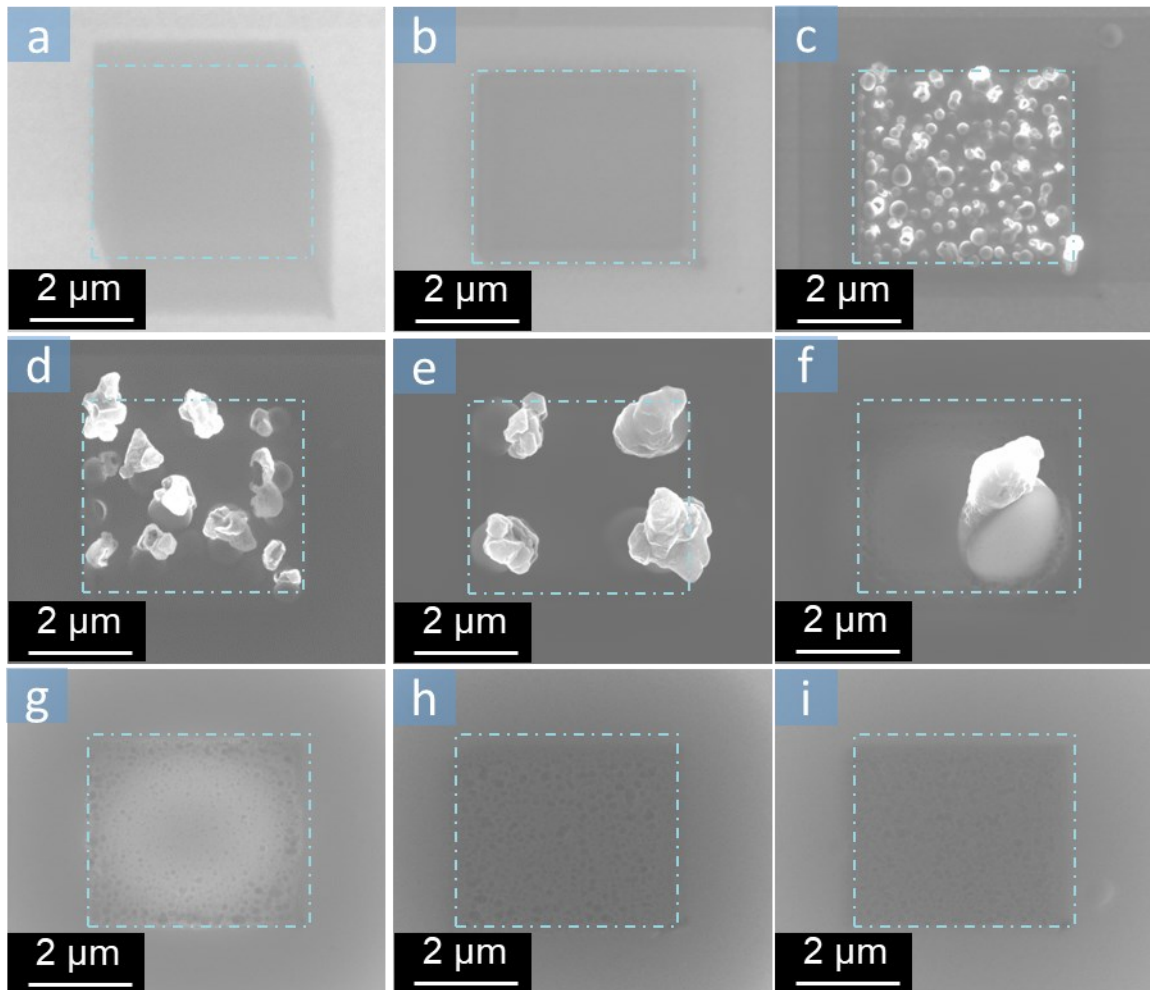
Figure 3.3. SEM imaging of a LiPON thin film at different acceleration voltages after applying a total dose of 3500 e/nm^2 to the blue rectangular region. At low voltages, some drift was unavoidable; **a**. 0.5 kV; **b**. 1 kV; **c**. 2 kV; **d**. 3 kV; **e**. 5 kV; **f**. 10 kV; **g**. 15 kV; **h**. 20 kV; **i**. 30 kV.

In addition to adjusting the acceleration voltage, conductive layer-coating is an alternative method to minimize the charging effect in the SEM. [219] In this work, the Na-β″-alumina and NZSP

pellets were coated with Au for the TEM sample preparation. Here, the behavior of Au-coated and uncoated Na-β″-alumina pellets using the same imaging condition (**Figure 3.4**) were compared at a common acceleration voltage of 5 kV. In analogy to LiPON, whisker growth was observed at uncoated Na-β″-alumina starting with a dose of around 600 e/nm^2 (white arrows in **Figure 3.4b**). Moreover, after a dose of around 1200 e/nm^2, more whiskers grew around the edge of the scan area (**Figure 3.4c**), which is also similar to the observations in LiPON. Nevertheless, the Au-coated sample did not show any whisker growth under the same dose condition (**Figure 3.4d - f**) and even at a much higher dose of around 60000 e/nm^2 (**Figure 3.4g - i**). The successful protection from whisker growth by Au-coating during SEM imaging is another indication that the whisker growth is related to surface charges and the resulting electric field. In turn, the Au coating is an efficient protection preventing metal ion migration in the SEM.
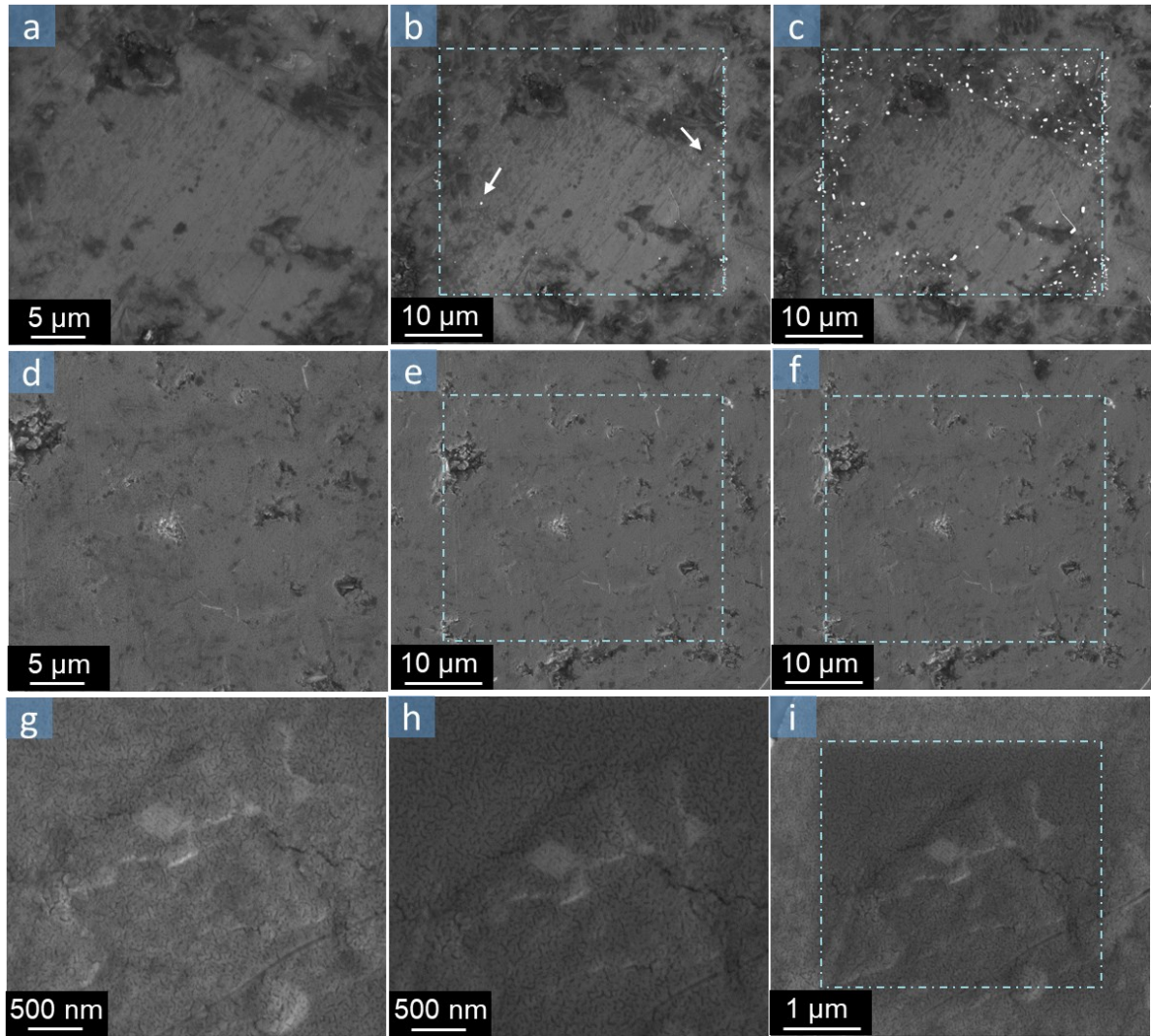
Figure 3.4. SEM imaging at an acceleration voltage of 5 kV of a pristine (**a-c**) and an Au-coated (**d-i**) Na-β″-alumina pellet with increasing dose applied to the area indicated by the blue rectangle; **a.** Initial structure of the scanned region of the pristine Na-β″-alumina. **b.** With a total dose of ~600 e/nm^2 applied to the area in the blue rectangle where the first Na whiskers were observed. **c.** When the total dose increased up to ~1200 e/nm^2 a large number of whiskers were visible around the edge of the scanned area **d**. Initial structure of the of Au-coated Na-β″-alumina. **e. & f.** With the total dose of ~600 e/nm^2 and ~1200 e/nm^2 applied to the area in blue rectangles. **g.** Initial structure of Au-coated Na-β″-alumina at higher magnification. The structure of Au-coated Na-β″-alumina at higher magnification after the total dose ~60000 e/nm^2 applied in (**h**) and the blue rectangle in (**i**).

3.3.2 Influence of FIB Processing on Na-β″-alumina and NZSP

Since Au-coating was discovered as an efficient way to prevent the whisker growth, it was employed to minimize the influence of SEM imaging to only explore the effect of FIB process on Na-β″-alumina and NZSP. During standard (s-FIB) TEM preparation of both Na-β″-alumina and NZSP, whiskers grew from the frame of the lamella and the thinned region as highlighted in **Figure 3.5a - d & f - i**. The whiskers on the frame continued to grow with continuous thinning. In the thinned region, this growth was not as obvious as further thinning partially removed the developing whiskers. However, it was also observed that the whiskers could appear again at the same position of the thinned region. Moreover, the whiskers with well-defined polyhedral shape are assumed to be metallic Na, [223] , which oxidized during sample transfer into the TEM. Despite the Na extraction from the SEs, the basic crystalline structure of the SEs is well maintained as can be seen from the electron diffraction data (**Figure 3.5e & j**), which is in excellent agreement with the NZSP and Na-β″-alumina structure. One can expect that the specific physical properties of the SEs, in particular the high mobility of Na^+ ions and the extremely low electronic conductivity contribute to the development of Na whiskers during the ion-polishing procedure. Radiolysis of ceramics typically leads to a displacement of atoms on the anion sublattice, [224] which further leads to a loss of oxygen (in case of oxide-based ceramics) [222] and ultimately to a damage of the crystalline lattice [224, 225]. Nevertheless, even during our room temperature sample preparation, the damage to the crystal lattice was apparently not significant enough to see noticeable changes in the diffraction patterns. However, the Na located in between the cation sublattice is highly mobile in SEs. In analogy to the electric field-induced damage mechanism suggested by Jiang et al. in STEM, [53, 54] it is proposed that the electric field induces Na^+ ion migration during FIB processing and SEM imaging as well. The Na^+ ions in the bulk are driven to migrate either directly in the electric field gradient of the ion/electron beam as well as towards the sample surface due to the electric field developing in the insulating sample and by the accumulation of surface charges from the SEM or FIB imaging. Once at the surface, the Na^+ ions can be reduced by surface electrons. This fits to the nucleation and growth of Na whiskers observed mostly at the edges of the thicker frame of the TEM lamella, where the strongest charging is expected, and a rich Na reservoir is present in close vicinity. In contrast, during the trench milling procedure, it was barely observed that Na whiskers grew on the surface of the specimen even though much larger ion doses have been employed. This is presumably related to the thick gold coating on the specimen surface, which is further connected via silver paste to the ground thus providing good electrical conductivity, preventing significant charge accumulation at the surface both for the bulk specimen as well as the

(still thick and well connected) TEM lamella. [219] Therefore, the main driving force for Na$^+$ ion migration and Na whisker growth is not present during this step.
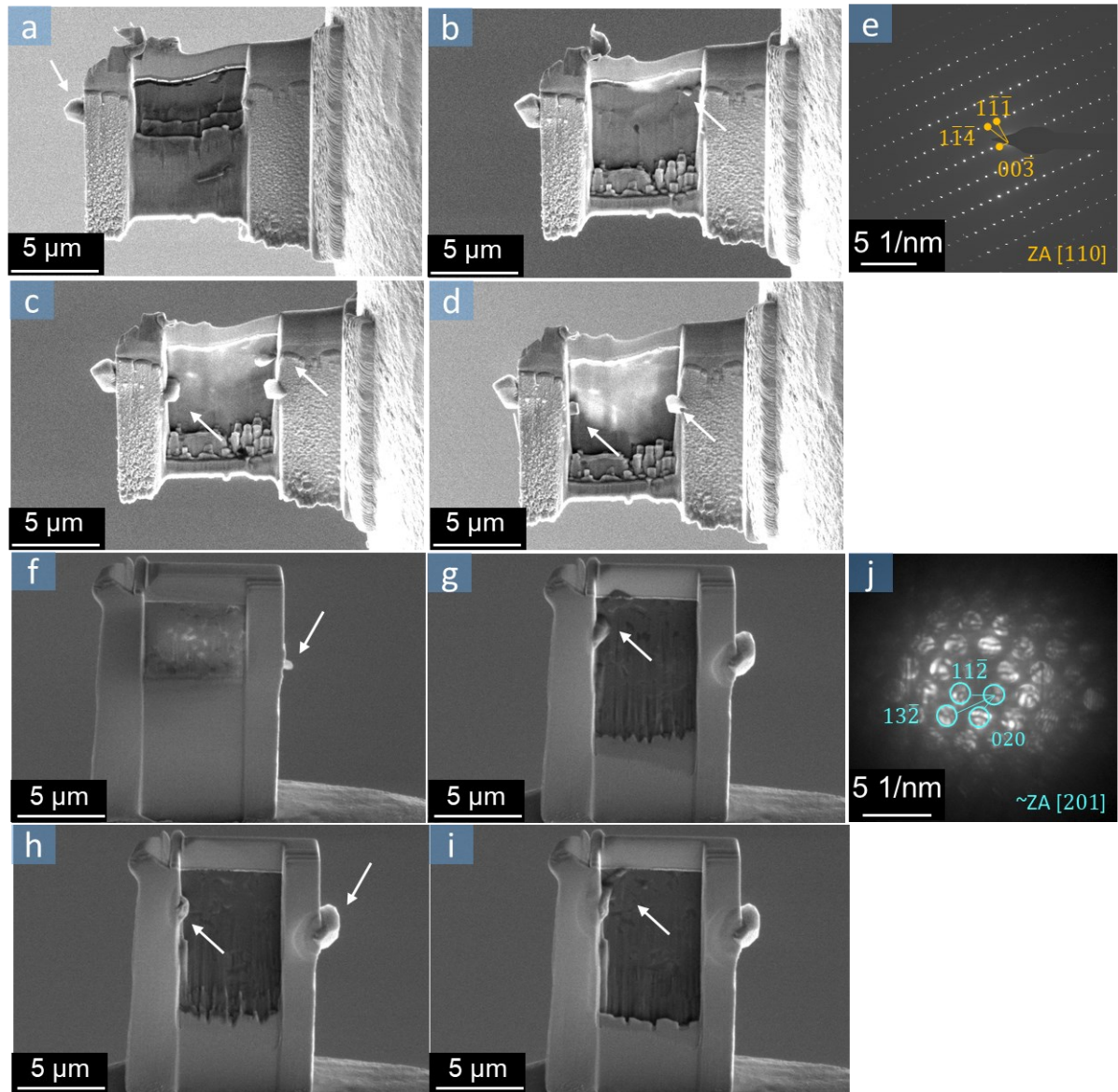
Figure 3.5. Na-β″-alumina and NZSP fabricated by s-FIB; **a.-d**. SEM images of Na-β″-alumina during the thinning procedure; **e.** SAED of Na-β″-alumina; **f.-i.** SEM images of NZSP during the thinning procedure; **j.** NBED of NZSP. Na whiskers are pointed out by white arrows.

To understand the influence of the standard FIB processing on the SEs, TEM characterization of the s-FIB fabricated lamellas was conducted. Surprisingly, the SAED pattern of the Na-β″-alumina TEM lamella (**Figure 3.5e**) can be clearly indexed as [110] zone axis of Na-β″-alumina (based on ICSD_200990). Similarly, the NBED of NZSP (**Figure 3.5j**) can be indexed [$\bar{1}$01] zone axis of the monoclinic NZSP structure [216] (based on ICSD_473). The measured and indexed lattice

spacing of both materials are listed in **Table 3-2**. The slight differences can be ascribed to slight calibration and measurement errors. It indicates the typical layer structure of the Na-β″-alumina material is maintained after the s-FIB process. Moreover, the lattice parameters are not strongly affected by the Na loss, which is in agreement with observations during synthesis of Na-β″-alumina with various Na content [226]. This indicates that the Na-whisker growth during thinning does not significantly influence the crystal structure of the SEs and the Na^+ ion transport path is presumably maintained after ion beam milling and polishing.

Table 3-2. Lattice spacing of Na-β″-alumina and NZSP. The references for Na-β″-alumina and monoclinic NZSP are based on ICSD_200990 and ICSD_473. The slight deviations can be attributed to slight calibration and measurement errors.

	Lattice plane	Reference lattice spacings/nm	ED based lattice spacings/nm
Na-β″-alumina	$(00\bar{3})$	1.12	1.12
	$(1\bar{1}\bar{1})$	0.48	0.47
	$(1\bar{1}\bar{4})$	0.42	0.41
	$(1\bar{1}\bar{2})$	0.47	0.46
	$(\bar{1}1\bar{5})$	0.39	0.39
NZSP (monoclinic phase)	$(11\bar{2})$	0.40	0.41
	$(13\bar{2})$	0.25	0.26
	(020)	0.45	0.47
	$(0\bar{2}0)$	0.40	0.43
	$(13\bar{2})$	0.25	0.26

At higher magnification, HAADF-STEM images and low dose EDS elemental maps of Na-β″-alumina (**Figure 3.6a - d**) show a reduced Al content indicating a thinner region compared to the adjacent grains, suggesting that this region was next to a void prior to specimen polishing. In addition, small particles can be seen in the vicinity of voids and GBs. With the corresponding Na maps, the small particles can be identified as Na oxide, which originated from oxidation of residual Na-whiskers after the thinning procedure. It suggests that the Na whiskers grow preferentially at voids and GBs during the thinning procedure. This has also been observed during *in-situ* TEM studies looking at the influence of grain boundaries on Na^+ ion migration in the next chapter. As

presented in **Figure 3.6a,** a triple boundary (orange arrow) presumably turned into the crack after thinning. This can be attributed to strain induced by the growth of Na whisker at the triple-grain boundary. This indicates that the growth of the Na whiskers may lead to microstructural changes.

Analogous to the s-FIB processed Na-β″-alumina, Na was also found in the vicinity of voids/gaps of s-FIB processed NZSP TEM lamella as indicated by the white arrow in **Figure 3.6e & f**. Moreover, local Na loss is also visible close to the vicinity of the Au coating layer as presented in **Figure 3.6e - j**.
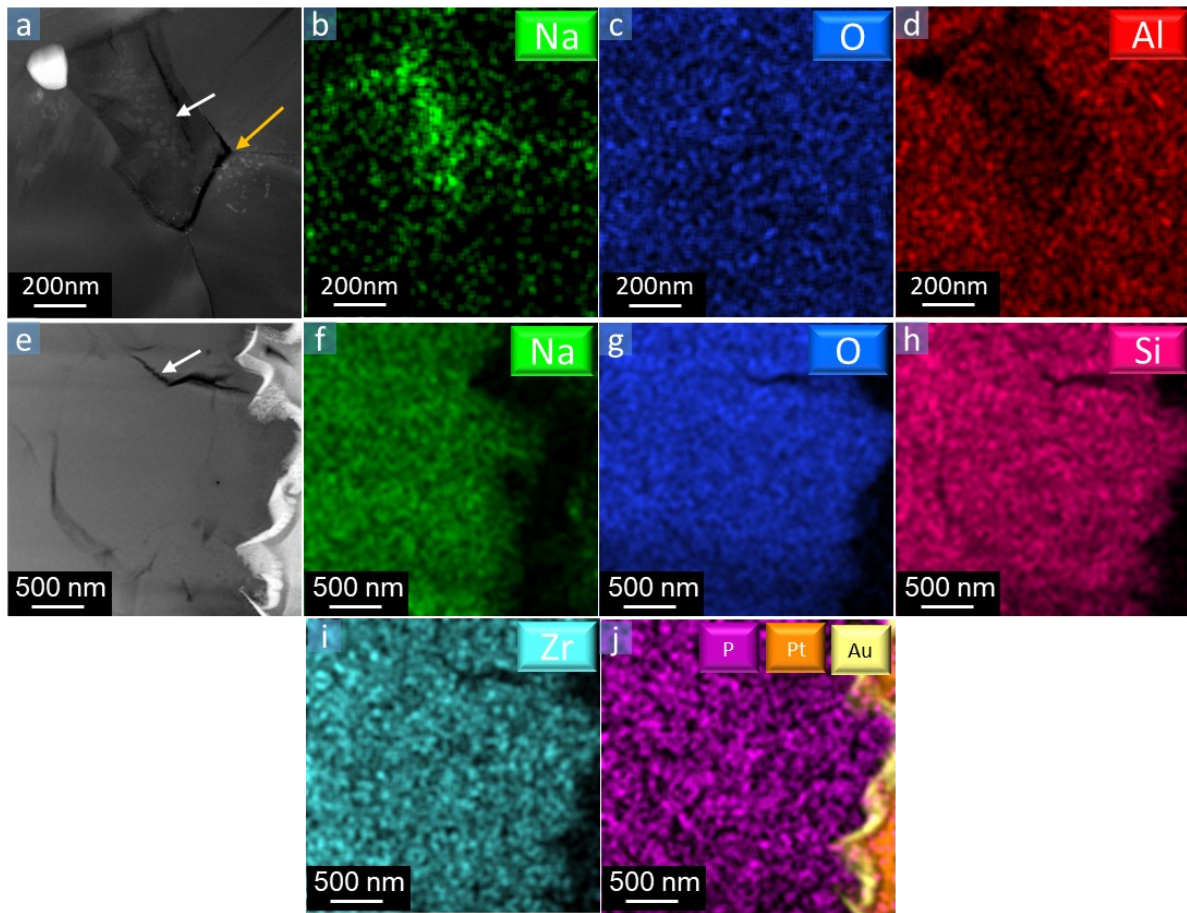
Figure 3.6. s-FIB fabricated TEM lamellas of Na-β″-alumina and NZSP; **a. - d**. HAADF-STEM image and low dose EDX net intensity maps of Na, O and Al of Na-β″-alumina, **e. - i.** HAADF-STEM image and low dose EDX net intensity maps for Na, O, Zr, and Si of NZSP, **j**. Overlaid P, Pt, and Au low dose EDX net intensity map of NZSP.

Although the crystal structure of the Na-β″-alumina and NZSP material is maintained after s-FIB processing, the Na whiskers growing from the frame of the lamella have a huge influence on the

Na content of the thinned area due to the high mobility of Na ions in the SEs. The Na content of the thinned area is critical for the working condition of the SE, for instance, the ionic conductivity and the driving force for Na^+ ion migration, in *in situ* TEM experiments of oxide-SE-based micro-/nano-batteries will be affected. [226, 227] STEM-EDX analysis of the thinned area of the Na-β″-alumina and NZSP lamellas (**Figure 3.7a & b**) reveals that the Na content of the thinned lamella is significantly reduced when looking at the Al : Na (Na-β″-alumina) and Si : Na (NZSP) atomic ratio. The Al:Na ratio measured in s-FIB fabricated Na-β″-alumina was around 1 : 0.06, but in bulk Na-β″-alumina it was 1 : 0.16. Similarly, the Si:Na ratio measured in s-FIB fabricated NZSP was around 1 : 1.11, but for as-prepared NZSP it was 1 : 1.42. This indicated indicates that there was around 60% Na loss by thinning the Na-β″-alumina lamella and around 20% Na loss in the thinned NZSP lamella.
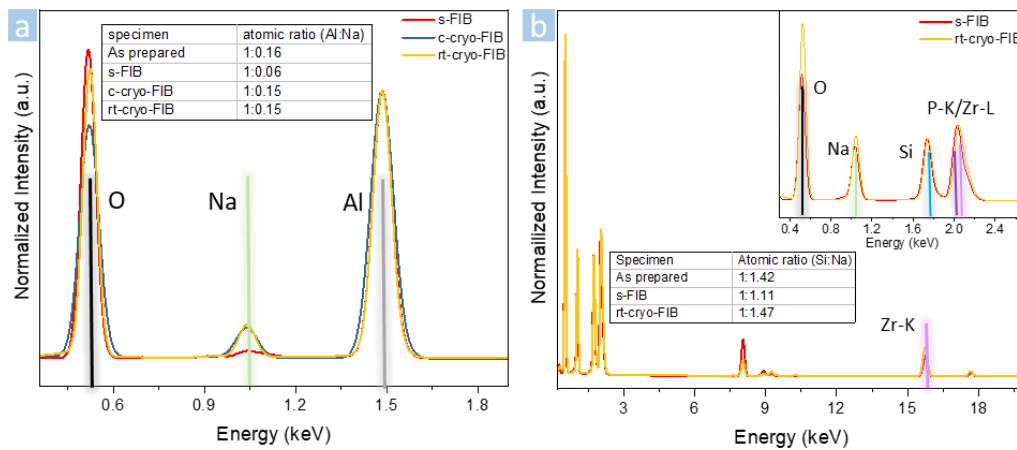
Figure 3.7. EDX spectra of different FIB fabricated Na-β″-alumina (**a**) and NZSP samples (**b**). Their corresponding atomic Al : Na (Na-β″-alumina) and Si : Na (NZSP) ratios are listed in the inset tables.

As the crystal lattice of both Na-β″-alumina and NZSP can be maintained well after standard FIB preparation and the most critical change during s-FIB fabrication is Na loss due to high mobility of Na^+, cryogenic conditions are expected to help to maintain the chemical composition by decreasing their mobility. Ideally, the whole preparation should be performed under cryo conditions, but with a standard FIB system this cannot be achieved. Compared to the ion dose used in the trench milling and lamella thinning, cutting off the lamella during the lift-out process

requires significantly lower dose. Therefore, the lift-out process is expected to have only a small influence on the overall lamella preparation. Hence, in this work, a standard FIB system equipped with a liquid nitrogen cooling stage was used to maintain cryogenic condition for trench milling and thinning (c-cryo-FIB), whereas the Pt electron and ion beam deposition as well as the lift-out procedure were done at room temperature. Since there was barely any noticeable Na wire growth during trench milling in a well-coated sample, the fabrication procedure was furtherly simplified by applying the cryogenic condition only during TEM lamella thinning and polishing (rt-cryo-FIB). No Na whiskers formed during the cryogenic thinning procedure of both SEs (**Figure 3.8**). A clean surface and uniform Na distribution were observed as shown in **Figure 3.9a & e**. Furthermore, the average Na content of the lamellas fabricated by c-cryo-FIB and rt-cryo-FIB have been determined by EDX (**Figure 3.7**). With both cryogenic milling and polishing procedures, the atomic ratio between Al and Na was enhanced to 1 : 0.15, which is close to the bulk Na-β''-alumina composition. Similarly, in NZSP, the Si to Na atomic ratio is at the same level as in the as-prepared bulk NZSP when using cryogenic polishing. This indicates that the cryogenic conditions prevent Na loss in the processed region, showing that cryogenic polishing during FIB processing is an efficient way to prepare TEM lamella of oxide SEs.
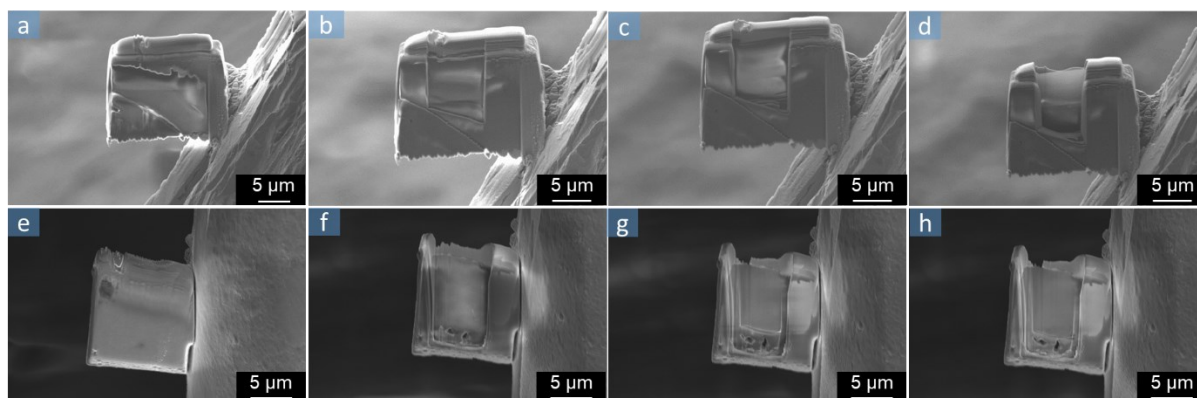
Figure 3.8. Thinning TEM lamella at cryogenic condition; **a. - d.** Na-β''-alumina; **e. - h.** NZSP.
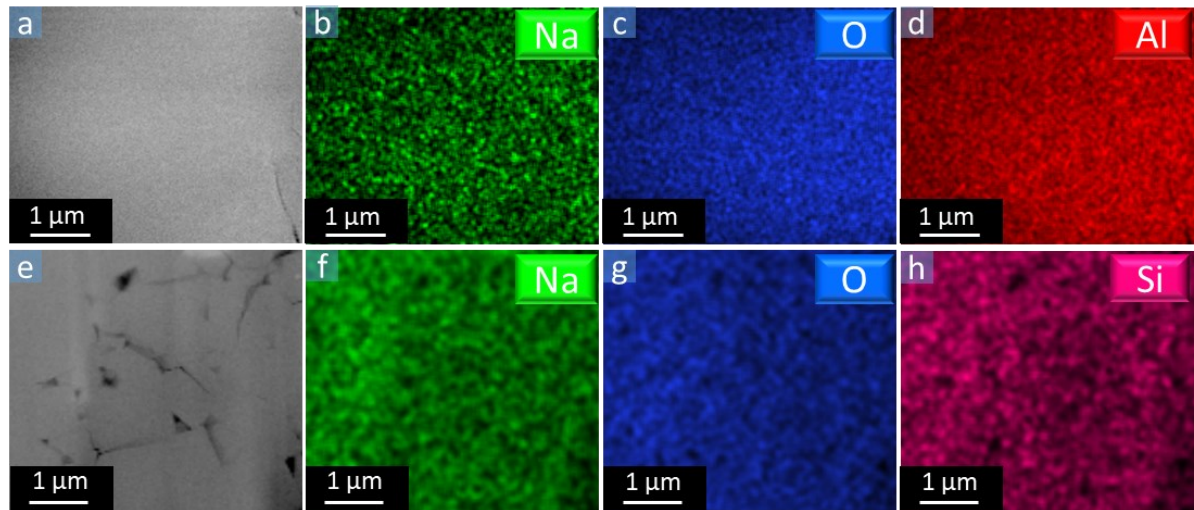
Figure 3.9. The rt-cryo-FIB fabricated TEM lamellas of Na-β″-alumina and NZSP; **a. - d.** HAADF-STEM image and low dose EDS net intensity maps of Na, O, and Al of Na-β″-alumina; **e. - h.** HAADF-STEM image and low dose EDS net intensity maps of Na, O, and Si of NZSP.

3.4   Summary

In this chapter, the influence of SEM imaging and FIB processing on oxide SEs during imaging and TEM sample preparation was explored. Not only the Ga^+ ion beam is changing the sample, but already SEM imaging can induce significant Li^+/Na^+ ion migration in SEs. Li/Na Whisker growth was observed during SEM imaging both for LiPON thin films and Na-β″-alumina ceramics. The damage depends on acceleration voltage and results in significant whisker growth between 2 and 10 kV acceleration voltages. The local electric fields generated by the electron/ion beam and, more dominant, charging of the insulating SE samples is presumable the driving force for Li/Na migration. Applying a protective conductive layer strongly reduces surface charging, thus efficiently reduces the damage during SEM imaging and helps during SEM characterization as well as for a good TEM sample preparation by FIB.

When good electrical contact of the SE is maintained, no significant Na loss was observed, but the final thinning and polishing procedure was still critical during FIB processing for TEM sample preparation. With typical room temperature FIB preparation, this resulted in a Na loss of around 60 % in case of Na-β″-alumina and 20 % in case of NZSP. Nevertheless, the crystal structure of both SEs was maintained during FIB preparation without noticeable changes in lattice parameters. To reduce Na migration during TEM sample preparation, cryogenic cooling to liquid N_2 was successfully applied, resulting in TEM samples where the nominal composition essentially

maintained. Even if only the final thinning and polishing was performed with liquid N_2 cooling, the preparation of TEM samples without noticeable changes was successful. This is a very efficient way to prepare sensitive samples.

Chapter 4

4. Microstructural Influence on the Na filament growth in ASSNBs

4.1 Introduction

ASSBs based on a metal anode (Li and Na) are projected to possess high energy and power density and overcome the safety limitations of their liquid electrolyte counterparts. However, the inevitable interfacial problem of dendritic growth is still a challenge in ASSBs. With the urgent commercial development, a series of comprehensive studies on Li-filament growth mechanisms were conducted. Rather than a directional dendrite growth as in the liquid electrolytes, a series of studies reported that dispersed Li filamentary dendrites nucleate at the micro-contact interface between Li/SEs and inside SEs (e.g. voids and GBs) and penetrate along the GBs of SEs towards the counter electrode (cathode). [114, 115, 117]

The Li penetration is reported to strongly depend on the SE material (e.g. LiPON, LLZO, and $Li_2S-P_2S_5$). [118, 119] Unlike the glassy sulfide- or polymer-based SEs, oxide SEs are polycrystalline with GBs contributing significantly to the microstructure. It is widely accepted that the higher resistance to Li^+ ion migration across GBs [127], the lower band gap [115] and shear modulus [136] of GBs result in Li nucleation and penetration. Despite these impediments created

by the GBs limiting the performance of ASSBs, it was found that they can also provide superior fast ion transport pathways as Li^+ prefers to transport along GBs. [132] In addition, Wang et al. discovered that ion transport along GBs showed a smaller energy barrier than across GBs in cubic Na_3PS_4 by first principles and phase field calculations. [228] In addition to the anisotropic effect of GBs on ion diffusion, anisotropic ion transport properties are also presented in the single crystalline bulk of NaSICON ($Na_3Zr_2Si_2PO_{14}$) [229] and, more pronounced, in Na-β''-alumina with its layered crystal structure and 2D transport path. However, the impact of these distinctive microstructural properties on the Na filament growth during Na deposition is still unclear.

Hence, for understanding the influence of microstructure and especially anisotropic ion transport on Na filament growth during Na deposition, a Na-β''-alumina-based model was built to realize cathodic sodium deposition in *in situ* TEM investigations. The experimental Na filament growth was combined with a crystal orientation analysis as basis for computational transport simulation to investigate the relationship between the microstructure and Na filament growth as well as Na^+ ion transport. The work was complemented by *post-mortem* SIMS analysis as bulk reference and to look at larger microstructural features (e.g. voids) to establish a microstructural model of Na filament formation. Moreover, this work is published in *Advanced Energy Materials*. [230]

4.2   Experimental

4.2.1   *In Situ* TEM Observation of Na filament Formation

A polycrystalline Na-β''-alumina SE pellet (Iontec. Ltd) was used in this work. To get access to its GBs in TEM, FIB was applied to prepare TEM lamella with a ~4 μm x 5 μm large and ~170nm thick electron transparent area. The preparation followed the RT-cryo-FIB procedure described in **chapter 3**. An Au layer deposited on the SE surface served as negative electrode together with the Pt layer, which was deposited for FIB processing, during the *in situ biasing* TEM measurements. The double aberration corrected Themis Z and probe corrected Themis 300 TEMs operated at 300 kV were used for TEM analysis. The *in situ* TEM setup based on the STM-TEM holder is shown schematically in **Figure 4.1,** which enables biasing of the TEM lamella between Cu grid and the grounded W tip.
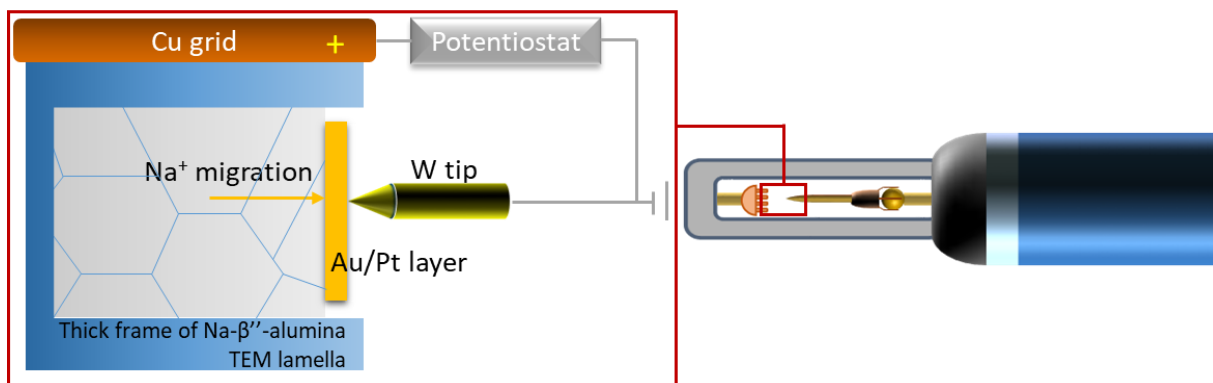
Figure 4.1. Schematic illustration of *in situ* biasing TEM setup based on FIB-processed TEM lamella of Na-β″-alumina coated with Au and Pt.

Once the W tip was manipulated to contact the specimen, a positive voltage in the range of 10 – 17 V was applied to the TEM Cu grid. Meanwhile, HAADF-STEM image series were acquired to record the morphological changes during biasing. Low-dose EDX elemental mapping was used to explore the compositional distribution. 4D-STEM and STEM based automated crystal orientation map (ACOM) analysis were employed to characterize the microstructure of Na-β″-alumina. The electron beam diameter was nominally 170 pm with a convergence angle of 30 mrad and a nominal screen current of 50 pA to conduct the HAADF-STEM imaging with a frame size of 1024 x 1024 pixels and a frame time of 1.57 s, while an electron probe with convergence angle of 0.5 mrad, nominal diameter of 2 nm, and the current of 50 pA were used for 4D-STEM and ACOM.

4.2.2 Modeling the Current Density Distribution in Polycrystalline Na-β″-alumina

To understand the microstructural influence on the Na-ion transport in the polycrystalline Na-β″-alumina, the current density distribution was modeled by Janis Eckhardt (from the group of Prof. Christian Heiliger, Institute for Theoretical Physics of Justus Liebig University Giessen). In accordance with the ADF-STEM image, the 4D-STEM grain map, and the ACOM map of the thin region in TEM lamella, its actual microstructural map was generated. The projected 2D structure was discretized into an array squared pixels. Each pixel was assigned to a specific grain G_i in the microstructure (with implicit GBs between them), ZrO_2 impurities, or the electrode. This enabled to cover the different structural conditions for transport modeling, e.g. transport within the grain bulk, transport across a GB, the insulating ZrO_2 impurities, and considering the charge transfer reaction at the electrode interface.

The 2D transport computations are based on an electric network model recently developed by Eckhardt et al. [231-233]. Transport behaviors are simplified using an array square resistor to simulate the direct current (DC) distribution in the involed material region. In this case, local resistors describing the transport between pixels in the electric field are set based on the different microstructure features, i.e. $2 \cdot R_{Bulk}$ for bulk transport, $2 \cdot R_{Bulk} + R_{GB}$ for transport across GB, and $R_{Bulk} + R_{CT} + R_{Elec}$ for charge transfer at the electrode interface. Moreover, ZrO_2 impurities are considered to be ideally blocking, i.e., $R_{ZrO2} = \infty$ Ω. The magnitude of the local resistance R_i is determined by the conductivity σ_i and the structural resolution, i.e. $R_i = 1/\sigma_i \cdot L_i/A$ where L_i and A are the length of the transport process and the interface area between two pixels.

The anisotropic transport properties of Na-β''-alumina were taken into account in the computations. This means that the orientation of the individual grains determined the bulk and GB conductivity σ_i in the x- and y-directions. To this end, the 3D orientation of each grain was illustrated with an atomic unit lattice model (generated by VESTA software) in **Figure 4.11**. For the calculation of the conductivities σ_i ($i = (x, y)$) in x- and y-directions of the surface of the TEM lamella (xy-plane), the orientation of the Na$^+$ ion conduction plane in the xy-plane was first determined from its projection, which is generated from the ACOM map (see **Figure 4.2**). As both direction and area of the projection of Na$^+$ ion conduction plane contribute to the individual conductivity σ_i in the xy-plane as depicted in **Figure 4.2**, it can be formulated following **Equation 4-1**:
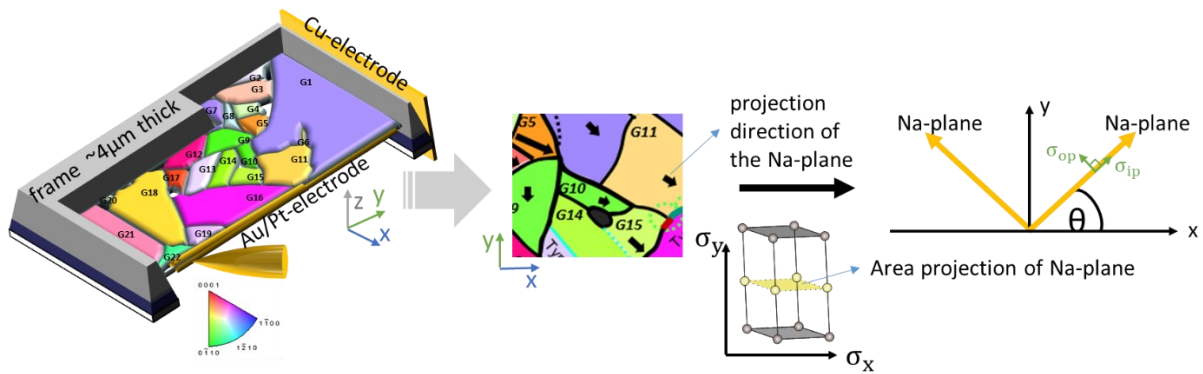
Figure 4.2. Calculation of the conductivity of individual grain based on the projection of Na$^+$ ion conduction plane on the surface of Na-β''-alumina TEM lamella (xy-plane). The projection direction of individual Na$^+$ ion conduction plane was normal to the projection of c-axis of Na-β''-alumina cystall on the surface of Na-β''-alumina TEM lamella. θ is the angle between the projection direction and x-axis of surface of Na-β''-alumina. The area projection of Na$^+$ ion plane was dependent on the angle α between itself and the surface of Na-β''-alumina.

$$\sigma_i(\theta, \alpha)$$

$$= \begin{cases} \sigma_{op} \cdot |\sin \alpha| \cdot |\sin \theta| + \sigma_{ip} \cdot (|\cos \theta| + |\cos \alpha| \cdot |\sin \theta) \\ \sigma_{ip} \cdot (|\sin \theta| + |\cos \alpha| \cdot |\cos \theta|) + \sigma_{op} \cdot |\sin \alpha| \cdot |\cos \theta| \end{cases}$$ **Equation 4-1**

Where θ is the angle between the projection direction of Na$^+$ ion conduction plane and the x-direction, α is the angle between Na$^+$ ion conduction plane and the surface of Na-β''-alumina, σ_{ip} and σ_{op} are the in-plane ionic conductivity along the Na$^+$ ion conduction plane and out-of-plane ionic conductivity across the Na$^+$ ion conduction and their ratio is assumed as $\sigma_{ip}/\sigma_{op} = 10^3$. This is based on the extreme high out-of-plane Na$^+$ ion diffusion activation energy compared to the one for diffusion along the Na$^+$ ion conduction plane.

In addition, the thickness of the GB was estimated to be 1 nm, and an isotropic GB conductivity was assumed to be twenty times smaller than the in-plane conductivity, i.e., $\sigma_{ip}/\sigma_{GB} = 20$. Ion migration along GBs was not considered in the simulations. The ionic conductivity of the frame of the TEM lamella, averaged over several grains with random/unknown orientation, was assumed to be 250 times smaller than the in-plane conductivity, i.e. $\sigma_{ip}/\sigma_{backbone} = 250$. In addition, the charge transfer reaction at the electrode interface and the transport within the electrode is assumed to be resistance-free.

4.2.3 *Post Mortem* ToF-SIMS Characterization on the Cycled Na-β''-alumina

To explore the macroscopic cyclic behavior of Na-β''-alumina during Na-deposition, post-mortem ToF-SIMS analysis was performed by Till Ortmann from the group of Prof. Jürgen Janek at the Institute for Physical Chemistry of the Justus Liebig University Giessen. A symmetrical cell (Na|Na-β''-alumina|Na) was assembled by isostatic pressing of Na foils on both sides of a Na-β''-alumina separator at 100 MPa for 15 minutes. Galvanostatic cycling of this symmetric cell was performed on a CompreDrive device (rdh, Darmstadt, Germany) in combination with a SP 200 potentiostat (BioLogic Science Instruments). In total, 110 cycles were conducted at the symmetric cell. For each cycle, after the working electrode was polarized for 2 minutes following 1-minute rest, the current direction was reversed following the same procedure. A current density of 260 $\mu A/cm^2$ was applied to the WE while 240 $\mu A/cm^2$ to counter electrode since the electrodes have slightly different area.

After cycling, the Na electrodes were removed from the Na-β″-alumina pellet using scalpel and it was broken to obtain a cross section of the cell. the cross-section was furtherly polished on the WE side with Ar^+ ions at 8 kV for 2 h under cryogenic conditions (150 K) using a Leica EM TIC 3X device (Leica Microsystems GmbH, Wetzlar, Germany) for SIMS analysis. For the reference measurement of as-prepared Na-β″-alumina, a cross-section was prepared and polished using the same conditions as for the cycled material.

ToF-SIMS analysis was performed using an M6 hybrid SIMS (IONTOF GmbH, Münster, Germany). All ToF-SIMS measurements were carried out in positive-ion mode. The topography mode of the analyzer was activated to increase the total ion count. Imaging was conducted with 60 keV Bi_3^{2+} primary ions with a cycle time of 60 µs and a low-energy electron flood gun for charge compensation. Both samples were analyzed on an area of 100 µm × 100 µm with 512 × 512 pixel and a total primary ion dose of $2.9 \cdot 10^8$. For depth profiling an area of 50 µm × 50 µm with 256 × 256 pixel was analyzed using same LMIG and analyzer setting as for imaging (total ion dose of primary ions = $5.8 \cdot 10^9$). Sputtering was performed with 2 kV O_2^- species on an area of 300µm ×300 µm with a total ion dose of $4 \cdot 10^{15}$.

Overlayer 2D images were created using the RGB function of SurfaceLab 7.2 (IONTOF GmbH) binning 4 pixels after shift correction. The depth profile binning 4 pixels in z-direction was created after shift correction with the RGB function.

4.3   *In Situ* TEM Characterization

4.3.1.   *In Situ* TEM Observation of Na filament Formation

To understand the impact of the microstructure of the polycrystalline Na-β″-alumina on the Na^+ ion transport and Na filament growth at room temperature, the *in situ* biasing TEM setup shown in **Figure 2.16.** was used. As the positive biasing voltage (i.e. 15 V) was applied on the Cu grid and the W tip connected Au/Pt electrode was grounded, Na^+ ion migration was facilitated towards the Au/Pt electrode in the TEM as depicted in **Figure 4.1**. The Na-β″-alumina at the positive electrode (Cu grid) was sacrificed as Na source to enable cathodic sodium deposition at the Au/Pt electrode [234, 235] or close to the contact with the W tip.

In a first experiment, the W tip was positioned with high precision to establish contact with the Na-β″-alumina as shown in **Figure 4.3 & Figure 4.4** and a bias voltage as high as 70 V was applied to the specimen. The hypothesis was that Na-plating would happen around the local electric contact

of the W tip to the Na-β″-alumina due to the strong electric field induced by the small contact area. Indeed, Na appeared in this region after biasing as shown by the STEM-EDX elemental mapping presented in **Figure 4.3c**. However, during biasing filamentary particles started to grow at a GB as indicated by green arrows in **Figure 4.4** rather than at the local electric contact with the W tip. This suggests that Na deposition varies for different microstructures and, in particular, GBs act as seed for Na filament growth inside Na-β″-alumina.
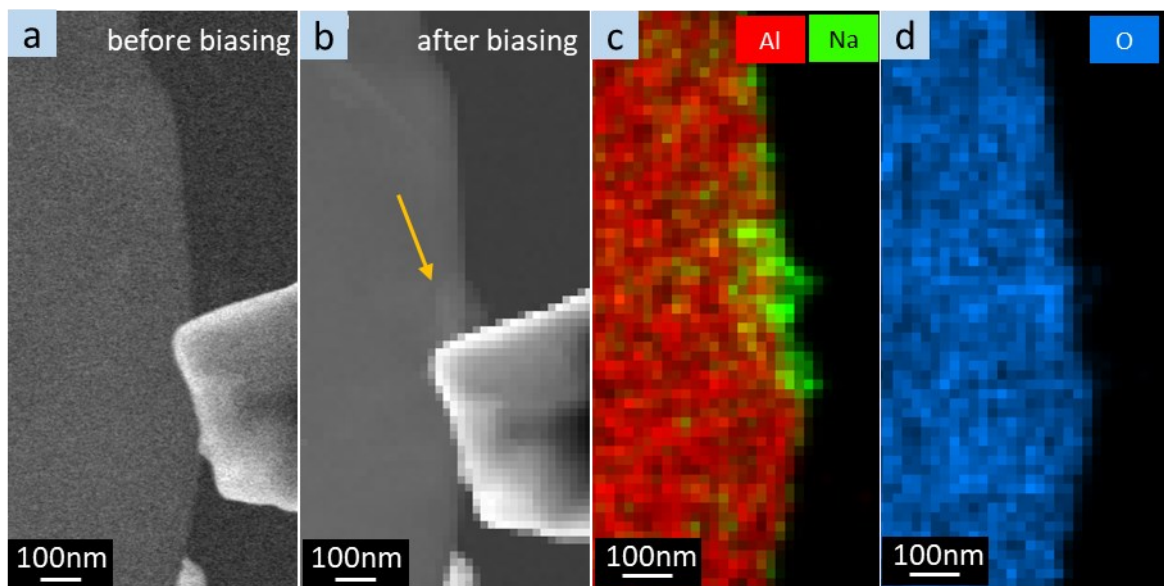
Figure 4.3. Local electrical contact with W tip to a large grain of Na-β″-alumina. HAADF-STEM image before biasing (**a**) and after biasing (**b**). The arrow indicates the position of the formed Na particle after biasing**.** The W tip was removed after biasing for the acquisition of the EDX elemental maps. **C**. Overlaid EDX elemental maps for Al (red) and Na (green); **d**. EDX O (blue) map.
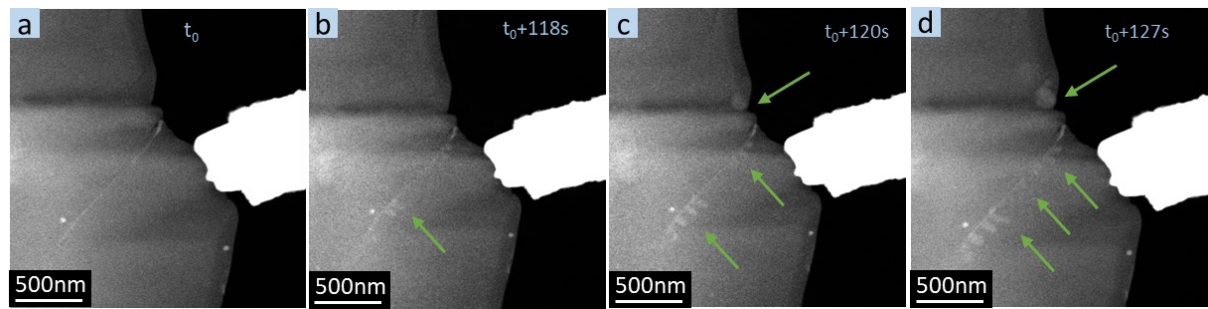
Figure 4.4. Local electrical contact between the W tip and Na-β″-alumina. **a. – d.** Time series HAADF-STEM images showing Na filament growth (pointed by green arrows) at a GB during biasing.

Since it was accepted in a previous study about high-temperature Na-S batteries that Na formation can be caused by high local fields, [236] the setup with local direct electric contact between the W tip and a single grain is not ideal to reveal the relationship between the microstructure and Na^+ ion transport and Na deposition. Therefore, a Na-β″-alumina│Au/Pt system was built to provide a uniform contact to the grains next to the Au/Pt electrode as shown in **Figure 4.1**. Another concern was anodic decomposition of β-alumina, which was found at high temperatures during Na deposition [214, 234-238] following the assumed reaction below:

$$Na_2O \cdot 11Al_2O_3 \rightarrow 2Na + \frac{1}{2}O_2 + 11Al_2O_3 \qquad \textbf{Equation 4-2}$$
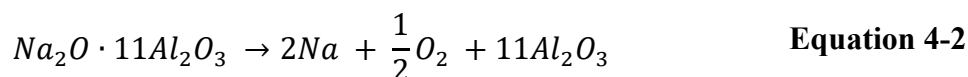
However, analyzing the filament formation shown in **Figure 4.4**, it became clear that neither thermal decomposition nor high local fields are responsible for Na filament formation in the *in situ* TEM experiments. During biasing, filaments appeared at the GB between the grains denoted as G1 and G2 as well as the Au/Pt electrode as shown in **Figure 4.5c** and were identified as Na based on the EDX Na map (**Figure 4.5d**). Apart from the EDX analysis, the appearance of the peak at around 6 eV in the EELS of the filament indicated the metallic state of the Na- filament. [239, 240] The filaments grew further during prolonged biasing as shown in **Figure 4.5e & f**. Comparison of the intensity of the O, Na, and Al EDX peaks (**Figure 4.5j & k**) acquired at regions without filament at different times during biasing, they suggest that the Na contents of grains G1 and G2 was maintained and even slightly increase during the prolonged biasing. This can be attributed to Na^+ ion transport from the grains attached to the Cu grid and far from the observed region towards the Au/Pt electrode. Moreover, the crystal structure of G1 was characterized by the NBED before (**Figure 4.5g**) and after Na filament growth (**Figure 4.5h**), which showed that the crystal structure

and orientation were maintained. The conservation of the Na content in the grains and their identical crystal structure/orientation before and after filament formation proves that the Na filament growth was not induced by degradation of Na-β″-alumina. Therefore, this experiment shows that the Na filament formation in the field of view is due to a process combining Na⁺ migration towards the W tip and Na deposition at the Au/Pt electrode as well as at the GB. This suggests that the Na filament growth inside the polycrystalline Na-β″-alumina SE may not relate to bulk decomposition in a running ASSB cell.
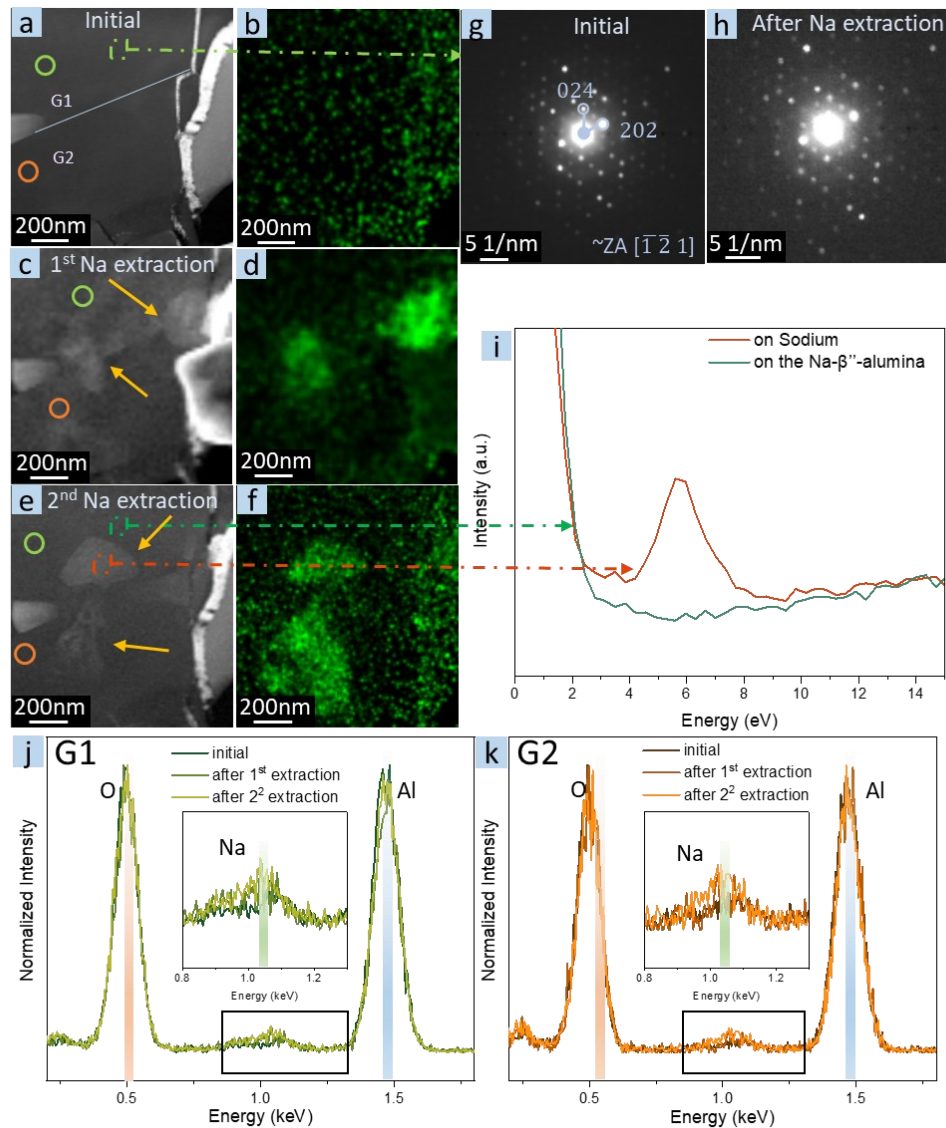
Figure 4.5. Comparison of the crystal structure and Na content in the pristine state and after Na extraction: **a. - f.** HAADF-STEM imaging and EDX Na maps (**a. – b.** Initial state, **c. - d.** After 1ˢᵗ Na extraction, **e. - f.** After further Na extraction). Two distinct grains of Na-β″-alumina denoted G1 and G2 and the corresponding GB is marked by the light blue line in (**a**). The Na filament

position is highlighted by yellow arrows. **g - h**. NBED of G1 in the pristine state and after Na extraction; **i**. Low loss EELS of a Na filaments (orange) and adjacent Na-β″-alumina grain (green). The EDX spectra of the circle-marked region are plotted in **j and k** for the G1 (green) and G2 (orange) grains.

The mechanism controlling the Na nucleation and growth is accepted as an analog to Li growth in ASSBs, i.e. highly dependent on electronic and ionic transport properties of the SE. [241] On the one hand, the local gradient of the transfer number is one of the reason resulting in the Na$^+$ ion reduction and Na nucleation A rather small band gap as low as 1-3 eV was found at some GBs in oxide SEs [242], which can trap excess electrons within polycrystalline Li SEs. [134] On the other hand, the ionic bottlenecks were assigned as the other reason leading to an overshoot of the local chemical potential of lithium μ_{Li} (i.e. $\mu_{Li} > \mu_{Li}^0$, the standard chemical potential of Li metal), which builds up a driving force for Li nucleation. [135, 243] However, the origin of the local over potential and blocking Na$^+$ ions at GBs are still unclear.

To reveal the origin within Na-β″-alumina and explore the effect of the microstructure on Na$^+$ migration and Na filament growth, the *in situ* biasing TEM measurements were carried on lamella with multiple grains as presented in **Figure 4.6a**. Some GBs exhibit blurry features in HAADF-STEM image (see **Figure 4.6**) due to similar contrast. Therefore, the polycrystalline nature of the specimen (dark green inset rectangle in **Figure 4.6a**) was enhanced by the 4D-STEM generated RGB coded grain map (**Figure 4.7A**). Virtual images of individual grains (**Figure 4.7n - z**) were generated based on the distinctive reflections in diffraction (**Figure 4.7a - m**) and the individual grains color coded in RGB mode. The microstructural features (i.e. the geometry of GB network) are highly enhanced in this overlaid image (**Figure 4.7A**). With the help of the 4D-STEM based grain map, GBs were marked in the HAADF-STEM image in **Figure 4.6** to track the Na filament formation and its relation to the GB network during the *in situ* measurement. When the W tip was brought into contact with the Au/Pt layer (acting as electrode) and a bias voltage applied, the potential of the grains and corresponding GBs next to the Au/Pt layer is equivalent. During biasing we observed that Na segregated at the interface with the Au/Pt layer and formed small filamentary seeds growing with time. The real-time observation of the Na filament formation is presented in **Figure 4.6b - e**.
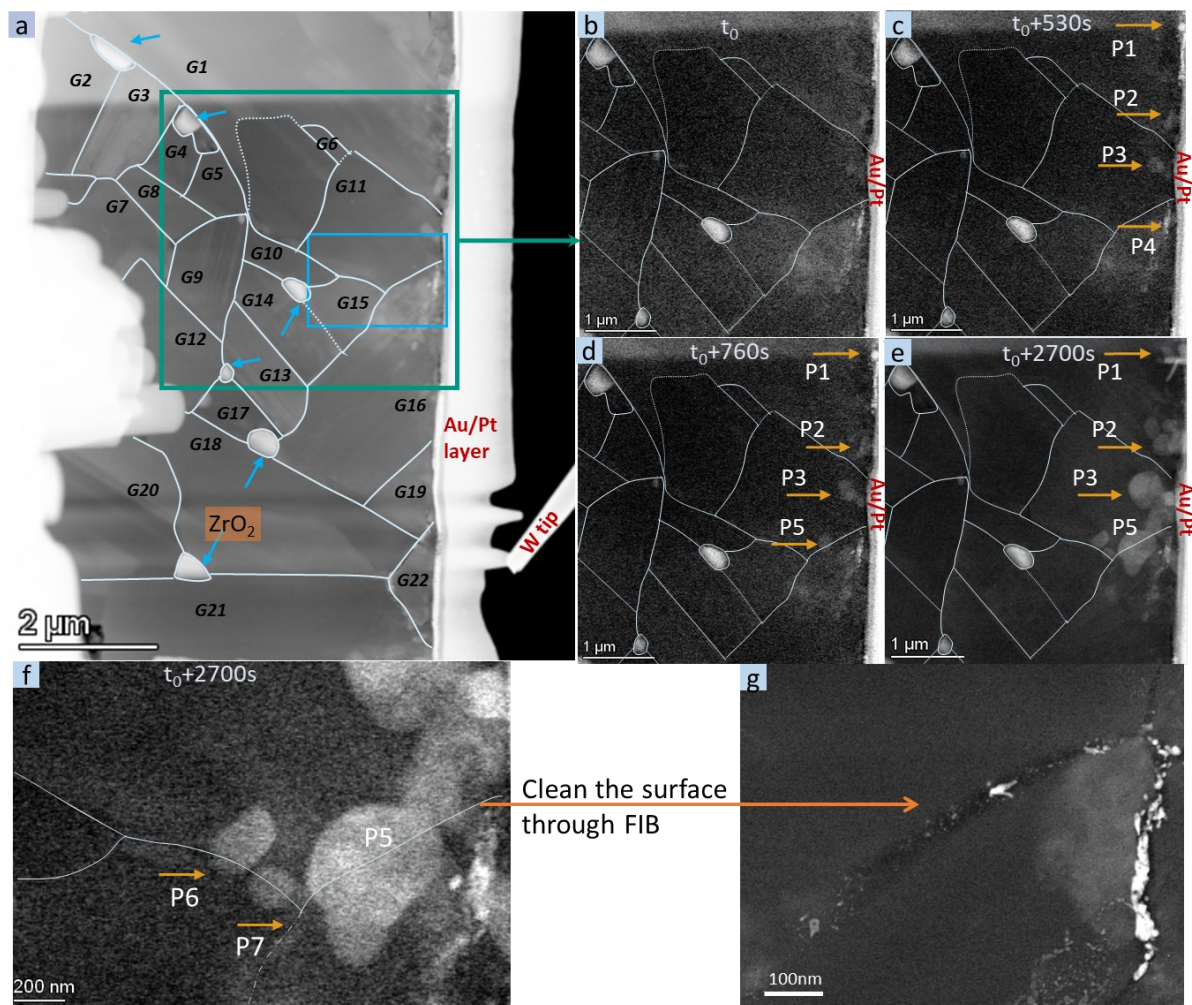
Figure 4.6. HAADF-STEM time series showing the Na filament growth during biasing: **a**. HAADF-STEM image for the whole thin area of the TEM lamella with GBs highlighted in white. The grains are numbered for further reference. The bright particles highlighted by blue arrows are ZrO_2. **b. – e.** Morphological evolution of the area highlighted by the green rectangle in (**a**) over time during biasing. **f**. Magnified images of the area indicated by the blue rectangle in (**a**) after 2700s of biasing. The apparent Na filament positions are pointed out by yellow arrows and labeled as P1 – P7. **g**. HAADF-STEM image of the region around P5 after further FIB polishing after the end of the *in situ* TEM measurement. A crack appeared at the GB where the P5 Na filament was located.
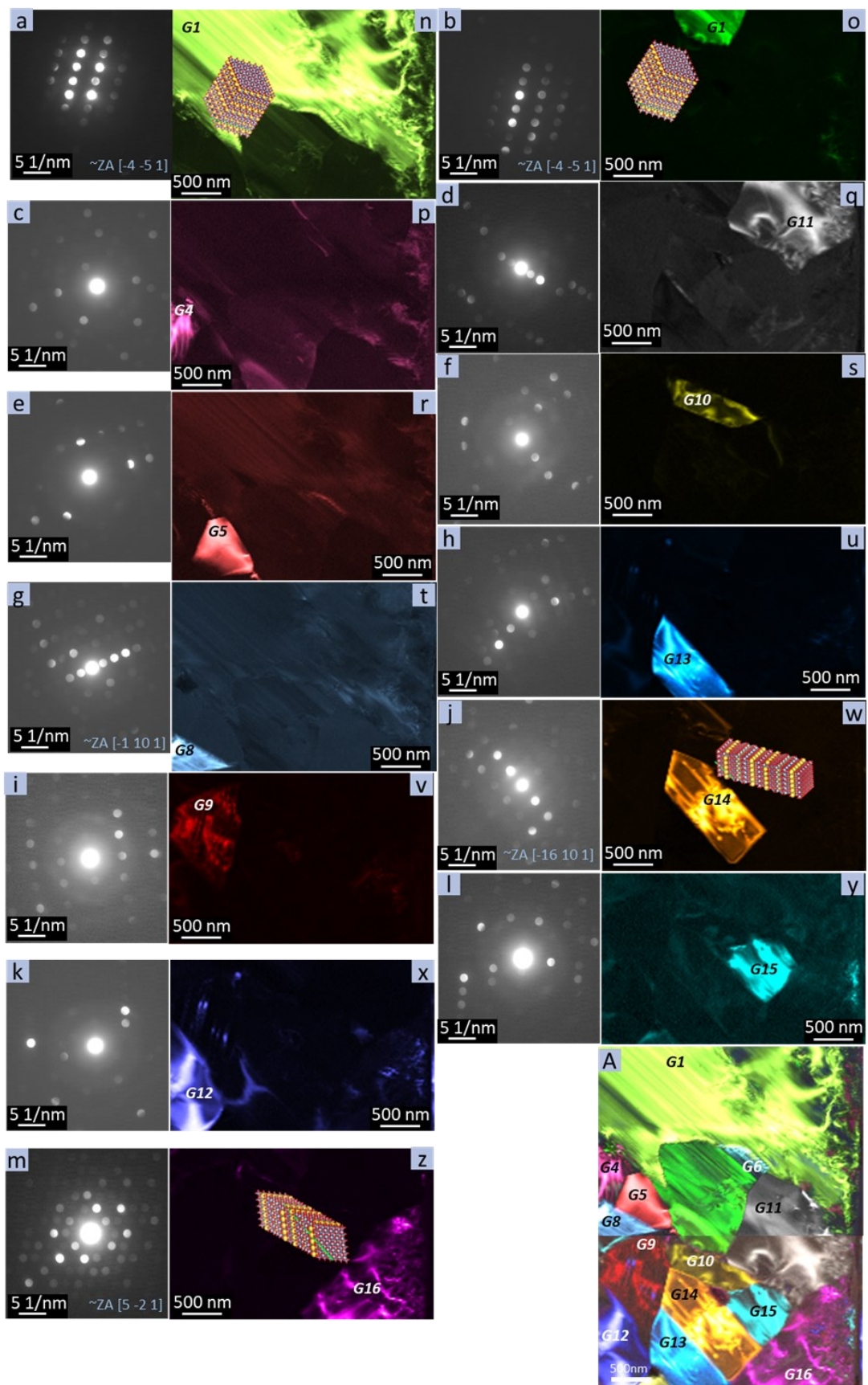
Figure 4.7. Virtual images (**n – z**) of all individual grains in the area marked by dark teal dashed rectangle in **Figure 4.6a**. They were generated from different diffraction patterns (**a – m**) in the

4D-STEM data cube. **A.** Overlay image of the RGB-coded individual grains. The grains are numbered for further reference.

The Na filaments appeared first inhomogeneously at the interface of Na-β''-alumina and Au/Pt layer (labeled P1, P2, P3, and P4 in **Figure 4.6c**) and then within the Na-β''-alumina (labeled P5 in **Figure 4.6d**). Since the contrast of the Na filamentary seeds is not too distinct from the Na-β''-alumina during early biasing, the differential images in **Figure 4.8a & b** are used to visualize the morphology changes. It is apparent that the Na filament P5 formed at the GB between the grains labeled *G11* and *G16*. This can also be seen in the overlay image with the grain map (**Figure 4.8c**) and further confirms that this GB is connected to the Au/Pt electrode. Maintaining the system at a constant bias for a longer time resulted in the further growth of the filament and more filamentary seeds appearing along the GB between *G11* and *G16* until it was fully occupied as shown in **Figure 4.6e and f**. As no Na was detected at the interface between *G16* and the Au/Pt interface, this indicates that Na$^+$ ions did not migrate extensively across the GB from *G11* to *G16* to reach the Au/Pt electrode.
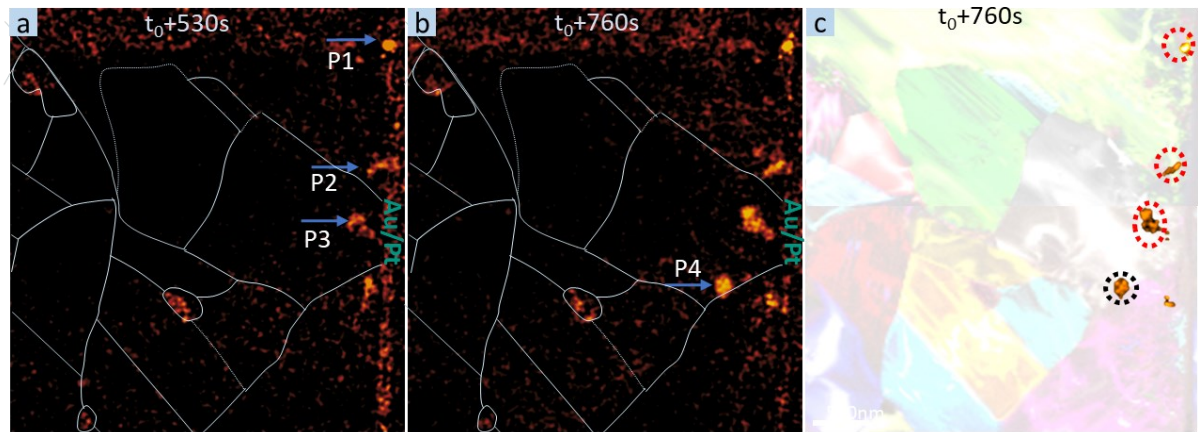
Figure 4.8. Differential HAADF-STEM images to enhance highlight the position and shape of the Na filaments. The HAADF-STEM image at t_0 (**Figure 4.6b**) was subtracted from the images at t_0+530s (**Figure 4.6c**) and $t_0+1100s$ (**Figure 4.6d**): **a.** Differential image at t_0+530s; **b.** Differential image at $t_0+1100s$; **c.** Overlaid image of **b** and **Figure 4.7A**. The blue arrows (P1-P4) indicate Na filaments growing at the interface between Na-β''-alumina and Au/Pt layer, while the blue arrow P5 is pointing at a Na filament grown at a GB within Na-β''-alumina.

Finally, it was observed that Na filaments penetrated to the GB between *G11* and *G15* as well as *G15* and *G16*. This has been attributed to the increasing electronic conductivity due to the Na filament connected to the Au/Pt layer. Interestingly, when the filament reached the triple boundary of *G11*, *G15*, and *G16*, it penetrated much more along the GB between *G11* and *G15* (as pointed out by the arrow P6 in **Figure 4.6f**) as the particle size is bigger. Nevertheless, at the GB of *G16* to *G15* a small filamentary seed was present (indicated by the arrow P7 in **Figure 4.6f**). This indicates that more Na$^+$ ions appeared at *G11*/*G15* GB than at *G15*/*G16* GB. This is one example that different GBs exhibited different behavior in terms of Na filament growth.

Moreover, the morphology of the Na filaments did not exhibit any preferential faceting or geometry as most of them grew close to a spherical shape. This can be attributed to the small current and the small volume of the Na filament. [244] In addition to the Na filament growth in the thin region of the TEM lamella, larger polyhedral-shaped whiskers were found to grow from the frame of the lamella as shown in **Figure 4.9**. This demonstrates that the Na filaments do not only appear in the thin region in contact with the At/Pt electrode, but also in the thick region far from the electrode.
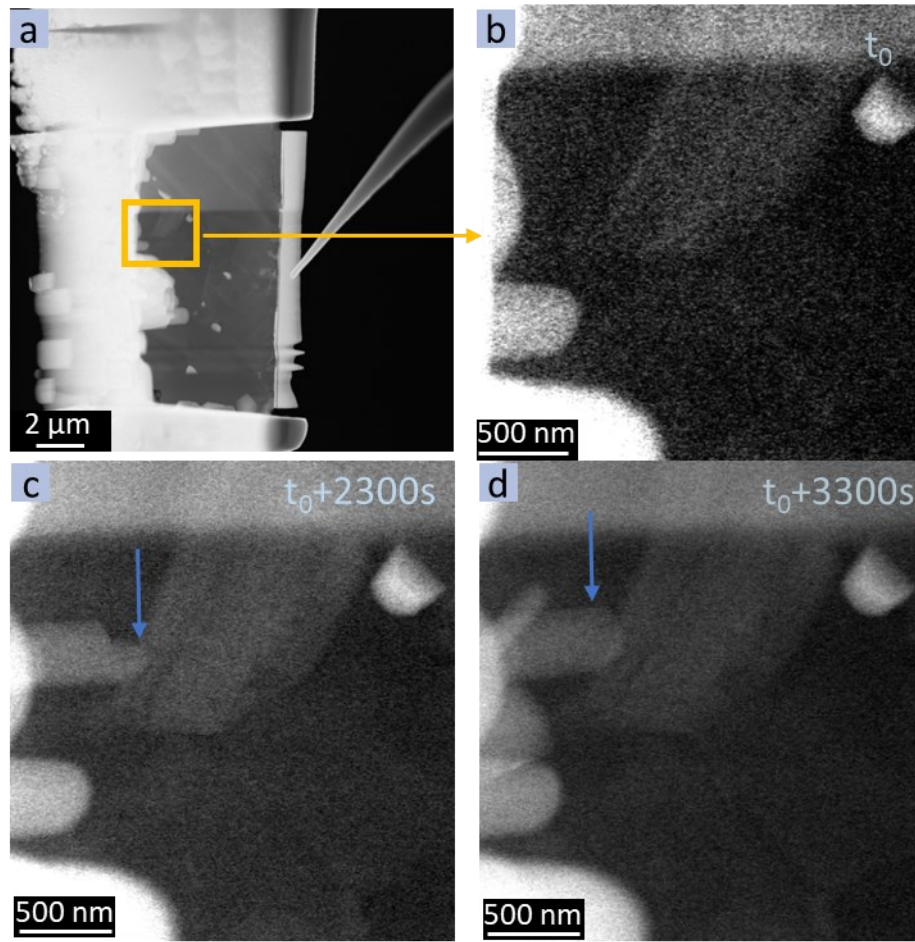
Figure 4.9. Polyhedral shaped Na filament growth from the frame region of Na-β″-alumina TEM lamella used in **Figure 4.6**. **a.** HAADF-STEM image of the overview of the *in situ* setup during prolonged biasing; **b. - d.** HAADF-STEM series images of Na-whisker growth at the area indicated by the yellow inset in **a**. The blue arrows indicate Na whiskers.

After the *in situ* biasing experiment, the Na filaments on the surface of the lamella were removed by FIB cleaning. STEM analysis of the cleaned lamella reveals the existence of a pronounced crack along the entire GB between G11 and G16 as shown in **Figure 4.6g**. This is presumably caused by the Na filament growth induced strain. The shear modulus of GBs in SEs is believed to be lower compared to the bulk. [136]

4.3.2. Microstructural Characterization of the *In Situ* Biasing Specimen

To assess the microstructural features leading to blockade of Na^+ ion transport and formation of the filaments in the *in situ* TEM measurements, crystallographic information including crystal

orientation and type of GBs was obtained by automated crystal orientation mapping (ACOM). To obtain high quality data for ACOM, the specimen was further thinned by FIB after the *in situ* TEM analysis as shown in **Figure 4.10a**. This produced a hole and damaged the adjacent region of the specimen; thus the reliability and index are low in this region, and consequently, on the orientation map is marked black there in **Figure 4.10b**. Nevertheless, together with the previous 4D-STEM grain map, the orientation information for each grain is still sufficient. Based on the calculated Euler angles, the crystallographic relationship of all adjacent grains was computed, and the type of GB defined. Some of the misorientation angles between adjacent grains are listed in **Table 4-1**.
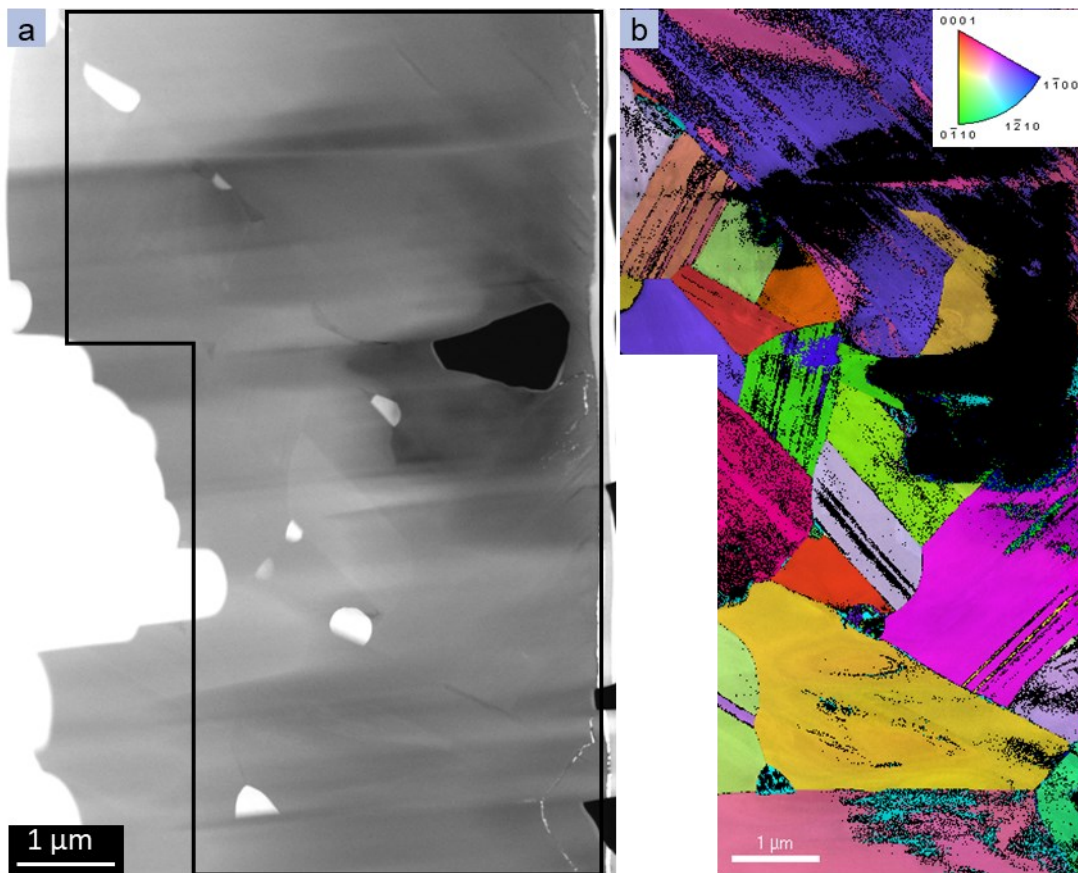
Figure 4.10. a. HAADF-STEM image of the specimen in after further thinning by FIB. An automated crystal orientation map (ACOM) analysis was done for the indicated region. **b.** Overlaid map of orientation, index, and reliability. The values of the index below 600 and reliability under 5 were cut-off.

Table 4-1 Misorientation between adjacent grains

GB	Misorientation [°]	Misorientation of Na$^+$ ion transport path of adjacent grains [°]
G1/G11	51	14
G9/G5	82	66
G9/G7	88	29
G9/G8	76	66
G9/G10	55	79
G9/G12	71	55
G9/G13	90	53
G9/G14	79	53
G10/G15	35	27
G11/G15	23	10
G11/G16	64	85
G15/G16	63	79
G14/G16	70	89
G13/G16	74	89

A schematic illustration of the crystal orientation, the GB information and the Na$^+$ ion conduction plane is shown in **Figure 4.11a**. An atomic lattice model for each individual grain has been generated in **Figure 4.11b.** The indexed ACOM data indicates a random orientation of grains. GB misorientation values above 15° indicate that most of the GBs are high-angle GBs (HAGBs), except for the ones between *G14* and *G15* as well as *G6* and *G11*, analogous to observations in Li oxide solid electrolytes [132]. The low-angle GB (LAGB) of *G14/G15* was formed by two opposing (0 0 1) facets, which is a unique GB in Na-β″-alumina. [245] Among the HAGBs, the grains denoted as *G13* and *G14* as well as *G5* and *G8* can be considered as coincidence site lattices (CSL) GBs of type $\sum$3 and $\sum$21. Moreover, the facets at both GBs can be recognized as (0 0 1). It is widely accepted that the Al-O spinel blocks on the (0 0 1) facet hinder Na$^+$ out-of-plane migration. Similarly, a blocking effect is expected at these GBs. This is just one example illustrating that the resistivity for Na$^+$ ion migration across different GBs is expected to vary depending on the crystallographic relationships between adjacent grains. A distinctive overall ionic conductivity of oriented polycrystalline Na-β″-alumina in different directions has also been revealed experimentally. [60] In addition, it is interesting to note that the GBs with a CSL relation, which are commonly considered in simulation models for the ionic conductivity and activation energy calculation, are rare compared to arbitrary high-angle ones.
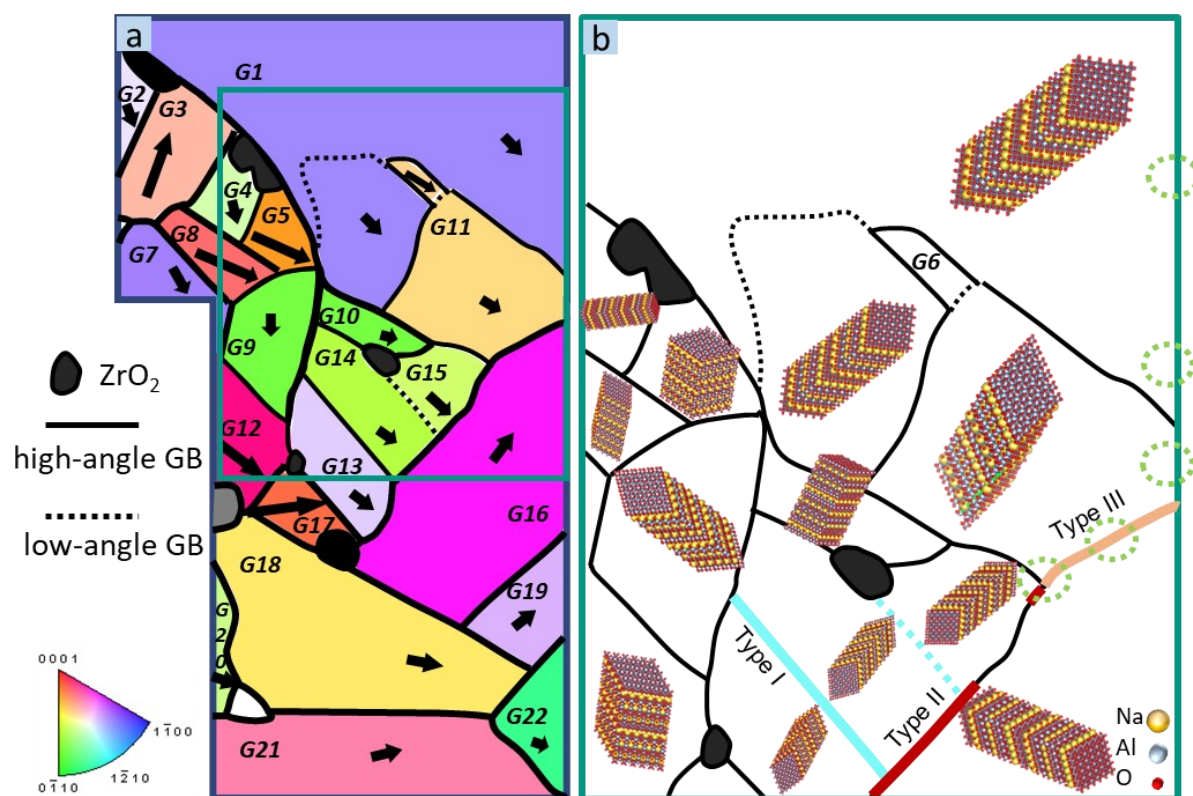
Figure 4.11. **a.** Schematical illustration of the crystal orientation of the TEM lamella shown in **Figure 4.7**A and **Figure 4.10b**. The color code for the grain orientation follows the color code in the inverse pole figure. The black arrows represent the direction for easy Na^+ ion migration in the individual grains, i.e. the projection of the Na^+ ion conductive plane onto the surface of the TEM lamella. Their length indicates the angle between the Na^+ ion conduction plane and the surface of the lamella. The longer the arrow, the more parallel the conduction plane of Na-β″-alumina to the surface of the lamella. **b**. Crystal models for the individual grains in the dark green rectangle of **a**. Solid lines represent HAGBs, while dashed lines indicate LAGBs. The color code for the GBs in (**b**) is based on **Figure 4.12**. The green dashed circles indicate the region where Na filament grew during biasing.

4.3.3. Discussion of the Local Grain Boundary Effects

The first observation concerns the Na filamentary particles that formed in the Na-β″-alumina/Au(Pt) interface region. The Na^+ ion conduction plane of the grains marked as *G1*, *G11*, and *G16* is aligned towards the Au/Pt electrode (**Figure 4.11b**). As a consequence, Na^+ ion migration towards the electrode and accumulation at the interface was highly facilitated in the

applied electric field. Once Na$^+$ ions reached the electrode, they were reduced to Na^0 followed by nucleation and growth of Na particles. Therefore, it was expected to observe the initial particle growth as Na-deposition around the electrode areas presented in **Figure 4.6c**. The inhomogeneous growth of the Na filaments can presumably be attributed to defects at the interface. We did not observe Na-plating at other grains at the interface, e.g. at *G19* or *G22*. We assume that there was insufficient Na$^+$ ion transport in the lower part of the lamella (Error! Reference source not found.**Figure 4.1**), which is supported by the ion transport simulations shown later.

Since the orientation of the grains has to be taken into account for the Na-plating at the interface, Na segregation and filament growth at GBs were assumed to be related to the crystallographic relationship between the neighboring grains and their orientation relative to the applied electric field. While the crystallographic misorientation at the GB is commonly analyzed in ACOM, this misorientation angle does not necessarily represent the angle between the Na$^+$ ion conduction planes as shown in **Table 4-1**. To describe the anisotropic transport in an electric field between adjacent grains, the misorientation of Na$^+$ ion planes is critical information.

To understand the effect of GBs on anisotropic Na$^+$ ion transport, the misorientation of the Na$^+$ ion conduction planes in adjacent grains and the external electric field direction were coupled. For the schematic depiction in **Figure 4.12**, the effect of the virtual electric field pointing to the right and pointing down are considered for 3 scenarios: GBs parallel (type I), perpendicular (type II), and oblique (type III). The transport path in both grains in the external electric fields is indicated by the arrows in **Figure 4.12**.
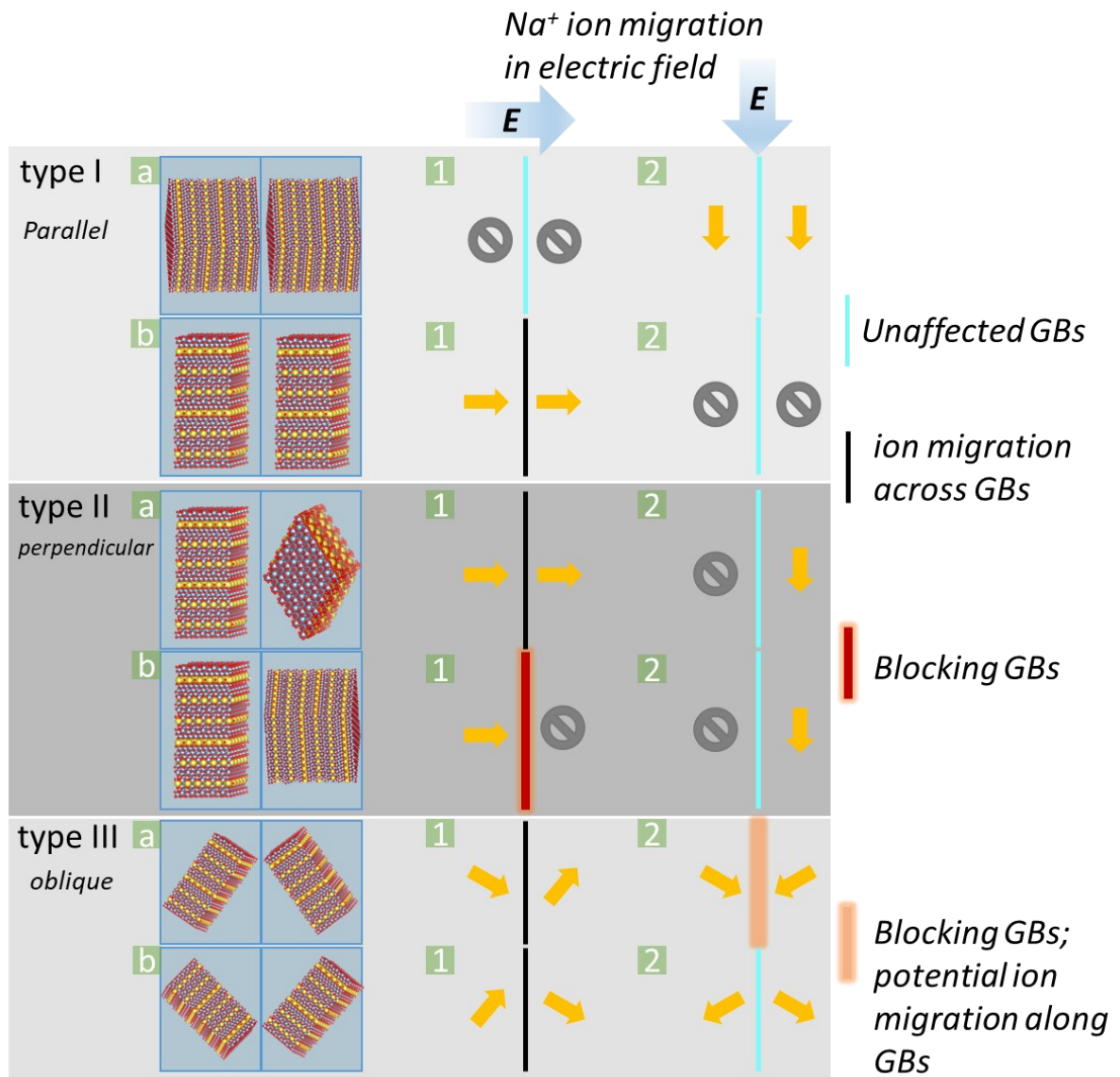
Figure 4.12. Schematic illustration of the relationship between the orientation of adjacent grains and the direction of the Na⁺ ion migration in an external electric field. The orientation relationship of Na⁺ ion conduction planes in adjacent grains was summarized for 3 types: parallel (type I), perpendicular (type II), and oblique (type III). The Na⁺ ion migration direction in different external electric fields (blue arrows) are marked by orange arrows and gray stop signs. Depending on the orientation of the Na⁺ ion transport plane, the GBs exhibited different migration behaviors, e.g. without involving migration across GB (cyan), easy migration across GB (black), and blockade of ion migration (red and orange).

In the extreme case of the HAGBs illustrated in **Figure 4.12** type I, the misorientation angle between adjacent grains can be arbitrary, but their Na⁺ ion conductive planes are aligned parallel.

This results either in connected (type I b) or disconnected (type I a) grains by the Al-O spinel block. For type I a orientation relationships, the blocking effect of GBs is irrelevant as the migration path is unaltered by the GB. Similarly, GBs in type I b2 also do not join the ion migration between adjacent grains in the external electric field. By tuning the direction of electric field to enable the ion migration across GBs, which is assigned as type I b1, its resistance only depends on the structure mismatch of GBs. In the experimental specimen, the relationship between *G13* and *G14* can be considered to be of this type (type I a1), while two GBs between *G1* and *G11* are close to typ I a2 and typ I b1 as shown in **Figure 4.11b**.

Only a small blocking effect of GBs is also expected for adjacent grains with perpendicular Na^+ ion planes if they are aligned as illustrated for type II a. However, Na^+ ion migration will be blocked by the Al-O spinel arranged in GBs of type II b1 as the electric field drives Na^+ migration from the left grain towards the GB, but the orientation of the right grain does not allow further migration along the electric field. The GB *G15/G16* in **Figure 4.11b** is of type II b1. Nevertheless, with the same orientation between adjacent grains in type II b2, a block-effect is not present as the electric field does not induce ion migration across the GB. This indicates the importance of both the electric field and GB orientation for the ion migration behavior at GBs.

A more oblique orientation relationship of neighboring grains is shown in Error! Reference source not found. type III. This is a general case in the randomly oriented polycrystalline Na-β''-alumina as shown in **Figure 4.11** (e.g.: GBs *G1/G11*, *G10/G15*, *G9/G14*, and *G12/G17*). The Na^+ ion transport path in adjacent grains depends strongly on the orientation of the electric field. For instance, Na^+ ions may migrate from the left grain across the GBs to the right in the electric field as illustrated in Error! Reference source not found. type III a1 & b1. Due to the misorientation of the Na^+ ion planes to the electric field direction, the driving force for Na^+ ion migration in adjacent grains may be different. Therefore, the Na^+ ion flux in adjacent grains can be influenced by the direction of the external electric field and the misorientation angle between the two Na^+ ion planes. For instance, in the specimen of **Figure 4.11**, the GBs *G5/G9*, *G8/G9*, and *G9/G13* belonged to this type when the bias was applied. Their crystallographic misorientation angles were 82°, 76°, and 90° (as shown in **Table 4-1**), while the misorientation of the Na^+ ion transport path was 66°, 66°, and 53°. As shown in the schematic for Error! Reference source not found. type III a2 & b2, the Na^+ ion migration at GBs can behave distinctively different depending on the orientation in the electric field. In the case of type III b2, Na^+ ions migrate away from the GB in the electric field, which means that there is no driving force for ions crossing the GB. In contrast, for GBs with low ion conductivity along the boundary, blockade would be expected when the Na^+ ions in both adjacent grains migrate towards the GB as illustrated type III a2. In the experimental specimen of

Figure 4.11, GB *G11/G16* belongs to this type. However, in some cases also enhanced ion migration along this type of GB has been observed in the *in situ* TEM studies with Na segregating at the triple boundary between two Na- β″-alumina grains and the Au/Pt electrode (**Figure 4.13e & g**). This is strongly suggesting that fast Na$^+$ ion transport can occur along the involved GB, which also fits to type III a2 based on the orientation relationship of the yellow and green grain in **Figure 4.13a**.
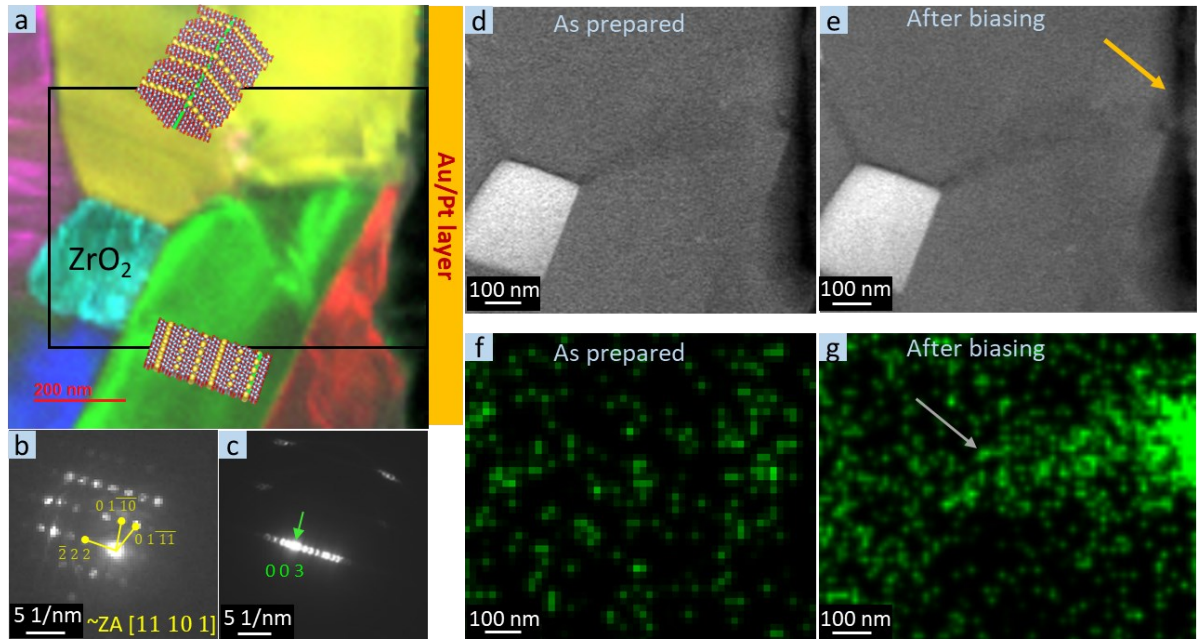
Figure 4.13. Na filament growth the triple boundary between grains and the Au/Pt electrode. The involved GB belongs to type III a2. **a.** RGB-coded grain map. The position of the Au/Pt electrode is schematically illustrated. **b. & c.** NBEDs of yellow and green grains in (**a**). The crystal models for the yellow grains were obtained based on their corresponding NBEDs (**b**). The orientation of the Na$^+$ ion conduction plane (0 0 3) in the green grain was obtained based on its corresponding NBED (**c**) and accordingly, its crystal model is drawn. **d**. HAADF-STEM image of the pristine state of the region marked by the black rectangle (**a**). **e**. HAADF-STEM image of the same region after biasing of 1400s. The Na filament is indicated by an arrow. **f. & g.** Low-dose EDX Na map in the as prepared state and after-biasing specimen.

Moreover, during the *in situ* bias experiment in **Figure 4.6**, initially Na filament formation was observed at the GB *G11/G16* connecting to the Au/Pt electrode and further Na filament growth mainly occurred at GB *G11/G15*, but little at GB *G15/G16*. It indicates a higher amount of Na$^+$ ions are transported at GB *G11/G15*. Since the Na$^+$ ion conduction plane of *G10* and the orientation

of GB *G11/G15* were well aligned with the external electric field, more Na^+ ions may reach this GB from *G10*, *G11*, and *G15* leading to a larger Na filament growth. Nevertheless, at the other GBs connect to the Au/Pt electrode (GB *G1/G11, G16/G19*, and *G19/G22*), no Na filament formation occurred. In the case of GB *G1/G11*, this can be attributed to the non-blocking character of this grain boundary, whereas in the case of GB G16/19 and G19/G22, this is related to the low overall ion current in that part of the specimen.

While the ZrO_2 impurities are in principle also non-negligible microstructural feature in the Na-β″-alumina SE, the *in situ* experiments did not show a significant contribution to the Na filament growth.

4.4   Beam Blank Reference

In addition to the previously shown *in situ* experiments, an electron-beam blanked experiment was performed as reference to eliminate the electron beam effects on the observed behavior. The initial morphology presented in **Figure 4.14a.** Similar to the *in situ* beam-on experiment, after biasing a Na particle was found at the GB and the interface between Na-β″-alumina and Au/Pt electrode as shown in **Figure 4.14b.** In addition, a high Na EDX signal was found along a GB as well (**Figure 4.14c**). Moreover, a grain map of the yellow inset rectangle region of **Figure 4.14b** was obtained by 4D-STEM as shown in **Figure 4.14e**. It was found that the GB, where the Na particle appeared, belonged to type III a2. This is similar to the Na filament formation P5 in **Figure 4.6d**.
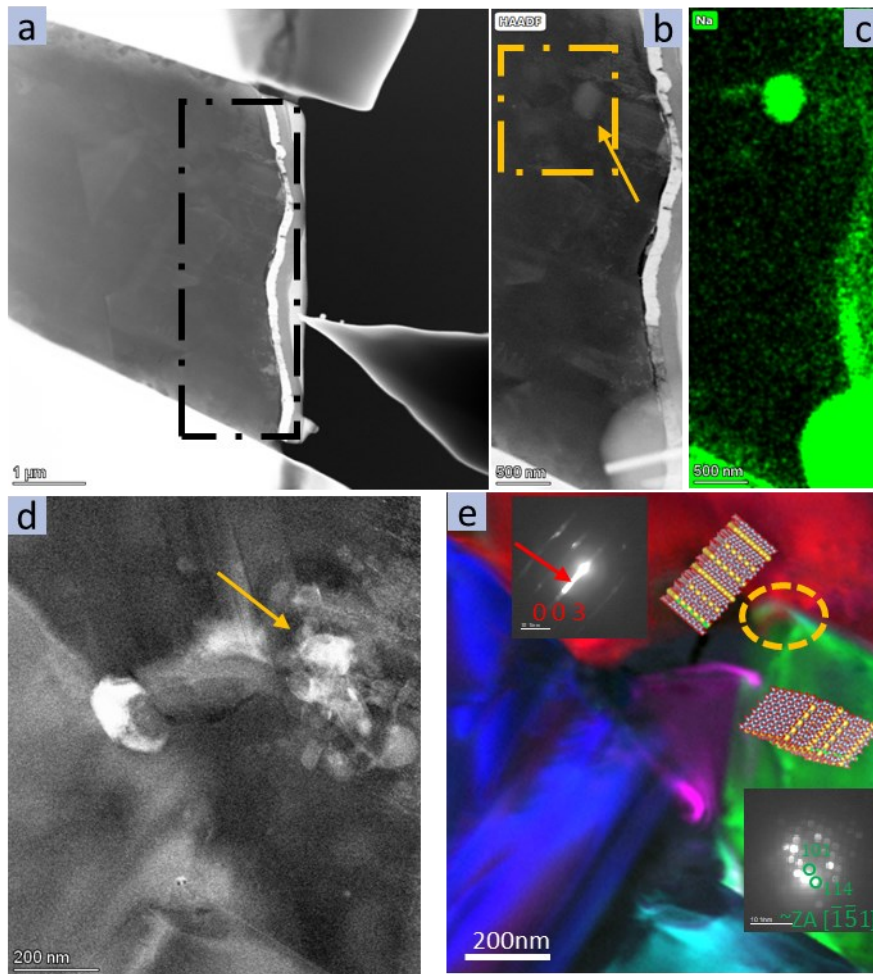
Figure 4.14. Beam blank reference experiment: **a**. HAADF-STEM image of initial sample. **b.** HAADF-STEM image and **c**. EDX Na map of the area indicated by the black rectangle in **a** after biasing. **d**. Higher magnification ADF-STEM image of the region in the yellow rectangle in **b**. The arrow points at the Na particle. **e**. RGB color coded grain map. The crystal model of green grain is drawn based on the indexed inset electron diffractions from 4D-STEM data cube. Since the orientation of Na^+ ion conduction plane is obtained through the index of lattice plane (0 0 3) in electron diffractions of red grain, its crystal model is drawn based on the orientation of Na^+ ion conduction plane.

4.5 Modelling the Current Density Distribution of the Na-β″-alumina during Biasing

Since the two electrodes are not opposed to each other as shown in **Figure 4.2**, the current density in the sample was not uniform, but a significant gradient in the y-direction of the specimen was present as shown in **Figure 4.15a** when the microstructure is ignored. In contrast, the current

distribution in the system changes significantly when the actual microstructure is considered (**Figure 4.15c & d**). Unfortunately, the microstructure and grain orientation in the frame of the lamella are unknown. Therefore, two computational model systems were considered: a reduced system (**Figure 4.15c**), which neglects the contribution of the frame to Na$^+$ ion transport and a full system (**Figure 4.15d**), which assumes an effective isotropic conductivity for the backbone.
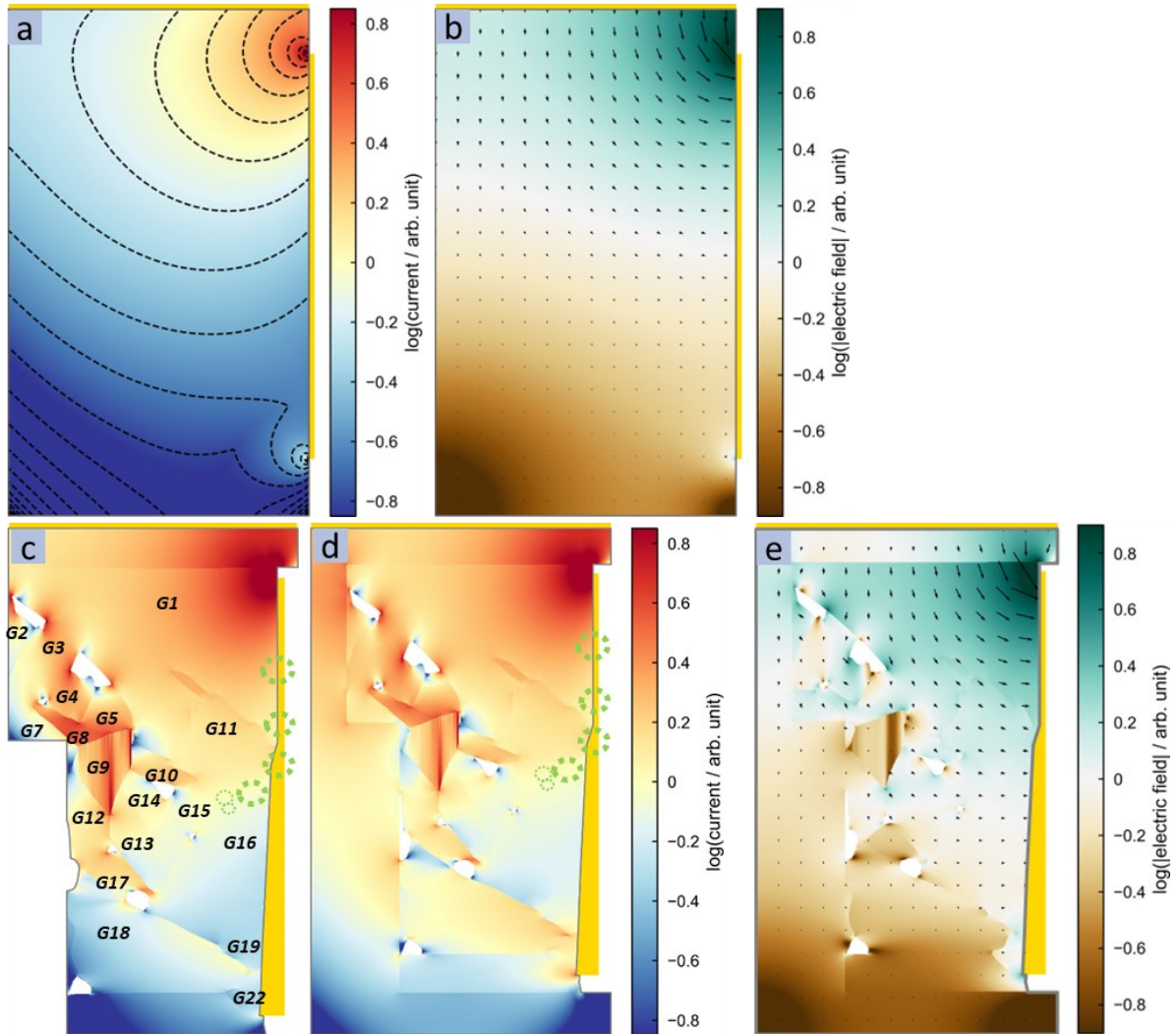
Figure 4.15. Computed current density distribution in the Na-β′′-alumina: **a. & b.** Current density and electric field distribution for an isotropic SE. The dashed line indicates the iso-current and the arrows point out the direction of the electric field. **c. - d.** Current density distribution considering the microstructure of the thin region of the TEM lamella. The backbone of the TEM lamella was not considered as reduced system (**c**) and considered as full system (**d**). **e.** Electric field distribution considering the microstructure of the thin region of the TEM lamella and the isotropic property was assumed for the thick frame around it. The green dashed circles indicate the position of the Na filament.

In the reduced system (**Figure 4.15c**), the current density distribution is distinctively different among grains rather than the uniform gradient without considering of the microstructure. For instance, it was found that the current density through grain *G10* was higher than in the adjacent grains *G1* and *G11*, even though it was further away from the electrodes. This non-uniform current density distribution is even more obvious in the full system (**Figure 4.15d**). This demonstrates that the anisotropic Na^+ ion transport leads to an uneven current density distribution in adjacent grains as seen e,g, for *G11* and *G16*, *G10* and *G15*, *G9* and *G13*, and *G9* and *G15* (**Figure 4.15c**). During biasing, a local electric field between these adjacent grains would build due to the current differences as depicted in **Figure 4.15e**. Hence, an excess potential develops between these adjacent grains, which can affect the chemical potential of sodium μ_{Na}. Nevertheless, Na filament growth was only found at the GB G11/G16 and not at the other three GBs with large current differences. This can be attributed to this GB being directly connected to the Au/Pt electrode, which enables reduction of Na^+ at the electrode. For the GBs far from the interface between Na-β''-alumina and Au/Pt electrode, the developed excess potential is presumably not sufficient for driving sodium reduction and nucleation. However, Na filament growth inside the bulk Na-β''-alumina may occur once the local electric field reaches a strength to sufficiently shift the electrochemical potential. In addition, the other GBs (*G1/G11* and *G16/G19*, and *G19/G22*) connected to the Au/Pt electrode did not show significant Na filament growth occurred**.** This can be attributed to the well aligned Na^+ ion plane with external electric field resulting in an absence of GB blockade for GB *G1/G11* and the low current at *G16/G19* and *G19/G22* is presumably preventing filament formation at the GBs.

Furthermore, after the Na filament penetrated GB *G11/G16*, Na filament was observed along the GB between *G11* and *G15*, whereas only a small Na filament was growing from triple boundary to the GB between *G15* and *G16*. This is in line with the computed current density distribution at these two regions (**Figure 4.15c**). Since ion transport along the GB was not considered in the computed current densities, it can be speculated that the actual current density difference between *G11/G15* and *G15/G16* GBs is even higher due to ion migration from grain *G10*, which possesses a high current density, via the triple boundary to *G11/G15* GB. Consequently, the filament size at *G11/G15* GB is much larger than at *G15/G16* GB. Furthermore, the Na filament at GB *G11/G16* connecting the interface in Na-β''-alumina to the Au/Pt electrode speeds up the electron transport along the GB and therefore facilitates Na nucleation at neighboring GBs.

4.6 *Post Mortem* Characterization of Cycled Na-β″-alumina

In addition to the GB network, the Na-β″-alumina has voids as typical microstructural features as shown in **Figure 4.16**. To understand the influence of the microstructure on a larger scale, ToF-SIMS was used to investigate the cycled bulk Na-β″-alumina. The as-prepared Na-β″-alumina was investigated as reference and exhibits a fairly uniform Na distribution as shown in **Figure 4.17a.** Only slight Na segregation appears on the surface, presumably due to ion polishing artifacts, whereas no segregation was found in the bulk as shown in 3D Na map (**Figure 4.17e**).
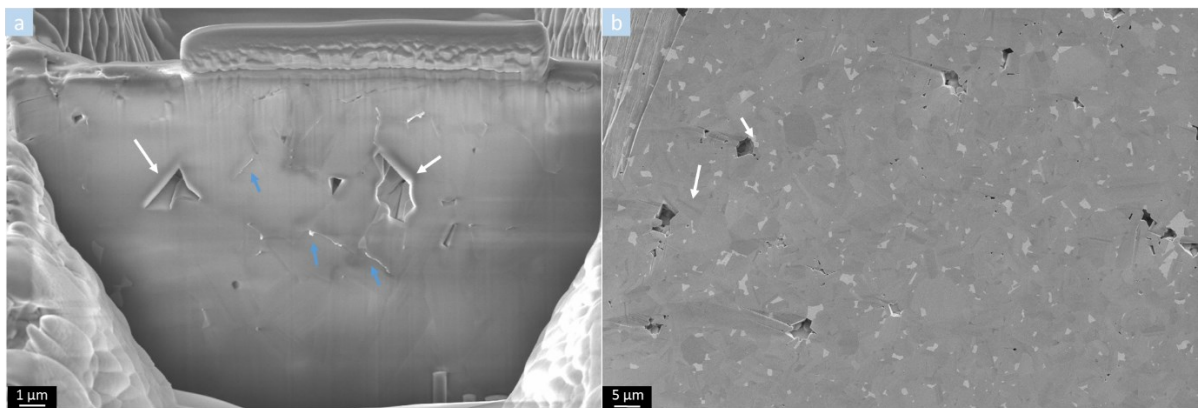
Figure 4.16. SEM images of pristine Na-β″-alumina: **a**. FIB fabricated cross-section of Na-β″-alumina; **b.** Ion polished cross-section of Na-β″-alumina. The white arrows indicate the micron-sized voids. The blue arrows indicate the beam induced Na segregation at GBs.
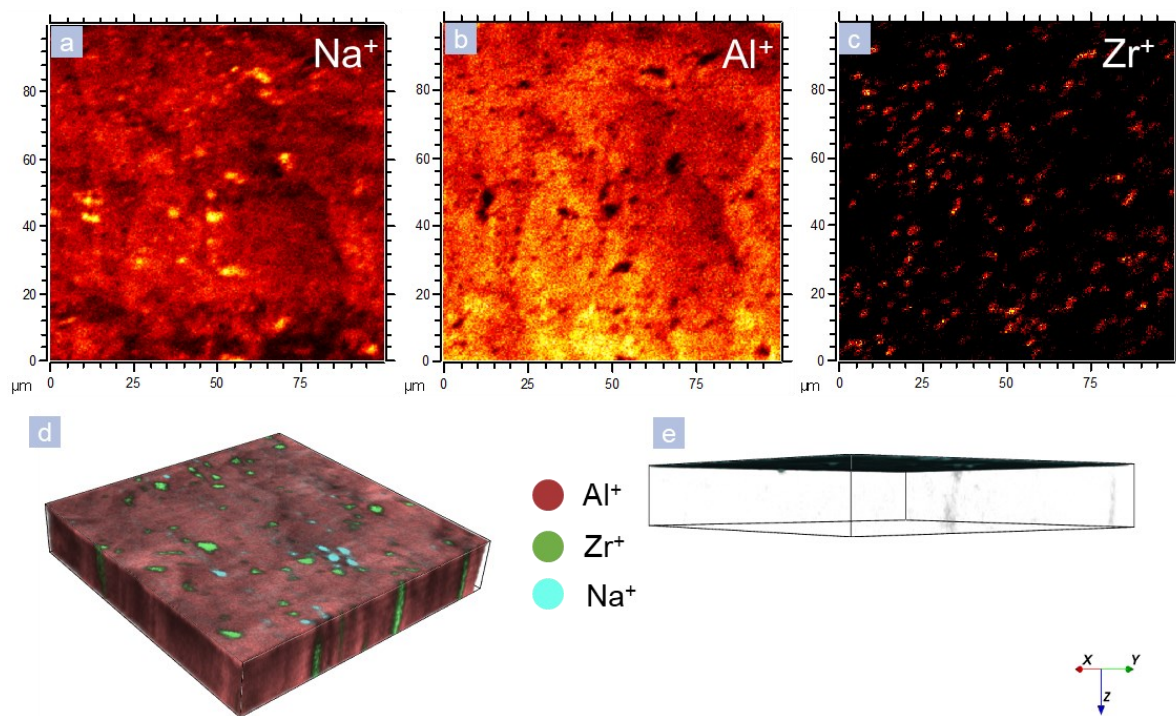
Figure 4.17. ToF-SIMS elemental analysis of the pristine Na-β″-alumina: **a**. Na 2D map; **b**. Al 2D map; **c**. Zr 2D map; **d.** Overlaid Al, Zr, and Na 3D map; **e**. Side view of the Na distribution in (**d**).

In the cross-section of the cycled Na-β″-alumina, which is prepared in the same way as as-prepared sample for SIMS analysis in **Figure 4.17**, Na segregation is evident in as presented in **Figure 4.18b & g.** Since the same ion dose was used during SIMS analysis for both specimens, the segregation is believed to be induced by the cycling process. Due to the limited resolution of the Na maps, the individual nanometer sized Na filaments cannot be seen. However, it was found that Na segregation was distributed mainly at three types of morphological features in 2D Na maps: isolated non-regular micron-sized Na particles (indicated by golden arrows in **Figure 4.18g & h**), a connection of the micron-sized Na particles and zig-zag line-shaped Na filaments (indicated by white arrows in **Figure 4.18b & e**), and line-shaped Na filaments (indicated by blue arrows in **Figure 4.18b, g, & h**). The micron-sized Na particles were found filling voids in Na-β″-alumina as shown in the SEM image (**Figure 4.18e**) and the corresponding inset in the rectangle region in the Na map (**Figure 4.18b**). Tian et. al. revealed that significant excess electrons can be trapped on the surface of some oxide electrolytes e.g. LLZO due to the lower band gap compared to the bulk. [134] Moreover, lower mechanical back stress has been shown to contribute to the Li dendrite growth. [246] In analogy, Na growth in voids within Na-β″-alumina can be attributed to the low band gap of the surface and absence of the back stress. In addition to the micron-sized Na particles,

the line-shaped Na filaments grow along GBs based on the correlative SEM image in **Figure 4.18e**. Most of the GBs, which are connected to micron-sized Na-filled voids, contain small amount of Na filaments as shown in the **Figure 4.18b & e**. This suggested that Na probably first grew in the voids, which enabled further nucleation at the adjacent GBs. Furthermore, the isolated line-shape Na appearing in the Na map indicates that Na filament growth may initiate from GBs inside the bulk electrolyte during cycling. In addition, the thick line-shaped Na filaments were recognized as cracks based on the Na and Al maps in **Figure 4.18b & c**. This is caused by the strain due to the large Na filament growth.
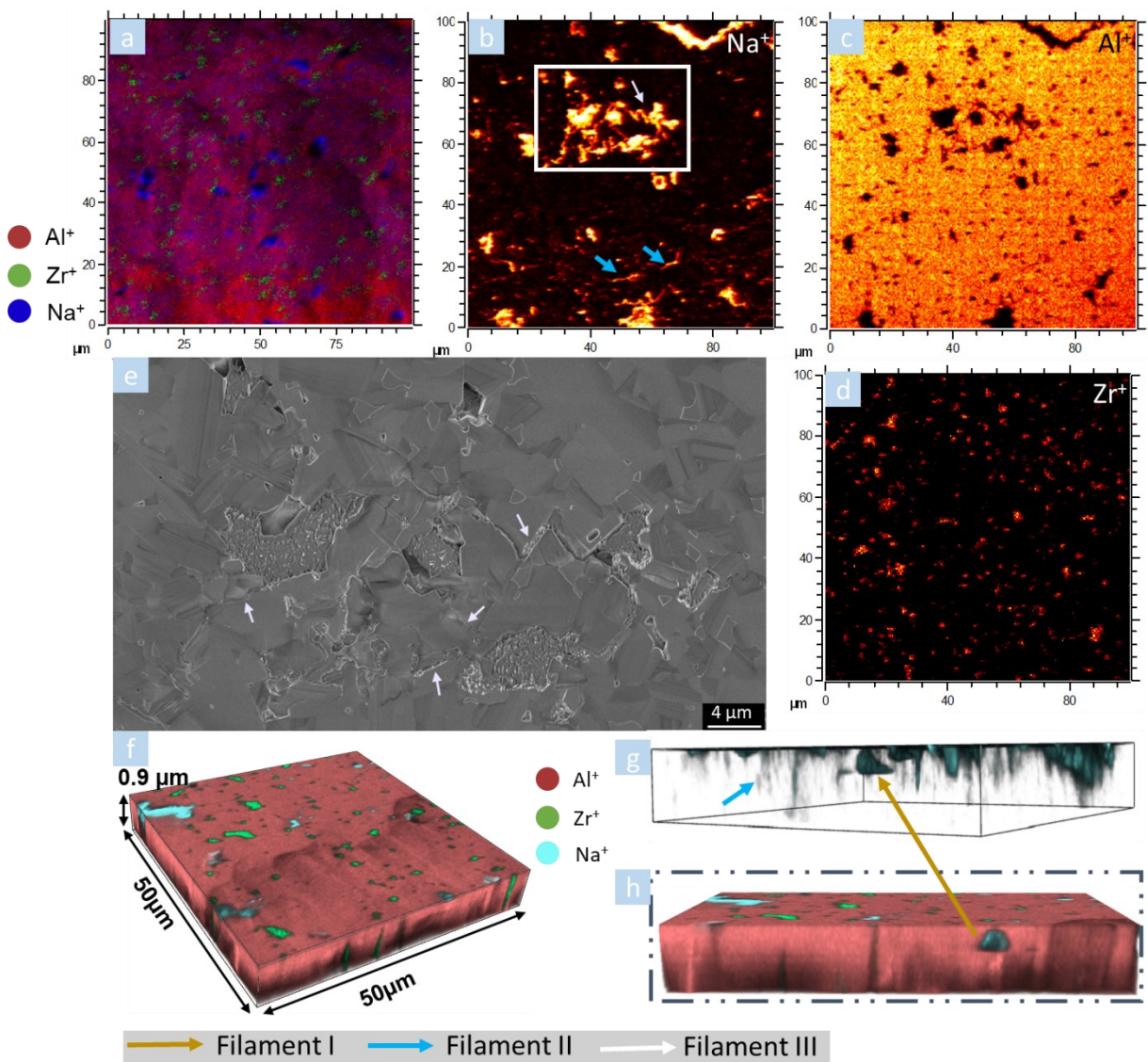
Figure 4.18. 2D and 3D ToF-SIMS maps and a correlative scanning electron microscopy (SEM) image of Na-β''-alumina after cycling: **a.** Overlaid ToF-SIMS 2D maps of Na^+, Al^+, and Zr^+ (Field of view: 100 µm x 100 µm). **b - d**. ToF-SIMS 2D maps of Na^+, Al^+, and Zr^+. **e**. Correlative SEM

image of the area marked by the rectangle in (**b**); **f**. ToF-SIMS 3D map of a sputtered volume of 0.9 μm x 50 μm x 50 μm with an overlay of Al^+, Zr^+, and Na^+; **g**. side view of the Na^+ distribution. **h**. Cross-section of the 3D map in y direction. Three types of Na filaments can be seen: filament I (isolated micron-sized Na particles) indicated by golden arrows; filament II (isolated line-shaped Na filament) indicated by blue arrows; filament III (connection of micron-sized Na particle and line-shaped Na filaments) indicated by white arrows.

Furthermore, similar to the *in situ* TEM observations, no connection between ZrO_2 impurities and the location of Na filaments was observed in the cycled specimen (**Figure 4.18b & d**). It suggested that ZrO_2 does not contribute to the Na nucleation.

4.7   Discussion of Na Filament Formation

Based on the *in situ* biasing results in combination with the simulations and the *post-mortem* analysis, Na filament growth is clearly related to the microstructure of the Na-β″-alumina electrolyte. It can initiate from the interface between Na metal and SSE, where GBs are located as schematically shown in **Figure 4.19a**. The anisotropic ion transport can increase filament formation at GBs as Na^+ ions are blocked resulting in an increasing overpotential for Na nucleation. In addition, some GBs in Na-β″-alumina may also exhibit a low band gap contributing to Na nucleation as Na filaments appeared at GBs fully inside the bulk. Apart from GBs, Na filaments also form at voids, which act as seeds for filament penetration along conneted GBs. Therefore, a Na filament network (**Figure 4.19b**) can be formed in Na-β″-alumina during Na deposition, which ultimately leads to failure of the battery.
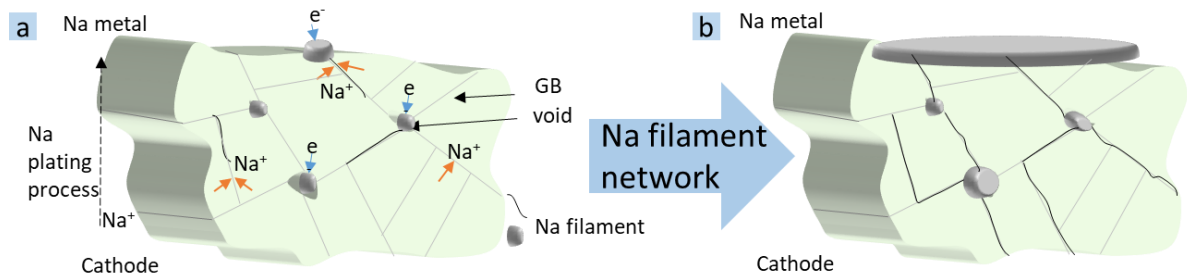
Figure 4.19. Na filament network formation in the Na-β″-alumina based on its microstructure.

4.8   Summary

In this chapter, *in situ* TEM biasing experiments were conducted to realize Na deposition in a Na-β″-alumina/Au(Pt) multilayer system at room temperature. The Na deposition occurred not only at the interface between Na-β″-alumina and Au/Pt but also at the GBs in Na-β″-alumina. Once the Na filaments occupied the whole GB connected to the Au/Pt electrode, further penetration from this GB to neighboring GBs was also observed. In addition, it was also found that Na can diffuse along GBs. In addition to Na filament formation along GBs at the interface of electrolyte/electrode, filament formation was also observed at unconnected GBs in the by *post-mortem* ToF-SIMS analysis on the cycled Na-β″-alumina. In addition to GBs, the voids can also be a starting point for Na plating, probably due to the reduced surface potentital. Nevertheless, in both *in situ* biasing experiments and post-mortem analysis, there was no evidence for a relationship between the impurity of ZrO_2 and Na filament growth.

Furthermore, the relationship between the GB-related microstructure and Na filament growth as well as Na-ion transport was explored through an orientation analysis. The crystals are randomly oriented in the polycrystalline Na-β″-alumina and consequently HAGBs are dominant in the material. Among these HAGBs, CSL boundaries, which are preferentially used in the transport computations, only make up a small minority of the boundaries. Moreover, Na filament growth occurred at random HAGBs. Since Na-β″-alumina has a typical layer structure resulting in 2D ion transport, the influence of the anisotropic ion transport on GB blockage was investigated looking at the combined effects of the orientation of Na-ion transport planes and the electric field. Three scenarios were developed based on the orientation relationship of the Na-ion transport planes in adjacent grains: parallel (Type I), perpendicular (Type II), and random (Type III). Considering two principle electric field directions, the blockage effect for ion migration across GBs can be significant (Type II b1 and Type III a2). In *in situ* experiments, Na filaments started to appear at GBs belonging to Type III a2. Moreover, the simulation of the microscopic Na-ion transport in the TEM lamella indicated that the anisotropic Na-ion migration plays a significant role for the uneven current density distribution in Na-β″-alumina, which leads to current density difference between neighboring grains. This may induce a local overpotential inside the electrolyte leading to Na^+ reduction.

As the microstructure and in particular the GB network present a major bottleneck for Na^+ ion transport and with the Na filament formation on the stability of SSE, this work suggests that tuning the synthesis to enabled formation of textured SSEs could be a way to significantly improve SSE performance and stability.

Chapter 5

5. Au Interlayer Behavior during Inhomogeneous Sodium Deposition in an "Anode-Free" ASSB

5.1 Introduction

It is widely accepted that inhomogeneous cathodic Li deposition at defects in the SSE/anode interface can facilitate dendrite formation. [114] As one state-of-art strategy for improving the deposition behavior, an interlayer has been added between the SSE and the current collector in "anode-free" cells. This is supposed to reduce Li nucleation and enhance Li diffusion to minimize inhomogeneous deposition. Currently, three main types of interlayers are employed: lithiophilic metals/alloys (e.g. Au) [114], carbon [123, 247], and carbon loaded with Ag nanoparticles [124]. However, the microscopic interlayer behavior during deposition has not been investigated in detail.

As Na ASSBs exhibit similar challenges as Li ASSBs with filament formation and anisotropic deposition as described in **chapter 4**, an interlayer setup is expected to be beneficial for the development of an "anode-free" solid cell. S. Tang et al. showed that sodiophilic alloy interlayers (e.g. Au) can decrease the overpotential for nucleation due to the formation of an intermetallic

Na$_2$Au phase during cathodic sodium deposition. [248] Moreover, Na$^+$ ion liquid cells with an Au interlayer exhibit the best cyclic performance. [248] In this chapter, the morphological and microstructural evolution of Au interlayers was explored by *in situ biasing* TEM. In particular, the influences of the thickness and roughness of the Au interlayer and biasing voltages will be discussed.

5.2   Experimental

The sample preparation followed the same workflow described in **chapter 4**. By controlling the sputtering time, nominally ~70 nm and ~170 nm thick Au layers were separately coated on top of a polished Na-β″-alumina. Electron and ion beam deposited Pt layers (labeled as e-Pt(C) layer and i-Pt(C) layer, respectively) were deposited on top of the Au layer for further FIB processing. The Pt layers were used to protect the Au interlayer during FIB processing and work as the current collector providing equivalent potential for the system during *in situ biasing* TEM measurements. With this Na-β″-alumina│Au/e(i)-Pt(C) multilayer system it was possible to investigate the cathodic sodium deposition in a TEM as shown in **Figure 5.1** with different biasing voltages. Notably, in this setup, the Na$^+$ flux can alter with different biasing voltages. The resultant phenomenon by altering biasing voltages cannot be definitely distinguishable resulting from different deposition overpotentials and/or the Na$^+$ flux. In this work, the influence of the biasing voltages is investigated by simplification since it is the directly controllable parameter. The influence of Na$^+$ flux should be investigated further.
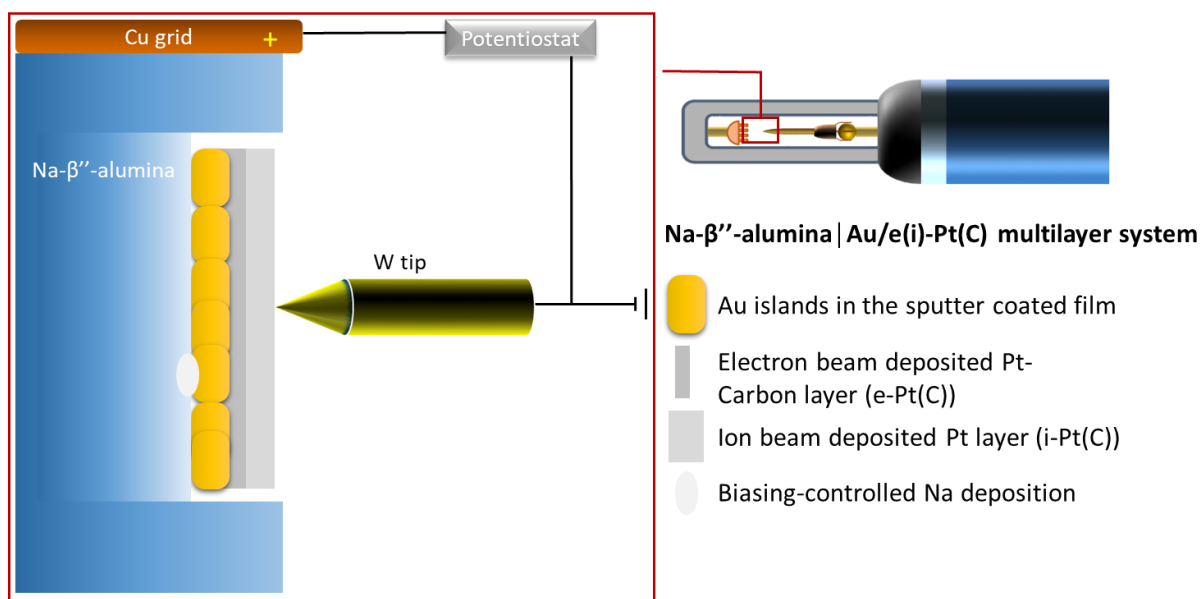
Figure 5.1. *In situ* biasing TEM setup using a FIB processed Na-β″-alumina│Au/e(i)-Pt(C) multilayer system.

5.3   Results

5.3.1   Microstructure of Au Interlayer with Different Thickness

Au interlayers with different thickness were deposited on the surface of polished Na-β″-alumina by magnetron sputter deposition. As shown in **Figure 5.2**, a continuous Au-layer was deposited, but the dark features pointed out by the blue arrow in **Figure 5.2a** indicate some surface roughness from Au deposition. This suggests that the sputter deposited Au films on the surface of Na-β″-alumina exhibit a characteristic islands structure. [249] In addition, voids can be also present at the interface between Na-β″-alumina and the Au interlayer as pointed out by arrows in the cross-section image in **Figure 5.2b & c**. The voids are larger for the thicker Au interlayer. This means that the interface between Na-β″-alumina and Au interlayer can exhibit regions with poor contact. Since the influence of the Au interlayer roughness on the behavior during cathodic sodium deposition is one of key interests, there was no focus to improve the roughness in this study. Nevertheless, in principle, it can be improved through tuning the deposition parameters or using different deposition techniques. [250, 251] The Au films exhibit an aggregated structure consisting of smaller grains. For instance, the ~70 nm thick Au layer consists of irregular-shaped grains with a diameter of ~30 nm as presented in **Figure 5.2d**.
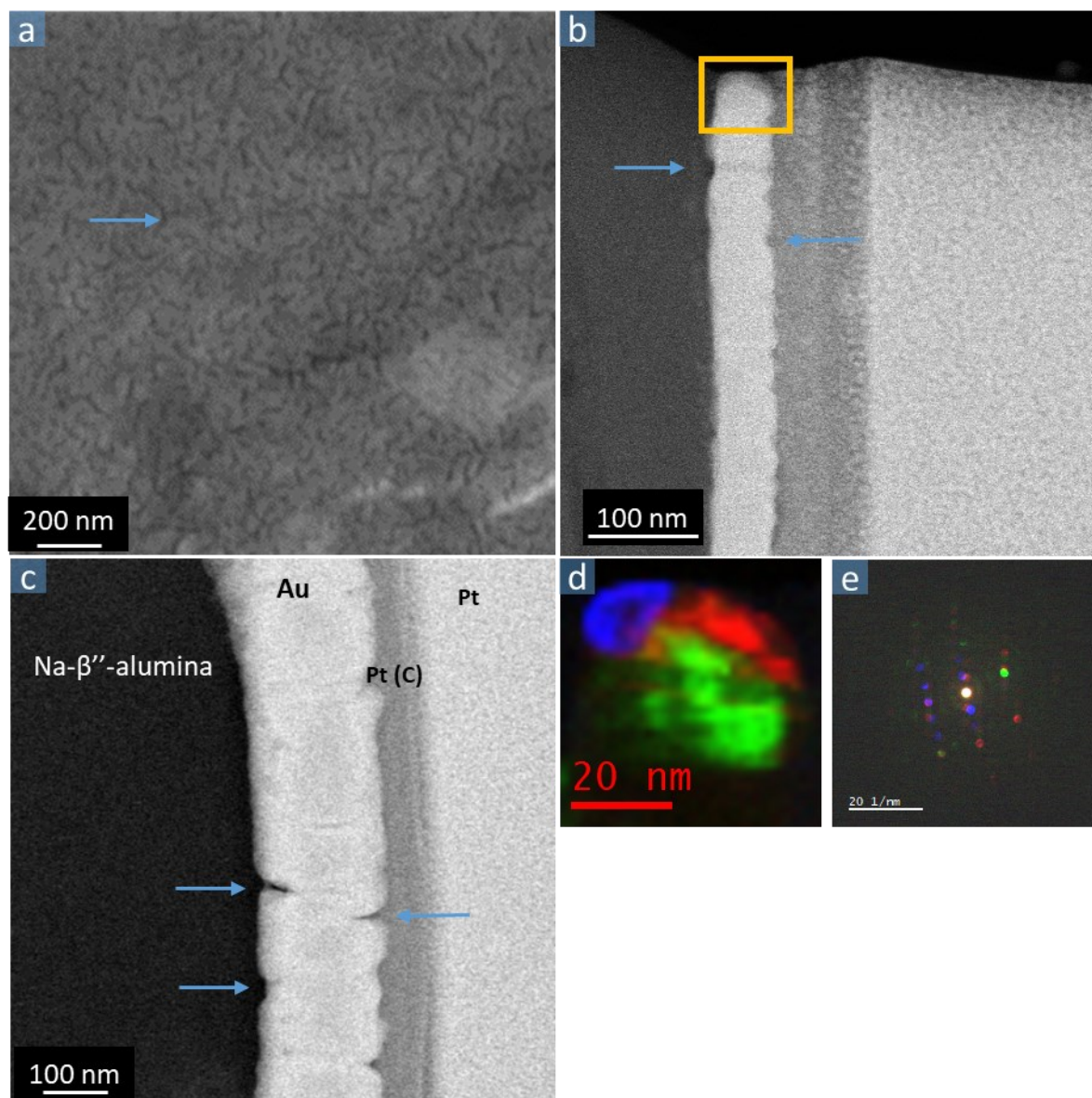
Figure 5.2. Morphology of sputter-coated Au interlayers: **a.** SEM image of an Au interlayer with a thickness of ~70 nm. **b. & c.** HAADF-STEM images of cross-sections of Na-β″-alumina │ Au/e(i)-Pt(C) multilayer systems with Au interlayer thicknesses of ~70 nm (**b**) and ~170 nm (**c**). The blue arrows indicate voids between Au islands. **d.** Overlaid 4D-STEM generated virtual dark field images of individual grains in the inset orange rectangle area in (**b**). **e.** Overlaid NBEDs of the corresponding grains in (**d**).

5.3.2 Microstructural Evolution of the ~70 nm Au Interlayer during Sodium Deposition

To investigate the microstructural evolution of the Au interlayer with non-uniform cathodic sodium deposition, *in situ* TEM measurements were performed on the Na-β″-alumina │ Au/e(i)-

Pt(C) multilayer system using the same setup as in **chapter 4**. In the system shown in **Figure 5.3**, one large grain of Na-β''-alumina was partially covered with a ~70 nm thick Au interlayer and the rest of the grain was in direct contact with e-Pt(C) layer. As a biasing voltage of 15 V was applied to the system, non-uniform cathodic sodium deposition started. This can be attributed to the surface defects and the poor contact between Na-β''-alumina and Au/e-Pt(C). Irregular shaped Na filament formation was observed at the interface between Na-β''-alumina and Pt(C) similar to the growth reported in **chapter 4**. In contrast, at the Au-coated region, a reaction at the Au interlayer occurred at the poor contact area indicated by the red arrow leading to the formation of a small, initially roughly spherical, Na-Au alloy particle between the Na-β''-alumina and e-Pt(C) layer during the early stage of cathodic sodium deposition as indicated by orange arrows in **Figure 5.3**. With the volume increasing with sodium deposition, the particle became more faceted and grew out of the surface of the Pt layer due to a lack of mechanical restriction in this direction. This results in the isolation of the Na-Au alloy particle from the Au interlayer, which triggered a redistribution of Au in the Au interlayer. This potentially affects the cyclic performance of the Au interlayer.

The morphology did not change significantly at the interface between the Na-β''-alumina and Au interlayer after $t_0 + 1993s$ apart from the slight Na filament growth underneath the Na-Au alloy particle as depicted in **Figure 5.3g & h**. This can be attributed to the poor contact between deposited Na and the Au interlayer restricting the alloy reaction as the adjacent Au diffused to form the Na-Au alloy whisker. This poor contact can trace back to the gap between Au grains within Au interlayer i.e. high roughness leading to the discontinuous Na diffusion and Au diffusion. The biasing voltage was increased to 16V at $t_0 + 2250s$ to boost the sodium deposition. An additional thin faceted Na-Au alloy whisker grew by Au diffusion from the Au interlayer and alloying with the deposited Na. This faceted growth became more obvious when the bias voltage was increased to 17V, facilitating the Na-Au alloy reaction forming Na_2Au [248] and its growth with a preferential facet [252]. As a consequence, Au diffusion is enhanced significantly. However, it is unclear if the Na^+ flux also plays a role for this faceted whisker growth as increasing the bias voltage is always accompanied by a higher Na^+ flux. Besides, the lack of stack pressure on the outer surface in this *in situ* setup can also contribute to the significant faceted growth along the external electric field direction on the e/i-Pt(C) layer surface. Notably, Au only diffuses from the Au interlayer below the deposited Na (as indicated by the yellow arrow in **Figure 5.3k & l**, whereas the upper gold layer is maintained as indicated by the blue arrow. This can presumably be attributed to the poor contact between the upper part of the Au interlayer and deposited Na restricting Na diffusion for further alloy reaction. This suggests that the Na-Au alloy reaction and Na diffusion facilitate Au diffusion.
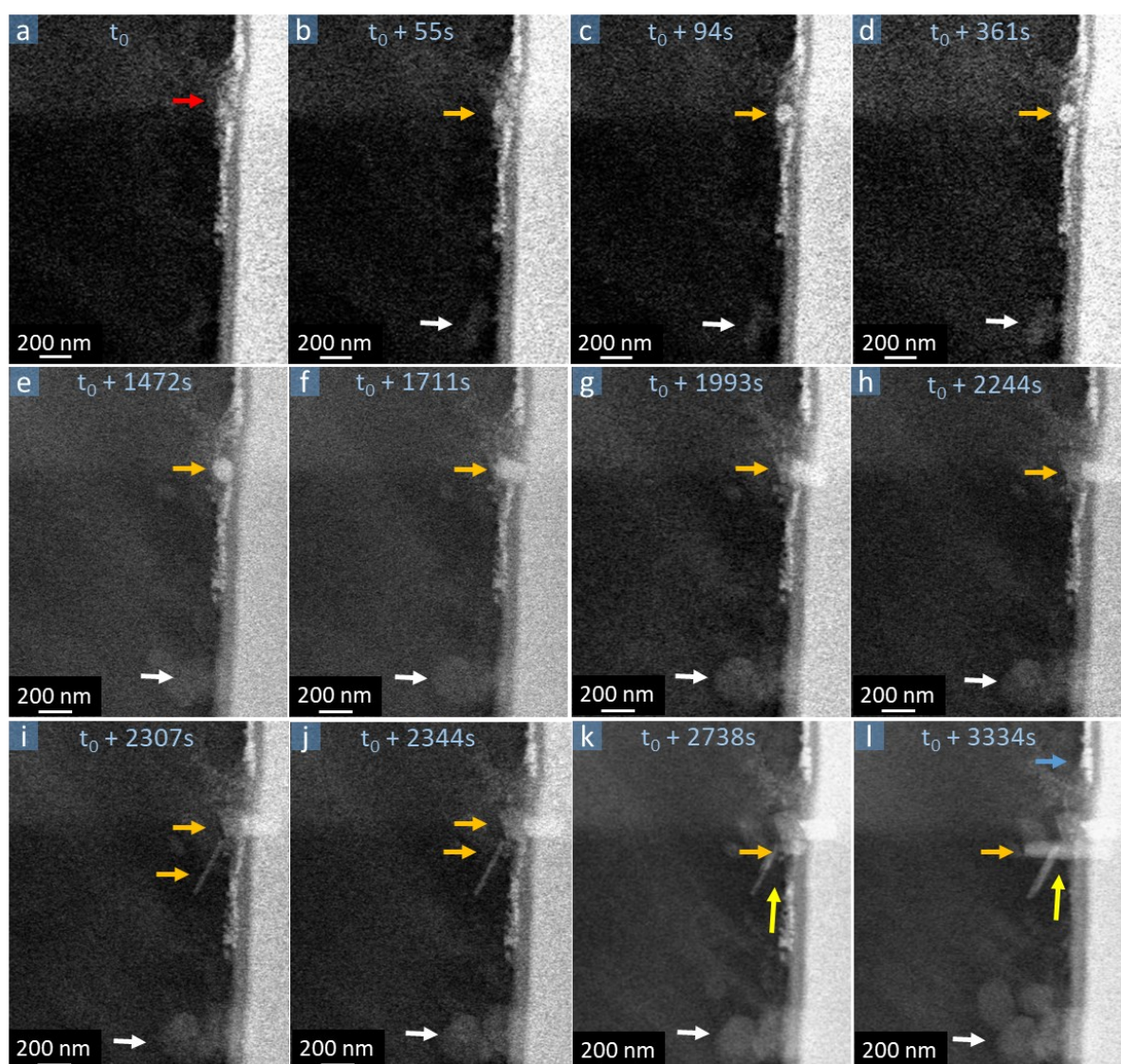
Figure 5.3. Microstructural evolution of a ~70 nm thick Au interlayer during cathodic sodium deposition at a biasing voltage range from 15 V to 17V. Time-series HAADF-STEM images of Na-β″-alumina│Au/e(i)-Pt(C) multilayer system at a biasing voltage of 15V (**a – h**): **a**. t_0; **b**. t_0 + 55s; **c**. t_0 + 94s; **d**. t_0 + 361s; **e**. t_0 + 1472s; **f**. t_0 + 1711s; **g**. t_0 + 1993s; **h**. t_0 + 2292s; Biasing volatages of 16V and 17V started from t_0 + 2250s and t_0 + 2708s, respectively: **i**. t_0 + 2581s; **j**. t_0 + 2344s; **k**. t_0 + 2738s; **l**. t_0 + 3334s. The red arrow indicates the poor contact between the Na-β″-alumina and Au interlayer, in which small Au aggregates are distributed. The orange arrows indicate the Na-Au alloy formed at the poor contact between Na-β″-alumina and Au/Pt layer, while the white arrow highlights Na filaments growing at the interface between Na-β″-alumina and Pt layer. The blue arrow indicates that the upper part of the Au interlayer is maintained after biasing, whereas the yellow arrows indicate the direction of Au diffusion and the depletion of the lower part of the Au interlayer.

After the *in situ* biasing, low-dose EDX was used to characterize the Na and Au distribution. The filaments marked by a blue circle in **Figure 5.4** at the interface between Na-β″-alumina and e-Pt(C) layer mainly consist of Na. The whiskers marked by orange circles contain both Au and Na. This indicates that during sodium deposition the Au interlayer reacted and formed Na-Au alloy whiskers, which is presumably the thermodynamically stable intermetallic phase Na_2Au [248]. Aside from the Na-Au whiskers and Na filaments, Na is evenly distributed at the interface between the Na-β″-alumina and the e/i-Pt(C) layer as depicted in **Figure 5.4d**. Therefore, in addition to Au diffusing and alloying with Na, it is suspected that Na diffusion occurs in the Au interlayer, which facilitates Au counter diffusion towards the Na-Au filament. Interestingly, Na is distributed quite uniformly along the e-Pt(C) layer, while no other obvious morphological changes were observed during cathodic sodium deposition. The observed oxygen signal at the whisker and filament position presumably stems from an overlay with the Na-β″-alumina. In addition, some oxidation of Na in the TEM column can occur after biasing.
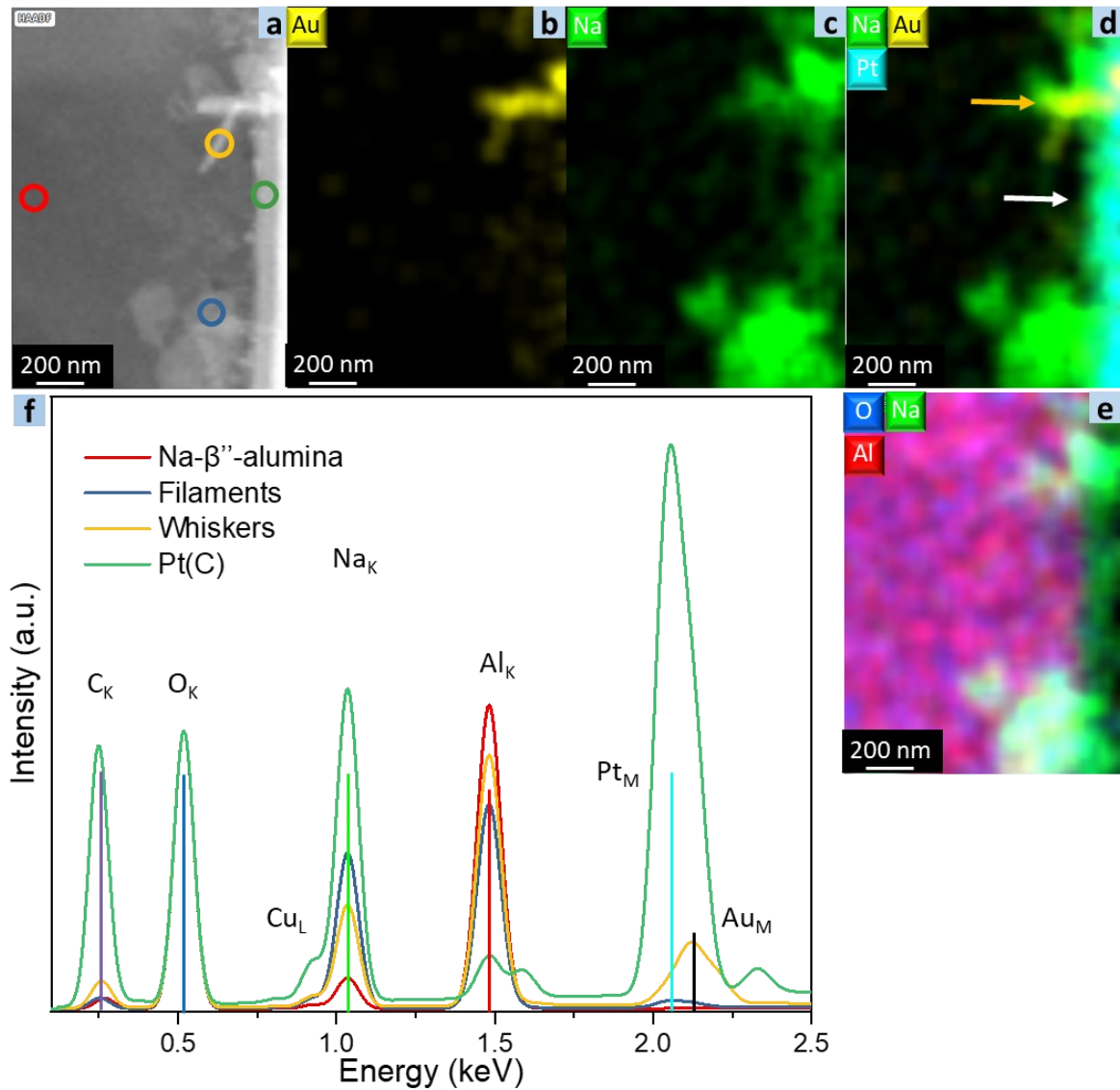
Figure 5.4. Low-dose STEM-EDX analysis of the Na-β''-alumina│70 nm Au/e(i)-Pt(C) multilayer system after biasing (same region as in **Figure 5.3**). **a.** HAADF-STEM image; **b.** EDX Au net intensity map (yellow); **c.** EDX Na net intensity map (green); **d.** Overlaid EDX Na (green), Au (yellow), and Pt (cyan) net intensity map; The orange arrow indicates Na-Au alloy whiskers and the white arrow uniform sodium deposition at the interface to Pt(c). **e.** Overlaid EDX O (blue), Al (red), and Na (green) net intensity map. **f.** STEM-EDX spectra corresponding to the regions marked by circles in (**a**): Na-β''-alumina (red), filament (blue), whisker (orange), and e-Pt(C) (green).

For further investigation of the Na and Au diffusion behavior, sodium deposition was conducted in another multilayer system with a ~70 nm thick Au interlayer shown in **Figure 5.5**. Here, Na started to deposit at cracks within the Na-β''-alumina. This is in line with the observation in

chapter 4. Besides, significant Na filament growth was also observed at the upper edge of the thin lamella during the 1st biasing at 15V. In addition to the filament formation, Na diffused towards the Au interlayer and reacted there to form a large Na-Au alloy particle growing out of the interlayer due to volume expansion of the Au interlayer. For a closer observation of the Au interlayer, the biasing was stopped to acquire a higher magnification image (**Figure 5.5e**). Interestingly, the shape and size of the Na-Au alloy particle continued to change quickly when decreasing the bias voltage down to 0 V. This can presumably be attributed to a continuous local reaction between the deposited Na and the Au underneath, independent of the applied bias voltage resulting in the Na-Au alloy particle growth. Nevertheless, this reaction did not occur in the bulk of the lower part of the Au interlayer, presumably because no free Na was available there without further biasing. With prolonged biasing, further Na diffusion occurred. This suggests that the Na diffusion along the Au interlayer may be triggered by the bias voltage. Comparing the shape of the particle formed here to the data shown in **Figure 5.3** suggests that the bias voltage affects the shape of the Na-Au alloy particle, i.e. anisotropic faceted growth. In addition, a darker line appears at the lower part of the Au interlayer, at the interface to the Na-β''-alumina due to Na diffusion from top to bottom accompanied by Au counter diffusion during Na deposition. At the same time, nano particles with high intensity, which formed due to alloy formation during interdiffusion, are located at the surface of the Na-β''-alumina next to the Au interlayer as depicted in **Figure 5.5f**. This preferential interfacial location can presumably be attributed to the low mechanical restriction at the surface compared to the bulk of the Au interlayer. Moreover, the slight gap between the Au interlayer and the Na-β''-alumina may be the result of this consumption of Au during alloy particle formation (**Figure 5.5f**).

With the continued Na diffusion along the Au interlayer during a 2nd biasing at 12V, the Au started to counter diffuse. As a consequence, the Au interlayer was converted to an Na-Au interlayer and a Na-Au alloy particle grew at the region, where Na had been deposited. This suggests that the Au diffusion is probably a response to the Na diffusion during the biasing. Moreover, besides a small Na-Au whisker at the end of the Na-Au interlayer, a slight volume expansion at the upper edge of the TEM lamella was observed after the 2nd biasing at 12V, while Na-Au alloy particles appeared at the surface of the e-Pt(C) layer based on the increased intensity there. Nevertheless, the lower part of the layered structure was mostly maintained. This can be attributed to the low mechanical restriction at the edge of the lamella and the high amount of Na deposited there, available for an alloying reaction. Moreover, the distinctive morphological changes of the Na-Au alloy particle compared to the oriented Na-Au alloy whisker in **Figure 5.3** can presumably be attributed to a faceted growth with the bias voltage applied. Low-loss EELS exhibits a peak at around 6 eV

indicating metallic Na deposition at crack regions and the upper edge of the TEM lamella, and diffusion of metallic Na along the e-Pt(C) layer. Interestingly, the low-loss EELS spectra of the Na-Au particle and Na-Au interlayer exhibit a peak at a similar position. However, without low-loss EELS measurements for pure Na-Au available as reference, it is unclear if this peak can be attributed to metallic Na being present there as well.
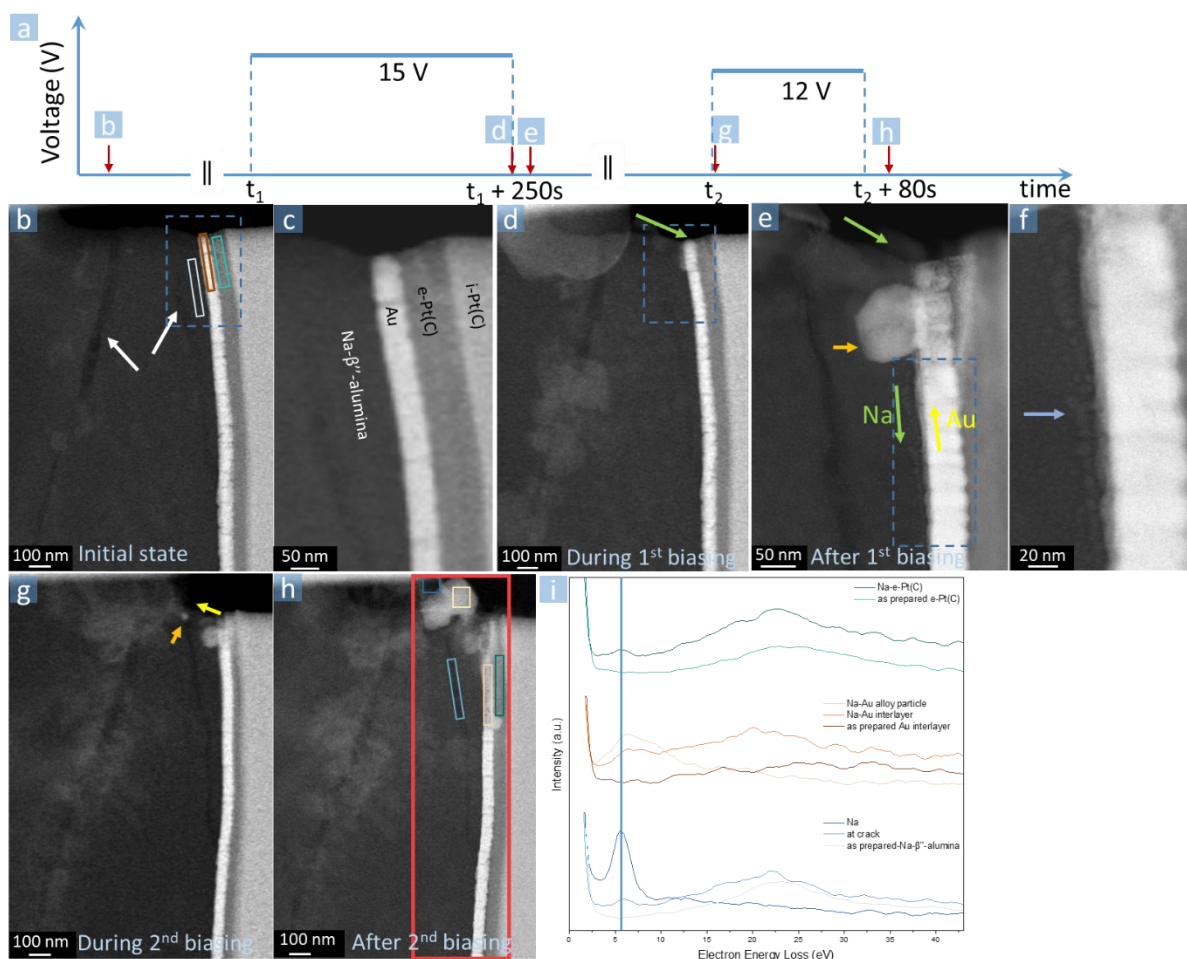
Figure 5.5. HAADF-STEM images of the Na-β''-alumina│Au/e(i)-Pt(C) system at different biasing states as indicated in the profile of voltage vs. time plot (**a**). This profile includes the 1st biasing, applying 15V from t_1 to $t_1 + 250s$ and the 2nd biasing applying 12V from t_2 to $t_2 + 80s$. The ramping time is ignored in the profile. **b**. Initial state with the ~70 nm thick Au interlayer. **c**. Magnified image of the area marked by blue dashed rectangle in (**b**); The Au interlayer exhibits a fairly uniform contrast. **d**. The image has been acquired with a voltage of 15V applied at $t_1 + 250s$; **e**. Image acquired after the first biasing. **f**. Magnified image of the area marked by a blue dashed rectangle in (**e**); **g**. During the 2nd biasing; **h**. After the 2nd biasing. White arrows indicate cracks within the Na-β''-alumina where Na filament grew after biasing. Orange arrows indicate Na-Au

alloy particles. Green arrows indicate the direction of Na diffusion, while yellow arrows indicate the counter direction of Au diffusion. With the diffusion, Na-Au alloy formation occurs along the interface of Au interlayer as the intensity of the Au interlayer decreases and bright spots become visible at the surface of Na-β″-alumina, which are indicated by the blue arrow in (**f**). This presumably also results in the small gap at the interface. **i.** Low-loss EELS acquired at the regions marked in (**b**) and (**h**) with the color corresponding to rectangles indicating the respective area.
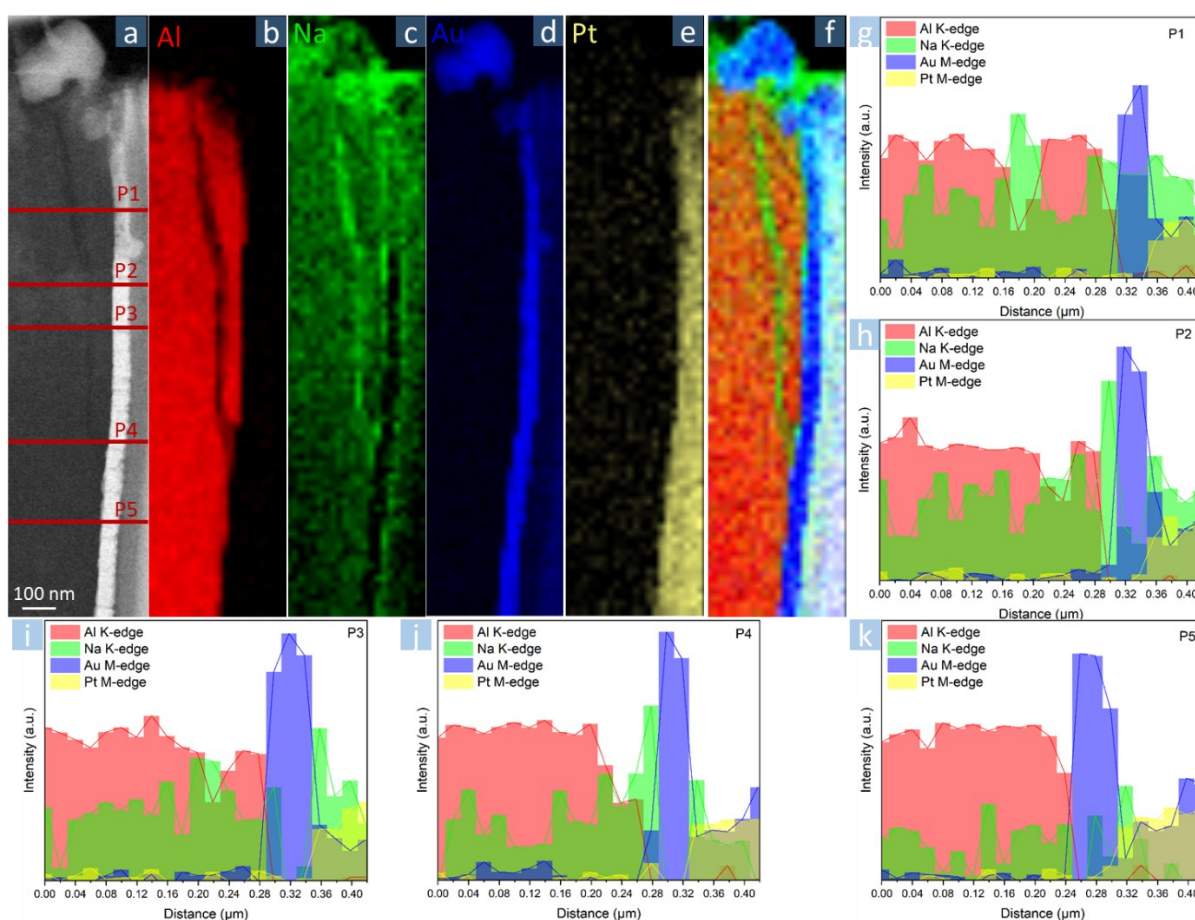
Figure 5.6. Core-loss EELS maps of the sample after biasing of the area marked by the red rectangle in **Figure 5.5e. a.** HAADF-STEM image; **b.** Al K-edge map; **c.** Na K-edge map; **d.** Au M-edge map; **e.** Pt M-edge map; **f.** Overlaid maps; **g. – k.** Line profiles of Al K-edge, Na K-edge, Au M-edge, and Pt M-edge at the positions P1 - P5 marked in (**a**).

Complementing the morphological evolution seen in the HAADF-STEM images, elemental distribution maps were acquired after biasing based on the core-loss EELS Al K-edge, Na K-edge, Au M-edge, and Pt M-edge (**Figure 5.6**) for the region marked in **Figure 5.5h**. The Na signal extending full through the Au layer and beyond indicates the conversion of the Au interlayer to an Na-Au interlayer up to line P2. This is in agreement with the previous interpretation based on the

morphological changes in **Figure 5.5**. The high Na content at the Na-β″-alumina/Na-Au interface around P4 is presumably due to a crack present there. In addition, the strong Na signal is present at the e-Pt(C) layer indicates Na diffusion along/into the e-Pt(C) layer in this part of the sample.

Down the sample at P3-P5, a high Na signal is present at the interface between the Au interlayer and the Na-β″-alumina and the e-Pt(C) layer, but almost no Na is detected within the Au layer itself. While the Na at the Na-β″-alumina/Au interface might be due to deposition from the Na-β″-alumina, the high Na content at the Au/e-Pt(C) interface clearly shows that Na is quickly diffusing along the interface and deposited there, also fitting to the observed gradient down the interface. Interestingly, the enhanced Na content at the Au/e-Pt(C) interface is extending further than at the Na-β″-alumina/Au, suggesting faster diffusion at this interface. In addition, a slight Na gradient is also observed into the e-Pt(C) layer from the interface with the Au layer, which indicates some Na diffusion into the e-Pt(C) layer after the interface deposition.

5.3.3   Microstructural Evolution of the ~170 nm Au Interlayer with Sodium Deposition

The investigation of the volume expansion and reaction of a thicker Au interlayer is presented in **Figure 5.7**. Initially, as Na deposits at the interface between Na-β″-alumina and a ~170 nm thick Au interlayer, the contacted area of the Au interlayer starts to expand slightly. To visualize the expansion, differential time series images (**Figure 5.8**) have been calculated by subtracting the HAADF-STEM image at t_0 from all following images. The area with high contrast at the Na-β″-alumina side of the interface to the Au interlayer indicates an increasing volume of the Au interlayer (as pointed out by orange arrows). This high contrast is accompanied by a lower contrast on the Au interlayer side of the interface. Both changes are attributed to a Na-Au alloy reaction during sodium deposition. Starting from the initial alloying point, alloy formation mostly extends along the interface during biasing with Na diffusing in the Au layer. Interestingly, the major direction of this diffusion and alloying is along the interface between the Au interlayer and Na-β″-alumina rather than perpendicular to it into the Au interlayer. This is in line with experiments shown in **Figure 5.5**. This can presumably be ascribed to a lower activation energy for interface compared to bulk diffusion. In addition, the mechanical back stresses from the Pt(C) layer may also restrain the volume expansion in the perpendicular direction. With further sodium deposition, the volume expansion became more obvious and Na-Au alloy particle formation at the contact region between the Na filament and Au interlayer can be seen in **Figure 5.7f**. Nevertheless, this Na-Au alloy particle is still connected to the Au interlayer.
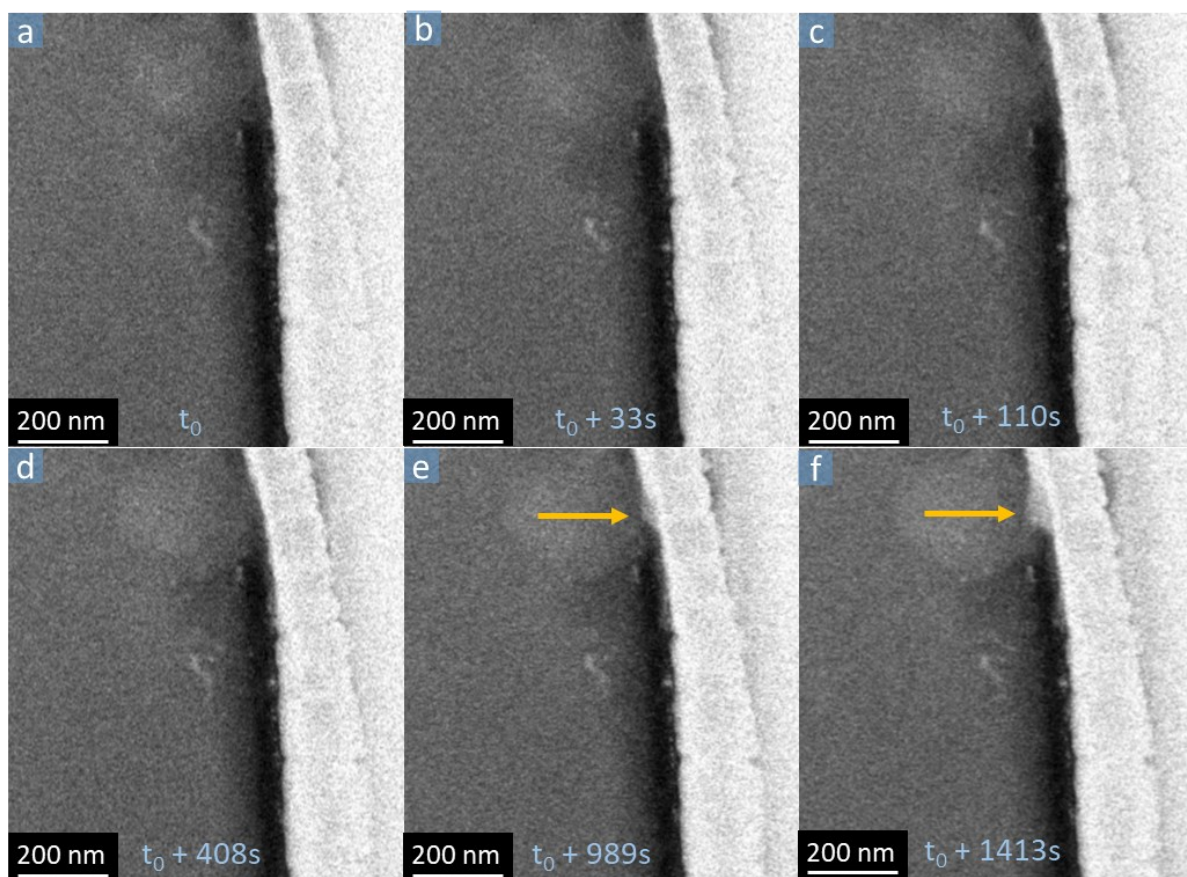
Figure 5.7. Microstructural evolution of a ~170 nm thick Au interlayer during cathodic sodium deposition. Time-series HAADF-STEM images of Na-β''-alumina│Au/e(i)-Pt(C) multilayer system: **a**. t_0; **b**. $t_0 + 33s$; **c**. $t_0 + 110s$; **d**. $t_0 + 408s$; **e**. $t_0 + 989s$; **f**. $t_0 + 1413s$. The orange arrows indicate the volume expansion of the Au interlayer by sodium deposition, i.e. Na-Au alloy formation.
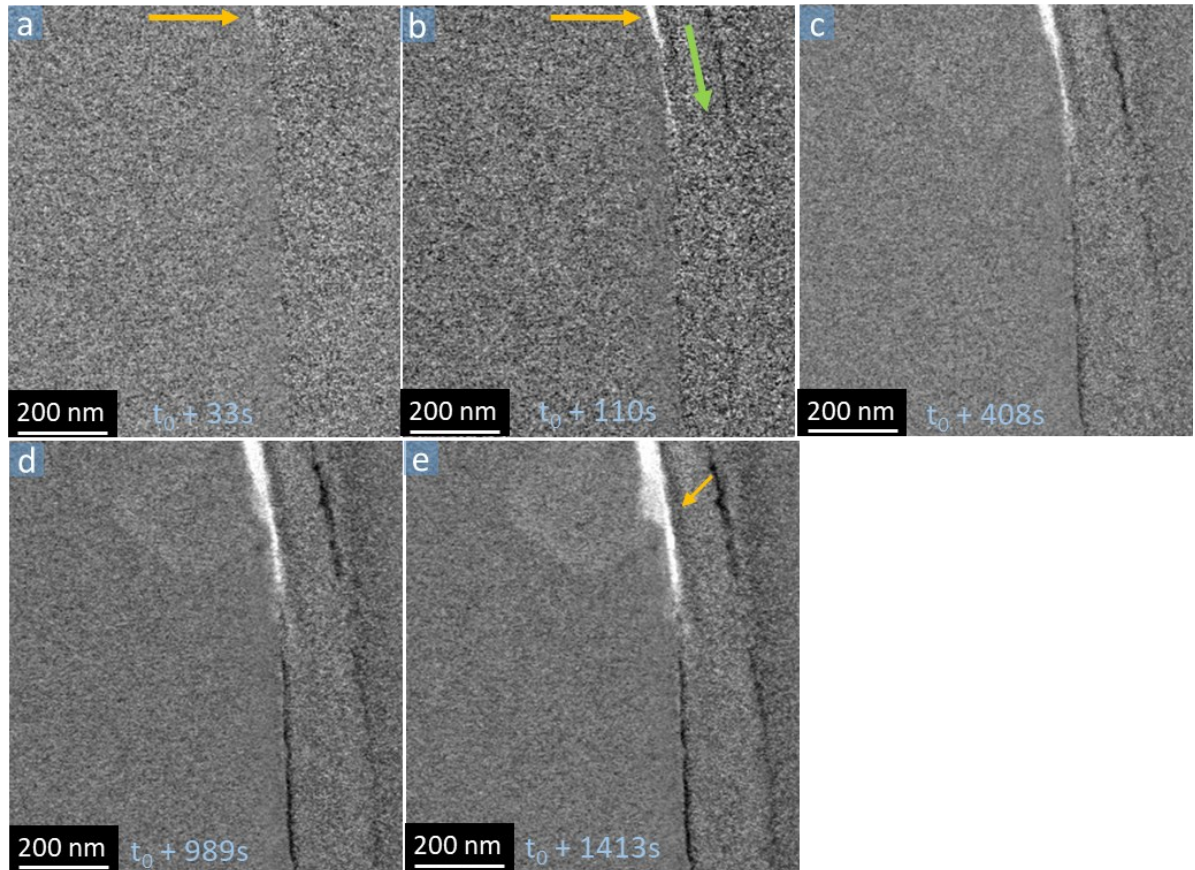
Figure 5.8. The features of microstructural evolution during deposition were enhanced by the differential images obtained by subtracting the image at t_0 in **Figure 5.7**. **a.** $(t_0 + 33s) - t_0$; **b.** $(t_0 + 110s) - t_0$; **c.** $(t_0 + 408s) - t_0$; **d.** $(t_0 + 989s) - t_0$; **e.** $(t_0 + 1413s) - t_0$. The orange arrows indicate the volume expansion of the Au interlayer by sodium deposition, i.e. Na-Au alloy formation. The Na diffusion and resultant alloy formation direction were pointed out by the green arrow.

With further accumulation of Na at the interface, a hundred nanometer long whisker grew in the vicinity of the Au-Na alloy particle, which is analyzed in detail in **Figure 5.9**. This growth continued even after the biasing was stopped, accompanied by a shrinkage of the Na-Au alloy particle and the Na filament as shown in **Figure 5.9b**, similar to the experiment in **Figure 5.5**. This could be an indication that the Na-Au alloy particle that initially formed at the interface was not thermodynamically stable. The Au from the Na-Au alloy particle and the deposited Na continued to react and formed the thermodynamically stable Na_2Au phase in the well faceted whisker, similar to the observations shown in **Figure 5.5c**. This is also supported by the NBED analysis in **Figure 5.9d - f**. The measured reciprocal lattice spacings of the whisker are 2.2 1/nm for O'A', O''A'' and O'B' and O''B'' and 1.9 1/nm for A'B' and A''B'', which can be indexed as $(\bar{1}\,0\,1)$, $(0\,\bar{1}\,1)$,

and $(1\,\bar{1}\,0)$ lattice planes of Na_2Au seen in $[1\,1\,1]$ zone axis orientation. The same distances are also observed for the diffraction spots indicated by the orange circles in **Figure 5.9d.** However, the measured values for OA_b, OB_b, and OC_b are all 4.1 1/nm (blue circles in **Figure 5.9d**, **Table 5-1**), which belong to neither of the two thermodynamically stable phases Na_2Au or Au_2Na indicating that the Na-Au alloy particle consists of Na_2Au and another Na-Au phase.
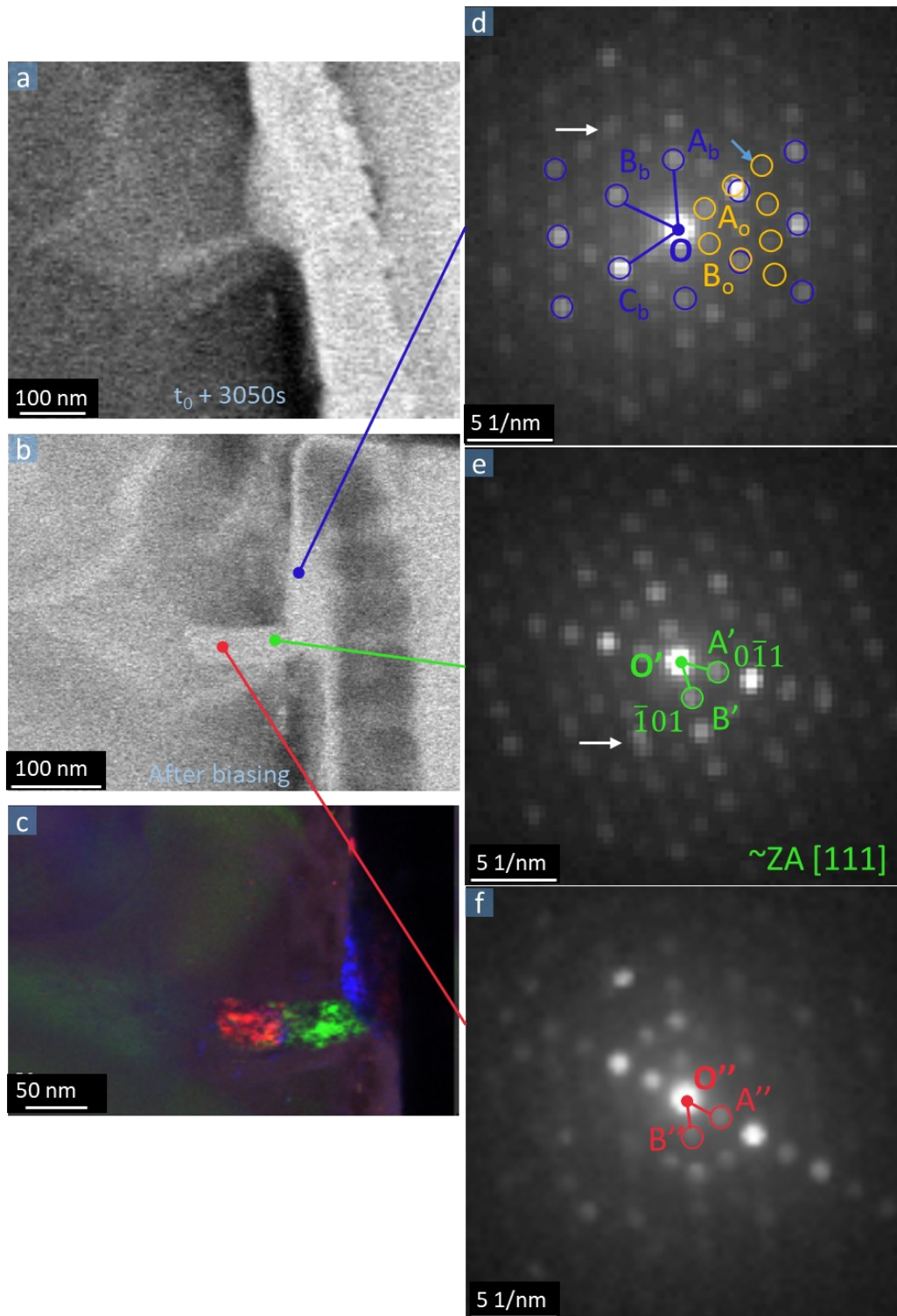
Figure 5.9. Whiskers formed after prolonged sodium deposition following the deposition in **Figure 5.7**. **a.** HAADF-STEM image of the Na-β″-alumina │ Au/e(i)-Pt(C) system after biasing at $t_0 + 3050s$. **b.** ADF-STEM image after biasing. **c.** Overlaid virtual darkfield image generated based on the NBEDs (**d** – **f**) in 4D-STEM data cube. **d.** – **f.** NBED patterns of the Na-Au alloy particle and whisker region. Based on the marked diffraction spots, the corresponding virtual dark-field images were generated. In (**d**), diffraction patterns of two crystals are marked with blue and orange circles. The white arrows indicate the diffraction patterns from the overlaid grains.

Table 5-1. Lattice plane and their reciprocal distances for different metals and intermetallic phase

	CRYSTAL STRUCTURE	h k l 1/NM	h k l 1/NM	h k l 1/NM
Au	face centered cubic	$\bar{2}\,0\,2$	$0\,\bar{2}\,2$	$2\,\bar{2}\,0$
	ICSD_52249	6.84	6.84	6.84
Au₂Na	face centered cubic	$\bar{2}\,0\,2$	$0\,\bar{2}\,2$	$2\,\bar{2}\,0$
	ICSD_108001	3.62	3.62	3.62
Na₂Au	Tetragonal	$\bar{1}\,0\,1$	$0\,\bar{1}\,1$	$1\,\bar{1}\,0$
	ICSD_58527	2.26	2.26	1.90
Na	body centered cubic	$\bar{1}\,0\,1$	$0\,\bar{1}\,1$	$1\,\bar{1}\,0$
	ICSD_644901	3.35	3.35	3.35
Figure 5.9d		$OA_b = 4.1$	$OB_b = 4.1$	$OC_b = 4.1$
		$OA_o = 2.2$	$OB_o = 2.2$	$OC_o = 1.9$
Figure 5.9e		$O'A' = 2.2$	$O'B' = 2.2$	$A'B' = 1.9$
Figure 5.9f		$O''A'' = 2.2$	$O''B'' = 2.2$	$A''B'' = 1.9$

Compared to the Au interlayer with low roughness in **Figure 5.7**, the rougher Au interlayer (**Figure 5.10**) shows a more apparent morphological change during conversion from the Au to a Na-Au interlayer. Na and Au interdiffuse along the Au interlayer during biasing as indicated by the green and yellow arrows, leading to a conversion to the Na-Au interlayer and the formation and growth of additional Na-Au alloy particles at region 1 and the volume expansion of the interlayer. The volume expansion in region 1 is much more pronounced compared to region 2. These two regions were initially separated by small voids, which suggests that the interface

roughness or gaps in the Au interlayer play a significant role in the diffusion process. Afterwards, the local difference in the volume expansion were also seen in region 3 (**Figure 5.10e – g**), which was originally separated by a large gap from region 2.

The atomic ratio of Na and Au is close to 2 : 1 in regions 1, 2 and 3. This indicates that Na diffusing from the deposited Na along the Au interlayer reacts to form the thermodynamically stable intermetallic Na_2Au phase. [248, 253].

A fairly uniform Na distribution along the e-Pt(C) layer is observed (**Figure 5.10i**) similar to the Na distribution in **Figure 5.6**. However, Na did not diffuse along the i-Pt(C) layer, which has a lower carbon content, as no Na is distributed there. This suggested that the Au/amorphous carbon interface contributes to this diffusion rather than the Pt.
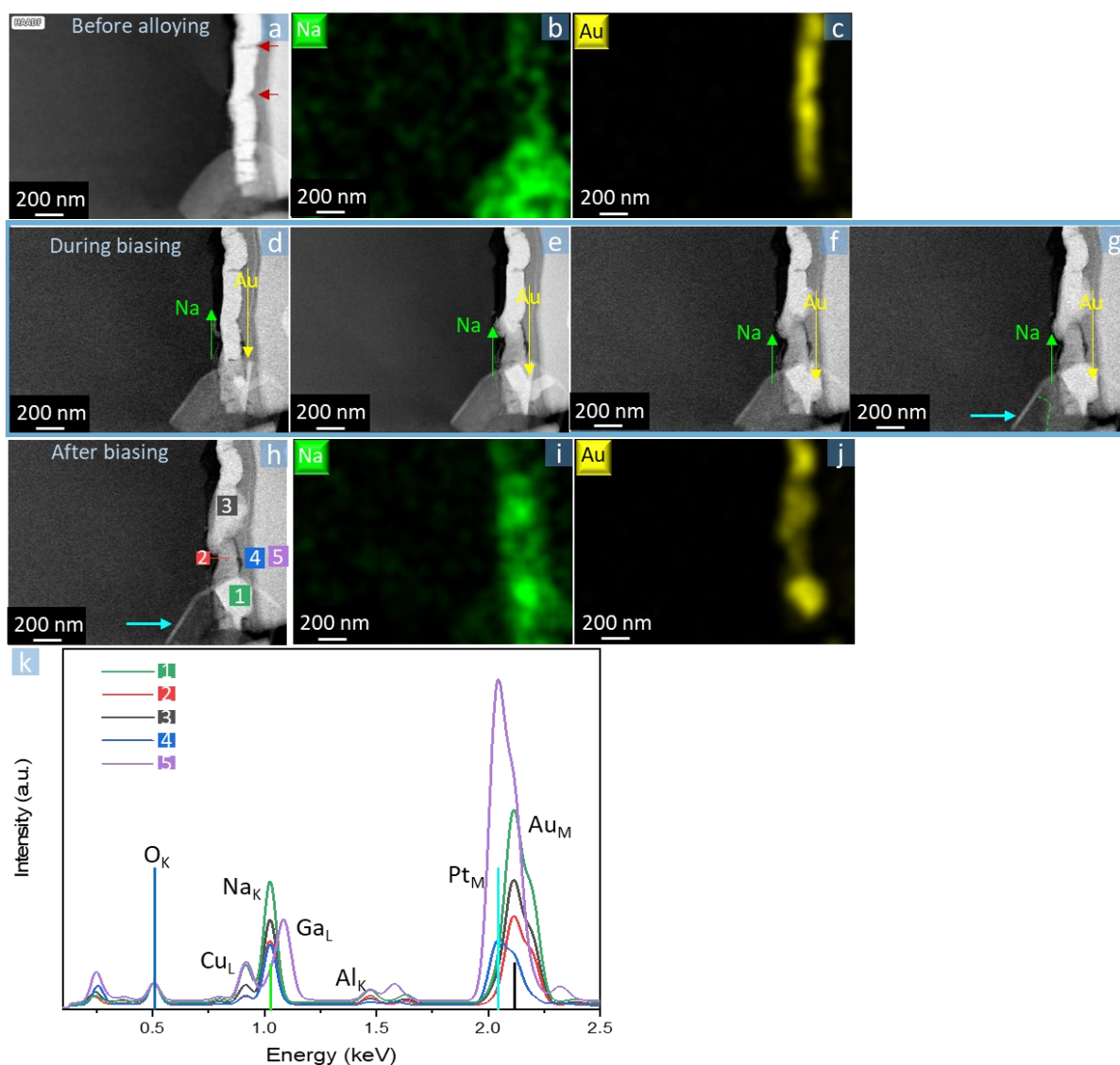
Figure 5.10. HAADF-STEM images of the microstructural evolution of the Na-β″-alumina│170 nm Au/e(i)-Pt(C) system (**a**) before, (**d-g**) during, and (**h**) after biasing; **b – c.** EDX Na and Au net intensity maps before alloying and after biasing (**i– j**) at the Au/Na-Au interlayer. **k.** EDX spectra of the regions marked in (**h**). The red arrows (in **a**) indicate gaps within the Au interlayer. The green arrow indicates the direction of Na diffusion, while the yellow arrow points out the direction of Au diffusion. The cyan arrow indicates the core shell of the oxidized Na in TEM. The green dashed line indicates the Na depletion front within the Na whisker.

5.4   Discussion

With the *in situ* biasing experiments described in this chapter, cathodic sodium deposition was realized in the Na-β″-alumina│Au/e(i)-Pt(C) multilayer micro-system in a TEM. While inhomogeneous sodium deposition occurred at the interface of Na-β″-alumina to the Au interlayer, a more uniform Na and Au alloy formation occurred accompanied by slight volume expansion compared to the significant Na filament growth at the Na-β″-alumina │ e-Pt(C) interface shown in **Figure 5.3**. Furthermore, the Na-Au alloy particle growth seems to depend on the bias voltage and/or the Na^+ flux. A higher bias voltage, which results in a high Na^+ flux, seems to facilitate direct formation of Na_2Au whiskers with anisotropic shape. This assumption is supported by the observation of the Na_2Au whisker growth changing shape with and without bias voltage applied as seen when comparing **Figure 5.5** and **Figure 5.8**.

Besides the alloy formation and the Na-Au alloy particle growth, significant Na and Au counter diffusion occur at the same time in all *in situ* experiments. Based on the EDX and EELS analysis, this interdiffusion process is part of the Au interlayer converting to a Na-Au interlayer during sodium deposition. However, the morphology of Na-Au interlayer differs. This seems to be related to the position where Na initially deposits with high rate, Na and Au diffusion rates, the morphology of the as-prepared Au interlayer, and its thickness. Au diffuses in the Au interlayer towards the position where sodium deposits and reacts with deposited Na to form Na-Au alloy particles. Their growth can lead to redistribution of Au and disconnected gaps in the thin Au interlayer, which potentially influence further cyclic performance. For example, in the extreme case, the ~70nm thick Au interlayer was depleted to form a Na_2Au whisker during sodium deposition at high bias voltage as depicted in **Figure 5.3**. The continuous covering nature of the interlayer was destroyed for the further protection. Nevertheless, the overall connectivity of the thicker Au interlayer (~170nm) still remained during sodium deposition even though Na_2Au

whiskers formed as depicted in **Figure 5.9** and **Figure 5.10**. This is expected to be beneficial for further cyclic performance as a continuous interlayer can facilitate Na diffusion due to the highly sodiophilic nature of Au and Na-Au alloys and support a more homogeneous Na deposits. [123] Besides, at low bias voltage, the morphology of the ~70nm thick Au interlayer also remained fairly constant during conversion to a Na-Au interlayer (**Figure 5.5**). This suggests that the bias voltage influences the Na and, indirectly, also the Au diffusion rate as Au diffusion only occurs in the Au interlayer where Na diffuses. The diffusion and alloying reaction results in a chemical potential gradient along the Au interlayer. A high roughness with the appearance of gaps in the Au interlayer seems to influence the Na and Au diffusion rate, resulting in a disconnectivity between the Na-Au alloy particle and Au interlayer (**Figure 5.3g - h**) and/or local volume expansion of the interlayer with noticeable morphological changes as shown in **Figure 5.10**. However, measurement of the diffusion and reaction rate under different conditions have not been attempted as part of this work. Since EDX analysis indicates an atomic ratio (Na:Au) of around 2:1, the Na-Au alloy formed at the interlayer is the presumably thermodynamically stable intermetallic phase Na_2Au. In addition to directly forming the thermodynamically stable intermetallic phase, other Na-Au alloy phases have been observed where Na was initially deposited during biasing as depicted in **Figure 5.9**. These phases are reactive and continue to change even when the biasing is stopped.

The observed morphological changes of the Au interlayer during sodium deposition depend on different factors, including bias voltage and initial morphology. These factors are assumed to influence the diffusion and reaction rate. This indicates that the factors which affect the diffusion and reaction rate such as deposition potential, deposition current, and the thickness and roughness of the interlayer, need to be considered. This needs to be analyzed in a follow-up study in more detail.

Na diffuses along the Au/e-Pt(C) interface as well as within the e-Pt(C) layer without any observed Na whisker formation. This is presumably related to the high amorphous carbon content in the electron beam deposited Pt as no significant Na diffusion was observed in the ion beam deposited Pt (i-Pt(C)). The diffusion path at the Au/Pt(C) interface is longer than within the Au interlayer (**Figure 5.6**), suggesting Na diffuses faster at this interface.

5.5   Summary

In summary, the Au interlayer behavior including composition and microstructural changes during inhomogeneous cathodic sodium deposition was explored via *in situ biasing* measurements using

Au thin films deposited on the oxide SE with varying morphology and thickness. The resulting morphology after sodium deposition was investigated and discussed also considering the bias voltage.

During sodium deposition, it reacts with the Au interlayer and forms a Na-Au alloy both within the interlayer as well as faceted whiskers growing from the interlayer. A high bias voltage seems to facilitate anisotropic growth of the Na_2Au whiskers. As part of the alloy formation, Na diffuses along the Au interlayer and Au counter diffuses in the Au interlayer towards the position of sodium deposition. This Au counter diffusion is presumably affected by the Na diffusion as it only starts when Na diffuses into the Au interlayer, leading to a chemical potential gradient along the Au interlayer and volumetric expansion of the interlayer. This process finally leads to the conversion of the Au interlayer into the thermodynamically stable Na_2Au interlayer and Au redistribution. This is associated with a morphological change of the interlayer including volume expansion and formation of faceted alloy whiskers and disconnected Na-Au regions within the interlayer. The Au counter diffusion accompanying the Na diffusion along the Au interlayer presumably helps to decrease the volumes expansion at the cost of local formation of Na-Au alloy particles at the initial sodium deposition site. However, in some cases this also leads to an Au redistribution and even formation of discontinuities of the interlayer. This morphological change is especially critical for the cyclic performance as the discontinuous nature of the interlayer may decrease the ability of Na diffusion during the next sodium deposition. Controlling the Au counter diffusion can be beneficial for an even Au distribution and enhanced connectivity of the interlayer during sodium deposition and diffusion.

As the morphological evolution during biasing varies with the bias voltages and Au interlayer morphology and thickness, these factors are assumed to result in different Na and Au reaction and diffusion rates. Even when biasing is stopped, locally the alloy reaction can continue, whereas further Na diffusion along the Au interlayer hardly occurs. This suggests that the diffusion along the Au interlayer may be limited by the bias voltage. Moreover, the current may play a role here as the bias voltage does not only alter the deposition voltage but also the Na^+ ion flux in Na-β''-alumina towards its interface to the Au interlayer in this *in-situ* setup. The influence of current and voltage needs to be studied further. Moreover, a high roughness, i.e. gaps within the Au layer, seem to decrease the diffusion rate along the interlayer, but, enhances the local reaction as volume expansion often happens next to gap regions. However, this gap may also increase the discontinuity of the interlayer after Au counter diffusion as no Na diffuses into the vicinity of interlayer. A thicker (~170 nm) Au interlayer did not lose its connectivity in the current work. This is probably due to the larger amount of Au supporting the alloy reaction with the limited

sodium deposition and diffusion process. To maintain an even Au distribution for long-term stable cycling, the morphology and thickness of the Au interlayer and the corresponding deposition potential and current need to be considered for the battery design. In addition, it was found that amorphous carbon can also be a good candidate to enhance Na uniform diffusion along the Pt(C) layer.

Chapter 6

6. Conclusion and Outlook

6.1   Conclusion

As a critical challenge in Na metal anode based ASSBs, the uncontrolled filamentary dendrite growth within SEs and at the interface between SE and anode significantly limits their overall performance during operation. An "anode-free" ASSB configuration, just with an interlayer between SE and current collector, is a novel approach for easier cell production and to reduce filament growth at the interface between the SE and anode during cycling. This thesis undertakes a comprehensive exploration of ion transport limitations and filament growth within SEs at internal interfaces and delves into the behavior of an Au interlayer in response to inhomogeneous sodium deposition at the interface between the SE and current collector. The thesis sheds light on some of the fundamental processes limiting Na^+ transport and deposition in ASSNBs and how they are related to the microstructure, thus providing new ideas for microstructure and interface engineering to advance the development of ASSNBs.

As Na-β″-alumina is a SE known to exhibit good chemical and electrochemical stability against metallic Na, it is used as a model material for this in-depth investigation. The core of this research

evolved around understanding the intricate relationship between microstructure, microstructural evolution and the resulting electrochemical behavior of Na-β″-alumina in a solid cell. The focus is on an understanding of the role of internal interfaces within the polycrystalline Na-β″-alumina as well as the interfaces that emerge between the SE and anode/current collector, i.e. an Au interlayer. To delve deep into this multifaceted investigation, a combination of *in situ* biasing in the TEM with nanoscale analytical techniques such as EDX, EELS as well as 4D-STEM based orientation mapping have been combined for high temporal and spatial resolution analysis of the microstructural evolution.

For getting access to the microstructural features of SE materials and preparing the *in situ* TEM measurements, FIB processing has been applied to make electron transparent Na-β″-alumina│Au/e-(i)Pt(C) multilayer micro-systems. To perform reliable and meaningful TEM measurements, the impact of SEM imaging and FIB processing on oxide-based SEs has been investigated and summarized in **chapter 3**. This exploration was not only conducted on Na-β″-alumina but included various typical SE materials such as LiPON thin films and NZSP pellets to confirm the generality of the observations. Whisker-like Li/Na particles were observed to grow from the surface of the SE both during SEM imaging and FIB processing. With increasing electron dose this damage became worse, especially at low acceleration voltages. The whisker formation was associated with a significant loss of Na in the TEM lamella of the two Na SEs (Na-β″-alumina & NZSP) even though the crystal structure remained intact. From the observations, it has been concluded that the migration of Li^+/Na^+ ions is primarily driven by the local electric fields generated by charging effects of the electron/ion beam during SEM imaging and FIB processing in the electrically insulating SE. To reduce these charging effects, good electrical contact was found to be effective. However, the final thinning and polishing procedure during FIB processing remained critical. Notably, during this part of the overall sample preparation, cryogenic preparation at liquid N_2 temperature was employed successfully to strongly reduce Na^+ ion mobility. The cryo FIB preparation resulted in TEM samples, where the chemical composition was well preserved. The combination of conductive coating and only performing the final thinning under cryo conditions enabled the use of a standard FIB equipped with a cryogenic stage for the SE TEM sample preparation, whereas no dedicated cryo FIB was required.

Using the above-mentioned FIB processing, electron transparent Na-β″-alumina│Au/e(i)-Pt(C) multilayer micro-systems have been prepared for *in situ* biasing TEM measurements. Cathodic sodium deposition in these systems was induced by employing an STM-TEM holder. In **chapter 4**, the influence of the microstructure, especially of the layered crystal structure leading to anisotropic ionic transport and the role of GBs, on Na filament growth and Na^+ ion transport is

discussed. **chapter 5** focuses on exploring the behavior of Au interlayers, which is known for its ability to protect against filament growth at the interface between SE and anode in an "anode-free" cell, during inhomogeneous sodium deposition.

During *in situ* biasing TEM measurements, Na filament growth was observed at GBs of Na-β''-alumina. Once Na filaments completely occupied a GB, thus establishing a conductive contact to the Au/Pt electrode, they proceeded to penetrate into adjacent GBs. This deposition behavior was not only limited to GBs; it was also observed within voids in bulk cycled Na-β''-alumina. Intriguingly, ZrO_2 was not observed to contribute to filament formation. The resulting formation of a Na filament network among GBs and voids during cathodic sodium deposition is one of the SE based failure modes in solid state cells. To delve deeper into the relationship between GB microstructure and Na filament growth as well as Na^+ ion transport, the local grain orientation was taken into account. The anisotropic ion transport, inherent to the layered crystal structure, in combination with the local electric field orientation leads to a distinct ion migration behavior at different GBs. As a simplified description, the GBs have been classified into 3 main groups with a total of 12 subgroups. These classifications are based upon the orientation of adjacent grains and their alignment in conjunction with the relative orientation of GBs with respect to the applied electric field. A blockade of Na^+ ion migration across GBs has been predicted for specific types of GBs, i.e. type II b1 and type III a2. In agreement with this prediction, during *in situ* biasing TEM measurements Na filament growth has been observed initiated at a type III a2 GBs connected to the electrode. Moreover, modeling based on the full microstructure of the cell used for the *in situ* biasing, revealed an highly uneven current density distribution among grains. This underscores that anisotropic ion transport can exacerbate the impediment on Na^+ ion migration at GBs, resulting in an elevated overpotential at these sites. This elevated overpotential at GBs, in turn, potentially enhances Na^+ reduction and Na filament formation within SEs. Furthermore, the filament formation can induce cracking at the GB, thus influencing the charge transfer and the overall mechanical stability of SEs.

Based on these observations it is expected that SE synthesis/processing leading to preferential orientation (crystallographic texture) and the alignment of this texture with the electric field during battery operation will emerge as pivotal factors to improve the ion transport at GBs and to diminish the potential for Na filament growth within SEs.

In addition to the investigation on sodium deposition at GBs within the SE, the initiation of Na filament growth at the interface between the Na-β''-alumina and the Pt layer is another crucial phenomenon during the *in situ* biasing measurements. In the "anode-free"

Na-β″-alumina │ Au/e(i)-Pt(C) model system, the nanocrystalline Au interlayer behaves in a markedly distinct manner compared to the continuous Na filament growth at the interface between the Na-β″-alumina and Pt layer during cathodic sodium deposition. At the Na-β″-alumina interface coated with Au, Na-Au alloy particles formed during the cathodic sodium deposition. Moreover, aside from the local alloy reaction, Na diffusion occurred along the Au interlayer, while the Au diffused in the opposite direction. This interplay leads to a reduction of local Na filament growth and a conversion of the Au interlayer to a Na-Au interlayer, consisting of thermodynamically stable Na_2Au particles. Importantly, the morphological changes during this conversion vary with biasing voltages and the initial morphology of the Au interlayer including its thickness and the uniformity of the Au layer. These factors seem to significantly influence the alloy particle growth and the Na and Au diffusion rate. At a higher biasing voltage, an anisotropic growth of Na_2Au whisker was observed at the region where sodium deposited. Nevertheless, due to the fast Au and Na diffusion at the high biasing voltage, the morphology of the interlayer may remain fairly unchanged as the additional Na and Au diffuse away, rather than engaging in local alloy reactions that would lead to volume expansion. However, this apparently alters the Au distribution and results in isolated particles detached from the interlayer in the case of a thin Au interlayer. This suggests that the continuity of the Au interlayer and its protective function during further battery cycling is weakened. Furthermore, the inhomogeneity of the Au film seems to impede the diffusion rates, causing volume expansion due to localized alloy reaction and Na-Au alloy particle growth.

In light of these findings, the use of an Au interlayer to mitigate the risk of Na filament growth in "anode-free" cells and to improve cyclic performance mandates careful consideration of the interlayer's thickness and morphology and operating voltage (and/or current) during the construction and operation of the cell. Employing a low bias voltage and ensuring good homogeneity of Au film is expected to play a beneficial role in maintaining the interlayer connectivity during battery operation. Moreover, the amorphous carbon layer can be a good candidate material serving as interlayer as a uniform Na distribution at the Pt(C) layer was observed without morphological changes during sodium deposition.

6.2   Outlook

Aside from the aforementioned insights into the material and battery engineering, there are still open fundamental questions and technical obstacles for TEM characterization worth further investigation.

So far, the impact of crystallographic orientation together with the anisotropic ion transport Na-β″-alumina on blocking ion transport has been studied. However, the extent of filament formation presumably depends on various other factors including the local gradient of ionic/electronic transference numbers, the mechanical properties of the system, and the electronic properties of the GB. To address these issues, a comprehensive exploration of the electronic structure of GBs and their correlation with crystallographic orientation is needed.

Here, local monochromated low-loss EELS studies at GBs together with the known crystal orientation mapping of the neighboring grains is proposed to provide valuable insights into the electronic structure. However, irradiation damage resulting in material changes have to be taken into account as it may influence the results.

Besides band gap changes at some GBs, the space charge layer at GBs is another crucial interfacial effect, which can influence ion transport at GBs. However, there is currently very limited direct microscopic information on the space charge layer and how it is related to the GB character. *In situ* biasing TEM measurements coupled with differential DPC STEM could be a dedicated approach to follow the dynamic processes of the space charge layer at GBs during ion transport.

The anisotropic ion transport leads to the uneven current density distribution. As a consequence, distinctive electric field distribution between adjacent grains with specific orientations are expected due to the current difference. This apparent local electric field distribution can potentially be mapped during the *in situ* biasing TEM measurement and quantified based on STEM-DPC measurements. However, sample bending and movement as a result of mechanical pressure of the W tip and the applied electric field within the STM *in situ* setup have a strong influence on the data acquisition and analysis including the electric field and space charge mapping. Therefore, it is imperative to further refine the protocols for sample preparation and experimental operation to ensure reliable data acquisition and analysis.

In the last part of this study, the primary focus was to follow the microstructural evolution of Au interlayers. Notably, a uniform distribution of Na was also observed at the interface with the amorphous carbon layer. One noteworthy aspect that warrants further investigation is the competitive roles and/or interaction between the amorphous carbon and certain metals, which have the potential for alloying with both Na and Li. An essential next step in understanding this interplay is to explore the microstructural behavior of carbon composite layers with a combination of metal nanoparticles such as Sn, Ag, and Au.

Reference

1.   Meier, P.J., et al., US electric industry response to carbon constraint: a life-cycle assessment of supply side alternatives. Energy Policy, 2005. **33**(9): p. 1099-1108.

2.   Yang, Z., et al., *Electrochemical energy storage for green grid.* Chemical reviews, 2011. **111**(5): p. 3577-3613.

3.   *Global energy perpective 2022.* 2022; Available from: https://www.mckinsey.com/industries/oil-and-gas/our-insights/global-energy-perspective-2022.

4.   Dunn, B., H. Kamath, and J.-M. Tarascon, *Electrical energy storage for the grid: a battery of choices.* Science, 2011. **334**(6058): p. 928-935.

5.   Allen, M.J., *Energy Storage: The Emerging Legal Framework (And Why It Makes a Difference).* Nat. Resources & Env't, 2015. **30**: p. 20.

6.   Guney, M.S. and Y. Tepe, *Classification and assessment of energy storage systems.* Renewable and Sustainable Energy Reviews, 2017. **75**: p. 1187-1197.

7.   Company, M., Systemiq, and W.E. Forum, *A Vision for a Sustainable Battery Value Chain in 2030: Unlocking the Full Potential to Power Sustainable Development and Climate Change Mitigation.* 2019: https://www.weforum.org/. p. 1-52.

8.   *Demand for lithium worldwide in 2020, with a forecast for 2025 and 2030, by application.* Available from: https://www.statista.com/statistics/1220158/global-lithium-demand-volume-by-application/.

9.   Christoph Vaalma, et al., *A cost and resource analysis of sodium-ion batteries.* Nature Reviews Materials, 2018. **3**.

10.   *Advanced and Post Lithium-ion Batteries 2016-2026: Technologies, Markets, Forcasts.* 2016; Available from: https://www.idtechex.com/it/research-report/advanced-and-post-lithium-ion-batteries-2016-2026-technologies-markets-forecasts/449.

11.   SMM Information & Technology Co., L. *Latest update in the SMM Lithium Market.* 2023 [cited 2023 16th Aug. 2023]; Available from: https://www.metal.com/Lithium.

12.   SMM Information & Technology Co., L. *Sodium metal price.* 2023 [cited 2023 16th Aug. 2023]; Available from: https://www.metal.com/search?keyword=sodium&type=price.

13.   Toyota. *Solid-state batteries.* Available from: https://www.toyota.ie/company/news/2021/solid-state-batteries.

14.   Lee, Y.-G., et al., *High-energy long-cycling all-solid-state lithium metal batteries enabled by silver–carbon composite anodes.* Nature Energy, 2020. **5**(4): p. 299-308.

15.   Lou, S., et al., *Interface Issues and Challenges in All-Solid-State Batteries: Lithium, Sodium, and Beyond.* Adv Mater, 2021. **33**(6): p. e2000721.

16.   Ma, Q. and F. Tietz, *Solid-State Electrolyte Materials for Sodium Batteries: Towards Practical Applications.* ChemElectroChem, 2020. **7**(13): p. 2693-2713.

17.   Bragg, W.L., C. Gottfried, and J. West, *The Structure of β Alumina.* Zeitschrift für Kristallographie - Crystalline Materials, 1931. **77**(1-6): p. 255-274.

18.   Beevers, C.A. and M.A.S. Ross, *The Crystal Structure of "Beta Alumina" Na2O·11Al2O3.* Zeitschrift für Kristallographie - Crystalline Materials, 1937. **97**(1-6): p. 59-66.

19.   Pujar, P., et al., *Sodium ion incorporated alumina - A versatile anisotropic ceramic.* Journal of the European Ceramic Society, 2019. **39**(15): p. 4473-4486.

20.   Sudworth, J.L., *Zebra batteries.* Journal of Power Sources, 1994. **51**: p. 105-114.

21.   Banerjee, A., et al., *Interfaces and Interphases in All-Solid-State Batteries with Inorganic Solid Electrolytes.* Chem Rev, 2020. **120**(14): p. 6878-6933.

22.   Xu, L., et al., *Interfaces in Solid-State Lithium Batteries.* Joule, 2018. **2**(10): p. 1991-2015.

23.   Xiao, Y., et al., *Understanding interface stability in solid-state batteries.* Nature Reviews Materials, 2019. **5**(2): p. 105-126.

24.   Lee, B., et al., *Sodium Metal Anodes: Emerging Solutions to Dendrite Growth.* Chemical Reviews, 2019. **119**(8): p. 5416-5460.

25.   Yang, H.-L., et al., *Progress and Challenges for All‐Solid‐State Sodium Batteries.* Advanced Energy and Sustainability Research, 2021. **2**(2).

26.   Zhang, Z., et al., *New horizons for inorganic solid state ion conductors.* Energy & Environmental Science, 2018. **11**(8): p. 1945-1976.

27.   Zhou, W., et al., *Rechargeable Sodium All-Solid-State Battery.* ACS Cent Sci, 2017. **3**(1): p. 52-57.

28.   Tsai, C.-L., et al., *A garnet structure-based all-solid-state Li battery without interface modification: resolving incompatibility issues on positive electrodes.* Sustainable Energy & Fuels, 2019. **3**(1): p. 280-291.

29.   Zhao, C., et al., *Solid-State Sodium Batteries.* Advanced Energy Materials, 2018. **8**(17).

30.   Wu, J.F., et al., *Inorganic Solid Electrolytes for All‐Solid‐State Sodium Batteries: Fundamentals and Strategies for Battery Optimization.* Advanced Functional Materials, 2020. **31**(13).

31.   Wang, Y., et al., *Design principles for solid-state lithium superionic conductors.* Nature Materials, 2015. **14**(10): p. 1026-1031.

32.   He, X., Y. Zhu, and Y. Mo, *Origin of fast ion diffusion in super-ionic conductors.* Nature Communications, 2017. **8**(1): p. 15893.

33.   Pering, S.R. and P.J. Cameron, *The effect of multiple ion substitutions on halide ion migration in perovskite solar cells.* Materials Advances, 2022. **3**(21): p. 7918-7924.

34.   Yung-Fang Yu, Y. and J.T. Kummer, *Ion exchange properties of and rates of ionic diffusion in beta-alumina.* Journal of Inorganic and Nuclear Chemistry, 1967. **29**(9): p. 2453-2475.

35.   Boilot, J.P., G. Collin, and P. Colomban, *Relation structure-fast ion conduction in the NASICON solid solution.* Journal of Solid State Chemistry, 1988. **73**(1): p. 160-171.

36.   Krauskopf, T., et al., *Influence of Lattice Dynamics on Na+ Transport in the Solid Electrolyte Na3PS4–xSex.* Chemistry of Materials, 2017. **29**(20): p. 8859-8869.

37.   Reddy, M.V., et al., *Sulfide and Oxide Inorganic Solid Electrolytes for All-Solid-State Li Batteries: A Review.* Nanomaterials, 2020. **10**(8): p. 1606.

38.   Li, C., et al., *NaSICON: A promising solid electrolyte for solid-state sodium batteries.* Interdisciplinary Materials, 2022. **1**(3): p. 396-416.

39.   Deng, Z., et al., *Phase Behavior in Rhombohedral NaSiCON Electrolytes and Electrodes.* Chemistry of Materials, 2020. **32**(18): p. 7908-7920.

40.   Duchardt, M., et al., *Vacancy-Controlled Na+ Superion Conduction in Na11Sn2PS12.* Angewandte Chemie International Edition, 2018. **57**(5): p. 1351-1355.

41.   Moon, C.K., et al., *Vacancy-Driven Na+ Superionic Conduction in New Ca-Doped Na3PS4 for All-Solid-State Na-Ion Batteries.* ACS Energy Letters, 2018. **3**(10): p. 2504-2512.

42.   Milan, E. and M. Pasta, *The role of grain boundaries in solid-state Li-metal batteries.* Materials Futures, 2022. **2**(1).

43.   Heinz, M.V.F., et al., *Grain size effects on activation energy and conductivity: Na-β″-alumina ceramics and ion conductors with highly resistive grain boundary phases.* Acta Materialia, 2021. **213**.

44.   Xin Guo, Wilfried Sigle, and J. Maire, *Blocking Grain Boundaries in Yttria-Doped and undoped Ceria ceramics of high purity.* Journal of the American Ceramic Society, 2003. **86**(1): p. 77-87.

45.   Wu, J.F. and X. Guo, *Origin of the low grain boundary conductivity in lithium ion conducting perovskites: Li(3x)La(0.67-x)TiO(3).* Phys Chem Chem Phys, 2017. **19**(8): p. 5880-5887.

46.   Wang, Y., et al., *The effect of grain boundary on Na ion transport in polycrystalline solid-state electrolyte cubic Na3PS4.* Materials Research Express, 2021. **8**(2).

47.   Yang, H. and N. Wu, *Ionic conductivity and ion transport mechanisms of solid-state lithium-ion battery electrolytes: A review.* Energy Science & Engineering, 2022. **10**(5): p. 1643-1671.

48.   Lu, Z. and F. Ciucci, *Metal Borohydrides as Electrolytes for Solid-State Li, Na, Mg, and Ca Batteries: A First-Principles Study.* Chemistry of Materials, 2017. **29**(21): p. 9308-9319.

49.   Sadaoka, Y., et al., *Ionic conductivity in Na5YSi4O12-based ceramics with and without additives.* Journal of Materials Science, 1992. **27**(18): p. 5045-5051.

50.   Noi, K., A. Hayashi, and M. Tatsumisago, *Structure and properties of the Na2S–P2S5 glasses and glass–ceramics prepared by mechanical milling.* Journal of Power Sources, 2014. **269**: p. 260-265.

51.   Neyret, M., et al., *Ionic transport of alkali in borosilicate glass. Role of alkali nature on glass structure and on ionic conductivity at the glassy state.* Journal of Non-Crystalline Solids, 2015. **410**: p. 74-81.

52.   Jiang, N. and J.C.H. Spence, *On the dose-rate threshold of beam damage in TEM.* Ultramicroscopy, 2012. **113**: p. 77-82.

53.   Jiang, N., *Damage mechanisms in electron microscopy of insulating materials.* Journal of Physics D: Applied Physics, 2013. **46**(30): p. 305502.

54.   Jiang, N., *Electron beam damage in oxides: a review.* Reports on Progress in Physics, 2016. **79**(1): p. 016501.

55.   Lu, Y., et al., *Electrolyte and Interface Engineering for Solid-State Sodium Batteries.* Joule, 2018. **2**(9): p. 1747-1770.

56.   Li, Z., et al., *Solid-State Electrolytes for Sodium Metal Batteries.* Energy & Fuels, 2021. **35**(11): p. 9063-9079.

57.   Lu, X., et al., *Advanced materials for sodium-beta alumina batteries: Status, challenges and perspectives.* Journal of Power Sources, 2010. **195**(9): p. 2431-2442.

58.   Fertig, M.P., et al., *From High‐ to Low‐Temperature: The Revival of Sodium‐Beta Alumina for Sodium Solid‐State Batteries.* Batteries & Supercaps, 2021. **5**(1).

59.   Koganei, K., et al., *C-axis oriented β″-alumina ceramics with anisotropic ionic conductivity prepared by spark plasma sintering.* Solid State Ionics, 2014. **267**: p. 22-26.

60.   Li, K., et al., *Highly oriented β″-alumina ceramics with excellent ionic conductivity and mechanical performance obtained by spark plasma sintering technique.* Journal of Materials Science, 2020. **55**(20): p. 8435-8443.

61.   Goodenough, J.B., H.Y.P. Hong, and J.A. Kafalas, *Fast Na+-ion transport in skeleton structures.* Materials Research Bulletin, 1976. **11**(2): p. 203-220.

62.   Ihlefeld, J.F., et al., *Scaling Effects in Sodium Zirconium Silicate Phosphate (Na1+xZr2SixP3−xO12) Ion-Conducting Thin Films.* Journal of the American Ceramic Society, 2016. **99**(8): p. 2729-2736.

63.   Samiee, M., et al., *Divalent-doped Na3Zr2Si2PO12 natrium superionic conductor: Improving the ionic conductivity via simultaneously optimizing the phase and chemistry of the primary and secondary phases.* Journal of Power Sources, 2017. **347**: p. 229-237.

64.   Zhang, Z., et al., *A Self-Forming Composite Electrolyte for Solid-State Sodium Battery with Ultralong Cycle Life.* Advanced Energy Materials, 2017. **7**(4): p. 1601196.

65.   Tiwari, A., et al., *Diffusion mechanism in a sodium superionic sulfide-based solid electrolyte: Na11Sn2AsS12.* Journal of Physics D: Applied Physics, 2022. **55**(35): p. 355503.

66.   Zhang, L., et al., *Na3PSe4: A Novel Chalcogenide Solid Electrolyte with High Ionic Conductivity.* Advanced Energy Materials, 2015. **5**(24): p. 1501294.

67.   Marchiori, C.F.N., et al., *Understanding the Electrochemical Stability Window of Polymer Electrolytes in Solid-State Batteries from Atomic-Scale Modeling: The Role of Li-Ion Salts.* Chemistry of Materials, 2020. **32**(17): p. 7237-7246.

68.   Chen, L., et al., *Electrochemical Stability Window of Polymeric Electrolytes.* Chemistry of Materials, 2019. **31**(12): p. 4598-4604.

69.   Lacivita, V., et al., *Ab initio investigation of the stability of electrolyte/electrode interfaces in all-solid-state Na batteries.* Journal of Materials Chemistry A, 2019. **7**(14): p. 8144-8155.

70.   Tian, Y., et al., *Compatibility issues between electrodes and electrolytes in solid-state batteries.* Energy & Environmental Science, 2017. **10**(5): p. 1150-1166.

71.   Luntz, A.C., J. Voss, and K. Reuter, *Interfacial challenges in solid-state Li ion batteries.* J Phys Chem Lett, 2015. **6**(22): p. 4599-604.

72.   Han, F., et al., *Interphase Engineering Enabled All-Ceramic Lithium Battery.* Joule, 2018. **2**(3): p. 497-508.

73.   Banerjee, A., et al., *Revealing Nanoscale Solid-Solid Interfacial Phenomena for Long-Life and High-Energy All-Solid-State Batteries.* ACS Appl Mater Interfaces, 2019. **11**(46): p. 43138-43145.

74.   Pang, Y., et al., *Electrolyte/Electrode Interfaces in All-Solid-State Lithium Batteries: A Review.* Electrochemical Energy Reviews, 2021. **4**(2): p. 169-193.

75.   Oh, J.A.S., et al., *Inorganic sodium solid-state electrolyte and interface with sodium metal for room-temperature metal solid-state batteries.* Energy Storage Materials, 2021. **34**: p. 28-44.

76.   Goodenough, J.B. and Y. Kim, *Challenges for Rechargeable Li Batteries.* Chemistry of Materials, 2010. **22**(3): p. 587-603.

77.   Kehne, P., et al., *Electrochemical Performance of All-Solid-State Sodium-Ion Model Cells with Crystalline NaxCoO2 Thin-Film Cathodes.* Journal of The Electrochemical Society, 2019. **166**(3): p. A5328-A5332.

78.   Wei, T., et al., *An All-Ceramic Solid-State Rechargeable Na+-Battery Operated at Intermediate Temperatures.* Advanced Functional Materials, 2014. **24**(34): p. 5380-5384.

79.   Noguchi, Y., et al., *Fabrication and performances of all solid-state symmetric sodium battery based on NASICON-related compounds.* Electrochimica Acta, 2013. **101**: p. 59-65.

80.   Gao, H., et al., *A Plastic–Crystal Electrolyte Interphase for All-Solid-State Sodium Batteries.* Angewandte Chemie International Edition, 2017. **56**(20): p. 5541-5545.

81.   Zhang, Z., et al., *A ceramic/polymer composite solid electrolyte for sodium batteries.* Journal of Materials Chemistry A, 2016. **4**(41): p. 15823-15828.

82.   Gao, R., et al., *Nanofiber networks of Na3V2(PO4)3 as a cathode material for high performance all-solid-state sodium-ion batteries.* Journal of Materials Chemistry A, 2017. **5**(11): p. 5273-5277.

83.   Lan, T., et al., *Room-temperature all-solid-state sodium batteries with robust ceramic interface between rigid electrolyte and electrode materials.* Nano Energy, 2019. **65**: p. 104040.

84.   Lu, Y., et al., *A High-Performance Monolithic Solid-State Sodium Battery with Ca2+ Doped Na3Zr2Si2PO12 Electrolyte.* Advanced Energy Materials, 2019. **9**(28): p. 1901205.

85.   Zhou, W., et al., *Rechargeable Sodium All-Solid-State Battery.* ACS Central Science, 2017. **3**(1): p. 52-57.

86.   Santhosha, A.L., et al., *Exfoliated MoS2 as Electrode for All-Solid-State Rechargeable Lithium-Ion Batteries.* The Journal of Physical Chemistry C, 2019. **123**(19): p. 12126-12134.

87.   Yue, J., et al., *Long Cycle Life All-Solid-State Sodium Ion Battery.* ACS Appl Mater Interfaces, 2018. **10**(46): p. 39645-39650.

88.   Hayashi, A., et al., *Superionic glass-ceramic electrolytes for room-temperature rechargeable sodium batteries.* Nature Communications, 2012. **3**(1): p. 856.

89.   Yoshida, K., et al., *Fast sodium ionic conduction in Na2B10H10-Na2B12H12 pseudo-binary complex hydride and application to a bulk-type all-solid-state battery.* Applied Physics Letters, 2017. **110**(10): p. 103901.

90.   Koerver, R., et al., *Capacity Fade in Solid-State Batteries: Interphase Formation and Chemomechanical Processes in Nickel-Rich Layered Oxide Cathodes and Lithium Thiophosphate Solid Electrolytes.* Chemistry of Materials, 2017. **29**(13): p. 5574-5582.

91.   Hao, F., et al., *Architectural design and fabrication approaches for solid-state batteries.* MRS Bulletin, 2018. **43**(10): p. 775-781.

92.   Famprikis, T., et al., *Fundamentals of inorganic solid-state electrolytes for batteries.* Nat Mater, 2019. **18**(12): p. 1278-1291.

93.   Hlushkou, D., et al., *The influence of void space on ion transport in a composite cathode for all-solid-state batteries.* Journal of Power Sources, 2018. **396**: p. 363-370.

94.   Doux, J.-M., et al., *Pressure effects on sulfide electrolytes for all solid-state batteries.* Journal of Materials Chemistry A, 2020. **8**(10): p. 5049-5055.

95.   McGrogan, F.P., et al., *Compliant Yet Brittle Mechanical Behavior of Li2S–P2S5 Lithium-Ion-Conducting Solid Electrolyte.* Advanced Energy Materials, 2017. **7**(12): p. 1602011.

96.   Bay, M.-C., et al., *Low Na-β″-alumina electrolyte/cathode interfacial resistance enabled by a hydroborate electrolyte opening up new cell architecture designs for all-solid-state sodium batteries.* Materials Futures, 2022. **1**(3).

97.   Yamauchi, H., et al., *Pressureless all-solid-state sodium-ion battery consisting of sodium iron pyrophosphate glass-ceramic cathode and β″-alumina solid electrolyte composite.* Journal of the American Ceramic Society, 2019. **102**(11): p. 6658-6667.

98.   Zhu, Y., X. He, and Y. Mo, *Origin of Outstanding Stability in the Lithium Solid Electrolyte Materials: Insights from Thermodynamic Analyses Based on First-Principles Calculations.* ACS Applied Materials & Interfaces, 2015. **7**(42): p. 23685-23693.

99.   Perdew, J.P., *Density functional theory and the band gap problem.* International Journal of Quantum Chemistry, 1985. **28**(S19): p. 497-523.

100.   Zhang, W., et al., *The Detrimental Effects of Carbon Additives in Li10GeP2S12-Based Solid-State Batteries.* ACS Applied Materials & Interfaces, 2017. **9**(41): p. 35888-35896.

101.   Swift, M.W. and Y. Qi, *First-Principles Prediction of Potentials and Space-Charge Layers in All-Solid-State Batteries.* Physical Review Letters, 2019. **122**(16): p. 167701.

102.   Katzenmeier, L., et al., *Properties of the Space Charge Layers Formed in Li-Ion Conducting Glass Ceramics.* ACS Applied Materials & Interfaces, 2021. **13**(4): p. 5853-5860.

103.   Nomura, Y., et al., *Direct Observation of a Li-Ionic Space-Charge Layer Formed at an Electrode/Solid-Electrolyte Interface.* Angew Chem Int Ed Engl, 2019. **58**(16): p. 5292-5296.

104.   Wang, L., et al., *In-situ visualization of the space-charge-layer effect on interfacial lithium-ion transport in all-solid-state batteries.* Nat Commun, 2020. **11**(1): p. 5889.

105.   Wenzel, S., et al., *Interfacial Reactivity Benchmarking of the Sodium Ion Conductors Na(3)PS(4) and Sodium beta-Alumina for Protected Sodium Metal Anodes and Sodium All-Solid-State Batteries.* ACS Appl Mater Interfaces, 2016. **8**(41): p. 28216-28224.

106.   Ortmann, T., et al., *Kinetics and Pore Formation of the Sodium Metal Anode on NASICON-Type Na3.4Zr2Si2.4P0.6O12 for Sodium Solid-State Batteries.* Advanced Energy Materials, 2022. **n/a**(n/a): p. 2202712.

107.   Deysher, G., et al., *Evaluating Electrolyte-Anode Interface Stability in Sodium All-Solid-State Batteries.* ACS Appl Mater Interfaces, 2022. **14**(42): p. 47706-47715.

108.   Tang, H., et al., *Probing Solid–Solid Interfacial Reactions in All-Solid-State Sodium-Ion Batteries with First-Principles Calculations.* Chemistry of Materials, 2018. **30**(1): p. 163-173.

109.   Tian, Y., et al., *Reactivity-Guided Interface Design in Na Metal Solid-State Batteries.* Joule, 2019. **3**(4): p. 1037-1050.

110.   Uchida, Y., et al., *Insights into Sodium Ion Transfer at the Na/NASICON Interface Improved by Uniaxial Compression.* ACS Applied Energy Materials, 2019. **2**(4): p. 2913-2920.

111.   Bay, M.C., et al., *Sodium Plating from Na‐β″‐Alumina Ceramics at Room Temperature, Paving the Way for Fast‐Charging All‐Solid‐State Batteries.* Advanced Energy Materials, 2019. **10**(3).

112.   Gao, Z., et al., *Stabilizing Na3Zr2Si2PO12/Na Interfacial Performance by Introducing a Clean and Na-Deficient Surface.* Chemistry of Materials, 2020. **32**(9): p. 3970-3979.

113.   Spencer Jolly, D., et al., *Sodium/Na β″ Alumina Interface: Effect of Pressure on Voids.* ACS Applied Materials & Interfaces, 2020. **12**(1): p. 678-685.

114.   Liu, H., et al., *Controlling Dendrite Growth in Solid-State Electrolytes.* ACS Energy Letters, 2020. **5**(3): p. 833-843.

115.   Liu, X., et al., *Local electronic structure variation resulting in Li 'filament' formation within solid electrolytes.* Nat Mater, 2021. **20**(11): p. 1485-1490.

116.   Sun, B., et al., *Design Strategies to Enable the Efficient Use of Sodium Metal Anodes in High-Energy Batteries.* Adv Mater, 2020. **32**(18): p. e1903891.

117.   Cao, D., et al., *Lithium Dendrite in All-Solid-State Batteries: Growth Mechanisms, Suppression Strategies, and Characterizations.* Matter, 2020. **3**(1): p. 57-94.

118.   Han, F., et al., *High electronic conductivity as the origin of lithium dendrite formation within solid electrolytes.* Nature Energy, 2019. **4**(3): p. 187-196.

119.   Yue, J. and Y.-G. Guo, *The devil is in the electrons.* Nature Energy, 2019. **4**(3): p. 174-175.

120.   Iermakova, D.I., et al., *On the Comparative Stability of Li and Na Metal Anode Interfaces in Conventional Alkyl Carbonate Electrolytes.* Journal of The Electrochemical Society, 2015. **162**(13): p. A7060.

121.   Fuchs, T., et al., *Current-Dependent Lithium Metal Growth Modes in "Anode-Free" Solid-State Batteries at the Cu|LLZO Interface.* Advanced Energy Materials, 2023. **13**(1): p. 2203174.

122.   Kim, S., et al., *The Role of Interlayer Chemistry in Li-Metal Growth through a Garnet-Type Solid Electrolyte.* Advanced Energy Materials, 2020. **10**(12): p. 1903993.

123.   Park, S.H., et al., *Clarification of Li deposition behavior on anodes with a porous interlayer in Li-free all-solid-state batteries.* Journal of Materials Chemistry A, 2022. **10**(41): p. 21995-22006.

124.   Chen, Z., et al., *Bulk/Interfacial Synergetic Approaches Enable the Stable Anode for High Energy Density All-Solid-State Lithium–Sulfur Batteries.* ACS Energy Letters, 2022. **7**(8): p. 2761-2770.

125.   Ma, C., et al., *Atomic-scale origin of the large grain-boundary resistance in perovskite Li-ion-conducting solid electrolytes.* Energy & Environmental Science, 2014. **7**(5): p. 1638-1642.

126.   Lee, T., et al., *Atomic-scale origin of the low grain-boundary resistance in perovskite solid electrolyte Li0.375Sr0.4375Ta0.75Zr0.25O3.* Nature Communications, 2023. **14**(1): p. 1940.

127.   Dawson, J., et al., *Towards Understanding the Different Influences of Grain Boundaries on Ion Transport in Sulfide and Oxide Solid Electrolytes.* 2019. **ChemRxiv**.

128.   Jonghe, L.C.D., *Grain boundaries and ionic conduction in sodium beta alumina.* Journal of Materials Science, 1979. **14**: p. 33-48.

129.   Aaron, H.B. and G.F. Bolling, *Free volume as a criterion for grain boundary models.* Surface Science, 1972. **31**: p. 27-49.

130.   Pal, S., et al., *The spectrum of atomic excess free volume in grain boundaries.* Journal of Materials Science, 2021. **56**(19): p. 11511-11528.

131.   Polczyk, T., et al., *Mitigation of grain boundary resistance in La2/3-xLi3xTiO3 perovskite as an electrolyte for solid-state Li-ion batteries.* Journal of Materials Science, 2020. **56**(3): p. 2435-2450.

132.   Cheng, L., et al., *Effect of surface microstructure on electrochemical performance of garnet solid electrolytes.* ACS Appl Mater Interfaces, 2015. **7**(3): p. 2073-81.

133.   Saranya, A.M., et al., *Engineering Mixed Ionic Electronic Conduction in La0.8Sr0.2MnO3+δ Nanostructures through Fast Grain Boundary Oxygen Diffusivity.* Advanced Energy Materials, 2015. **5**(11): p. 1500377.

134.   Tian, H.-K., et al., *Interfacial Electronic Properties Dictate Li Dendrite Growth in Solid Electrolytes.* Chemistry of Materials, 2019. **31**(18): p. 7351-7359.

135.   Krauskopf, T., et al., *Physicochemical Concepts of the Lithium Metal Anode in Solid-State Batteries.* Chemical Reviews, 2020. **120**(15): p. 7745-7794.

136.   Yu, S. and D.J. Siegel, *Grain Boundary Softening: A Potential Mechanism for Lithium Metal Penetration through Stiff Solid Electrolytes.* ACS Appl Mater Interfaces, 2018. **10**(44): p. 38151-38158.

137.   Rees, G.J., et al., *Imaging Sodium Dendrite Growth in All-Solid-State Sodium Batteries Using (23) Na T(2) -Weighted Magnetic Resonance Imaging.* Angew Chem Int Ed Engl, 2021. **60**(4): p. 2110-2115.

138.   Sakuda, A., A. Hayashi, and M. Tatsumisago, *Interfacial Observation between LiCoO2 Electrode and Li2S−P2S5 Solid Electrolytes of All-Solid-State Lithium Secondary Batteries Using Transmission Electron Microscopy.* Chemistry of Materials, 2010. **22**(3): p. 949-956.

139.   Liu, X.H. and J.Y. Huang, *In situ TEM electrochemistry of anode materials in lithium ion batteries.* Energy & Environmental Science, 2011. **4**(10): p. 3844-3860.

140.   Liu, X.H., et al., *Anisotropic Swelling and Fracture of Silicon Nanowires during Lithiation.* Nano Letters, 2011. **11**(8): p. 3312-3318.

141.   Ruzmetov, D., et al., *Electrolyte Stability Determines Scaling Limits for Solid-State 3D Li Ion Batteries.* Nano Letters, 2012. **12**(1): p. 505-511.

142.   Wang, Z., et al., *In Situ STEM-EELS Observation of Nanoscale Interfacial Phenomena in All-Solid-State Batteries.* Nano Letters, 2016. **16**(6): p. 3760-3767.

143.   Hammad Fawey, M., et al., *In situ TEM studies of micron-sized all-solid-state fluoride ion batteries: Preparation, prospects, and challenges.* Microsc Res Tech, 2016. **79**(7): p. 615-24.

144.   Jiang, N., *On the in situ study of Li ion transport in transmission electron microscope.* Journal of Materials Research, 2014. **30**(3): p. 424-428.

145.   Egerton, R.F., P. Li, and M. Malac, *Radiation damage in the TEM and SEM.* Micron, 2004. **35**(6): p. 399-409.

146.   Qian, D., et al., *Advanced analytical electron microscopy for lithium-ion batteries.* NPG Asia Materials, 2015. **7**(6): p. e193-e193.

147.   Lee, J.Z., et al., *Cryogenic Focused Ion Beam Characterization of Lithium Metal Anodes.* ACS Energy Letters, 2019. **4**(2): p. 489-493.

148.   Nomura, Y., et al., *Visualization of Lithium Transfer Resistance in Secondary Particle Cathodes of Bulk-Type Solid-State Batteries.* ACS Energy Letters, 2020. **5**(6): p. 2098-2105.

149.   Ortmann, T., et al., *Kinetics and Pore Formation of the Sodium Metal Anode on NASICON-Type Na3.4Zr2Si2.4P0.6O12 for Sodium Solid-State Batteries.* Advanced Energy Materials, 2023. **13**(5): p. 2202712.

150.   Dolenko, G.N., O.K. Poleshchuk, and J.N. Latosińska, *X-Ray Emission Spectroscopy, Methods*, in *Encyclopedia of Spectroscopy and Spectrometry (Third Edition)*, J.C. Lindon, G.E. Tranter, and D.W. Koppenaal, Editors. 2017, Academic Press: Oxford. p. 691-694.

151.   Hubbell, J.H., *Radiation Physics*, in *Encyclopedia of Physical Science and Technology (Third Edition)*, R.A. Meyers, Editor. 2003, Academic Press: New York. p. 561-580.

152.   Wells, O.C., *Scanning Electron Microscopy*, in *Encyclopedia of Materials: Science and Technology*, K.H.J. Buschow, et al., Editors. 2001, Elsevier: Oxford. p. 8265-8269.

153.   Egerton, R.F., *Radiation damage to organic and inorganic specimens in the TEM.* Micron, 2019. **119**: p. 72-87.

154.   David B. Williams and C.B. Carter, *Transmission electron microscopy_ a textbook for materials science.* 2009: Springer.

155.   Egerton, R.F., *Mechanisms of radiation damage in beam-sensitive specimens, for TEM accelerating voltages between 10 and 300 kV.* Microsc Res Tech, 2012. **75**(11): p. 1550-6.

156.   Bai, M., W.D. Meisburger, and R.F.W. Pease, *Transient measurement of resist charging during electron beam exposure.* Journal of Vacuum Science & Technology B: Microelectronics and Nanometer Structures Processing, Measurement, and Phenomena, 2002. **21**(1): p. 106-111.

157.   Rau, E.I., et al., *Second crossover energy of insulating materials using stationary electron beam under normal incidence.* Nuclear Instruments and Methods in Physics Research Section B: Beam Interactions with Materials and Atoms, 2008. **266**(5): p. 719-729.

158.   Cazaux, J., *Correlations between ionization radiation damage and charging effects in transmission electron microscopy.* Ultramicroscopy, 1995. **60**(3): p. 411-425.

159.   Giannuzzi, L.A., B.I. Prenitzer, and B.W. Kempshall, *Ion - Solid Interactions*, in *Introduction to Focused Ion Beams: Instrumentation, Theory, Techniques and Practice*, L.A. Giannuzzi and F.A. Stevie, Editors. 2005, Springer US: Boston, MA. p. 13-52.

160.   Wagner, A., *High Resolution Focused Ion Beams: FIB and Its Applications.* Physics Today, 2004. **57**(1): p. 54-55.

161.   Preiß, E.I., et al., *Applicability of focused Ion beam (FIB) milling with gallium, neon, and xenon to the fracture toughness characterization of gold thin films.* Journal of Materials Research, 2021. **36**(12): p. 2505-2514.

162.   Littmark, U. and J.F. Ziegler, *Ranges of energetic ions in matter.* Physical Review A, 1981. **23**(1): p. 64-72.

163.   Liu, J., et al., *Effect of Ion Irradiation Introduced by Focused Ion-Beam Milling on the Mechanical Behaviour of Sub-Micron-Sized Samples.* Scientific Reports, 2020. **10**(1): p. 10324.

164.   Microscopewiki. *Scanning Electron Microscope*. 2022 2022.10.06; Available from: https://microscopewiki.com/scanning-electron-microscope/.

165.   Mayer, J., et al., *TEM Sample Preparation and FIB-Induced Damage.* MRS Bulletin, 2007. **32**(5): p. 400-407.

166.   Yan, J. and N. Takayama, *1 - Introduction*, in *Micro and Nanoscale Laser Processing of Hard Brittle Materials*, J. Yan and N. Takayama, Editors. 2020, Elsevier. p. 1-16.

167.   Wolff, A., *Focused ion beams: An overview of the technology and its capabilities*, in *Wiley Analytical Science*. 2020, Wiley.

168.   Giannuzzi, L.A., et al., *FIB Lift-Out Specimen Preparation Techniques*, in *Introduction to Focused Ion Beams: Instrumentation, Theory, Techniques and Practice*, L.A. Giannuzzi and F.A. Stevie, Editors. 2005, Springer US: Boston, MA. p. 201-228.

169.   Tomus, D. and H.P. Ng, *In situ lift-out dedicated techniques using FIB-SEM system for TEM specimen preparation.* Micron, 2013. **44**: p. 115-9.

170.   Chang, Y., et al., *Ti and its alloys as examples of cryogenic focused ion beam milling of environmentally-sensitive materials.* Nature Communications, 2019. **10**(1): p. 942.

171.   Zhou, J., et al., *Cryogenic Focused Ion Beam Enables Atomic-Resolution Imaging of Local Structures in Highly Sensitive Bulk Crystals and Devices.* Journal of the American Chemical Society, 2022. **144**(7): p. 3182-3191.

172.   Parmenter, C.D. and Z.A. Nizamudeen, *Cryo-FIB-lift-out: practically impossible to practical reality.* J Microsc, 2021. **281**(2): p. 157-174.

173.   Cole, D.A., S. Attavar, and L. Zhang, *Chapter 8 - Surface Analysis Methods for Contaminant Identification*, in *Developments in Surface Contamination and Cleaning (Second Edition)*, R. Kohli and K.L. Mittal, Editors. 2016, William Andrew Publishing: Oxford. p. 333-394.

174.   Hofmann, J.P., M. Rohnke, and B.M. Weckhuysen, *Recent advances in secondary ion mass spectrometry of solid acid catalysts: large zeolite crystals under bombardment.* Phys Chem Chem Phys, 2014. **16**(12): p. 5465-74.

175.   Walther, F., et al., *Influence of Carbon Additives on the Decomposition Pathways in Cathodes of Lithium Thiophosphate-Based All-Solid-State Batteries.* Chemistry of Materials, 2020. **32**(14): p. 6123-6136.

176.   Walther, F., et al., *Visualization of the Interfacial Decomposition of Composite Cathodes in Argyrodite-Based All-Solid-State Batteries Using Time-of-Flight Secondary-Ion Mass Spectrometry.* Chemistry of Materials, 2019. **31**(10): p. 3745-3755.

177.   Bessette, S., et al., *Nanoscale Lithium Quantification in LiXNiyCowMnZO2 as Cathode for Rechargeable Batteries.* Scientific Reports, 2018. **8**(1): p. 17575.

178.   Sui, T., et al., *Nanoscale chemical mapping of Li-ion battery cathode material by FIB-SEM and TOF-SIMS multi-modal microscopy.* Nano Energy, 2015. **17**: p. 254-260.

179.   Xue, W., et al., *Ultra-high-voltage Ni-rich layered cathodes in practical Li metal batteries enabled by a sulfonamide-based electrolyte.* Nature Energy, 2021. **6**(5): p. 495-505.

180.   Zuo, J.M. and J.C.H. Spence, *Advanced transmission electron microscopy imaging and diffraction in nanoscience.* 2017: Springer Nature.

181.   Lee, M., *Transmission electron microscopy (TEM) of Earth and planetary materials: A review.* Mineralogical Magazine, 2010. **74**.

182.   Stadelmann, P. *jems*. 2019; Available from: https://www.jems-swiss.ch/Home/jemsWebSite/jems.html.

183.   Rauch, E.F. and M. Véron, *Automated crystal orientation and phase mapping in TEM.* Materials Characterization, 2014. **98**: p. 1-9.

184.   von Ardenne M and B. DZ., *Untersuchung von metalloxyd-rauchen mit dem universal-elektronenmikroskop.* Electrochemie, 1940. **46**(270-7).

185.   Pennycook, S.J., *A Scan Through the History of STEM*, in *Scanning Transmission Electron Microscopy: Imaging and Analysis*, S.J. Pennycook and P.D. Nellist, Editors. 2011, Springer New York: New York, NY. p. 1-90.

186.   Haider, M., et al., *A spherical-aberration-corrected 200kV transmission electron microscope.* Ultramicroscopy, 1998. **75**(1): p. 53-60.

187.   Batson, P.E., N. Dellby, and O.L. Krivanek, *Sub-ångstrom resolution using aberration corrected electron optics.* Nature, 2002. **418**(6898): p. 617-20.

188.   Kisielowski, C., et al., *Detection of single atoms and buried defects in three dimensions by aberration-corrected electron microscope with 0.5-A information limit.* Microsc Microanal, 2008. **14**(5): p. 469-77.

189.   A., H., *Image-contrast and localized signal selection techniques.* J Microsc, 1979. **117**: p. 11-23.

190.   Gammer, C., et al., *Diffraction contrast imaging using virtual apertures.* Ultramicroscopy, 2015. **155**: p. 1-10.

191.   Ahmed, S., et al., *Visualization of Light Elements using 4D STEM: The Layered-to-Rock Salt Phase Transition in LiNiO2 Cathode Material.* Advanced Energy Materials, 2020. **10**(25).

192.   Zuo, J.-M. and X. Zhu, *Strategies for fast and reliable 4D-STEM orientation and phase mapping of nanomaterials and devices.* Microscopy and Microanalysis, 2021. **27**(S1): p. 762-763.

193.   Jeong, J., et al., *Automated Crystal Orientation Mapping by Precession Electron Diffraction-Assisted Four-Dimensional Scanning Transmission Electron Microscopy Using a Scintillator-Based CMOS Detector.* Microscopy and Microanalysis, 2021. **27**(5): p. 1102-1112.

194.   Mukherjee, D., et al., *4D-STEM Differential Phase Contrast Microscopy Across Ferroelectric Domain Walls.* Microscopy and Microanalysis, 2018. **24**(S1): p. 228-229.

195.   Hÿtch, M.J. and A.M. Minor, *Observing and measuring strain in nanostructures and devices with transmission electron microscopy.* MRS Bulletin, 2014. **39**(2): p. 138-146.

196.   Gammer, C., et al., *Local nanoscale strain mapping of a metallic glass during in situ testing.* Applied Physics Letters, 2018. **112**(17): p. 171905.

197.   Cliff, G. and G.W. Lorimer, *The quantitative analysis of thin specimens.* Journal of Microscopy, 1975. **103**(2): p. 203-207.

198.   J. I. Goldstein, D. B. Williams, and G. Cliff, *Quantitative X-Ray Analysis*, in *Principles of Analytical Electron Microscopy*, D.C. Joy, A.D. Romig, and J.I. Goldstein, Editors. 1986, Springer US: Boston, MA. p. 156.

199.   Thermofisher. *ChemiSTEM Technology: A revolution in EDX analytics*. Available from: https://assets.thermofisher.com/TFS-Assets/MSD/Application-Notes/ChemiSTEM-Application-Brochure.pdf.

200.   Mansour, H. *The importance of hardware components for EDS: the sensor*. 2021; Available from: https://nano.oxinst.com/library/blog/importance-of-the-sensor.

201.   Gubbens, A., et al., *The GIF Quantum, a next generation post-column imaging energy filter.* Ultramicroscopy, 2010. **110**(8): p. 962-970.

202.   *Electron energy loss spectroscopy*. Available from: https://eels.info/about/overview.

203.   Mathiru Kociak, et al., *Spatially Resolved EELS: The Spectrum-Imaging Technique and Its Applications*, in *Scanning Transmission Electron Microscopy*. 2011, Springer.

204.   Nigel D. Browning, et al., *Low-Loss EELS in the STEM*, in *Scanning Transmission Electron Microscopy: Imaging and Analysis*, S. J.Pennycook and P.D. Nellist, Editors. 2011, Springer. p. 660-662.

205.   Zhang, H., C. Wang, and G. Zhou, *Ultra-Microtome for the Preparation of TEM Specimens from Battery Cathodes.* Microsc Microanal, 2020. **26**(5): p. 867-877.

206.   Chae, J.E., et al., *Transmission Electron Microscope Specimen Preparation of Si-Based Anode Materials for Li-Ion Battery by Using Focused Ion Beam and Ultramicrotome.* Applied Microscopy, 2018. **48**(2): p. 49-53.

207.   Park, J.S., et al., *TEM sample preparation of microsized LiMn2O4 powder using an ion slicer.* Appl Microsc, 2021. **51**(1): p. 19.

208.   López, I., et al., *A critical discussion on the analysis of buried interfaces in Li solid-state batteries. Ex situ and in situ/operando studies.* Journal of Materials Chemistry A, 2021. **9**(45): p. 25341-25368.

209.   Song, X., et al., *A special TEM Li-ion battery sample preparation and application technique for investigating the nano structural properties of the SEI in lithium ion batteries.* MRS Advances, 2020. **5**(27): p. 1415-1421.

210.   Masuda, H., et al., *Internal potential mapping of charged solid-state-lithium ion batteries using in situ Kelvin probe force microscopy.* Nanoscale, 2017. **9**(2): p. 893-898.

211.   Lee, J.Z., et al., *Focused Ion Beam Fabrication of LiPON-based Solid-state Lithium-ion Nanobatteries for In Situ Testing.* J Vis Exp, 2018(133).

212.   Li, S., et al., *Direct Observation of Defect-Aided Structural Evolution in a Nickel-Rich Layered Cathode.* Angew Chem Int Ed Engl, 2020. **59**(49): p. 22092-22099.

213.   Zhao, S., et al., *Fundamental air stability in solid-state electrolytes: principles and solutions.* Materials Chemistry Frontiers, 2021. **5**(20): p. 7452-7466.

214.   Tietz, F., J. Koepke, and W. Urland, *Analytical investigations of β-Al2O3 and β″-Al2O3 crystals.* Journal of Crystal Growth, 1992. **118**(3): p. 314-318.

215.   Ding, Z., et al., *Exploring the influence of focused ion beam processing and scanning electron microscopy imaging on solid-state electrolytes.* Microscopy, 2022. **72**(4): p. 326-335.

216.   Ma, Q., et al., *Room temperature demonstration of a sodium superionic conductor with grain conductivity in excess of 0.01 S cm−1 and its primary applications in symmetric battery cells.* Journal of Materials Chemistry A, 2019. **7**(13): p. 7766-7776.

217.   Hausbrand, R., et al., *Surface and Interface Analysis of LiCoO2 and LiPON Thin Films by Photoemission: Implications for Li-Ion Batteries.* Zeitschrift für Physikalische Chemie, 2015. **229**(9): p. 1387-1414.

218.   Fertig, M.P., et al., *Humidity-Induced Degradation of Lithium-Stabilized Sodium-Beta Alumina Solid Electrolytes.* Batteries, 2022. **8**(9).

219.   Kim, K.H., et al., *Charging Effects on SEM/SIM Contrast of Metal/Insulator System in Various Metallic Coating Conditions.* MATERIALS TRANSACTIONS, 2010. **51**(6): p. 1080-1083.

220.   Kanaya, K., et al., *Observations on charging effects of non-conductive and uncoated materials by ion beam pre-bombardment in scanning electron microscopy.* Micron and Microscopica Acta, 1992. **23**(3): p. 319-335.

221.   Neelisetty, K.K., et al., *Electron Beam Effects on Oxide Thin Films—Structure and Electrical Property Correlations.* Microscopy and Microanalysis, 2019. **25**(3): p. 592-600.

222.   Molinari, A., et al., *Configurable Resistive Response in BaTiO3 Ferroelectric Memristors via Electron Beam Radiation.* Advanced Materials, 2020. **32**(12): p. 1907541.

223.   Geng, L., et al., *In situ imaging the dynamics of sodium metal deposition and stripping.* Journal of Materials Chemistry A, 2022. **10**(28): p. 14875-14883.

224.   Hobbs, L.W., et al., *Radiation effects in ceramics.* Journal of Nuclear Materials, 1994. **216**: p. 291-321.

225. Parajuli, P., et al., *Direct Observation of Electron Beam-Induced Phase Transition in MgCrMnO4.* Chemistry of Materials, 2020. **32**(24): p. 10456-10462.

226. Naqash, S., et al., *Impact of sodium excess on electrical conductivity of Na3Zr2Si2PO12 + x Na2O ceramics.* Solid State Ionics, 2019. **336**: p. 57-66.

227. Naqash, S., et al., *Microstructure-conductivity relationship of Na3Zr2(SiO4)2(PO4) ceramics.* Journal of the American Ceramic Society, 2019. **102**(3): p. 1057-1070.

228. Wang, Y., et al., *The effect of grain boundary on Na ion transport in polycrystalline solid-state electrolyte cubic Na3PS4.* Materials Research Express, 2021. **8**(2): p. 025508.

229. Zou, Z., et al., *Identifying Migration Channels and Bottlenecks in Monoclinic NASICON-Type Solid Electrolytes with Hierarchical Ion-Transport Algorithms.* Advanced Functional Materials, 2021. **31**(49).

230. Ding, Z., et al., *The Impact of Microstructure on Filament Growth at the Sodium Metal Anode in All-Solid-State Sodium Batteries.* Advanced Energy Materials. **n/a**(n/a): p. 2302322.

231. Eckhardt, J.K., et al., *Understanding the Impact of Microstructure on Charge Transport in Polycrystalline Materials Through Impedance Modelling.* Journal of The Electrochemical Society, 2021. **168**(9).

232. Eckhardt, J.K., et al., *Interplay of Dynamic Constriction and Interface Morphology between Reversible Metal Anode and Solid Electrolyte in Solid State Batteries.* ACS Applied Materials & Interfaces, 2022. **14**(31): p. 35545-35554.

233. Eckhardt, J.K., et al., *3D Impedance Modeling of Metal Anodes in Solid-State Batteries–Incompatibility of Pore Formation and Constriction Effect in Physical-Based 1D Circuit Models.* ACS Applied Materials & Interfaces, 2022. **14**(37): p. 42757-42769.

234. Aceves, J.M., B.G. Cooksley, and A.R. West, *Charge storage in the gold/β-alumina cell.* Journal of Electroanalytical Chemistry and Interfacial Electrochemistry, 1978. **90**(2): p. 295-297.

235. Ansell, R.O., A. Gilmour, and R.J. Cole, *The role of oxygen ion diffusion in the electrode reactions of β″ alumina.* Journal of Electroanalytical Chemistry and Interfacial Electrochemistry, 1988. **244**(1): p. 123-131.

236. Tang, T.B. and M.M. Chaudhri, *Electrical degradation of ß-alumina.* Journal of Materials Science, 1982. **17**(1): p. 157-163.

237. Bovin, J.O., *On the Degradation of β″-Alumina Ceramics.* Naturwissenschaften, 1984. **71**(5): p. 263-264.

238. Ansell, R., *The chemical and electrochemical stability of beta-alumina.* Journal of Materials Science, 1986. **21**(2): p. 365-379.

239. Jiang, N., et al., *Electron energy loss spectroscopy of Na in Na, Na2O, and silicate glasses.* Journal of Materials Research, 2011. **23**(9): p. 2467-2471.

240. Li, Y., et al., *Unraveling the Reaction Mystery of Li and Na with Dry Air.* Journal of the American Chemical Society, 2023.

241. De Jonghe, L.C., L. Feldman, and A. Beuchele, *Slow degradation and electron conduction in sodium/beta-aluminas.* Journal of Materials Science, 1981. **16**(3): p. 780-786.

242. Liu, X., et al., *Local electronic structure variation resulting in Li 'filament' formation within solid electrolytes.* Nature Materials, 2021.

243. Dong, Y., et al., *Potential jumps at transport bottlenecks cause instability of nominally ionic solid electrolytes in electrochemical cells.* Acta Materialia, 2020. **199**: p. 264-277.

244. Geng, L., et al., *In situ observation of electrochemical Ostwald ripening during sodium deposition.* Nano Research, 2021. **15**(3): p. 2650-2654.

245.   De Jonghe, L.C., *Grain boundaries and ionic conduction in sodium beta alumina.* Journal of Materials Science, 1979. **14**(1): p. 33-48.

246.   Raj, R. and J. Wolfenstine, *Current limit diagrams for dendrite formation in solid-state electrolytes for Li-ion batteries.* Journal of Power Sources, 2017. **343**: p. 119-126.

247.   Futscher, M.H., et al., *Influence of amorphous carbon interlayers on nucleation and early growth of lithium metal at the current collector-solid electrolyte interface.* Journal of Materials Chemistry A, 2022. **10**(29): p. 15535-15542.

248.   Tang, S., et al., *Stable Na Plating and Stripping Electrochemistry Promoted by In Situ Construction of an Alloy-Based Sodiophilic Interphase.* Advanced Materials, 2019. **31**(16): p. 1807495.

249.   Leosson, K., et al., *Ultra-thin gold films on transparent polymers.* Nanophotonics, 2013. **2**(1): p. 3-11.

250.   Martin, P.J., *Ion-enhanced adhesion of thin gold films.* Gold Bulletin, 1986. **19**(4): p. 102-116.

251.   Sharko, S.A., et al., *A New Approach to the Formation of Nanosized Gold and Beryllium Films by Ion-Beam Sputtering Deposition.* Nanomaterials, 2022. **12**(3): p. 470.

252.   Liu, Q., et al., *In Situ Observation of Sodium Dendrite Growth and Concurrent Mechanical Property Measurements Using an Environmental Transmission Electron Microscopy–Atomic Force Microscopy (ETEM-AFM) Platform.* ACS Energy Letters, 2020. **5**(8): p. 2546-2559.

253.   Kienast, G., J. Verma, and W. Klemm, *Das Verhalten der Alkalimetalle zu Kupfer, Silber und Gold.* Zeitschrift für anorganische und allgemeine Chemie, 1961. **310**(3): p. 143-169.

Curriculum Vitae

ZIMING DING
Karlsruhe Institute of Technology (KIT)

EDUCATION

KIT- Karlsruhe Institute of Technology, Germany August 2022
TUD - Technical University of Darmstadt, Germany
Ph. D. program at TUD
Degree Type: Ph. D.
Major: Material science

KIT- Karlsruhe Institute of Technology. Germany August 2018
Degree Type: M. Sc.
Major: Material science and engineering
Master Thesis: supervised by Prof. Helmut Ehrenberg and Dr. Sonia Dsoke
The Influence of Functional Groups of Activated Carbon on its Electrochemical Performance in Supercapacitors

Kunming University of Science and Technology. China June 2014
Degree Type: B. Sc.
Major: Functional Materials

WORKING EXPERIENCE

TUD - Technical University of Darmstadt, Germany
August 2023 – Present
Research associate for doctorate
Project: FLAIR
- TEM Characterization of perovskite material for imaging space charge layers through in situ technique

KIT- Karlsruhe Institute of Technology, Karlsruhe, Germany
August 2019 – August 2023
Research associate for doctorate
Project: Excellent Cluster for post lithium batteries
- In situ TEM investigation on all solid-state sodium batteries
- Additional technique: EDX, EELS, 4D-STEM, ACOM
- FIB fabrication

List of publications (related to thesis)

Z. Ding, Y. Tang, T. Ortmann, J. K. Eckhardt, Y. Dai, M. Rohnke, G. Melinte, C. Heiliger, J. Janek, C. Kübel, *The Impact of Microstructure on Filament Growth at the Sodium Metal Anode in All-Solid-State Sodium Batteries*, Advanced Energy Materials (2023)
DOI: https://doi.org/10.1002/aenm.202302322

Z. Ding, Y. Tang, V. S. K. Chakravadhanula, Q. Ma, F. Tietz, Y. Dai, T. Scherer, and C. Kübel, *Exploring the influence of focused ion beam processing and scanning electron microscopy imaging on solid-state electrolytes*, Microscopy (2022)
DOI: 10.1093/jmicro/dfac064

Ortmann, T., Burkhardt, S., Eckhardt, J. K., Fuchs, T., **Ding, Z.**, Sann, J., Rohnke, M., Ma, Q., Tietz, F., Fattakhova-Rohlfing, D., Kübel, C., Guillon, O., Heiliger, C., Janek, J., *Kinetics and Pore Formation of the Sodium Metal Anode on NASICON-Type $Na_{3.4}Zr_2Si_{2.4}P_{0.6}O_{12}$ for Sodium Solid-State Batteries*. Adv. Energy Mater. (2023)
https://doi.org/10.1002/aenm.202202712

Ortmann, T., Fuchs, T., Eckhardt, J. K., **Ding, Z.**, Ma, Q., Tietz, F., Kübel, C., Rohnke, M., Jürgen, J., *Deposition of Sodium Metal at the Copper-NaSICON Interface for Reservoir-free Solid-State Sodium Batteries,* accepted by Advanced Energy Materials (2023)

List of other publications during PhD

Y. Xiu, Z. Li, V. Bhaghavathi Parambath, **Z. Ding**, L. Wang, A. Reupert, M. Fichtner, Z. Zhao-Karger, *Combining Quinone-Based Cathode with an Efficient Borate Electrolyte for High-Performance Magnesium Batteries*, Batteries & Supercaps, (2021)
https://doi.org/10.1002/batt.202100163

J. Wang, S.L. Dreyer, K. Wang, **Z. Ding**, T. Diemant, G. Karkera, Y. Ma, A. Sarkar, B. Zhou, M. V. Gorbunov, *P2-type layered high-entropy oxides as sodium-ion cathode materials*, Materials Futures, (2022)
DOI 10.1088/2752-5724/ac8ab9

Xiu, Y., Mauri, A., Dinda, S., Pramudya, Y., **Ding, Z.**, Diemant, T., Sarkar, A., Wang, L., Li, Z., Wenzel, W., Fichtner, M., Zhao-Karger, Z., *Anion Storage Chemistry of Organic Cathodes for High-Energy and High-Power Density Divalent Metal Batteries*, Angew. Chem. (2023)
https://doi.org/10.1002/anie.202212339

Wang, K., Hua, W., Huang, X. **Ding, Z.**, *et al. Synergy of cations in high entropy oxide lithium ion battery anode*. Nat Commun., (2023)
https://doi.org/10.1038/s41467-023-37034-6

Lin, L., **Ding, Z.**, Karkera, G., Diemant, T., Kante, M.V., Agrawal, D., Hahn, H., Aghassi-Hagmann, J., Fichtner, M., Breitung, B., Schweidler, S., *High-Entropy Sulfides as Highly Effective Catalysts for the Oxygen Evolution Reaction*. Small Struct., (2023)
https://doi.org/10.1002/sstr.202300012

Fu, Q., Schwarz, B., **Ding, Z**., Sarapulova, A., Weidler, P. G., Missyul, A., Etter, M., Welter, E., Hua, W., Knapp, M., Dsoke, S., Ehrenberg, H., *Guest Ion-Dependent Reaction Mechanisms of New Pseudocapacitive Mg₃V₄(PO₄)₆/Carbon Composite as Negative Electrode for Monovalent-Ion Batteries*. Adv. Sci. (2023)
https://doi.org/10.1002/advs.202207283

List of previous publications

Ding, Z., Trouillet, V., Dsoke, S., *Are Functional Groups Beneficial or Harmful on the Electrochemical Performance of Activated Carbon Electrodes?* Journal of The Electrochemical Society (2019)